3-17-2021

Development of Phosphorus-Based Electrode Materials for Energy Storage Applications

Amin Rabiei Baboukani
Florida International University, 5865712@fiu.edu

FLORIDA INTERNATIONAL UNIVERSITY

Miami, Florida

DEVELOPMENT OF PHOSPHORUS-BASED ELECTRODE MATERIALS FOR ENERGY STORAGE APPLICATIONS

A dissertation submitted in partial fulfillment of the

requirement for the degree of

DOCTOR OF PHILOSOPHY

in

MATERIALS SCIENCE AND ENGINEERING

by

Amin Rabiei Baboukani

2021

To: Dean John L. Volakis
College of Engineering and Computing

This dissertation, written by Amin Rabiei Baboukani, and entitled Development of Phosphorus-Based Electrode Materials for Energy Storage Applications, having been approved in respect to style and intellectual content, is referred to you for judgment.

We have read this dissertation and recommend that it be approved.

_____
Norman D. H. Munroe

_____
Bilal El-Zahab

_____
Wenzhi Li

_____
Nezih Pala

_____
Chunlei Wang, Major Professor

Date of Defense: March 17, 2021

The dissertation of Amin Rabiei Baboukani is approved.

_____
John L. Volakis
Dean of College of Engineering and Computing

_____
Andrés G. Gil
Vice President for Research and Economic Development
and Dean of the University Graduate School

Florida International University, 2021

DEDICATION

I dedicate this thesis to my parents Mehri and Ahmad and also my brother Amir. Without their support, love, patience, and understanding the completion of this work would not have been possible.

ACKNOWLEDGMENTS

First and foremost, I would like to express my deepest appreciation to my advisor Dr. Chunlei Wang for her guidance, vision and support throughout my doctoral program. I also appreciate her efforts on reviewing and critiquing my research and writing, which helped me in improving the quality of my work.

I would like to extend my gratitude to the members of my dissertation committee – Dr. Norman Munroe, Dr. Bilal El-Zahab, Dr. Wenzhi Li, and Dr. Nezih Pala for their willingness to serve on my committee and for providing unwavering support, professionally and personally, along the way. My sincere thanks also goes to Dr. Vadym Drozd, Dr. Anis Allagui, Dr. Yusuf Emirov, Dr. Andriy Durygin, and Dr. Sadegh Mehdi Aghaei for their help and support during the course of my PhD. I am also thankful to Dr. Zhe Cheng and Dr. Jinhua Chen for their valuable comments.

I am very thankful to the University Graduate School (UGS) at Florida International University for supporting me through Dissertation Evidence Acquisition (DEA), and Dissertation Year Fellowship (DYF) awards. I am also thankful to the Department of Mechanical and Materials Engineering (MME) at FIU for providing me with teaching assistantship (TA) and the National Science Foundation (NSF) to support my PhD program.

This work would not have been possible without the technical facilities provided at Advanced Materials Engineering Research Institute (AMERI) and the Center of Study Matter at Extreme Condition (CeSMEC) at FIU. I am very grateful to Dr. Patrick Roman, Dr. Alexander Franco Hernandez, Dr. Meer Safa, Jonathan Comparan, and Steward Schwarz for their patience and help with my experimentation.

I am thankful to our previous and present members of my research group – Dr. Yong Hao, Dr. Richa Agrawal, Dr. Ebenezer Dotun Adelowo, Dr. Wei Shang, Iman Khakpour, Shahrzad Forouzanfar, Omena Okpowe, Azmal Chowdhury, Borzooye Jafarizadeh, and Ana Claus for their company and help during my PhD.

Last but not the least; I would also like to express my appreciations to my parents and my brother Amir and my close friends at FIU. Also, I would like to acknowledge the teachers, professors, and other professionals who either directly trained me, or inspired me in some way.

ABSTRACT OF THE DISSERTATION

DEVELOPMENT OF PHOSPHORUS-BASED ELECTRODE MATERIALS FOR ENERGY STORAGE APPLICATIONS

by

Amin Rabiei Baboukani

Florida International University, 2021

Miami, Florida

Professor Chunlei Wang, Major Professor

With the rapid development of modern society, the huge demand for energy storage systems from fossil fuels leads to dramatic increasing of greenhouse gases. Therefore, an efficient green energy storage system with high energy density and stable cyclability is urgently required for advanced electronics. The electrochemical performance of energy storage devices strongly depends on the electrode materials. Among the recent advances on electrode materials, phosphorus as an earth-abundant element with high theoretical specific capacity (2596 $mAhg^{-1}$) and low cost has attracted intensive attention. However, low conductivity and high volume expansion of phosphorus-based electrodes hindered its real performance in energy storage applications. Moreover, exfoliation of BP into phosphorene nanosheets is still time-consuming, toxic, and leads to high defect concentration. This dissertation is tailored to overcome both materials engineering and eco-friendly and scalable manufacturing issues to make high-performance phosphorus-based electrode materials.

In the first part of this dissertation, RP with sulfurized polyacrylonitrile (RP-SPAN) hybrids were synthesized via electrostatic spray deposition (ESD) and characterized

as an anode material for lithium-ion batteries (LIBs). The developed hybrid anode delivered excellent specific capacity up to 1605 $mAhg^{-1}$ at 0.1 A g^{-1} at 100 cycles. The fabricated electrode improved the conductivity of RP and also endured its large volume changes upon cycling. Moreover, the fabricated RP-based LIBs were evaluated in both frequency and time domains in terms of stationarity, stability, and linearity, as well as degradation with extended charge/discharge cycling.

Exfoliation and deposition of BP into 2D phosphorene nanosheets through the novel one-step, facile, and environmentally friendly method of bipolar electrochemical exfoliation (BPE) on the feeding electrodes was other major goal of the dissertation. The presence of point defects, grain boundaries, and amorphization of bipolar exfoliated phosphorene nanosheets was evaluated through high-resolution transmission electron microscopy (HRTEM) analysis and density functional theory (DFT) calculations. The electrochemical performance of the bipolar exfoliated phosphorene nanosheets with an orthorhombic crystal structure was also evaluated in a symmetric two-electrode configuration for supercapacitor applications. The fabricated device delivered a high power density of 351 mW cm^{-2} at a constant current load discharge of 500 mA cm^{-2} with high stability and reversibility for at least 40000 cycles. The results in this dissertation could open up new horizons to improve the performance of P-based electrodes for energy storage applications.

TABLE OF CONTENTS

LIST OF TABLES

TABLE PAGE

LIST OF FIGURES

FIGURE PAGE

1. Introduction

1.1 Overview

With the fast development of the worldwide economy, increasing population, fossil fuel consumption, and also global warming sustainable and renewable energy technologies are needed for future energy storage devices. Most renewable energy sources are dependent on weather conditions and time of the day. Rechargeable batteries and electrochemical supercapacitors with high power/energy densities are the most important electrochemical energy storage devices based on the conversion of chemical energy into electrical energy and have been successfully commercialized for a wide range of applications such as portable power sources and electric vehicles. However, there is a concern about the ability of rechargeable battery and supercapacitor technology to meet the growing demands of electronic devices [1, 2].

Each battery or supercapacitor device is composed of negative and positive electrodes separated by a separator that allows ion transfer in a specific electrolyte solution with mobile ionic species [3]. The key factors for an ideal electrochemical energy storage device include high energy storage density, power density, excellent cyclability, and rate capability, which are strongly dependent on the type of electrode materials [4]. Among different types of rechargeable batteries, lithium-ion batteries (LIBs) providing a high gravimetric energy density of about 250 W h kg-1 with long service life. However, the sluggish oxidation/reduction reaction, electrode instability, and unpredictable side reactions at electrode/electrolyte interfaces in LIBs limiting its actual performance. Supercapacitors with high power density, fast charging/discharging rate, and long cycle life (more than 100000 cycles) have attracted attention in both academia and industry [5]. However, their insufficient

energy density <10 W h kg-1 hinders their widespread application in electronic devices [6].

Enhancing the performance of advanced energy storage devices through the development of electrode materials is one of the promising approaches for the future of energy industries. From the electrode point of view, different one-dimensional (1D) and two-dimensional (2D) nanostructured materials have been utilized in batteries and supercapacitors to improve the cyclability and rate capability. Moreover, many kinds of hybrid composite materials have been developed in order to improve the electrochemical performance of energy storage devices. In terms of structure, various types of one-dimensional (1D) and two-dimensional (2D) nanosheets have been evaluated for high-performance energy storage devices. However, developing a novel environmentally friendly electrode material with high electrochemical performance is still challenging. Moreover, providing a facile, straightforward, and scalable technique to produce novel materials for energy storage devices is necessary.

1.2 Research Problems

The ultimate goal of this dissertation is to develop and assess high electrochemical performance LIBs and supercapacitors through novel phosphorus-based electrode material synthesis. The research problems encountered in this dissertation and their possible solutions are discussed as follows:

1. How to increase the electrochemical performance of Phosphorus-based material for energy storage devices?

Poor conductivity and large volume expansion: Phosphorus-based electrodes have been studied as an electrode material for LIBs and supercapacitors because of their chemical stability in an ambient environment. However, its low conductivity (~ 10^{-4}

S/cm) and volume expansion up to 300% leading to pulverization of the electrode material, and thus poor reversibility and fast capacity fading [7]. Due to the nature of phosphorus as a nonmetallic element, there is a far away between its theoretical capacity (2596 m A hg^{-1}) and experimental results [8, 9]. To address this problem, various strategies have been explored. It has been evaluated that the conductivity of phosphorus-based electrodes can be improved by introducing a conductive carbonaceous agent and providing a hybrid composite. Different types of 1D and 2D carbon materials have been incorporated with phosphorus for different energy storage systems [10]. However, using a carbon-based material with stable chemical bonding with phosphorus is still a challenge, and therefore developing a unique conductive matrix to realize the strong chemical interaction with phosphorus is still lacking. Obtaining stable cycling performance of P-based electrodes need a high percentage of carbon source up to 70% and as a results, decreases a real energy density. Moreover, the electrochemical stability of the P-based electrodes in energy storage applications is still unclear. Obtaining stable cycling performance needs a high proportion of the low capacity carbon from 30 to 70%, results in the decrease of real battery energy density.

2. How to effectively develop the single-step exfoliation and deposition of black phosphorus?

In recent years, exfoliation and preparation of black phosphorus (BP) as a 2D material knows as phosphorene through top-down and bottom-up techniques have been demonstrated. Specifically, liquid-based exfoliation of bulk BP is considered an inexpensive method to produce BP nanosheets in large quantities. However, typically these methods are time-consuming, toxic, multi-step, and not scalable. Moreover,

degradation of the synthesized material hindered its real performance in energy storage applications. As a result, *providing a single-step, facile, and scalable exfoliation and deposition of BP into phosphorene nanosheets* is necessary. Furthermore, optimization of the exfoliation of BP setup in terms of voltage, current, and size of the conductive substrate through the process is still challenging. Therefore, choosing *the optimal experimental procedure* can enhance the exfoliation of nanosheets.

3. What are the defects structures for the bipolar exfoliated phosphorene nanosheets via transmission electron microscopy (TEM) analysis?

Researchers handled phosphorene nanosheets under ambient conditions for a short period of time, but invariable instability and degradation of phosphorene nanosheets still have been a major impediment in different exfoliation techniques and the presence of lone pairs of phosphorus atoms at the surface of nanosheets makes it air-sensitive. Therefore, there is a need to understand the fundamental properties of BP nanosheets. Despite the theoretical calculation efforts, *in-depth experimental defect analysis of BP nanosheets* has not been extensively explored so far. Evaluating the types of defects on exfoliated phosphorene nanosheets via TEM may open a new horizon to control its degradation and improve its electrochemical performance.

1.3 Hypotheses

Phosphorus-based electrodes are very promising for rechargeable batteries and supercapacitors. As discussed in the previous section, a various type of conductive carbonaceous hosts has been applied to Phosphorus-based electrodes to improve the conductivity and control the volume expansion during cycling. The hypothesis encountered in this thesis are as follows:

1. The strong chemical bonding of phosphorus with the conductive agent could maintain the electrical connection and suppress the huge volume change of phosphorus and thus maintain its structural stability during cycling. Forming an effective chemical bond among hybrid electrodes could improve the kinetics and electrochemical performance of phosphorus-based electrodes.

2. Single-step bipolar electrochemistry (BPE) technique could create enough potential on the bipolar electrode to break the bonds between the BP layers and exfoliate BP into crystalline phosphorene nanosheets with low defect concentration.

3. Due to the redox reactions on the two poles of the bipolar electrode, BP nanosheets with different functionality could deposit on different sides of conductive feeding electrodes. By tuning the applied voltage, current, and time, phosphorene nanosheets with preferred thickness and high stability could deposit on the conductive substrates.

4. The unique vertically aligned 2D phosphorene nanosheets on the conductive substrate via the BPE method could improve the kinetics and provide a binder-free electrode material for high-performance energy storage applications.

1.4 Research Plan

The research plan adopted for this dissertation is presented in Figure 1.1; the specific goals that were worked toward are as follows:

1. *Material development and synthesis:* In order to overcome the low conductivity and large volume expansion of red phosphorus (RP) as an anode material for LIBs, it is imperative to identify the novel conductive matrix. To attain this goal, sulfurized polyacrylonitrile (SPAN) was synthesized from a mixture of PAN and sulfur, and the developed anodes were prepared via ball milling and electrostatic spray deposition (ESD) techniques and were characterized from both materials and electrochemical

aspects. Moreover, the electrochemical stability and linearity/nonlinearity of the developed anode was evaluated through small-amplitude sinusoidal voltage excitations and its time-domain constant-current charge/discharge dynamics. Moreover, single-step exfoliation and deposition of BP into phosphorene nanosheets via novel bipolar electrochemistry method was evaluated. Due to the anodic and cathodic reaction on the two poles of the bipolar electrode, exfoliated nanosheets migrate and deposit on both feeding electrodes. The possibility of exfoliation and deposition, the chemical composition, and the surface properties on two positive and negative feeding electrodes were investigated using different material characterization techniques. The exfoliation parameters were optimized for maximal uniform deposition of nanosheets for high-performance energy storage applications.

2. *Defect characterization of phosphorene nanosheets:* Possible formation of defects and amorphization in bipolar exfoliated phosphorene nanosheets were evaluated through transmission electron microscopy (TEM) analysis and Density Functional Theory (DFT) calculations.

3. *Electrochemical performance of the developed electrode material*: The hybrid RP-SPAN electrode material and the exfoliated phosphorene nanosheets were evaluated as electrode material for energy storage devices such as batteries and supercapacitors.

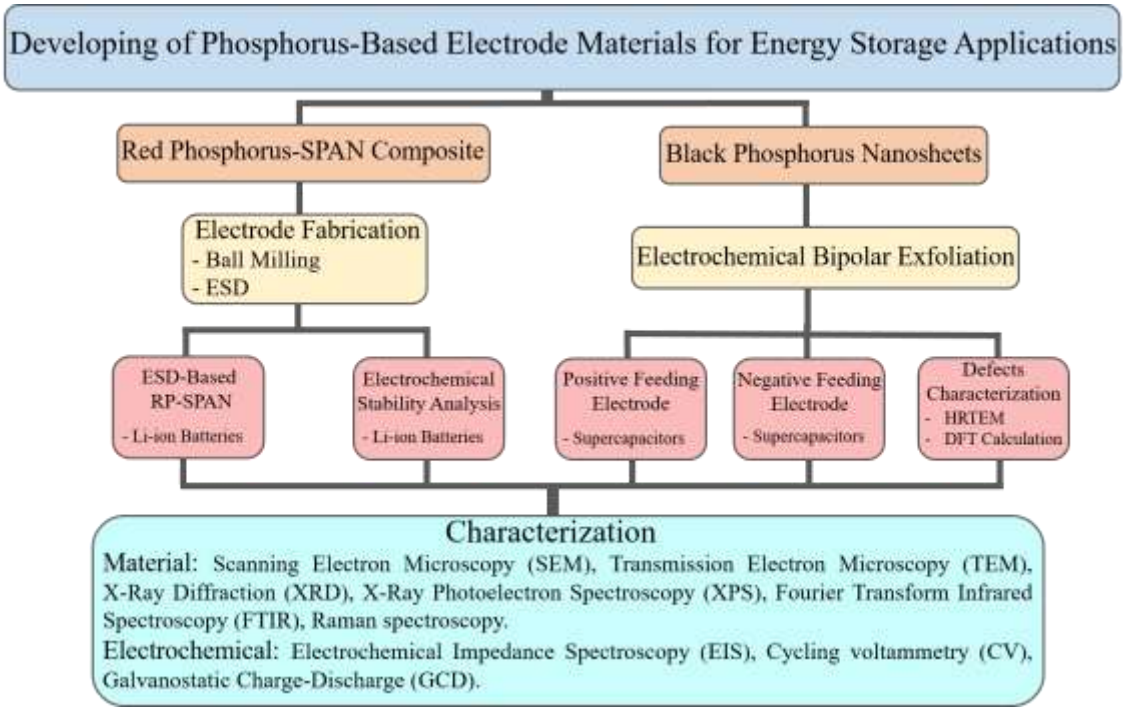

Figure 1.1: Flow chart of the research plan.

1.5 Scope of the Dissertation

My PhD dissertation consists of eight chapters. Chapter 1 is highlighted the motivation, research problem and hypothesis. Chapter 2 provides the background of the dissertation about the phosphorus properties. The two main allotropes of phosphorus which are RP and BP have been discussed for energy storage applications. In order to provide an insight for further investigation of BP, the historical background of its liquid-based exfoliation and its application for energy storage devices were discussed comprehensively. Chapter 2, in part, is a reprint of the material "Liquid-Based Exfoliation of Black Phosphorus into Phosphorene and Its Application for Energy Storage Devices" as it appears in the Small Structures, A. Rabiei Baboukani, I. Khakpour, V. Drozd, C. Wang, (2021), 306, 2000148. The dissertation author was the first author of this paper.

Chapter 3 provides a detailed methodology of the experimental methods adopted for this dissertation including ESD and BPE techniques. Moreover, different materials and electrochemical characterization techniques were highlighted.

Chapter 4 presents the results of RP-SPAN anode material by electrostatic spray deposition for LIBs. The half-cell performance of the developed anode was evaluated with lithium metal as the counter and reference electrode. Chapter 4, in full, is a reprint of the material "High-performance red Phosphorus-sulfurized polyacrylonitrile composite by electrostatic spray deposition for lithium-ion Batteries" as it appears in the Electrochimica Acta, A. Rabiei Baboukani, I. Khakpour, E. Adelowo, V. Drozd, W. Shang, C. Wang, (2020) 345, 136227, 2020. The dissertation author was the primary investigator and first author of this paper.

Chapter 5 discusses ESD derived RP-SPAN electrode as an anode of LIBs with the transfer function stability analysis and the differential capacity analysis to evaluate the system's behavior in both frequency and time domains in terms of stationarity, stability, and linearity, as well as dissipation and degradation with extended charge/discharge cycling. Chapter 5, in full, is a reprint of the material "On the electrochemical stability analysis of red phosphorus-based anode for lithium-ion batteries" as it under review in the Electrochimica Acta, A. Allagui, A. Rabiei Baboukani, A. S. Elwakil, C. Wang. The dissertation author was the co-primary investigator and co-first author of this paper.

Chapter 6 investigates an in-depth study of exfoliation and deposition of BP into phosphorene nanosheet on the positive and negative feeding electrodes via single-step BPE technique. Also, the electrochemical performance of the exfoliated nanosheets on the positive feeding electrodes have been evaluated as an electrode for supercapacitor applications. Chapter 6, in part, is a reprint of the material "Single-step

exfoliation of black phosphorus and deposition of phosphorene via bipolar electrochemistry for capacitive energy storage application" as it appears in the Journal of Materials Chemistry A, A. Rabiei Baboukani, I. Khakpour, V. Drozd, A. Allagui, C. Wang (2019), 7(44), 25548-25556. The dissertation author was the primary investigator and first author of this paper.

Chapter 7 expands on the defect formation and degradation of exfoliated phosphorene nanosheets via the BPE method using TEM analysis and DFT calculations. Chapter 7, in full, is a reprint of the material "Atomic Defects Characterization of Bipolar Exfoliated Black Phosphorus Nanosheets Using Transmission Electron Microscopy", as it under review in the Journal of Nanotechnology, A. Rabiei Baboukani, S. M. Aghaei, I. Khakpour, V. Drozd, C. Wang. The dissertation author was the primary investigator and first author of this paper. Chapter 8 provides a conclusion and future work direction of this dissertation.

1.6 References

[1] X. Yao, Y. Zhao, Three-dimensional porous graphene networks and hybrids for lithium-ion batteries and supercapacitors, Chem 2(2) (2017) 171-200.

[2] M.F. El-Kady, Y. Shao, R.B. Kaner, Graphene for batteries, supercapacitors and beyond, Nature Reviews Materials 1(7) (2016) 1-14.

[3] J.-M. Tarascon, M. Armand, Issues and challenges facing rechargeable lithium batteries, Materials for sustainable energy: a collection of peer-reviewed research and review articles from Nature Publishing Group, World Scientific2011, pp. 171-179.

[4] P. Simon, Y. Gogotsi, B. Dunn, Where do batteries end and supercapacitors begin?, Science 343(6176) (2014) 1210-1211.

[5] C. Zhong, Y. Deng, W. Hu, J. Qiao, L. Zhang, J. Zhang, A review of electrolyte materials and compositions for electrochemical supercapacitors, Chemical Society Reviews 44(21) (2015) 7484-7539.

[6] A. González, E. Goikolea, J.A. Barrena, R. Mysyk, Review on supercapacitors: Technologies and materials, Renewable and Sustainable Energy Reviews 58 (2016) 1189-1206.

[7] A. Rabiei Baboukani, I. Khakpour, E. Adelowo, V. Drozd, W. Shang, C. Wang, High-performance red phosphorus-sulfurized polyacrylonitrile composite by electrostatic spray deposition for lithium-ion batteries, Electrochimica Acta 345 (2020) 136227.

[8] W. Liu, H. Zhi, X. Yu, Recent progress in phosphorus based anode materials for lithium/sodium ion batteries, Energy Storage Materials 16 (2019) 290-322.

[9] Y. Sun, L. Wang, Y. Li, Y. Li, H.R. Lee, A. Pei, X. He, Y. Cui, Design of red phosphorus nanostructured electrode for fast-charging lithium-ion batteries with high energy density, Joule 3(4) (2019) 1080-1093.

[10] S. Wu, K.S. Hui, K.N. Hui, 2D black phosphorus: from preparation to applications for electrochemical energy storage, Advanced Science 5(5) (2018) 1700491.

2. Background and Literature Review

2.1 Historical Overview

With the increasing demand for energy and exhausting refined fossil fuels during the past decade, different types of clean energy sources are emerging very fast. Therefore, a large-scale energy storage systems such as rechargeable batteries and electrochemical capacitors (also known as supercapacitors or ultra-capacitors) are necessary for future practical applications [1]. Lithium-ion batteries (LIBs) as the most common rechargeable batteries have been presenting great promises due to their high energy conversion and stable cyclability. Since the first commercial LIB in early 1990s, this technology has been experiencing great progress in different applications ranging from portable electronics to electric vehicles and large industrial equipment [2]. Developing fabrication method along with advances in nanomaterials as an electrode, electrolytes and packaging, has resulted in improved electrochemical performance of LIBs [3]. However, due to the slow power delivery and resistive losses from sluggish electron and ion transport in LIBs, there is a need for fast and high power energy systems. On the other hand, supercapacitors provide high power density, fast charging/discharging, and great stability [4]. The energy density of supercapacitors (~ 5 W h kg^{-1}) is lower than LIBs, but provides higher power density up to 10 k W kg^{-1} in a few seconds. Figure 2.1 illustrates a plot of energy density versus power density known as a Ragone plot for different energy storage applications. Although the supercapacitors filled the gap between conventional capacitors and LIBs, their energy density is still too low for power future electronic. The report from the US Department of Energy has confirmed the importance of LIBs and supercapacitors for future energy storage applications [5].

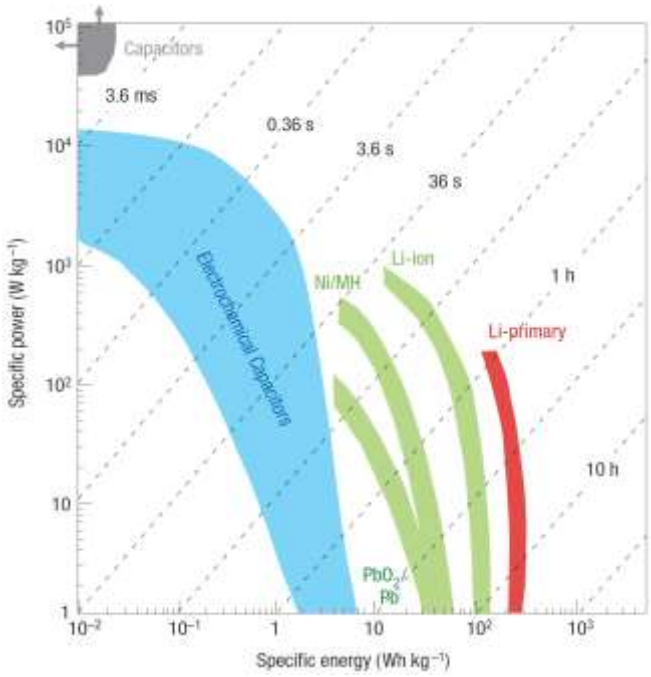

Figure 2.1: Ragone plot of specific power versus specific energy for different energy storage devices [5].

2.2 Phosphorus Allotropes

Phosphorus (P) as a nonmetallic element from group 15 of the periodic table and one of the most abundant element in the Earth's crust (0.105%) possesses four main allotropes: white phosphorus (WP), violet phosphorus (VP), red phosphorus (WP), and black phosphorus (BP), named based on their appearance (Figure 2.2). WP is highly symmetrical with tetrahedral crystal structure and large bonding strain. Meanwhile, WP is flammable in air at 34°C and very toxic which is not suitable for energy storage applications from the viewpoints of safety concern. However, WP always serves as the starting material to synthesis other allotrope of phosphorus. RP is an amorphous allotrope of phosphorus with covalent molecular structure obtained from cleavage of P_4 molecule. RP is thermodynamically stable in air and can directly obtained from WP in N_2 atmosphere at 300°C. As shown in Figure 2.2, VP can be synthesized through the annealing of WP at 550°C with the presence of molten lead.

In different types of phosphorus, BP is the most thermodynamically stable allotrope and can produces from WP or RP. BP presents higher electrical conductivity compared to RP and has a similar structure to graphite [7].

2.2.1 Red Phosphorus

RP is the most common allotrope of phosphorus which is stable in air up to 260°C and in terms of cost, it is comparable to graphite and much less expensive compared to silicon nanoparticles [8]. Many types of flares use RP to help in the ignition process. The sustained combustion of the flare is also achieved with the help of this allotrope. Moreover, the mixture of RP with magnesium and a binder, can be used as a smoke device that can create a smoke screen quickly. It also used as a flame retardant in many thermoplastics [9]. Considering the abundance, environmental friendliness, high chemical stability, and easy handling of RP, great progress has been made in the development of RP-based electrodes for high-performance energy storage application.

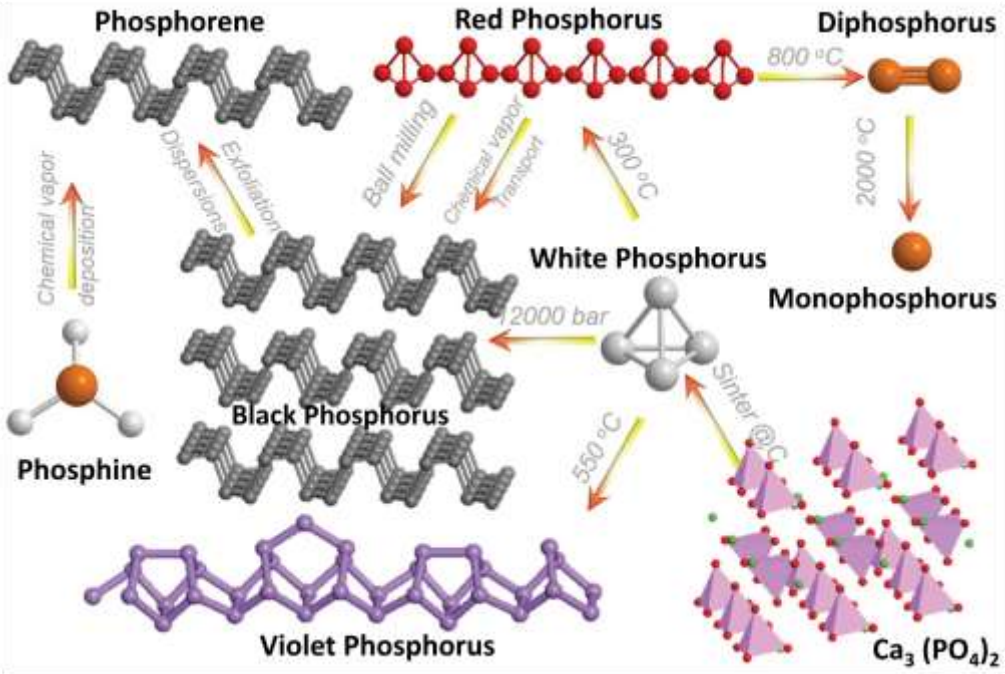

Figure 2.2: Different Phosphorus allotropes with their transformation reactions [7].

RP is a promising electrode material for energy storage application due to its high theoretical capacity of 2596 m A hg^{-1}. However, the drastic volume change (300%) of RP during cycling and its low conductivity (10^{-14} S cm^{-1}), limiting the actual performance of RP. To alleviate these issues, different strategies via the nanoscaling of RP particles and providing conductive materials have been evaluated to decrease the ion transport distance and improve the electrochemical performances. Up to now, Carbonaceous materials including graphene, reduced graphene oxide (rGO), activated carbon, carbon nanotube, etc., served as the conductive matrix to scaffold phosphorus. Very recently, conductive polymers were also introduced to phosphorus to form a heterostructure composite for high-performance energy storage devices by taking the advantages of both components [10]. The main synthesis techniques in preparing the RP-based composites are ball milling and vaporization-condensation. In the ball milling process, the bulk RP with the conductive hosts are mixing together under the argon atmosphere. During the process, particles milled into nano sized material with the formation of chemical bonds. This method is very simple and productive, that can control the ration of RP in the hybrid material precisely. The vaporization-condensation strategy is based on the sublimation of RP and conductive host. When the RP is heated above the 600°C (sublimation temperature) under the argon atmosphere or vacuum, the phosphorus sublimate diffuses into the pores due to the capillary forces and then, deposited or adsorbed on the surface of the host materials [11]. The general reaction of phosphorus with lithium during cycling are as follows:

$$P + xLi^{+} + xe^{-} \leftrightarrow Li_xP \tag{2.1}$$

$$Li_xP + \frac{3}{x}Li^{+} + \frac{3}{x}e^{-} \leftrightarrow Li_3P \tag{2.2}$$

During the lithiation step, phosphorus reacts with lithium and form Li_xP, with the final product of Li_3P. The Delithiation process is a stepwise extraction of lithium ion from the fully discharged Li_3P, which is detectable from several plateaus in charge/discharge and cyclic voltammetry profiles [10]. Although RP has been evaluated for different types of rechargeable batteries, the fundamental mechanism of its capacity decay even in the composite form is still unclear.

2.2.2 Black Phosphorus and Phosphorene Nanosheets

Since the discovery of graphene in 2004, 2D materials have attracted much attention in many fields, from materials science to biomedical and electrical engineering, due to their thermal conductivity, optical transparency, high carrier mobility, and surface area [12-14]. Among different 2D materials beyond graphene, metal dichalcogenides [15], boron nitride [16], carbon nitride [17], and MXenes [18] have been evaluated in recent years for energy storage applications due to their unique properties [19, 20]. Black phosphorus (BP) as a popular member of 2D materials was discovered in 1914 via high pressure (1.2 Gpa) and high temperature (200 °C) conversion of white phosphorus [21]. 2D BP was "rediscovered" in 2014 and attracted attention owing to its interesting anisotropic chemical and physical properties [22].

Among different allotropes of phosphorus, BP is non-toxic and the most thermodynamically stable allotrope with a tunable direct bandgap of 0.3-2.05 eV, high carrier mobility (≈1000 $cm^2\ V^{-1}\ s^{-1}$), moderate current on/off ratio (10^4 ~ 10^5), mechanical flexibility, and high theoretical capacity up to 2596 $mAhg^{-1}$ as an anode in rechargeable batteries [23-25]. Similar to graphite, in terms of structure (space group Cmca (64), Z=8), each layer of BP has a puckered honeycomb structure and BP layers adhere together with van der Waals interactions (20 meV $atom^{-1}$). These layers can

easily be separated to a few-layers or a monolayer of phosphorene, as shown in Figure 2.3 (a-c), through different exfoliation methods [7, 26, 27]. During the exfoliation of BP weak van der Waals bonds brakes and the phosphorene nanosheets with sp^3 hybridized P atoms and the bond angles of 96.3° and 102.1° are formed. The two bond lengths of 2.224 Å (in-plane) and 2.244 Å (out of plane) connect the P atom in either below or above the layer of BP [28]. The interlayer distance between phosphorene nanosheets is around 5.3 Å with the lattice constant of a=3.31 Å, b=10.47 Å, and c=4.37 Å [29, 30]. These unique crystal structure characteristics and physical properties make BP a promising 2D material for application in different fields of science and technology such as energy storage devices [7, 31-33], catalysts [34, 35], field-effect transistors [36, 37], sensors [38, 39], optoelectronics [40, 41], and biomedical devices [42, 43].

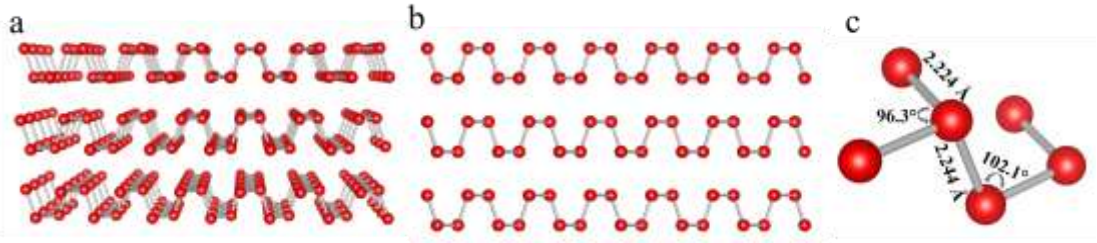

Figure 2.3: (a) The crystal structure of BP, (b) Crystal structure view along b axis, and (c) P-P bond distances and bond angles in the phosphorene.

The properties and the device performance of phosphorene largely depend on its thickness and preparation method. Generally, phosphorene nanosheets can be generated through bottom-up methods from the phosphorene precursors and through top-down techniques based on the breaking weak interactions between 2D layers in the bulk BP [44]. The typical bottom-up synthesis methods of BP include chemical vapor deposition (CVD) and pulsed laser deposition (PLD). The first report published in 2016 by Smith et al. describes growth of few-layer phosphorene nanosheets from

amorphous red phosphorus via the CVD method at 950°C under the pressure of 2758 KPa in the argon atmosphere [45]. Yang et al. synthesized amorphous phosphorene nanosheets with disordered structure on Si/SiO_2 or graphene/copper substrates using PLD technique at 150°C and the chamber pressure of 1.9×10^{-8} KPa [46]. However, CVD and PLD synthesis techniques are expensive and require ultra-high vacuum or high temperature [47]. Compared to the bottom-up methods, top-down techniques, which include mechanical and liquid exfoliations, are more common for the exfoliation of BP [48]. For the first time in 2014, high-quality phosphorene was obtained by mechanical exfoliation through repeatedly attaching and detaching bulk BP specimen onto adhesive tape and then transferring the produced phosphorene nanosheets onto Si/SiO_2 substrates [49]. However, the contamination caused by adhesive residue, low yield, and non-uniform distribution of phosphorene nanosheets at different thickness on the substrates make this method less attractive compared with other exfoliation techniques [50-52]. In comparison to the mechanical exfoliation, the liquid-based exfoliation of BP is a straightforward, scalable, and size-controllable [53-55] and has been widely employed to exfoliate different 2D materials such as graphene [56], hexagonal boron nitride [57], and transition metal dichalcogenides (TMDs) [58].

This chapter aims to highlight the liquid-based exfoliation of BP into phosphorene nanosheets via sonication, electrochemical anodic and cathodic exfoliation, and bipolar electrochemical exfoliation in terms of mechanism, material properties, and synthesis approach. In addition, the recent applications of exfoliated BP for energy storage devices such as secondary batteries and supercapacitors are summarized and discussed. Moreover, the challenges and perspectives of liquid-based exfoliation of

phosphorene and its application for energy storage devices will be presented to inspire the future opportunities of BP use.

2.3 Liquid-Based Exfoliation of Black Phosphorus

In liquid-based exfoliation, the bulk BP is suspended in a preferred solvent. The ionic species driven by applied ultrasound energy or voltage intercalate into the BP interlayer space. As a result of increasing lattice distance, bulk BP exfoliates into a few-layer or monolayer of phosphorene nanosheets with different size ranges [58]. Until now, exfoliation through ultrasonication, electrochemical anodic or cathodic techniques, and bipolar electrochemical methods are the main liquid-based methods for the preparation of phosphorene nanosheets. The schematic of the liquid-based exfoliations of BP are shown in Figure 2.4 (a-c). Moreover, microwave, microfluidics, laser-assisted, and wet-jet milling are also employed for the liquid exfoliation of BP. The effects of different conditions and parameters on the liquid-based exfoliation of BP into phosphorene will be briefly reviewed and discussed in this paper.

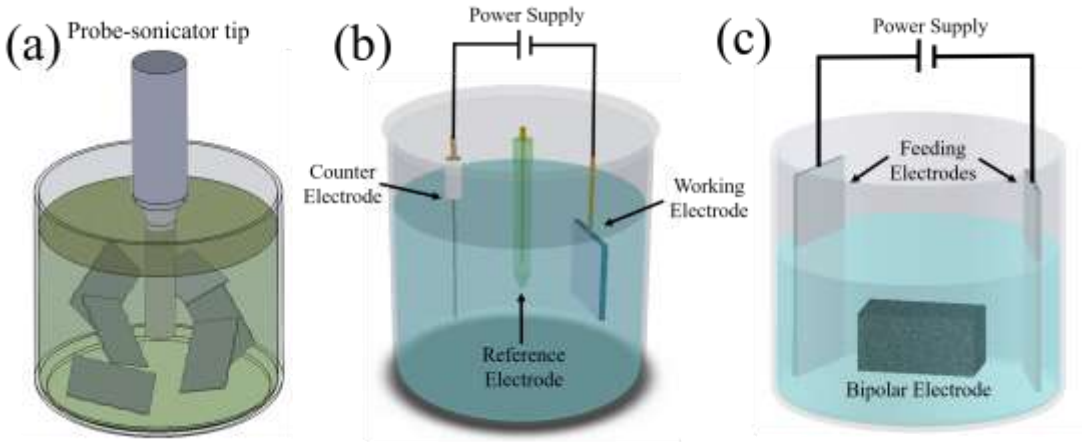

Figure 2.4: Schematic illustrations of the liquid-bases exfoliation, a) Sonication, b) Electrochemical Anodic/Cathodic, and c) Bipolar electrochemical exfoliation method.

2.3.1 Phosphorene Nanosheets via Sonication

In the ultrasonication exfoliation of BP as one of the straightforward methods, first, the bulk material is dispersed in a solvent, then the horn sonication is applied and finally, the exfoliated nanosheets are collected by the centrifuge process [44]. During the sonication, micro- and nano-sized bubbles are produced from fluctuations and shear forces, which together with the solvent molecules expand the BP layers via intercalation and disperse the phosphorene nanosheets into the solvent [59]. Selecting a suitable liquid system for the exfoliation and dispersion of the 2D phosphorene is a key factor of the liquid exfoliation through sonication. Theoretical calculations have been used to analyze the surface energy and tension of the solvents to provide the conditions for liquid exfoliation of 2D materials. Previous studies confirmed that similar to graphene and TMDs, by increasing the surface tension of the solvents, the exfoliation yield of BP increases dramatically [60-62]. Unlike the exfoliation of graphene, large scale exfoliation and production of phosphorene nanosheets must be in anhydrous and oxygen-free organic solvents, due to the chemisorption of oxygen atoms by phosphorus on the surface of nanosheets.

Regarding the surface energy of around 59 mJ m^{-2} for the phosphorene multilayers, it was predicted that the surface tension of around 40 mJ m^{-2} (such as for NMP and DMF) is enough for the exfoliation of BP [63]. Density functional theory (DFT) calculations also evaluated the effect of molecular shape of different solvents such as dimethyl sulfoxide (DMSO), N-methyl-2-pyrrolidone (NMP), isopropyl alcohol (IPA), and dimethylformamide (DMF) on the liquid exfoliation of phosphorene nanosheets [64]. Solvent molecules penetrating within phosphorus layers in BP stack can intercalate and exfoliate the phosphorene nanosheets [65]. The intercalation of the

abovementioned molecules in terms of Gibbs free energy (kJ/mol) and also the NMP intercalation into the BP monolayers gap during the exfoliation are shown in Figure 2.5 (a-d). Figure 2.5 (a) shows the potential of mean force (PMF) versus reaction coordinate (separations between the edges of both the uppermost phosphorene monolayer and the monolayer immediately below it). It is clear that the gradual solvent infiltration and exfoliation of BP occurs first at d=0.8 nm and continues to the values around d=1.2 nm. At low d values (<0.8 nm), the intercalation of molecules is sluggish due to the small interlayer gap between phosphorene layers. Figure 2.5 (c, d) displays the complete intercalation at d values around 1.0 nm. Sresht et al. proved that the BP exfoliation becomes easier for common solvents in the order of DMF>NMP>DMSO>IPA [64]. According to the theoretical studies, for successful exfoliation of BP, the adhesion between the phosphorene and solvent must be higher than the solvent's molecule cohesion.

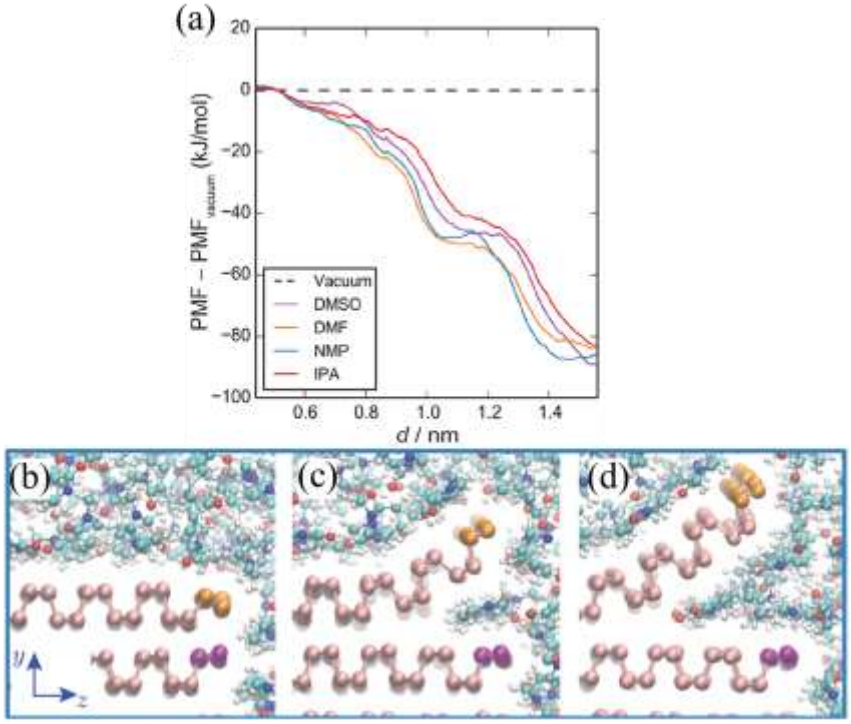

Figure 2.5: (a) Gibbs free energy by the phosphorene monolayers as a function of reaction coordinate in the presence of DMSO, DMF, NMP, and IPA, and intercalation of NMP molecules into the phosphorene nanosheets gap during the peeling apart for (b) d = 0.36, (c) d = 0.95, (d) 1.26 nm [64].

Since 2014, phosphorene nanosheets have been prepared by ultrasonication techniques in different solvents such as alcohols, acidic solutions, ionic liquids, and DI water, which are summarized in Table 2.1. Brent et al. evaluated the liquid-phase exfoliation of BP in NMP and confirmed the exfoliation of BP for up to five layers with a thickness of 4-5 nm [66]. Generally, a solvent for the successful exfoliation of BP must satisfy the following conditions: (1) exfoliate BP into phosphorene nanosheets, (2) disperse the nanosheets effectively without precipitation or flocculation, (3) control the oxidation and degradation of the nanosheets, (4) be efficiently removed from the surface of phosphorene without creating defects or introducing impurities [67, 68].

To evaluate the effect of centrifuge speed and to control the exfoliated BP nanosheets oxidation in NMP, Kang et al. fabricated a custom-tip sonicator setup sealed with polydimethylsiloxane and Teflon to restrict O_2 and H_2O penetration (Figure 2.6 a). In the meantime, the concentration of exfoliated BP in different solvents was evaluated through the same procedure. By increasing the centrifuge time, the exfoliated phosphorene dispersion's color changed from dark brown to yellow (Figure 2.6 b) [69]. As it's clear from Figure 2.6 (c), compared to the conventional solvents such as acetone, chloroform, ethanol, IPA, and DMF, NMP solvent with higher boiling point and surface tension provides stable dispersions of phosphorene with higher concentration. The same trend is reported for the exfoliated graphene via liquid exfoliation [60]. According to the literature, compared to IPA, DMF, and CHP, the solvation shell of NMP molecules could partially control the oxidation of phosphorene nanosheets [69]. Yasaei et al. in a comprehensive study evaluated the exfoliation yield of BP in DMSO and DMF as an organic, polar, and aprotic solvent.

Results showed that the ultrasound parameters such as power and time play a major role in the BP exfoliation yield in organic solvents. The prepared phosphorene nanosheets formed stable dispersions in both solvents and show low degradation over time [70, 71]. Moreover, the presence of polar molecules such as phytic acid (containing polar phosphate and hydroxyl groups) accelerated the exfoliation of large size of BP with high stability for large scale characterizations [72]. Exfoliation of BP in the presence of surfactants may weaken the interlayer bonds and reduce the damage caused by ultrasound on the produced phosphorene nanosheets.

Exfoliated phosphorene nanosheets are characterized by quantitative and qualitative methods. In particular, Raman spectroscopy, transmission electron microscopy (TEM), X-ray photoelectron spectroscopy (XPS), and atomic force microscopy (AFM) are main powerful tools used to evaluate the morphology (in terms of shape, thickness, and size), stability, and chemical properties of phosphorene nanosheets. It was found that the addition of NaOH as an auxiliary agent can apparently improve the exfoliation efficiency of phosphorene. Gue et al. introduced NaOH into NMP as a solvent to increase exfoliation yield and aqueous stability of phosphorene nanosheets. As it is clear from Figure 2.6 (d), they applied horn sonication for 4 hours to disperse BP and then centrifuged the suspension for 10 minutes to separate the exfoliated phosphorene from the bulk BP particles, and finally re-dispersed them in DI water [73]. Among six theoretical Raman vibration modes of BP, three of them (A_g^1, B_{2g}, and A_g^2) are active in the range of 300-500 cm^{-1} [23]. During the liquid exfoliation via sonication interaction of BP with solvent, produces strong stress due to intercalation of ions and bubbles. As a result, large distortion of the structure and restacking of phosphorene nanosheets occurs, as it evident from the changes in the Raman spectra

[74]. As shown in Figure 2.6 (e), there are three Raman active peaks at 362.2 cm^{-1}, 439.3 cm^{-1}, and 467.6 cm^{-1} for bulk BP, which correspond to the A_g^1, B_{2g}, and A_g^2 vibration modes, respectively. After the exfoliation, the decrease in the number of phosphorene layers manifests itself in a blue shift of three Raman modes [73]. The morphology, size, nanosheets' edges, and the number of the phosphorene layers are usually evaluated via TEM analysis [75]. Woomer et al. exfoliated BP in electronic grade isopropyl alcohol (IPA) for 16 hours in an inert atmosphere to control the oxidation rate. Figure 2.6 (f) shows the TEM image of the exfoliated phosphorene, which reveals the uniform transparent nanosheets with a planar morphology [76].

Exfoliation of BP using solvents which have high boiling point is typically toxic, and tough to be removed from the surface of nanosheets after exfoliation. Presence of absorbed solvent on the surface of phosphorene nanosheets limits application of the phosphorene. Hence, researchers began exploring the possibility of environmentally friendly BP exfoliation in DI water using the hydrophilic properties of BP [78]. Wang and co-workers for the first time prepared the ultrathin solvent-free phosphorene nanosheets in DI water with a concentration of 0.02 $mg.mL^{-1}$ through sonication in ice water for 8 hours [79]. By increasing the sonication time and power, the color of the solution changed from light yellow to dark brown. High-resolution TEM (HR-TEM) of the exfoliated phosphorene, which confirms the transparent orthorhombic crystal structure of a few-layer phosphorene nanosheets via liquid exfoliation, is shown in Figure 2.6 (g) [77]. To compare the phosphorene exfoliation yield in deoxygenated water and NMP as the most suitable solvent for the exfoliation of BP (Table 2.1), Kang et al. evaluated the effect of centrifuge speed on obtained nanosheets concentration. In order to stabilize the exfoliated BP, 2% (m/v) sodium dodecyl

sulfate (SDS) was added to the water. Figure 4 (h and i) shows the dispersion of phosphorene obtained at different centrifuge speeds (0-15000 rpm) in water and NMP. The darker yellow color of water compared to NMP confirms higher phosphorene nanosheets concentration. The phosphorene concentration in water is in an order of magnitude higher than in NMP as shown in Figure 2.6 (j) [78].

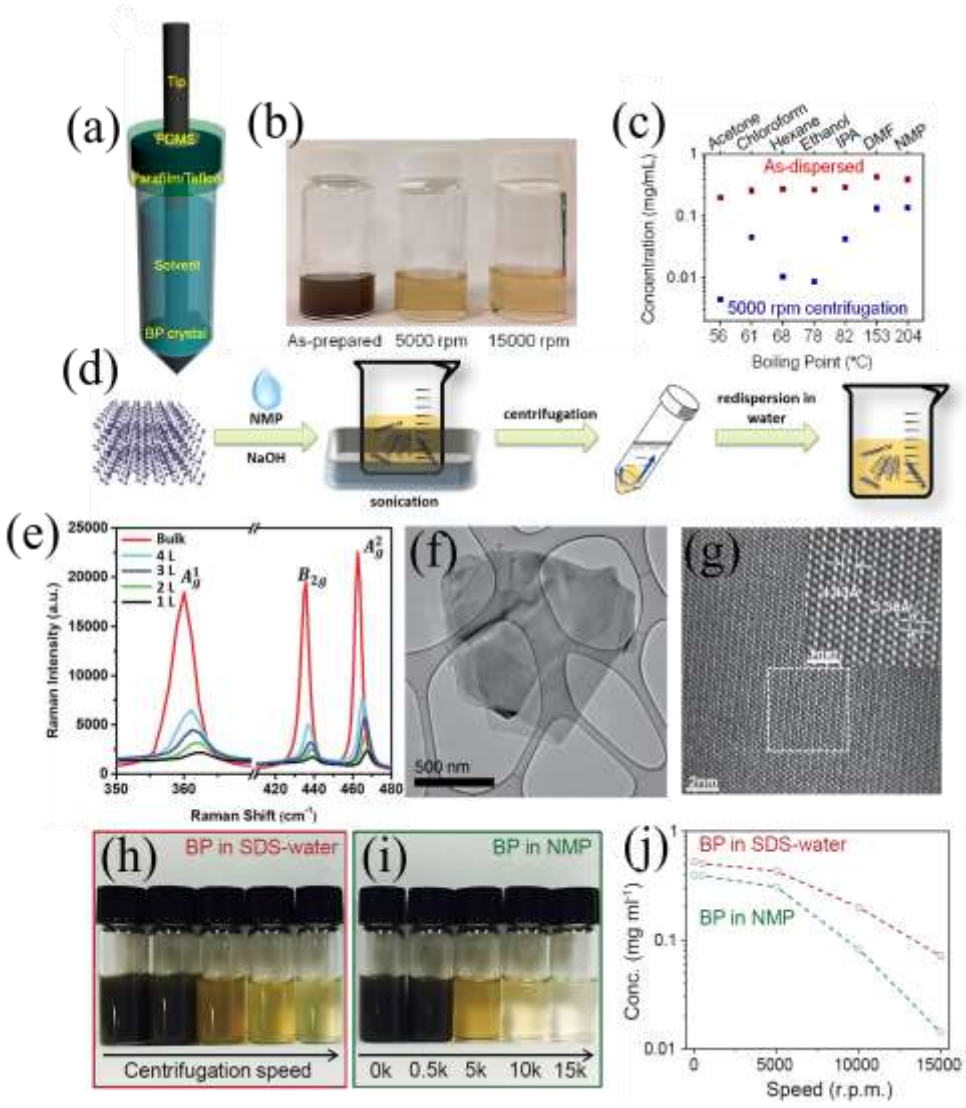

Figure 2.6: (a) Schematic of the ultrasonication setup in order to control the phosphorene nanosheets exposure to ambient air. (b) Dispersion of phosphorene nanosheets in NMP after 5000 and 15000 rpm centrifugation. (c) Concentration and boiling point relationship of phosphorene nanosheets for different solvents before and after 5000 rpm centrifugation [69]. (d) Schematic of the liquid exfoliation of BP in NMP/NaOH solution. (e) Raman spectra of BP and different numbers of phosphorene nanosheets obtained from liquid exfoliation in NMP/NaOH [73]. (f) TEM image of phosphorus nanosheets obtained by the liquid exfoliation of BP inside IPA [76]. (g) HRTEM image of a phosphorene nanosheets with orthorhombic crystal structure [77]. (h, i) Phosphorene nanosheets dispersions in water and NMP after different centrifugation speed. (j) Dispersion concentration of the phosphorene nanosheets [78].

Matching the surface tension between the bulk BP and solvent is the key factor for exfoliation of BP. One method to overcome this issue is the introduction of ionic liquids, polymers, surfactants, or organic compounds [80]. Ionic liquids have attracted attention recently due to their high stability, non-toxicity, and low vapor pressure [81]. Solvents with ionic liquids as molten salts may be adsorbed on the surface of phosphorene nanosheets and provide an electrostatic repulsion that controls the degradation of the phosphorene products at room temperature [82]. Zhao and co-workers for the first time developed the "green" exfoliation of BP in different types of ionic liquids. Their results confirmed sufficient dispersion of phosphorene nanosheets with high concentration (around 0.95 mg mL^{-1}) after 24 hours' sonication in 1-hydroxyethyl-3-methylimidazolium trifluoromethansulfonate ([HOEMIM]- [TfO]). The exfoliated nanosheets were stable in terms of morphology and degradation for one month, making them a suitable choice for device fabrication [80]. As shown in Figure 2.7 (a), to tackle the fast oxidation rate of phosphorene in the presence of light, Hu et al. focused on the liquid exfoliation, surface encapsulation, and passivation of a few-layer phosphorene with noncovalent conductive polymeric ionic liquids. The obtained highly conductive phosphorene nanosheets were stable in an ambient environment for more than 100 days [83]. XPS analysis is a powerful tool to investigate the chemical properties of the phosphorene nanosheets after liquid exfoliation. In general, the P $2p^{3/2}$ and P $2p^{1/2}$ doublet in the range of 129.5-131.0 eV, and the subbands of POx in the range of 133-135 eV correspond to the crystalline BP and oxidized phosphorus, respectively [84]. Changes in the phosphorus atoms bonding in phosphorene, produced in different solvents after exposure to air, can be monitored by the high-resolution P 2p spectra, as shown in Figure 2.7 (b). As it is clear, exfoliated phosphorene in two different polymeric ionic liquids compared to

pure water and DMF after 8 days' exposure to air, shows much weaker P-O bonds. This confirms higher stability of phosphorene nanosheets prepared in P([VPIm]PF_6) and P([VPIm]TFSI) [83]. Thickness of the phosphorene nanosheets after exfoliation can be measured using AFM by dividing the nanoflakes height by interlayer distances [75]. Figure 2.7 (c) shows the AFM image of the phosphorene nanosheets from the exfoliated BP in ([VPIm]TFSI), as an ionic liquid. Measured thickness of 2.5-7.6 nm corresponds to form 3 to 9 layers of phosphorene (based on the thickness of 0.85 nm for a mono layer of phosphorene) [83]. It is important to mention that the AFM provides very rough estimation of thickness and the result depends on the properties of the substrate such as hydrophobicity, roughness, and force magnitude of the tip [85]. Very recently, thionine (TH) and lithium hexafluorosilicate (Li_2SiF_6) have been used with organic solvents for the exfoliation of BP [86, 87]. Figure 2.7 (d) shows a nonoverlapping 3D layer of phosphorene nanosheets on silicon wafer obtained from the liquid exfoliation of BP into NMP/TH [86]. Such a morphology of phosphorene nanosheets provides longer diffusion pass for high-performance electrochemical applications.

As it is shown in Table 2.1, the liquid-based exfoliation of BP via sonication attracted a lot of attention due to its feasibility and scalability. However, the disadvantages of this method such as sonication long time requirement, causing defects especially on the edges, fast degradation of the phosphorene, high energy-extensive consumption, and difficulty with size control, convinced researchers to find alternative methods such as electrochemical anodic/cathodic and bipolar exfoliation.

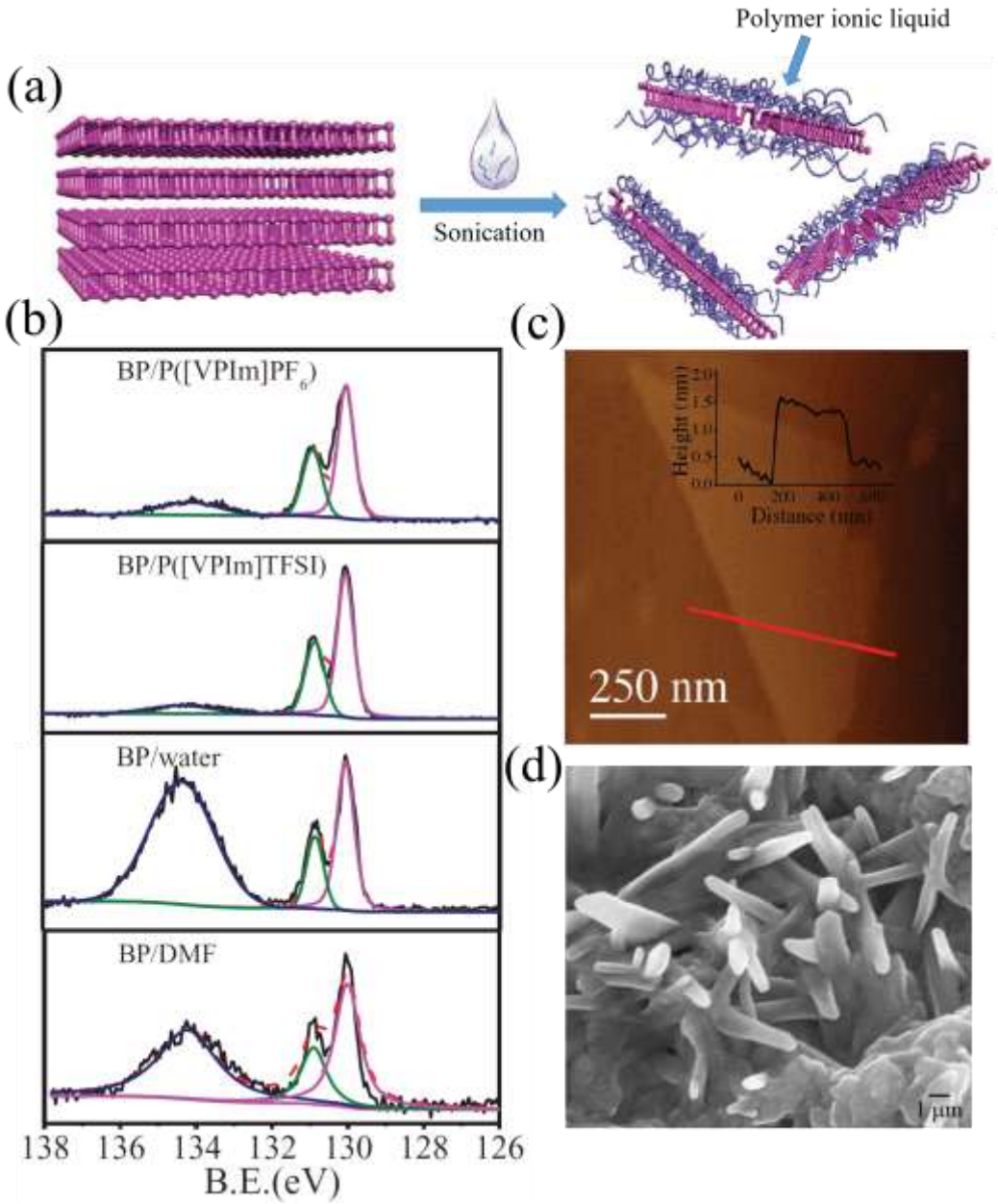

Figure 2.7: (a) Schematic illustration of the BP exfoliation in the polymer ionic liquid solution. (b) XPS spectra of the exfoliated BP in different solvents after 8 days exposure in the air, (c) AFM image of phosphorene nanosheets obtained from P([VPIm]TFSI) [83]. (d) SEM image of the phosphorene nanosheets obtained from the liquid exfoliation of BP in NMP/thionine [86].

Table 2.1: Summary of liquid exfoliation of BP via sonication, properties and applications of the product.

Solvent	Time	Sonication Power/Frequency	Size/Thickness	Application	Ref.
NMP[1]	1-24 h	30-820 W/20-40 kHz	6 nm-μm range/3.5-5 nm	Field effect transistors, Optical devices, Catalytic, Li/Na-ion batteries, Li-S batteries, Humidity sensors, Antibacterial applications, Flame retardant, Therapeutic application	[34, 39, 66, 69, 88-106]
IPA[2]	3-24 h	300-650 W/20 kHz	50 nm-μm range/0.26-22 nm	Solid-state laser, Memory devices, Field effect transistors, Flame retardant	[76, 107-111]
DMSO[3]	10-20 h	130-300 W/19-37 kHz	4.5-1200 nm/2-26 nm	Field effect transistors, Humidity	[70, 71, 112, 113]

				sensor, Therapeutic application	
Acetone	6-10 h	300 W/---	10-100 nm/7-10 nm	Supercapacitors, Li-ion batteries	[114-116]
CHP[4]	5-6h	750 W/---	60-100 nm/2.06-8.1 nm	Gas sensors, Li-ion batteries	[116, 117]
DMF[5]	6-15 h	130-500 W/---	190-200 nm/1-8 nm	Field effect transistors, Li-metal batteries	[70, 118]
Ethanol	43 h	400 W/---	100 nm /4-25 nm	Pulsed laser	[119]
GBL[6]	10 h	300 W/---	1-10 μm/---	Memory devices	[108]
Formamide	4 h	200 W/---	50 nm-1 μm/---	Li-ion batteries	[62]
PVP[7]	---	400 W/40 kHz	200 nm-4 μm/---	Catalytic devices	[120]
Acetonitrile	1 h	360 W/---	>10 μm/1.9-2.1nm	---	[121]
DMPU[8]	3 h	400 W/40 kHz	100 nm-4 μm/1200 nm	Antibacterial application	[122]
DGME[9]	3 h	130 W/---	---/7.56-24.1 nm	Gas sensors	[123]
NMP/NaOH				Ultrafast photonics,	

	4-12 h	300-400 W/25-40 kHz	100-670 nm/2-12 nm	Supercapacitors, Antibacterial application, Therapeutic application, pH sensors	[73, 124-127]
NMP/IPA	2 h	---	150-350 nm/4.9-13.9 nm	Optical devices	[128]
NMP/Acetone	1 h	125 W/35 kHz	99.8-159 nm/1.5 nm	---	[129]
NMP/Sodium citrate	4 h	540 W/---	---/0.9-9.6 nm	Catalytic devices	[130]
IPA/Li_2SiF_6	5 h	400 W/40 kHz	0.5-5 μm/3 μm	Antibacterial application	[87]
DMF/phytic acid	8 h	---/50 kHz	24-28 μm/3-4 nm	Catalytic devices	[72]
DMF/1-pyrenylbutyric acid	16 h	200 W/---	<200 nm/1.3 nm	Therapeutic application	[131]
NMP/NaOH/Ethanol	6 h	200 W/53 kHz	---	Supercapacitors	[132]
DMF, NMP, DIGLYM[10]	0.5-6 h	400 W/---	20-100 nm/2-5 nm	---	[133]
DI Water	1.5-10 h	90-950 W/---	200 nm- μm range/2-9.4 nm	Catalytic devices, Li-ion batteries, Supercapacitors	[77, 79, 134-136]
Deoxygenated water	1-6 h	70-100 W/20 kHz	μm range/1.1-8.3 nm	Field effect transistors, Antibacterial application	[78, 137]
Millipore water	8 h	37.5 W/---	208-884 nm/17.4-91.9 nm	Cytotoxicity application	[138]
DI water/Ethanol	0.33 h	100 W/20 kHz	756 nm/1-2.5 nm	Field effect transistors	[139]

([HOEMIM]- [TfO][11]	24 h	100 W/---	459 nm/3.58-8.90 nm	---	[80]
[Emim][Tf_2N][12]	1 h	---	600 nm/2-2.6 nm	---	[82]
NMP/TH[13]	8 h	200 W/50 kHz	μm range/---	Catalytic devices	[86]
DMF/ionic liquids	6 h	---/50 kHz	---/1.6-4.9 nm	Optoelectronic devices	[83]

[1] N-methyl-2- pyrrolidone, [2] Isopropyl alcohol, [3] Dimethyl sulfoxide, [4] N-cyclohexyl-2-pyrrolidone, [5] Dimethylformamide, [6] γ-butyrolactone, [7] Polyvinylpyrrolidone, [8] N,N'-dimethylpropyleneurea, [9] Diethylene glycol dimethyl ether, [10] Bis(2-methoxyethyl) ether, [11] 1-hydroxyethyl-3- methylimidazolium trifluoromethansulfonate, . [12] 1-ethyl-3-methylimidazolium bis(trifluoromethylsulfonyl)imide, [13] Thionine.

2.3.2 Phosphorene Nanosheets via Electrochemical Exfoliation

Electrochemical exfoliation of BP is an alternative liquid-based method which is more tractable, faster, and cheaper compared to liquid-based exfoliation via sonication [140]. This technique has been applied for exfoliation of the large variety of 2D materials [141]. Electrochemical exfoliation of BP is a very straightforward technique at ambient environment conditions and the reactions finish in a short period of time, that allows to control the degradation of obtained phosphorene nanosheets. This method is based on weak van der Waals interactions breaking, using relevant reduction and oxidation reactions to provide preferable nanosheets thicknesses with large-scale quantity for practical applications [142]. As it is clear from Figure 2 (b), a regular electrochemical exfoliation cell includes working and counter electrodes, which are connected to the power supply, and an optional reference electrode in an electrolyte (aqueous or nonaqueous solution). The exfoliation electrolytes with sufficient surface tension, support anions and cations migration to BP layers and prevent the restacking of nanosheets after exfoliation. In the presence of an optimal voltage/current applied to bulk BP as a working electrode, the ionic species from a solution intercalate into the bulk layered BP under the electric field and expand BP into phosphorene nanosheets [143, 144]. In general, ions intercalation, and their interaction with electrodes during exfoliation, control the exfoliation yield and properties of phosphorene nanosheets [145].

Depending on the applied potential and chemistry of intercalating anions/cations, electrochemical exfoliation can be classified as anodic and cathodic. In addition, bulk BP can act as an anode and cathode simultaneously in the bipolar electrochemical exfoliation method (Figure 2.4 c). As shown in Figure 2.8 (a, b), in the anodic

exfoliation, bulk BP acts as an anode and anions (negatively charge ions) from the electrolyte or produced via electrolysis intercalate between the layers of BP in the presence of positive bias. On the other hand, in cathodic exfoliation, bulk BP as a cathode under a negative bias, exfoliates into phosphorene nanosheets in the presence of cations (positively charge ions) [146]. As it is shown in Table 2, like for graphene, both anodic and cathodic exfoliation were evaluated for the exfoliation of bulk BP [54]. The phosphorene nanosheet's yield and quality depends on applied voltage, physical and chemical properties of electrolyte, and cation or anion size [140].

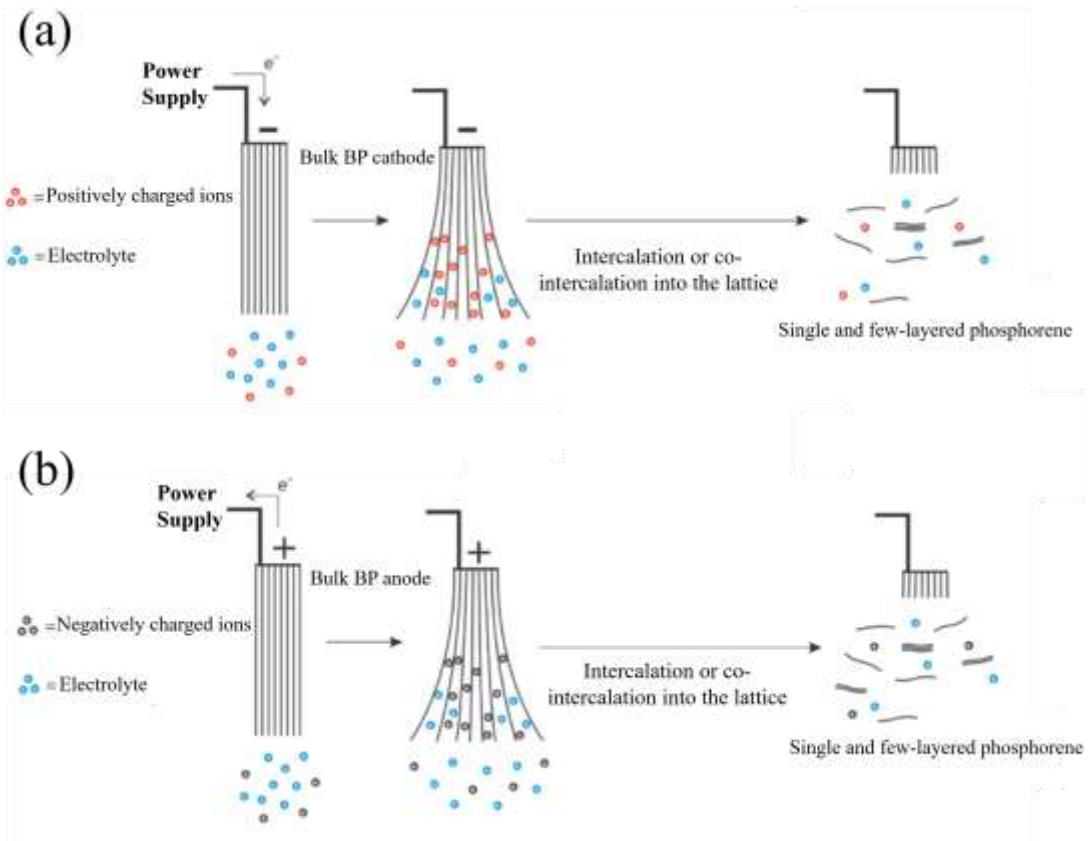

Figure 2.8: Mechanisms of electrochemical (a) cathodic and (b) anodic exfoliation of BP [146].

2.3.2.1 Phosphorene Nanosheets via Anodic Exfoliation

Anodic exfoliation in aqueous solutions of electrolytes such as H_2SO_4, Na_2SO_4, $NaClO_4$, and $NaNO_3$ has been evaluated for different types of 2D materials [147].

Evidently, sulfates are the most efficient negative ion intercalants for anodic exfoliation. The first attempt for anodic exfoliation of BP in 0.5 M Na_2SO_4 was made by Erande and co-workers. In their setup, BP and platinum wire were used as an anode and counter electrode, respectively, in the presence of an applied positive voltage of 7V (Figure 2.9 a) [148]. In a comprehensive study from the same group an exfoliation yield of up to 80% has been obtained in anodic exfoliation of BP, which is much higher compared to the previous liquid-based exfoliation of BP through sonication. Similar to anodic exfoliation of graphene, phosphorene nanosheets are more prone to oxidation during exfoliation [149]. By applying a negative bias, active radicals (oxides and hydroxides) are produced at anodic side around the bulk BP due to water electrolysis. The radicals attack the bulk BP together with SO_4^{2-}, weakening the van der Walls forces between the BP layers. Then, water oxidation generates O_2 molecules as gaseous species and exfoliate the phosphorene nanosheets. The overall reaction of anodic exfoliation of BP in sodium sulfate solution is as follows:

$$Na_2SO_4 \rightarrow 2Na^+ + SO_4^{2-} \quad (2.3)$$

$$2H_2O \rightarrow 2H_2(g) + O_2(g) \quad (2.4)$$

The reduction ($2H_2O + 2e^- \rightarrow H_2(g) + 2OH^-$) and oxidation ($4OH^- \rightarrow 2H_2O + 4e^- + O_2(g)$) reactions occur at the cathodic and anodic sites, respectively. As it is shown in Figure 2.9 (b, c), the selected area electron diffraction (SAED) pattern and HRTEM image confirmed the crystal structure of the phosphorene nanosheets via anodic exfoliation [149]. Ambrosi et al. evaluated the anodic exfoliation of BP in acidic solutions. Figure 2.9 (d-f) shows the electrochemical cell with diluted H_2SO_4 both in the absence and presence of applied 3V potential after two hours. As it is clear, over time, small particles are dispersed and

precipitated, and the color of the electrolyte are changed to dark yellow. In anodic exfoliation, working at lower potential may decrease the oxidation of the phosphorene nanosheets. The high-resolution XPS of nanosheets confirms the presence of phosphorus P 2P components (Figure 2.9 g). Higher intensity of POx peak of the exfoliated BP compared to the bulk BP indicates that the exfoliated phosphorene has a higher degree of oxidation due to its sensitivity to oxygen [150]. Recently, a large variety of electrolytes have been employed for modified anodic exfoliation of BP. Results confirmed that electrolytes containing sulfate anions are more favorable for the exfoliation of BP due to their lower reduction potential compared to anions such as ClO_4^- or NO_3^- (0.2V for SO_4^{2-}, 1.42V for ClO_4^-, and 0.96V for NO_3^-). The AFM and TEM images of the phosphorene nanosheets obtained from anodic exfoliation of BP in Na_2SO_4, show transparent nanoflakes with a thickness of 8 nm and their size being in the micron range (Figure 2.9 h, i) [151]. Furthermore, similar to the liquid-based exfoliation via sonication, anodic exfoliation of BP has been evaluated using polar solvents such as phytic acid to increase the exfoliation yield and to control the surface oxidation of the nanosheets [152]. Although there are a lot of research efforts in anodic exfoliation of 2D materials, employing this method for the preparation of BP nanosheets is in its early stages due to rapid phosphorene oxidation.

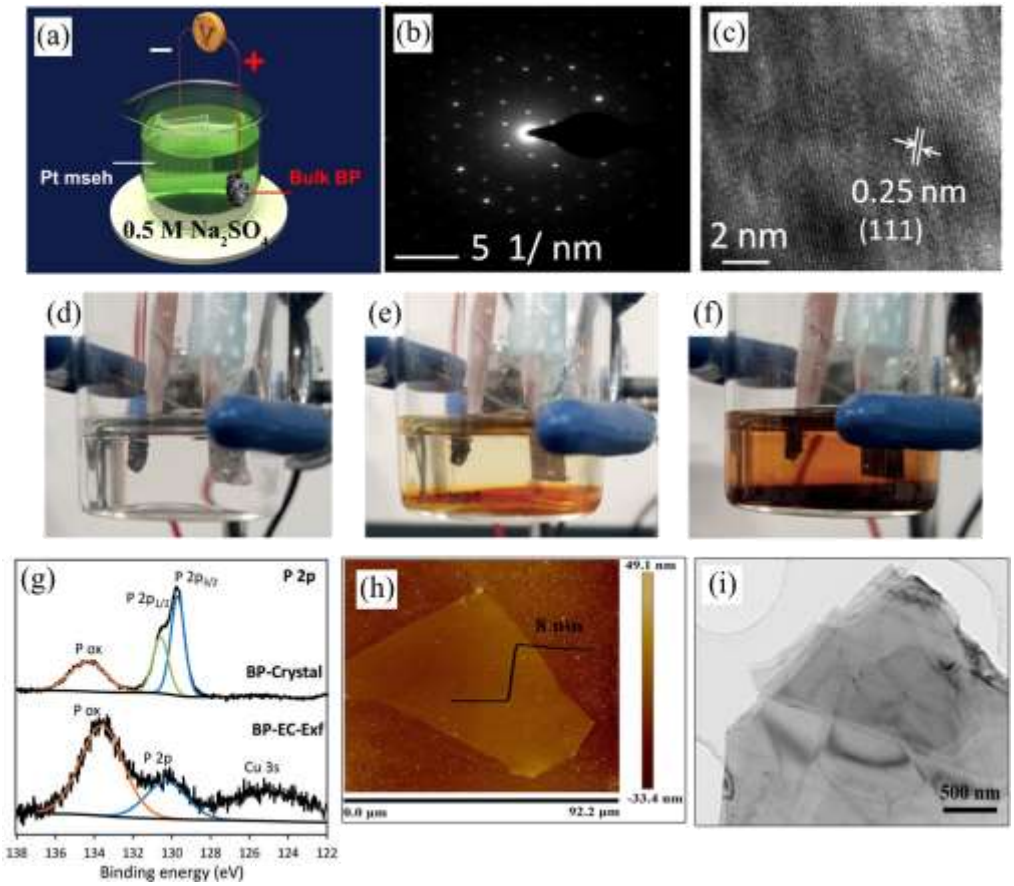

Figure 2.9: (a) Schematic of the anodic exfoliation of BP in Na_2SO_4 electrolyte [151], (b) SAED pattern, and (c) TEM image of the phosphorene nanosheets after anodic exfoliation [149], (d) Anodic exfoliation setup of BP in aqueous solution of H_2SO_4 electrolyte in the absence of potential, (e) After 20 minutes, V=3V, (f) After 2 hours, V=3V, (g) XPS analysis of bulk BP and anodic exfoliated BP in H_2SO_4 [150], (h) AFM image, and (i) TEM image of the phosphorene nanosheets obtained in Na_2SO_4 [151].

2.3.2.2 Phosphorene Nanosheets via Cathodic Exfoliation

In general, cathodic exfoliation is based on the application of negative potential and insertion of positive ions and electrolyte molecules into the layered BP. As it is shown in Table 2.2, cathodic exfoliation of BP has been more widely used in recent years compared to the anodic exfoliation because of very low oxidation rate during the process and low defect concentration in the final product due to the absence of oxygen-based radicals [141]. In general, the intercalating agent must have high solubility in the solvent to generate cations and exfoliate BP in the presence of applied voltage. Huang et al. evaluated the cathodic exfoliation of BP in the presence of

tetrabutylammonium hexafluorophosphate (TBAP) as an intercalating agent in DMF solution. They confirmed that the number of phosphorene layers (2 to 11) can be controlled by applied voltage and, as a result, by the intercalation rate [144]. Following this study, Li and co-workers developed a fast and high-yield cathodic exfoliation of BP in tetraalkylammonium (TAA) as a nonaqueous electrolyte in the presence of DMSO as a solvent. As shown in Figure 2.10 (a), in a two-electrode setup equipped with an optical microscope for in-situ characterization, BP and platinum wire act as a cathode and counter electrode, respectively. During the process, when the applied cathodic potential is lower than -4V, the intercalation of cations into the layered BP occurs and by decomposition of ions, gaseous species are produced, rapidly exfoliating the BP into 5-layer phosphorene (less than 10 minutes). DMSO as a polar solvent provides high solubility for alkylammonium salts and facilitates the exfoliation of BP at low voltage. TEM image and SAED pattern of the exfoliated BP in TAA revealed the microsized morphology and high crystallinity of the product (Figure 2.10 b) [153].

Yang et al. also investigated the cathodic exfoliation of BP in the presence of different cations such as Li^+, Na^+, tetramethylammonium (TMA^+), tetraethylammonium (TEA^+), and tetra-*n*-butylammonium (TBA^+) in propylene carbonate (PC) solution. Small Li^+ (r=0.09 nm) and Na^+ (r=0.12 nm) ions cannot effectively expand BP into phosphorene nanosheets due to their size. Among ammonium salts, TBA^+ (r=0.83 nm) could exfoliate BP with the exfoliation yield of up to 78%. Theoretical calculations confirmed that interlayer separation of 0.8 nm is enough for exfoliation of BP [154]. Following the diffusion of TBA^+ cations inside the layered BP, the

reduction of HSO_4^- anions produces hydrogen bubbles that increase the interlayer distance and accelerate the intercalation of cations:

$$TBA\,.\,HSO_4 \rightleftharpoons TBA^+ + HSO_4^- \quad (2.5)$$

$$HSO_4^- \rightleftharpoons SO_4^{2-} + H^+ \quad (2.6)$$

Figure 2.10 (c) shows the SEM images of the BP before and during the process of cathodic exfoliation for 150 seconds. Before exfoliation, the puckered structure of BP is well-defined, but after 150 seconds, dramatic inhomogeneous expansion and exfoliation of phosphorene nanosheets are achieved under ambient environment conditions. The Raman, XRD, and XPS analysis (Figure 2.10 d-f) confirmed defect-free and oxygen-free exfoliated phosphorene nanosheets with the lateral size up to 20.6 μm [155].

Very recently, Huang et al. developed a novel and scalable technique of plasma-assisted cathodic exfoliation of BP in DMF without an intercalating agent. As shown in Figure 2.11 (a-c), bulk BP and stainless steel needle tube served as a cathode and anode, respectively. By applying a high voltage (around 2 kV) and in the presence of stable plasma exfoliation of BP occurred in a short period of time (90 seconds) and the electrolyte turned to dark yellow (Figure 2.11 a). The high-resolution mass spectroscopy analysis of the DMF before and after plasma treatment is shown in Figure 2.11 (b). Decomposition of DMF molecules into cationic species such as $C_2H_4N^+$, $C_2H_8N^+$, and $C_2H_6N^+$, their intercalation into the layered BP, and formation of gas molecules from H^+ accelerate the expansion and exfoliation of BP [156]. The quality of exfoliated BP through cathodic exfoliation depends not only on the applied voltage, but also on solution temperature and concentration of electrolyte. Luo and co-workers confirmed that by increasing the electrolyte temperature up to 50°C and the

applied voltage of -30V, exfoliation of BP begins and temperature of 70°C provides high-yield exfoliation of BP. They also showed that the optimum hexadecyltrimethylammonium chloride (CTAC) electrolyte concentration is 0.5 M. It can be seen from Figure 2.11 (d, e), after applying a high voltage, the expansion of the phosphorene nanosheets can be detected by naked eye due to the diffusion of CTA^+ cations and generation of gaseous bubbles [157].

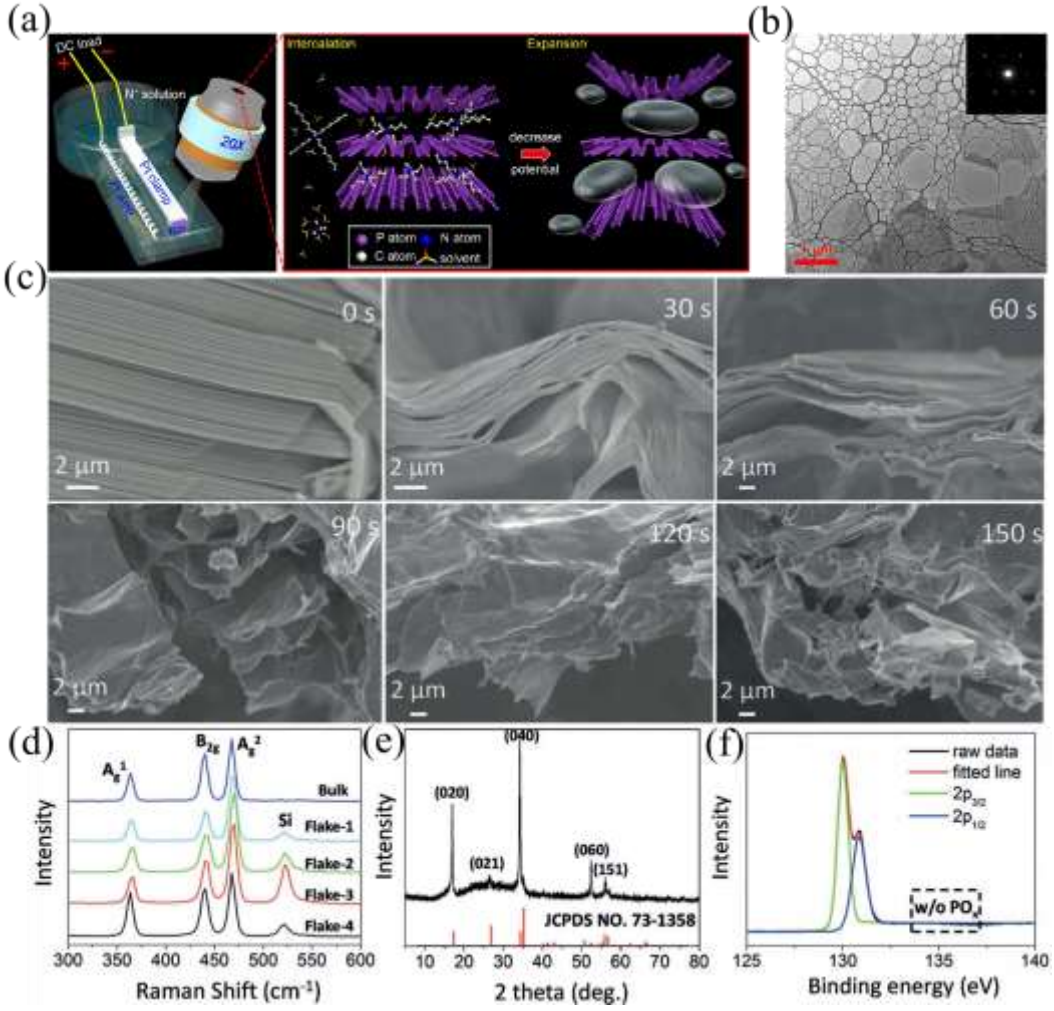

Figure 2.10: (a) Schematic illustration and intercalation mechanism of the cathodic exfoliation setup equipped with an optical microscope (b) TEM image of phosphorene nanosheets with SAED pattern [153], (c) SEM image of the BP exfoliation at different times, (d) Raman spectra, (e) XRD, and (f) XPS analysis of the phosphorene nanosheets [155].

High-yield up to 80%, large-size, crystallinity, and single-phase composition of cathodically exfoliated BP, make this technique more favorable for both industry and

academia compared to previously discussed liquid-based exfoliation methods. Nevertheless, compared to graphene exfoliation, the preparation of phosphorene nanosheets via the multi-step cathodic exfoliation is in its early stages. The post-sonication of the exfoliated BP in a separate solvent and transferring them for practical application may affect the quality and performance of the products. More in-detail studies are necessary to optimize the electrolyte composition and concentration, solvent quality, and electrochemical parameters.

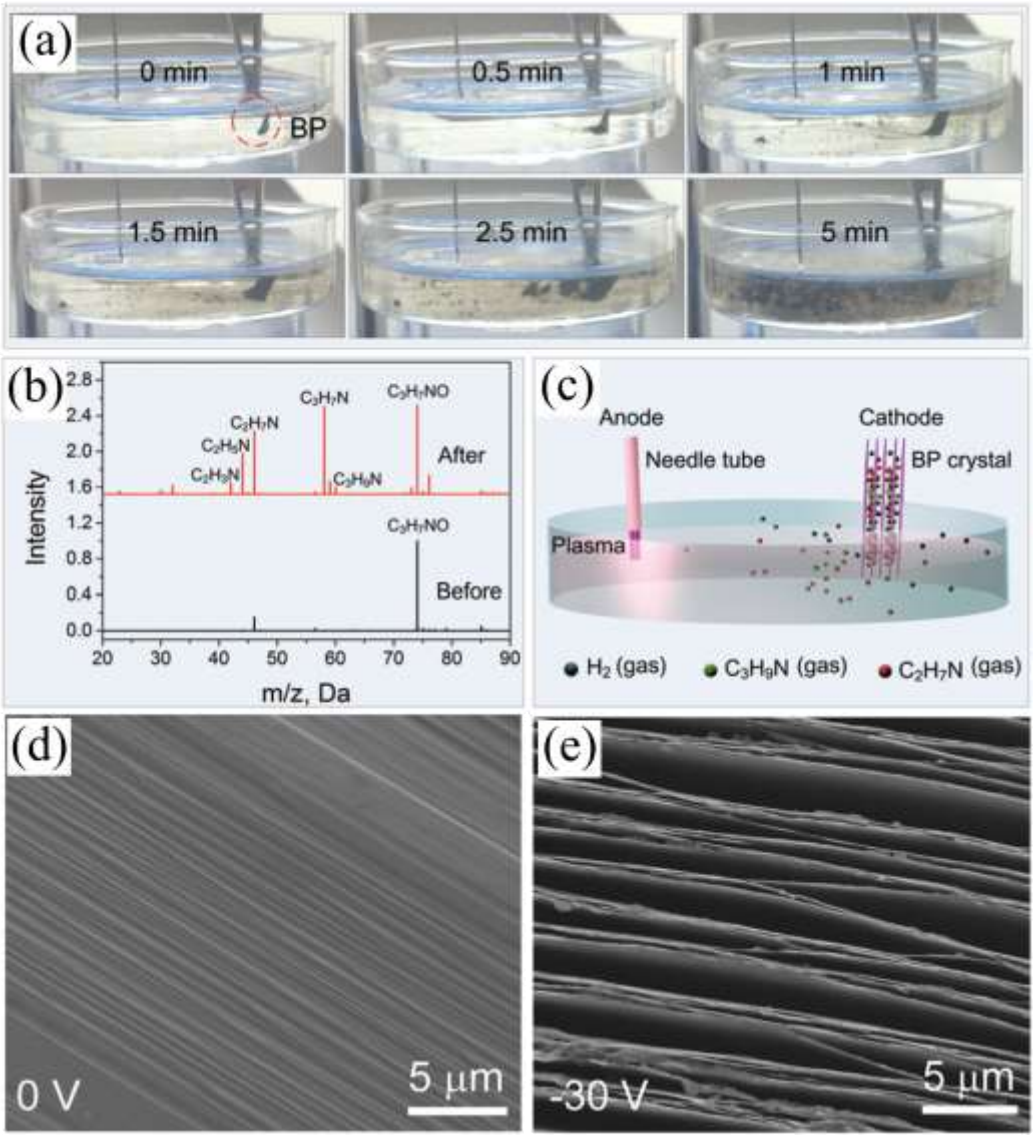

Figure 2.11: (a) Cathodic exfoliation process of BP at a different time in the presence of plasma treatment, (b) High-resolution mass spectroscopy analysis of DMF before and after plasma treatment, (c) Schematic illustration of cathodic exfoliation of BP with plasma treatment [156], SEM images of the cathodic exfoliation of BP (d) Before and (e) After applying -30V in CTAC electrolyte [157].

Table 2.2: A summary of the electrochemical exfoliation of BP into phosphorene by anodic and cathodic electrochemical methods, some properties and applications of the products.

Exfoliation type	Electrolyte	Applied Voltage	Time	Size/Thickness	Application	Ref.
Anodic	Na_2SO_4	+7 to +10 V	0.8-1.5 h	µm range/1.4-10 nm	Field emitters, Humidity sensor, Supercapacitors	[148, 149, 151]
Anodic	H_2SO_4	+3 V	2 h	µm range/---	---	[150]
Anodic	Phytic acid	+10 V	2 h	---/6.08 nm	Optical devices	[152]
Cathodic	TBAP[1]/DMF	-5 to -3.8 V	0.08-0.5 h	µm range/0.76-5.8 nm	Li/Na-ion batteries, Hybrid capacitors, Catalytic devices, Gas sensors	[144, 158-161]
Cathodic	TBATFB[2]/DMSO	-10 to -4.8 V	0.4-0.5 h	µm range/3.4-6 nm	Catalytic devices	[162-164]
Cathodic	TBAP/PC[3]	-30 to -5 V	12 h	µm range/2-7 nm	Electroactive tissues	[165, 166]
Cathodic	TBA·HSO_4/PC	-8 V	1 h	2-20.6 µm/1.3-9.5 nm	Field effect transistors	[155]

Cathodic	TAA[4]/DMSO	-5 V	0.15 h	---/1.1-3.7 nm	Optoelectronic devices	[153]
Cathodic	TBPB[5]/DMF	-5 V	0.05 h	μm range/4.8-4 nm	Supercapacitors	[167]
Cathodic	CTAC[6]	-30 V	0.5 h	μm range/5-8 nm	---	[157]
Cathodic	DMF	-2 kV	0.08 h	1-10 μm/3-5 nm	---	[156]
Cathodic	TBAP/AN[7]	-3.8 V	3 h	500 nm/3.5 nm	---	[159]
Cathodic	TBAP/DMSO	-3.8 V	5 h	4 μm/2.4 nm	Supercapacitors	[168]

[1] Tetrabutylammonium hexafluorophosphate, [2] Tetrabutylammonium tetrafluoroborate, [3] Propylene carbonate, [4] Tetraalkylammonium
[5] Tetrabutylphosphonium bromide, [6] Hexadecyltrimethylammonium chloride, [7] Acetonitrile

2.3.2.3 Phosphorene Nanosheets via Bipolar Electrochemical Exfoliation

In the liquid-based exfoliation through sonication, and also via anodic and cathodic electrochemical exfoliation of BP, post-treatment is required to collect the phosphorene nanosheets from solution, which may decrease the quality of produced 2D materials for practical applications. Recently, bipolar electrochemical exfoliation technique of 2D materials has been developed as a single-step, eco-friendly, scalable, and inexpensive method. Bipolar electrochemistry is a well-known technique from 1960s, based on the polarization of bipolar electrode in the presence of an electric field (Figure 2.4 c) [169]. Compared to the regular two- or three-electrode electrochemical systems, a bipolar electrode acts as a cathode and anode simultaneously [169-171]. A typical bipolar electrochemistry setup consists of two feeding electrodes (connected to the power supply) and a bipolar electrode placed between them wirelessly in a proper electrolyte [172]. By applying a potential between the two feeding electrodes, an electric field is introduced into the electrolyte. This electric field is constant throughout the volume of electrolyte due to electrolyte's electrical conductivity. The electric field produces interfacial potential differences (δ^+, δ^-) between the bipolar electrode and the electrolyte, leading to polarization of the bipolar electrode edges. It also drives reduction and oxidation reactions, which occur simultaneously on the cathodic and anodic poles of the bipolar electrode [173]. This interfacial potential depends on the length of the bipolar electrode and the applied potential. The opposite direction of the bipolar electrode poles with the feeding electrodes polarity is an important key parameter in the process [172, 174]. This technique has been evaluated for a large variety of applications such as electronic device fabrications, electrochemical sensing, and electrodeposition [169]. Recently,

this method has been employed for the exfoliation of 2D materials such as graphene [175-177], molybdenum diselenide ($MoSe_2$) [178], tungsten disulfide (WS_2) [179], and hexagonal boron nitride (hBN) [180].

Mayorga-Martinez et al. evaluated the bipolar electrochemical exfoliation of BP into phosphorene nanosheets in Na_2SO_4 solution. They sonicated the bulk BP for 4 hours and then, in the bipolar setup with two-platinum electrodes, applied 10V for 30 minutes and collected the supernatants after one week of aging [181]. Although the XPS and TEM analysis confirmed the successful exfoliation of BP, more in-depth characterization is needed to evaluate the bipolar electrochemical exfoliation mechanism and the quality of the obtained phosphorene nanosheets. Very recently, in our group, a novel single-step bipolar electrochemical exfoliation of BP and deposition of phosphorene nanosheets on conductive substrates in DI water was developed [23, 182]. Two stainless steel electrodes were used as a negative and positive feeding electrode and a bulk BP was placed in between, in the presence of 30V for 24 hours. By applying a voltage, hydrogen and oxygen bubbles were produced (due to the water electrolysis) at the extremities of the bulk BP specimen. Then, H^+ and OH^- ions, generated from water decomposition during the process, intercalate into the layered BP. The transport of ions produces phosphorene nanosheets due to weak van der Walls attractive forces between layers of BP. Because of the applied potential and electrophoresis phenomenon, exfoliated phosphorene migrates and deposits on the surface of stainless steel electrodes. However, controlling the oxidation of the phosphorene nanosheets through bipolar electrochemical exfoliation in DI water is still challenging.

2.3.3 Other Liquid-Based Exfoliation Methods

Given the size-dependent properties of 2D materials and the scalability of liquid-phase exfoliation of BP, other liquid-based techniques have been evaluated for the preparation of phosphorene nanosheets. Toward this, Bat-Erdene and co-workers reported a novel and ultra-fast two-step microwave-assisted liquid exfoliation of BP in an ambient environment [183]. As shown schematically in Figure 2.12 (a), the dispersion of BP in NMP solution was heated for 4 minutes at 50°C using microwave generating device (600 W power), followed by another 3 minutes long exfoliation at 70°C using the second microwave system (220 W power). Then, the exfoliated nanosheets were collected from solution through centrifugation. Weakening of the bulk BP van der Waals interactions in the first step and the expansion of the layers in the second step of microwave irradiation is the confirmed mechanism of BP exfoliation via microwave-assisted liquid exfoliation [184]. AFM characterization revealed the thickness of 2-15 nm of the phosphorene nanosheets with low oxidation rate after exfoliation in less than 10 minutes (Figure 2.12 b) [183]. Microfluidization as another liquid-based exfoliation technique has been used for the preparation of phosphorene with the low defect concentration in minute time-scale. The microfluidization is based on the high pressure in the solution and diffusion of fluid into the microchannels (diameter of microchannel, $d < 100$ μm) by pressure force [185]. This method provides mild exfoliation conditions which can control the formation of defects on the surface of phosphorene nanosheets. The schematic illustration of the exfoliation of BP via acoustic-microfluidics (AM) combined with the sonication method is shown in Figure 2.12 (c). A syringe pump, containing bulk BP as a dispersion in NMP, transfers the content to the sonication bath in the presence

of microfluidization. BP exfoliates into phosphorene inside the polytetrafluoroethylene (PTFE) tube. As shown in Figure 2.12 (d), the exfoliation yield of the AM technique depends on the flow rate during microfluidization. Flow rate 5 $mL.min^{-1}$ was found to be the optimum value for the exfoliation of BP. Raman spectroscopy (Figure 2.13 e) of the phosphorene nanosheets confirmed the successful exfoliation of BP by the blue-shift of Raman modes [186].

Laser-assisted exfoliation of BP has been evaluated as an eco-friendly method via laser irradiation/ablation without specific additives or solvents [187-189]. Very recently, Zheng et al. indicated the possibility of BP exfoliation via a Q-switched pulsed laser system in a 2-propanol solution. The proposed mechanism of the laser-assisted BP exfoliation is shown in Figure 2.12 (f). By the interaction of Nd:YAG pulsed laser beam (λ =1064 nm, 650 mJ) and generation of plasma from ns to μs duration range on the surface of bulk BP (stage I), small BP particles and fragments are dispersed into the solution. The high pressure and high temperature of the process produces bubbles and increases the energy of solvent molecules around the generated plasma that accelerates their movement (stage II). The generated bubbles and molecules diffuse into the layered BP in perpendicular and parallel directions and exfoliate the bulk BP into phosphorene with the yield up to 93% (stage III). The P 2p and O 1s XPS spectra of the bulk and exfoliated BP indicated the presence of phosphorus and oxygen (Figure 2.12 g, h). XPS analysis showed a higher areal ratio of unoxidized P in P-P bonding to oxidized P atoms, which increased from 2.3 in bulk BP to 4.6 in phosphorene, suggesting the reduction of nanosheets surface through laser treatment [190]. From the initial results, this method could offer an alternative path toward the exfoliation of BP. However, the morphology-controlled production of phosphorene nanosheets via laser-assisted exfoliation at a massive scale is not yet

available. The shear forces has been utilized in another liquid-based method for the exfoliation of bulk BP in an appropriate solvent [191]. Sajedi-Moghaddam et al. demonstrated the possibility of shear-assisted exfoliation of BP in the DMF solution. In this research the solution was stirred in the laminar regime at 15°C for one hour [192]. In terms of mechanism, the shear force, jet cavitation, and collision during the hydrodynamic exfoliation expand the layered BP [192, 193]. Wet jet milling is another liquid-based exfoliation technique that has been evaluated for the mass-production and exfoliation of layered materials [194]. As shown schematically in Figure 2.12 (i), the shear stress applied to the dispersed BP in acetone through the perforated disks (with adjustable hole diameters 0.1-0.3 mm, named nozzle) and piston-pass and the exfoliates phosphorene transferred to the second container from chiller and processor. The process time in this method is reduced to a fraction of a second compared to the time-consuming sonication process. This process reproducibly provides the appropriate thickness and dimensions. TEM analysis revealed the exfoliated phosphorene nanosheets with the lateral size of around 600 nm (Figure 2.12 j) [195].

Instability of exfoliated phosphorene nanosheets especially in ambient environment results in fast degradation [196]. Therefore, innovative techniques for protecting phosphorene nanosheets from degradation are much needed. Surface modification through passivation or functionalization by a protective layer can suppress the oxidation of the phosphorene nanosheets. However, passivation or functionalization of the phosphorene nanosheets may have complex effect on surface state and charge transport. Due to the relatively low reactivity of bulk BP, covalent functionalization has faces limited success. Using surfactants including ionic liquids as a non-covalent

functionalization agent that can be removed without altering the BP properties, may be promising for the BP protection [197].

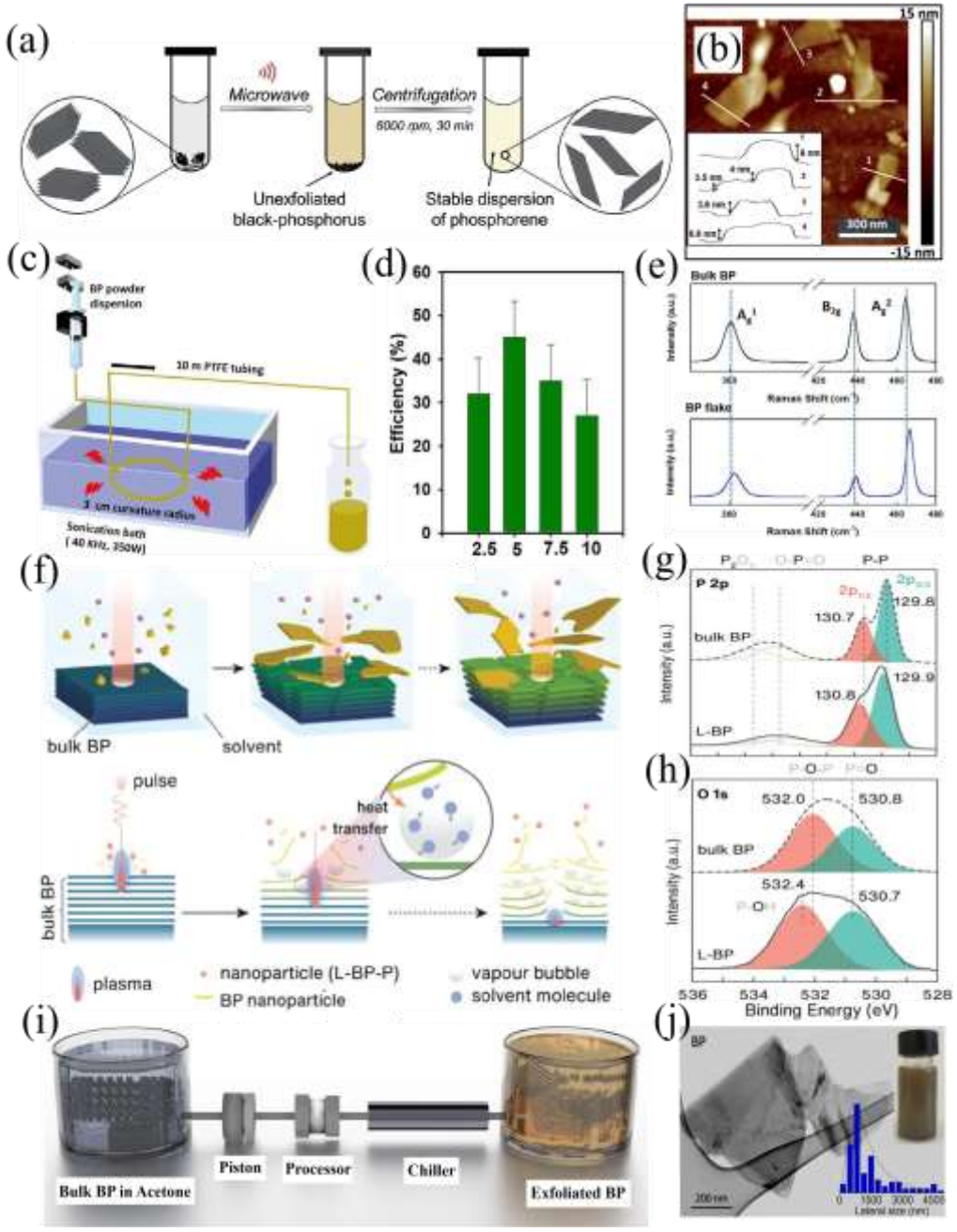

Figure 2.12: (a) Schematic illustration and (b) AFM analysis of the microwaved-assist liquid exfoliation of BP [183], (c) Schematics of the acoustic-microfluidic exfoliation of BP, (d) BP exfoliation efficiency at different flow rates, (e) Raman analysis of the bulk BP and phosphorene nanosheets after 6 minutes exfoliation [186], (f) Laser-assisted exfoliation mechanism of BP, (g and h) P 2p and O 1s XPS spectra of the exfoliated BP [190], (i) Schematic illustration of the exfoliation of BP via wet-jet milling, (j) TEM image of the exfoliated phosphorene with the average size diagram [195].

2.4 Phosphorus for Energy Storage Applications

Liquid-based exfoliated BP nanosheets with 2D structure and light molecular weight have been considered as a promising electrode material for energy storage devices such as rechargeable batteries (host for Li^+ and Na^+ ions) and supercapacitors due to their high theoretical capacity, surface area, and charge mobility. Phosphorene nanosheets-based electrodes have been employed as an anode material for Li-, Na-, Mg-ion, and Li-S batteries through the alloying-dealloying mechanism. However, large volume expansion up to 300% during cycling and sluggish reaction kinetics obstructed its real performance.

2.4.1 Phosphorus for Rechargeable Batteries

Theoretical calculations evaluated the favorable diffusion pass of Li atom on the surface of phosphorene nanosheets (Figure 2.13 a, b) [198]. As shown in Figure 2.14 (b), the low energy barrier of 0.08eV along the zigzag direction provides a diffusion pass for Li ions at room temperature with good reversibility. This high anisotropic properties of phosphorene block the Li^+ diffusion in the armchair direction with the high energy barrier of 0.68 eV. Li et al. showed that the intercalation of Li into phosphorene layers provided a good electrical conductivity with a high open-circuit potential of 2.9 V, which is sufficient for high-performance lithium ion batteries (LIBs) [198]. The theoretical specific capacity of 432.79 $mAhg^{-1}$ is found for the phosphorene nanosheets, which is higher compared to carbon (372 $mAhg^{-1}$) as the main commercial (LIB) anode [199]. Introducing defects on the surface of BP nanosheets can also improve the binding energy of Li and phosphorene from 1.73 eV to 3.31 eV. Moreover, introduction of conductive agent such as graphene to

phosphorene as a heterostructured anode improves the mobility of Li ions by reducing the polarization effect [200].

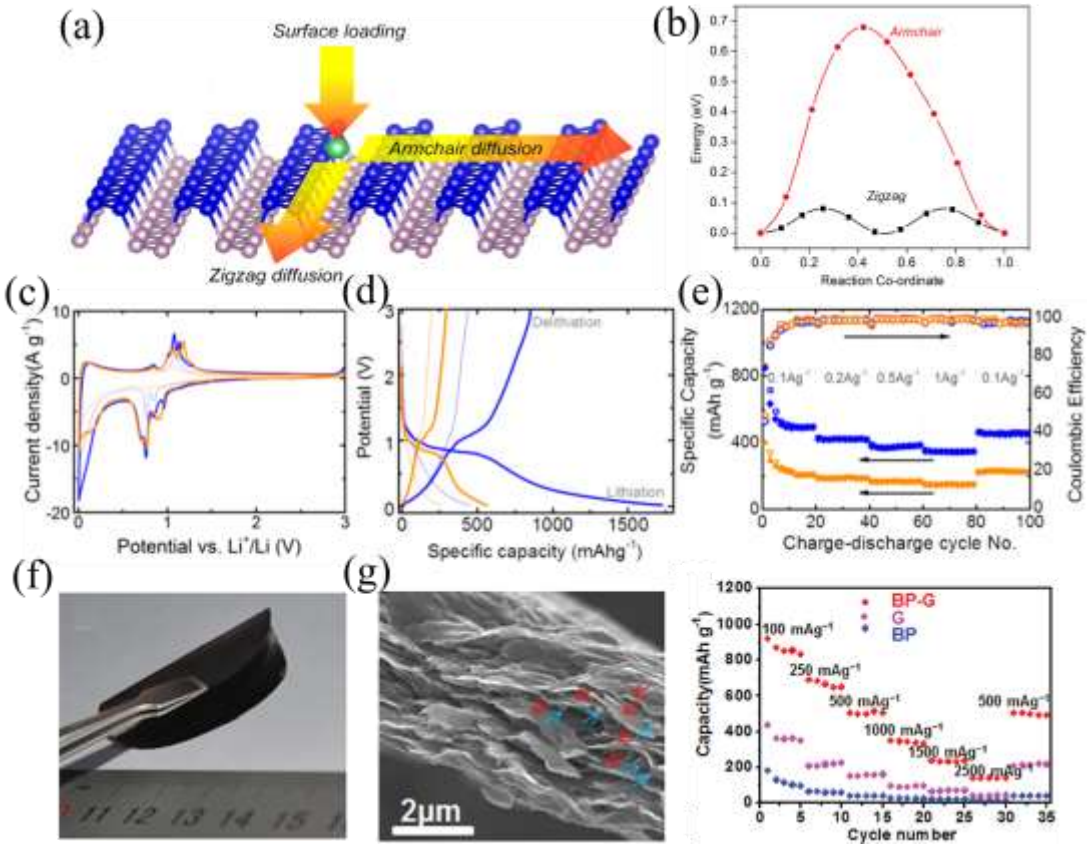

Figure 2.13: (a) Schematic illustration, and (b) Li-ion diffusion profile along with the zigzag and armchair directions of phosphorene [198], (c) Cyclic voltammetry at the rate of 30 μVs^{-1}, (d) Galvanostatic charge/discharge at 100 mAg^{-1} (thick line: cycle 1, thin line: cycle 20), and (e) Rate capability tests at a different current of the exfoliated phosphorene in acetone (blue lines) and CHP (orange lines) [116], (f) Photograph of the phosphorene/graphene flexible electrode, (g) Cross-section of phosphorene/graphene hybrid anode (red and blue arrows are graphene and phosphorene, respectively), and (h) Rate capability performance of the phosphorene, graphene and hybrid anode at different current densities [77].

Following the theoretical characterization, Castillo et al. evaluated the electrochemical performance of phosphorene nanosheets obtained via liquid exfoliation of BP in acetone and CHP (Figure 2.13 c-e) [116]. As shown in Figure 2.13 (c), the cyclic voltammetry of the half-cell anode in the voltage window of 0.05 to 3V exhibited the solid electrolyte interface (SEI) produced by the BP nanosheets and Li^+ reactions and lithitan-delithation of phosphorene in $LiPF_6$ solution. In general,

the electrochemical mechanism of BP nanosheets during charge-discharge cycles is as follows [201]:

Discharge process: $BP \rightarrow Li_nP \rightarrow LiP \rightarrow Li_2P \rightarrow Li_3P$ (n<1)

Charge Process: $Li_3P \rightarrow Li_2P \rightarrow LiP \rightarrow Li_nP \rightarrow BP$ (n<1)

Galvanostatic charge/discharge profiles revealed the initial capacity of 1732 and 545 $mAhg^{-1}$ at 100 mAg^{-1} for the exfoliated phosphorene in acetone and CHP, respectively. However, the huge capacity fading observed after 20 cycles (480 and 250 $mAhg^{-1}$ for acetone and CHP) is due to the large volume expansion of phosphorene. Furthermore, the rate capability performance of the anodes showed a low specific capacity of 345 and 200 $mAhg^{-1}$ for the exfoliated phosphorene in acetone and CHP at 1 Ag^{-1} [116]. In general, Li_3P formed in the first discharge cycle does not reversibly transform to BP in the subsequent charging cycle. The disbondment of the active phosphorene material from the current collector reduces the active sites for energy storage and as a result, the material shows high initial irreversible capacity, low columbic efficiency, and side reactions with electrolyte, which hinders the real performance of pure phosphorene in LIBs [202]. For the first time, Chen and co-workers evaluated the electrochemical performance of the paper-like exfoliated BP and a phosphorene (80 wt.%) with graphene (20 wt.%) hybrid obtained by vacuum filtration as a LIB anode. The synthesized composite is flexible, and the phosphorene and graphene nanosheets are stacked in parallel that improves the conductivity of phosphorene and shortens the lithium ions diffusion (Figure 2.13 f, g). Graphene nanosheets provide a preferential electrical highway for the transportation of electrons produced through the redox reaction of phosphorene. The structural stability during cycles was greatly improved by forming the chemical P–C bonds. As shown in Figure 2.13 (h), the hybrid anode delivers a specific capacity of

920 $mAhg^{-1}$ at the current density of 100 mAg^{-1} which is much higher compared to the pure phosphorene (180 $mAhg^{-1}$) and pure graphene (435 $mAhg^{-1}$). By increasing the current density up to 500 mAg^{-1} the hybrid anode still provides high specific capacity (501 $mAhg^{-1}$), reversibility, and rate capability [77]. Following this research, Zhang et al. evaluated the high yield exfoliated BP in formamide as an air-stable anode material for LIBs. Compared to graphene, they confirmed that the phosphorene nanosheets react much easier with graphene oxide. The developed anode showed high specific capacity of 1013 and 415 $mAhg^{-1}$ at the current density of 100 mAg^{-1} and 10 Ag^{-1}, respectively. Moreover, after 60 days of exposure to the ambient atmosphere, the specific capacity dropped slightly to 823 $mAhg^{-1}$, which confirms the passivation of phosphorene by graphene oxide [62]. Very recently, incorporation of other agents into phosphorene such as TiO_2 [203], cellulose [204], and carbon nanotube (CNT) [205] were evaluated for LIB applications. Zhang et al. selected CNT to provide a 3D phosphorene composite with stable chemical bonds (P-C, P-O-C, and P-N-C). The hybrid anode delivered a high capacity of 1088 $mAhg^{-1}$ at the current density of 100 mAg^{-1}. Figure 2.14 (a, b) shows the schematic illustration and SEM analysis of phosphorene and phosphorene/CNT anodes before and after 500 cycles. For the pure phosphorene, due to the volume expansion and produced cracks, the active material didn't recover to the original structure (Figure 2.14 a). In comparison, the hybrid composite presented a dense morphology without obvious cracks in the presence of conductive CNT as a supporting matrix even after 500 cycles (Figure 2.14 b). Figure 2.14 (c, d) displays the galvanostatic charge/discharge and cycling performance of hybrid composite at a moderate current density of 500 $mAhg^{-1}$. After the fast capacity fading in the second cycle (from 2229 to 1725.3 $mAhg^{-1}$), the capacity continues to fade until the 50^{th} cycle, declining very slowly to become stable at about 757 $mAhg^{-1}$

until 650 cycles [205]. It is reported that volume expansion in phosphorene-based electrodes is highly anisotropic in nature and the loss of electric contact is only associated to the de-lithiation step rather than lithiation [206] .

Due to the abundance, low cost, and eco-friendly compatibility of sodium compared to lithium, Na-ion batteries have attracted attention in recent years. Theoretical investigation for the sodiation mechanism of phosphorene nanosheets revealed that until the Na concentration of $Na_{0.25}P$, the chemical bonds in the layered BP are not altered but by increasing the Na content to $Na_{0.28}P$, the cleavage of P-P bonds starts precipitating the amorphous phase of Na_3P from Na_xP (Figure 2.15 a) [207]. The two-step process of Na storage in phosphorene is includes intercalation and alloying mechanisms. By the diffusion of Na ions along the zigzag direction, when the Na ion concentration is higher than $Na_{0.25}P$, the formation of Na_xP through alloying mechanism is suggested [208]. Notably, Kulish and co-workers calculated the energy barrier of 0.04 eV along the zigzag direction of phosphorene, which provides a fast diffusion path for Na ions [209]. Huang and co-workers directly employed a few-layer exfoliated phosphorene as an anode of SIBs in $NaClO_4$ solution. As shown in Figure 2.15 (b), the reversible redox peaks in the CV curves at around 0.45 and 0.9 V are related to the NaP formation and decomposition. The cycling performance of the anode at the current density of 100 $mAhg^{-1}$ presented a rise of specific capacity after 15 cycles due to the electrochemical activation of nanosheets (Figure 2.15 c). Furthermore, the galvanostatic charge/discharge profiles at different current density in the voltage range of 0.02 to 1.5 V plotted in Figure 2.15 (d) exhibited a specific capacity of 1878 and 321 $mAhg^{-1}$ at the current density from 100 mAg^{-1} to 2.5 Ag^{-1}, respectively, which is much better than the pure phosphorene-based anode for LIBs [144].

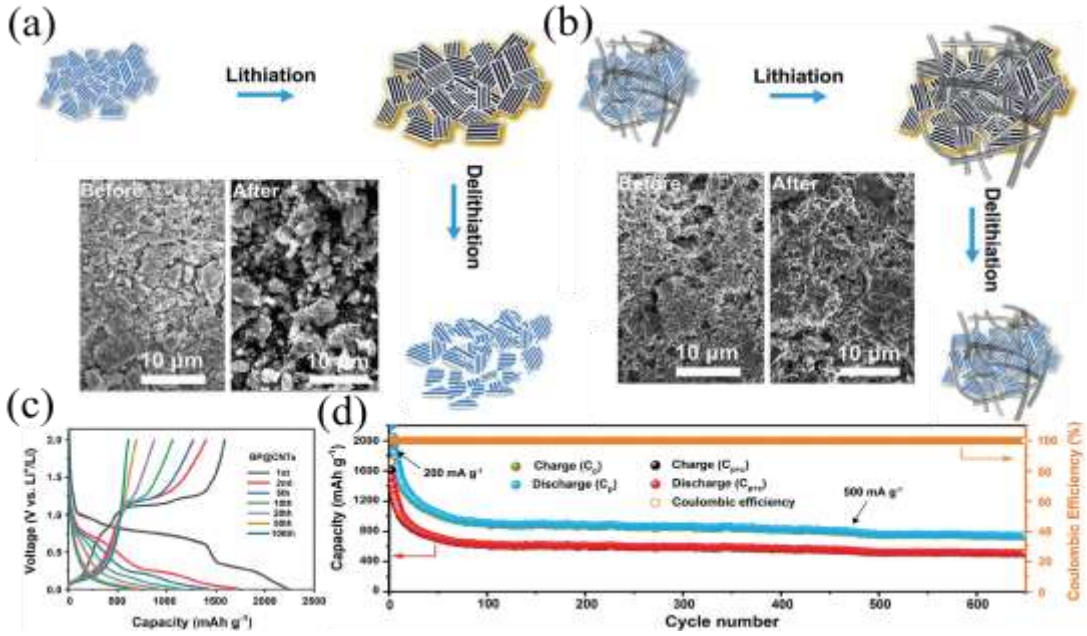

Figure 2.14: Schematic illustration and SEM images of (a) The phosphorene and (b) Phosphorene/CNT hybrid after 500 cycles as an anode of LIB, (c) Galvanostatic charge/discharge, and (c) Cycling performance of phosphorene/CNT hybrid at the current density of 500 mAg^{-1} [205].

Similar to LIBs, the electrochemical performance of the phosphorene nanosheets have been improved using carbonaceous materials [210, 211]. Sun et al. for the first time evaluated the nanostructured graphene in exfoliated phosphorene as a hybrid anode for SIB application. The exfoliated phosphorene through the sonication of BP in NMP, is mixed with graphene nanosheets to provide a self-assembly layer-by-layer composite. The hybrid anode exhibited a high specific capacity of 2080 and 497 $mAhg^{-1}$ at low and very high current of 0.05 and 26 Ag^{-1}, respectively. The combination of phosphorene/graphene provides fast transport for the ions and electrons and buffers the expansion of phosphorene. Moreover, in the presence of high-conductive graphene, phosphorene redox reactions are much faster [88]. Inspired by this work, Shuai and co-workers developed a phosphorene/graphene sandwich structure through the electrochemical exfoliation for SIB application. As shown in Figure 2.15 (e), the intercalation of phosphorene nanosheets between graphene layers through P-C and P-O-C chemical bonds provides a sandwich structure of the hybrid

anode with high Na^+ ion storage capability. The prepared hybrid anode with the 1:1 mass ratio delivered a high specific capacity of 1455 and 1011 $mAhg^{-1}$ after 200 cycles with more than 79% and 67% capacity retention at 1 and 5 Ag^{-1}, respectively (Figure 2.15 f) [158]. Due to the excellent electrochemical performance and the outstanding mechanical flexibility of phosphorene/graphene sandwich structure, the developed hybrid electrode could be used in wearable electronics in near future. Very recently, the electrochemical performance of the exfoliated phosphorene as an electrode material for K-ion and Li-S batteries was evaluated. However, the actual mechanisms of electrochemical reactions are still unclear and the obtained specific capacities are not comparable with the state of the arts [33, 92].

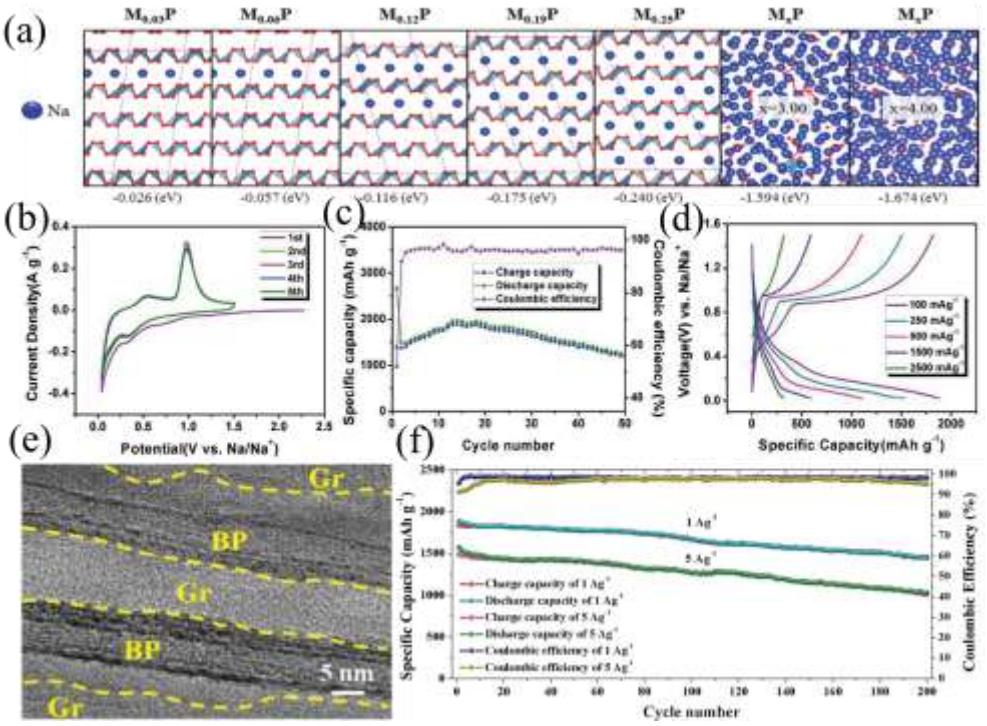

Figure 2.15: (a) Sodiation mechanism of phosphorene nanosheets (the solid gray is the supercell of phosphorus and the numbers are formation energy) [207], (b) CV at 0.1 mVs^{-1}, (c) Cycling performance at 100 $mAhg^{-1}$, and (d) Galvanostatic charge/discharge profiles at different current densities of exfoliated phosphorene as an anode of SIB [144], (e) TEM image of the cross-section of phosphorene/graphene hybrid, and (f) Cycling performance of phosphorene/graphene sandwich structure at the 1 and 5 Ag^{-1} [158].

2.4.2 Phosphorus for Capacitor Applications

Supercapacitors with high power density (~10^3 W kg^{-1}), great cyclability, and ultrafast charge/discharging rate (~1 s) have been attracting attention in different energy storage devices. Based on the charge storage mechanism, supercapacitors are divided into pseudocapacitors and electrical double-layer capacitors (EDLCs). Fast reversible redox reactions near the electrode/electrolyte and charge storage at the electrode/electrolyte interfaces are the main working mechanisms of pseudocapacitors and EDLCs, respectively [212]. Hao et al. for the first time investigated the exfoliated phosphorene nanosheets in all-solid-state supercapacitors. As shown schematically in Figure 2.16 (a), they dispersed the nanosheets on two coated platinum/polybutylene terephthalate electrodes and prepared a sandwich-type phosphorene electrode with the solid polyvinyl alcohol/phosphoric acid (PVA/H_3PO_4) as an electrolyte. The semi-solid gel electrolyte may control the oxidation of nanosheets at the ambient environment. The obtained double-layer capacitor delivered a high capacitance of 13.75 F cm^{-3} at 0.01 Vs^{-1} at the scan rate of 0.01 V S^{-1} with significant cyclability up to 30000 cycles [108]. Inspired by this study, Yang and co-workers designed solid-state micro-supercapacitors with a free-standing BP thin film electrode via the laser machining process. The CV curves of the symmetric device at different scan rates have rectangular shapes confirming an ideal double-layer capacitor behavior (Figure 2.16 b). The galvanostatic charge/discharge at different current densities also presented a linear capacitive performance with a very small ohmic drop (Figure 2.16 c). The fabricated device exhibited a high volumetric capacitance and energy density of 26.67 F cm^{-3} and 3.63 mWh cm^{-3} at 0.5 A cm^{-3}, respectively. As shown in Figure 2.16 (d), the high energy density of 1.53 mWh cm^{-3} remained at the very high power

density of 10.1 W cm^{-3}, which is higher than other 2D-based micro-supercapacitors and can successfully light the red LED [151].

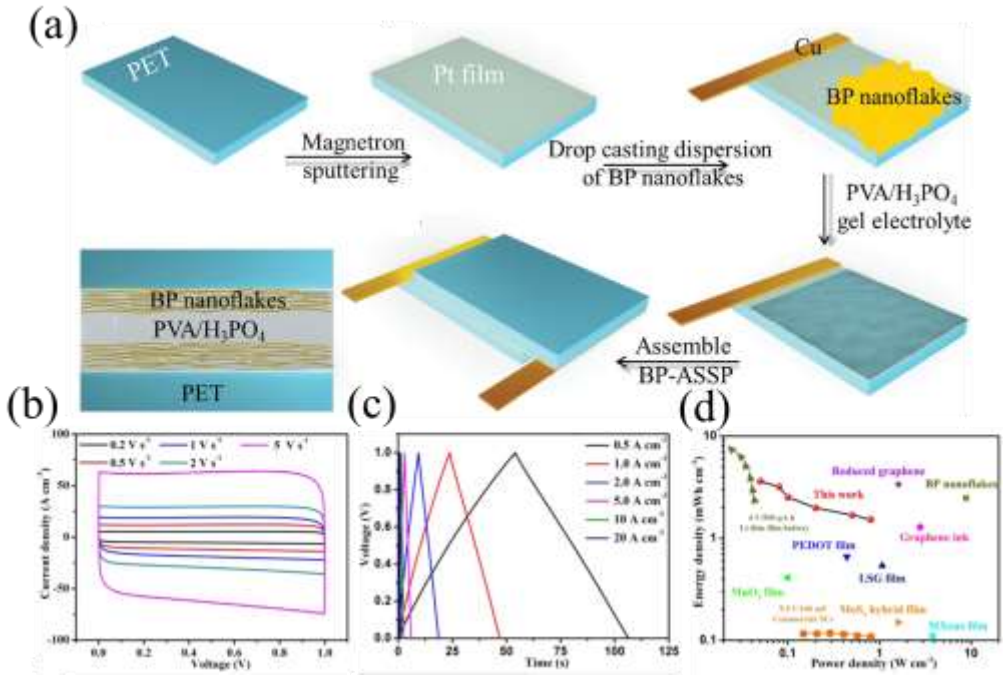

Figure 2.16: (a) Schematic fabrication process of the all-solid-state supercapacitors with sandwich structure with PVA/H_3PO_4 [114], (b) CV profiles at different scan rate, (c) Galvanostatic charge/discharge at different current densities, and (d) Ragone curve for the exfoliated PB-based supercapacitor with some other reports as a comparison [151].

Similar to rechargeable batteries, in order to improve the conductivity and to control the volume expansion, conductive agents are often introduced to the phosphorene nanosheets for capacitor applications [115, 124, 213, 214]. Xiao et al. fabricated a symmetric phosphorene/graphene hybrid composite through a mask-assisted filtration method for a flexible micro-supercapacitor application. As shown in Figure 2.17 (a), the exfoliated phosphorene and graphene inks were filtered onto a poly-tetrafluoroethylene (PTFE) membrane and then, transferred onto to PET substrate and packaged with 1-butyl-3-methylimidazolium hexafluorophosphate ($BMIMPF_6$) as an ionic liquid electrolyte. The phosphorene/graphene hybrid electrode can effectively hinder the disordered stacking and self-standing lamellar film with wrinkle inside,

thus arranging more ion-accessible sites for the active material on the substrate. The galvanostatic charge/discharge profiles for the EDLC-type hybrid composite and pure graphene, confirmed the synergetic effect of phosphorene nanosheets, which delivered remarkable aerial capacitance and energy density of 9.8 mF cm^{-2} and 11.6 mWh cm^{-3} at 5 mV s^{-1}, respectively (Figure 2.17 b). As shown in Figure 2.17 (c, d), similar to the one device performance, the three serially hybrid composites, presented a rectangular CV with the 9 V voltage extension, which can easily power a red LED [135]. Table 3.3 presents the research progress on the phosphorene-based electrodes for energy storage applications. As shown in Table 3.3, exfoliated phosphorene nanosheets stand out to be a promising candidate for rechargeable batteries and supercapacitors.

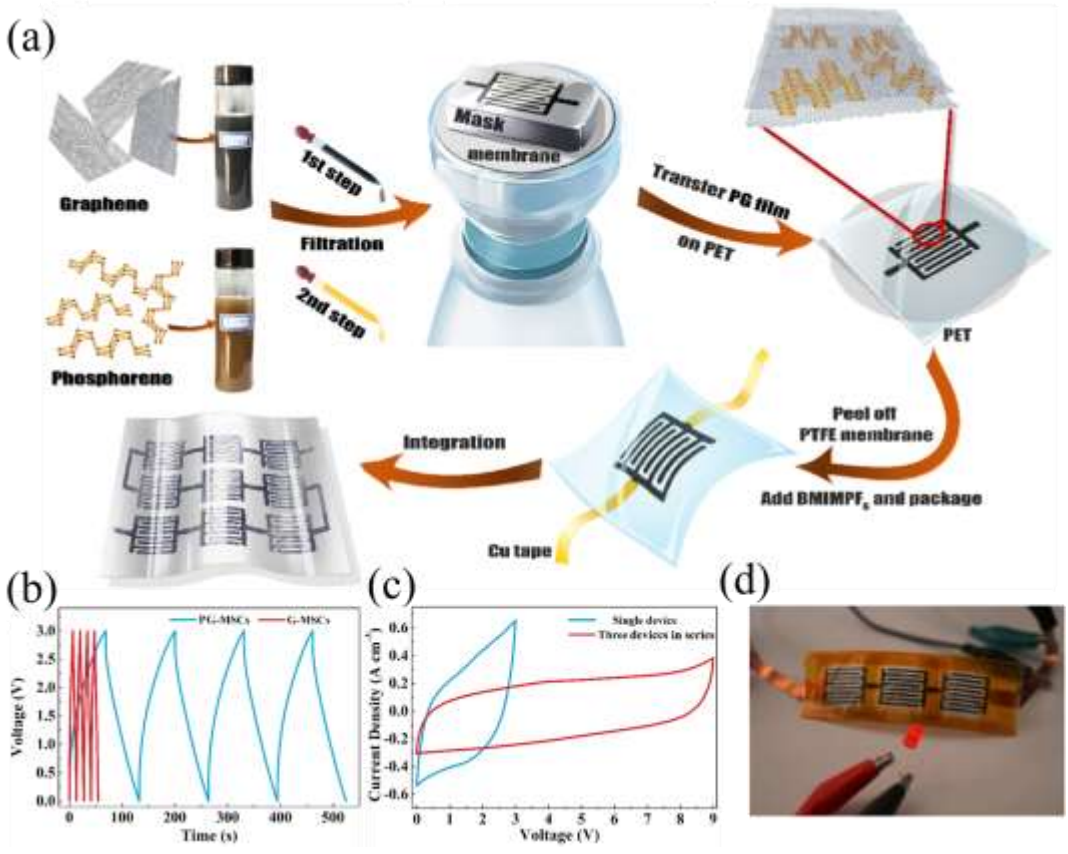

Figure 2.17: (a) Preparation and fabrication process of the mask-assisted phosphorene/graphene micro-supercapacitor, (b) Galvanostatic charge/discharge profiles for the graphene and phosphorene/graphene composite at 0.3 A cm^{-3}, (c) CV curves for the single and three serial hybrid electrode at 100 mV s^{-1}, and (d) Photograph of the three serial hybrid electrode to power a LED [135].

Table 2.3: Electrochemical performances of the liquid-based exfoliated BP for energy storage applications.

Material	Device	Voltage Window	Electrochemical Performance	Ref.
Phosphorene nanosheets	LIB	0.05-3 V	Specific capacity of 480 $mAhg^{-1}$ at 100 mAg^{-1}, capacity retention of 70.0% at 1 A g^{-1} after 100 cycles	[116]
Phosphorene nanosheets	LIB	0.001-3 V	Specific capacity of 510 $mAhg^{-1}$ at 200 mAg^{-1}, capacity retention of 103.9% at 200 A g^{-1} after 35 cycles	[190]
Phosphorene/graphene hybrid paper	LIB	0.001-3 V	Specific capacity of 920 $mAhg^{-1}$ at 100 mAg^{-1}, capacity retention of 80.2% at 0.5 A g^{-1} after 500 cycles	[77]
Phosphorene/graphene oxide hybrid paper	LIB	0.01-3 V	Specific capacity of 1013 $mAhg^{-1}$ at 100 mAg^{-1}, capacity retention of 91.9% at 10 A g^{-1} after 800 cycles	[62]
Phosphorene/Poly(3,4-ethylenedioxythiophene hybrid	LIB	0.01-3 V	Specific capacity of 1408 $mAhg^{-1}$ at 100 mAg^{-1}, capacity retention of 77.6% at 100 mAg^{-1} after 100 cycles	[94]
Phosphorene/graphene hybrid paper	LIB	0.01-3 V	Specific capacity of 1633 $mAhg^{-1}$ at 100 mAg^{-1}, capacity retention of 85.8% at 100 mAg^{-1} after 200 cycles	[215]
Phosphorene/graphene/TiO_2 composite	LIB	0.01-3 V	Specific capacity of 502.9 $mAhg^{-1}$ at 1.25 Ag^{-1} after 180 cycles	[203]
Phosphorene/nanocellulose composite	LIB	0.01-3 V	Specific capacity of 1020.1 $mAhg^{-1}$ at 100 mAg^{-1}, capacity retention of 87.1% at 100 mAg^{-1} after 230 cycles	[204]
Phosphorene/CNT hybrid composite	LIB	0.01-2 V	Specific capacity of 521.9 $mAhg^{-1}$ at 500 mAg^{-1}, capacity retention of 80.3% at 500 mAg^{-1} after 550 cycles	[205]
Phosphorene nanosheets	SIB	0.02-1.5 V	Specific capacity of 1878.4 $mAhg^{-1}$ at 100 mAg^{-1}, capacity retention of 102.1% at 1.5 Ag^{-1} after 100 cycles	[144]
Phosphorene/graphene hybrid	SIB	0.02-1.5 V	Specific capacity of 2080 $mAhg^{-1}$ at 50 mAg^{-1}, capacity retention of 83% at 50 mAg^{-1} after 100 cycles	[88]
Phosphorene/Poly(3,4-ethylenedioxythiophene hybrid	SIB	0.01-3 V	Specific capacity of 1397 $mAhg^{-1}$ at 100 mAg^{-1}, capacity retention of 67.4% at 100 mAg^{-1} after 100 cycles	[94]

Phosphorene/reduced graphene oxide hybrid	SIB	0.01-3 V	Specific capacity of 1472 $mAhg^{-1}$ at 100 mAg^{-1}, capacity retention of 82.2% at 100 mAg^{-1} after 50 cycles	[210]
Phosphorene/graphene hybrid	SIB	0.02-1.5 V	Specific capacity of 1297 $mAhg^{-1}$ at 100 mAg^{-1} after 100 cycles	[211]
Phosphorene/graphene hybrid	SIB	0.02-1.5 V	Specific capacity of 2311 $mAhg^{-1}$ at 100 mAg^{-1}, capacity retention of 83.9% at 100 mAg^{-1} after 100 cycles	[158]
Phosphorene/MXene hybrid	SIB	0.01-3 V	Specific capacity of 535 $mAhg^{-1}$ at 100 mAg^{-1}, capacity retention of 87% at 1 Ag^{-1} after 1000 cycles	[216]
Phosphorene nanosheets	Supercapacitor	0-1 V	Capacitance of 13.75 F cm^{-3} at 0.01 V s^{1}, capacity retention of 71.8% after 30000 cycles	[114]
Phosphorene nanosheets	Supercapacitor	-0.4-0.4 V	Specific capacitance of 80 F g^{-1} at 100 mVs^{-1}, capacity retention of 80% after 15000 cycles	[167]
Phosphorene nanosheets	Supercapacitor	0-1 V	Energy density of 3.63 mWh cm^{-3}, power density of 26.67 F cm^{-3}, capacity retention of 94.3% after 50000 cycles	[151]
Phosphorene nanosheets	Supercapacitor	0-0.7 V	Discharge energy of 0.01 mWh cm^{-2} and power density of 351 mW cm^{-2} at 500 mA cm^{-2} after 40000 cycles	[23]
Phosphorene nanosheets	Supercapacitor	-0.1-0.7 V	Specific capacitance of 12.3 F g^{-1} at 0.025 V s^{-1}, capacity retention of 82.3% at 0.5 V s^{-1} after 200 cycles	[168]
Phosphorene/graphene hybrid	Supercapacitor	0-3 V	Areal capacitance of 9.8 mF cm^{-2}, energy density of 11.6 mWh cm^{-3} at 5mV s^{-1}	[135]
Phosphorene/polyaniline hybrid	Supercapacitor	-0.4-0.6	Specific capacitance of 354 F g^{-1} at 0.3 A g^{-1}, capacity retention of 96% after 175 cycles	[192]
Phosphorene/CNT composite paper	Supercapacitor	0-1 V	Volumetric capacitance of 41.1 F cm^{-3}, power density of 821.62 Wcm^{-3}, capacity retention of 91.5% after 10000 cycles	[115]
Phosphorene/polypyrrole composite paper	Supercapacitor	0-0.7 V	Specific capacitance of 431.4 F g^{-1}, cycling stability up to 10000 cycles	[124]
Phosphorene/graphene oxide hybrid paper	Supercapacitor	0-1 V	Specific capacitance of 104.4 F g^{-1} at 0.25 A g^{-1}, capacity retention of 62.3% at 50 A g^{-1} after 5000 cycles	[214]
Phosphorene/CNT composite	Supercapacitor	0-3 V	Specific capacitance of 308.7 F g^{-1} at 0.1 A cm^{-3}, capacity retention of 90.2% after 10000 cycles	[213]

2.5 Conclusion

The research on novel 2D materials is an ongoing study and has attracted significant attention in recent years due to chemical, physical, and mechanical properties on these materials. In this chapter, we comprehensively summarized different exfoliation of BP into phosphorene techniques and its application for batteries and supercapacitors. The real electrochemical performance of phosphorene strongly depends on its preparation technique. Due to the high theoretical capacity, structural anisotropy, and surface area of phosphorus-based electrodes, their electrochemical performance has been demonstrated for rechargeable batteries and supercapacitors. Phosphorene-based anode material has shown high specific capacity and rate capabilities in LIBs. However, providing a scaled-up phosphorene-based electrode preparation for energy storage applications is still challenging. We believe that phosphorus-based material will develop in near future and contribute to reliable, eco-friendly, and high-performance energy storage devices.

2.6 References

[1] M. Salanne, B. Rotenberg, K. Naoi, K. Kaneko, P.-L. Taberna, C.P. Grey, B. Dunn, P. Simon, Efficient storage mechanisms for building better supercapacitors, Nature Energy 1(6) (2016) 1-10.

[2] D. Larcher, J.-M. Tarascon, Towards greener and more sustainable batteries for electrical energy storage, Nature chemistry 7(1) (2015) 19-29.

[3] Y. Wang, B. Liu, Q. Li, S. Cartmell, S. Ferrara, Z.D. Deng, J. Xiao, Lithium and lithium ion batteries for applications in microelectronic devices: A review, Journal of Power Sources 286 (2015) 330-345.

[4] Y. Shao, M.F. El-Kady, J. Sun, Y. Li, Q. Zhang, M. Zhu, H. Wang, B. Dunn, R.B. Kaner, Design and mechanisms of asymmetric supercapacitors, Chemical reviews 118(18) (2018) 9233-9280.

[5] P. Simon, Y. Gogotsi, Materials for electrochemical capacitors, Nanoscience and technology: a collection of reviews from Nature journals (2010) 320-329.

[6] T. Chen, L. Dai, Carbon nanomaterials for high-performance supercapacitors, Materials Today 16(7-8) (2013) 272-280.

[7] J. Pang, A. Bachmatiuk, Y. Yin, B. Trzebicka, L. Zhao, L. Fu, R.G. Mendes, T. Gemming, Z. Liu, M.H. Rummeli, Applications of phosphorene and black phosphorus in energy conversion and storage devices, Advanced Energy Materials 8(8) (2018) 1702093.

[8] Z. Yue, T. Gupta, F. Wang, C. Li, R. Kumar, Z. Yang, N. Koratkar, Utilizing a graphene matrix to overcome the intrinsic limitations of red phosphorus as an anode material in lithium-ion batteries, Carbon 127 (2018) 588-595.

[9] S.A. Ansari, M.O. Ansari, M.H. Cho, Facile and Scale Up Synthesis of Red Phosphorus-Graphitic Carbon Nitride Heterostructures for Energy and Environment Applications, Scientific Reports 6(1) (2016) 27713.

[10] A.R. Baboukani, I. Khakpour, E. Adelowo, V. Drozd, W. Shang, C. Wang, High-performance red phosphorus-sulfurized polyacrylonitrile composite by electrostatic spray deposition for lithium-ion batteries, Electrochimica Acta (2020) 136227.

[11] W. Liu, H. Zhi, X. Yu, Recent progress in phosphorus based anode materials for lithium/sodium ion batteries, Energy Storage Materials 16 (2019) 290-322.

[12] K.S. Novoselov, A.K. Geim, S.V. Morozov, D. Jiang, Y. Zhang, S.V. Dubonos, I.V. Grigorieva, A.A. Firsov, Electric Field Effect in Atomically Thin Carbon Films, Science 306(5696) (2004) 666-669.

[13] X. Cai, Y. Luo, B. Liu, H.-M. Cheng, Preparation of 2D material dispersions and their applications, Chemical Society Reviews 47(16) (2018) 6224-6266.

[14] M. Liu, R. Zhang, W. Chen, Graphene-Supported Nanoelectrocatalysts for Fuel Cells: Synthesis, Properties, and Applications, Chemical Reviews 114(10) (2014) 5117-5160.

[15] S. Manzeli, D. Ovchinnikov, D. Pasquier, O.V. Yazyev, A. Kis, 2D transition metal dichalcogenides, Nature Reviews Materials 2(8) (2017) 17033.

[16] R. Geick, C. Perry, G. Rupprecht, Normal modes in hexagonal boron nitride, Physical Review 146(2) (1966) 543.

[17] X. Wang, S. Blechert, M. Antonietti, Polymeric graphitic carbon nitride for heterogeneous photocatalysis, Acs Catalysis 2(8) (2012) 1596-1606.

[18] B. Anasori, M.R. Lukatskaya, Y. Gogotsi, 2D metal carbides and nitrides (MXenes) for energy storage, Nature Reviews Materials 2(2) (2017) 1-17.

[19] P. Vishnoi, K. Pramoda, C. Rao, 2D Elemental Nanomaterials beyond Graphene, ChemNanoMat 5(9) (2019) 1062-1091.

[20] A. Gupta, T. Sakthivel, S. Seal, Recent development in 2D materials beyond graphene, Progress in Materials Science 73 (2015) 44-126.

[21] P. Bridgman, FURTHER NOTE ON BLACK PHOSPHORUS, Journal of the American Chemical Society 38(3) (1916) 609-612.

[22] L. Li, Y. Yu, G.J. Ye, Q. Ge, X. Ou, H. Wu, D. Feng, X.H. Chen, Y. Zhang, Black phosphorus field-effect transistors, Nature nanotechnology 9(5) (2014) 372.

[23] A.R. Baboukani, I. Khakpour, V. Drozd, A. Allagui, C. Wang, Single-step exfoliation of black phosphorus and deposition of phosphorene via bipolar electrochemistry for capacitive energy storage application, Journal of Materials Chemistry A 7(44) (2019) 25548-25556.

[24] R. Ma, T. Sasaki, Two-Dimensional Oxide and Hydroxide Nanosheets: Controllable High-Quality Exfoliation, Molecular Assembly, and Exploration of Functionality, Accounts of Chemical Research 48(1) (2015) 136-143.

[25] X. Han, J. Han, C. Liu, J. Sun, Promise and challenge of phosphorus in science, technology, and application, Advanced Functional Materials 28(45) (2018) 1803471.

[26] A. Carvalho, M. Wang, X. Zhu, A.S. Rodin, H. Su, A.H.C. Neto, Phosphorene: from theory to applications, Nature Reviews Materials 1(11) (2016) 1-16.

[27] F. Xia, H. Wang, Y. Jia, Rediscovering black phosphorus as an anisotropic layered material for optoelectronics and electronics, Nature communications 5(1) (2014) 1-6.

[28] A. Carvalho, M. Wang, X. Zhu, A.S. Rodin, H. Su, A.H. Castro Neto, Phosphorene: from theory to applications, Nature Reviews Materials 1(11) (2016) 16061.

[29] R. Hultgren, N. Gingrich, B. Warren, The atomic distribution in red and black phosphorus and the crystal structure of black phosphorus, The Journal of Chemical Physics 3(6) (1935) 351-355.

[30] L.-F. Gao, J.-Y. Xu, Z.-Y. Zhu, C.-X. Hu, L. Zhang, Q. Wang, H.-L. Zhang, Small molecule-assisted fabrication of black phosphorus quantum dots with a broadband nonlinear optical response, Nanoscale 8(33) (2016) 15132-15136.

[31] Y. Zhang, Y. Zheng, K. Rui, H.H. Hng, K. Hippalgaonkar, J. Xu, W. Sun, J. Zhu, Q. Yan, W. Huang, 2D black phosphorus for energy storage and thermoelectric applications, Small 13(28) (2017) 1700661.

[32] C. Liu, Y. Wang, J. Sun, A. Chen, A review on applications of layered phosphorus in energy storage, Transactions of Tianjin University (2020) 1-23.

[33] H. Jin, H. Wang, Z. Qi, D.S. Bin, T. Zhang, Y. Wan, J. Chen, C. Chuang, Y.R. Lu, T.S. Chan, A Black Phosphorus–Graphite Composite Anode for Li-/Na-/K-Ion Batteries, Angewandte Chemie 132(6) (2020) 2338-2342.

[34] X. Ren, J. Zhou, X. Qi, Y. Liu, Z. Huang, Z. Li, Y. Ge, S.C. Dhanabalan, J.S. Ponraj, S. Wang, Few-layer black phosphorus nanosheets as electrocatalysts for highly efficient oxygen evolution reaction, Advanced Energy Materials 7(19) (2017) 1700396.

[35] Q. Jiang, L. Xu, N. Chen, H. Zhang, L. Dai, S. Wang, Facile synthesis of black phosphorus: an efficient electrocatalyst for the oxygen evolving reaction, Angewandte Chemie 128(44) (2016) 14053-14057.

[36] M. Buscema, D.J. Groenendijk, S.I. Blanter, G.A. Steele, H.S. Van Der Zant, A. Castellanos-Gomez, Fast and broadband photoresponse of few-layer black phosphorus field-effect transistors, Nano letters 14(6) (2014) 3347-3352.

[37] X. Li, Z. Yu, X. Xiong, T. Li, T. Gao, R. Wang, R. Huang, Y. Wu, High-speed black phosphorus field-effect transistors approaching ballistic limit, Science advances 5(6) (2019) eaau3194.

[38] A.N. Abbas, B. Liu, L. Chen, Y. Ma, S. Cong, N. Aroonyadet, M. Köpf, T. Nilges, C. Zhou, Black phosphorus gas sensors, ACS nano 9(5) (2015) 5618-5624.

[39] D.J. Late, Liquid exfoliation of black phosphorus nanosheets and its application as humidity sensor, Microporous and Mesoporous Materials 225 (2016) 494-503.

[40] X. Chen, J.S. Ponraj, D. Fan, H. Zhang, An overview of the optical properties and applications of black phosphorus, Nanoscale 12(6) (2020) 3513-3534.

[41] L. Zhang, B. Wang, Y. Zhou, C. Wang, X. Chen, H. Zhang, Synthesis Techniques, Optoelectronic Properties, and Broadband Photodetection of Thin-Film Black Phosphorus, Advanced Optical Materials (2020) 2000045.

[42] M. Luo, T. Fan, Y. Zhou, H. Zhang, L. Mei, 2D black phosphorus–based biomedical applications, Advanced Functional Materials 29(13) (2019) 1808306.

[43] J.R. Choi, K.W. Yong, J.Y. Choi, A. Nilghaz, Y. Lin, J. Xu, X. Lu, Black phosphorus and its biomedical applications, Theranostics 8(4) (2018) 1005.

[44] J. Kang, V.K. Sangwan, J.D. Wood, M.C. Hersam, Solution-Based Processing of Monodisperse Two-Dimensional Nanomaterials, Accounts of Chemical Research 50(4) (2017) 943-951.

[45] J.B. Smith, D. Hagaman, H.-F. Ji, Growth of 2D black phosphorus film from chemical vapor deposition, Nanotechnology 27(21) (2016) 215602.

[46] Z. Yang, J. Hao, S. Yuan, S. Lin, H.M. Yau, J. Dai, S.P. Lau, Field-effect transistors based on amorphous black phosphorus ultrathin films by pulsed laser deposition, Advanced Materials 27(25) (2015) 3748-3754.

[47] K. Lukaszkowicz, Review of nanocomposite thin films and coatings deposited by PVD and CVD technology, Intech, Rijeka (2011) 145-162.

[48] S. Wu, K.S. Hui, K.N. Hui, 2D Black Phosphorus: from Preparation to Applications for Electrochemical Energy Storage, 5(5) (2018) 1700491.

[49] H. Liu, A.T. Neal, Z. Zhu, Z. Luo, X. Xu, D. Tománek, P.D. Ye, Phosphorene: an unexplored 2D semiconductor with a high hole mobility, ACS nano 8(4) (2014) 4033-4041.

[50] K. Yan, H.-W. Lee, T. Gao, G. Zheng, H. Yao, H. Wang, Z. Lu, Y. Zhou, Z. Liang, Z. Liu, Ultrathin two-dimensional atomic crystals as stable interfacial layer for improvement of lithium metal anode, Nano letters 14(10) (2014) 6016-6022.

[51] J.D. Wood, S.A. Wells, D. Jariwala, K.-S. Chen, E. Cho, V.K. Sangwan, X. Liu, L.J. Lauhon, T.J. Marks, M.C. Hersam, Effective passivation of exfoliated black phosphorus transistors against ambient degradation, Nano letters 14(12) (2014) 6964-6970.

[52] L. Guan, B. Xing, X. Niu, D. Wang, Y. Yu, S. Zhang, X. Yan, Y. Wang, J. Sha, Metal-assisted exfoliation of few-layer black phosphorus with high yield, Chemical Communications 54(6) (2018) 595-598.

[53] S. Lin, Y. Chui, Y. Li, S.P. Lau, Liquid-phase exfoliation of black phosphorus and its applications, FlatChem 2 (2017) 15-37.

[54] L. Li, D. Zhang, J. Deng, Y. Gou, J. Fang, Electrochemical exfoliation of two-dimensional layered black phosphorus and applications, Journal of Energy Chemistry (2020).

[55] S. Witomska, T. Leydecker, A. Ciesielski, P. Samorì, Production and patterning of liquid phase–exfoliated 2D sheets for applications in optoelectronics, Advanced Functional Materials 29(22) (2019) 1901126.

[56] A.B. Bourlinos, V. Georgakilas, R. Zboril, T.A. Steriotis, A.K. Stubos, Liquid-phase exfoliation of graphite towards solubilized graphenes, small 5(16) (2009) 1841-1845.

[57] K.G. Zhou, N.N. Mao, H.X. Wang, Y. Peng, H.L. Zhang, A mixed-solvent strategy for efficient exfoliation of inorganic graphene analogues, Angewandte Chemie 123(46) (2011) 11031-11034.

[58] J.N. Coleman, M. Lotya, A. O'Neill, S.D. Bergin, P.J. King, U. Khan, K. Young, A. Gaucher, S. De, R.J. Smith, Two-dimensional nanosheets produced by liquid exfoliation of layered materials, Science 331(6017) (2011) 568-571.

[59] J.N. Israelachvili, Intermolecular and surface forces, Academic press2011.

[60] A. O'Neill, U. Khan, P.N. Nirmalraj, J. Boland, J.N. Coleman, Graphene dispersion and exfoliation in low boiling point solvents, The Journal of Physical Chemistry C 115(13) (2011) 5422-5428.

[61] G. Cunningham, M. Lotya, C.S. Cucinotta, S. Sanvito, S.D. Bergin, R. Menzel, M.S. Shaffer, J.N. Coleman, Solvent exfoliation of transition metal dichalcogenides: dispersibility of exfoliated nanosheets varies only weakly between compounds, ACS nano 6(4) (2012) 3468-3480.

[62] Y. Zhang, H. Wang, Z. Luo, H.T. Tan, B. Li, S. Sun, Z. Li, Y. Zong, Z.J. Xu, Y. Yang, An air-stable densely packed phosphorene–graphene composite toward advanced lithium storage properties, Advanced Energy Materials 6(12) (2016) 1600453.

[63] S.C. Dhanabalan, J.S. Ponraj, Z. Guo, S. Li, Q. Bao, H. Zhang, Emerging trends in phosphorene fabrication towards next generation devices, Advanced Science 4(6) (2017) 1600305.

[64] V. Sresht, A.A. Padua, D. Blankschtein, Liquid-phase exfoliation of phosphorene: design rules from molecular dynamics simulations, ACS nano 9(8) (2015) 8255-8268.

[65] V.V. Chaban, E.E. Fileti, O.V. Prezhdo, Imidazolium Ionic Liquid Mediates Black Phosphorus Exfoliation while Preventing Phosphorene Decomposition, ACS nano 11(6) (2017) 6459-6466.

[66] J.R. Brent, N. Savjani, E.A. Lewis, S.J. Haigh, D.J. Lewis, P. O'Brien, Production of few-layer phosphorene by liquid exfoliation of black phosphorus, Chemical Communications 50(87) (2014) 13338-13341.

[67] H. Liu, K. Hu, D. Yan, R. Chen, Y. Zou, H. Liu, S. Wang, Recent advances on black phosphorus for energy storage, catalysis, and sensor applications, Advanced Materials 30(32) (2018) 1800295.

[68] C. Xing, J. Zhang, J. Jing, J. Li, F. Shi, Preparations, properties and applications of low-dimensional black phosphorus, Chemical Engineering Journal 370 (2019) 120-135.

[69] J. Kang, J.D. Wood, S.A. Wells, J.-H. Lee, X. Liu, K.-S. Chen, M.C. Hersam, Solvent exfoliation of electronic-grade, two-dimensional black phosphorus, ACS nano 9(4) (2015) 3596-3604.

[70] P. Yasaei, B. Kumar, T. Foroozan, C. Wang, M. Asadi, D. Tuschel, J.E. Indacochea, R.F. Klie, A. Salehi-Khojin, High-quality black phosphorus atomic layers by liquid-phase exfoliation, Advanced Materials 27(11) (2015) 1887-1892.

[71] P. Yasaei, A. Behranginia, T. Foroozan, M. Asadi, K. Kim, F. Khalili-Araghi, A. Salehi-Khojin, Stable and selective humidity sensing using stacked black phosphorus flakes, ACS nano 9(10) (2015) 9898-9905.

[72] J.-Y. Xu, L.-F. Gao, C.-X. Hu, Z.-Y. Zhu, M. Zhao, Q. Wang, H.-L. Zhang, Preparation of large size, few-layer black phosphorus nanosheets via phytic acid-assisted liquid exfoliation, Chemical communications 52(52) (2016) 8107-8110.

[73] Z. Guo, H. Zhang, S. Lu, Z. Wang, S. Tang, J. Shao, Z. Sun, H. Xie, H. Wang, X.F. Yu, From black phosphorus to phosphorene: basic solvent exfoliation, evolution of Raman scattering, and applications to ultrafast photonics, Advanced Functional Materials 25(45) (2015) 6996-7002.

[74] S.J. Sandoval, D. Yang, R. Frindt, J. Irwin, Raman study and lattice dynamics of single molecular layers of MoS 2, Physical Review B 44(8) (1991) 3955.

[75] J. Ding, H. Zhao, Q. Wang, H. Dou, H. Chen, H. Yu, An ultrahigh thermal conductive graphene flexible paper, Nanoscale 9(43) (2017) 16871-16878.

[76] A.H. Woomer, T.W. Farnsworth, J. Hu, R.A. Wells, C.L. Donley, S.C. Warren, Phosphorene: synthesis, scale-up, and quantitative optical spectroscopy, ACS nano 9(9) (2015) 8869-8884.

[77] L. Chen, G. Zhou, Z. Liu, X. Ma, J. Chen, Z. Zhang, X. Ma, F. Li, H.-M. Cheng, W. Ren, Scalable Clean Exfoliation of High-Quality Few-Layer Black Phosphorus for a Flexible Lithium Ion Battery, Advanced Materials 28(3) (2016) 510-517.

[78] J. Kang, S.A. Wells, J.D. Wood, J.-H. Lee, X. Liu, C.R. Ryder, J. Zhu, J.R. Guest, C.A. Husko, M.C. Hersam, Stable aqueous dispersions of optically and electronically active phosphorene, Proceedings of the National Academy of Sciences 113(42) (2016) 11688-11693.

[79] H. Wang, X. Yang, W. Shao, S. Chen, J. Xie, X. Zhang, J. Wang, Y. Xie, Ultrathin black phosphorus nanosheets for efficient singlet oxygen generation, Journal of the American Chemical Society 137(35) (2015) 11376-11382.

[80] W. Zhao, Z. Xue, J. Wang, J. Jiang, X. Zhao, T. Mu, Large-scale, highly efficient, and green liquid-exfoliation of black phosphorus in ionic liquids, ACS applied materials & interfaces 7(50) (2015) 27608-27612.

[81] C. Hardacre, J.D. Holbrey, M. Nieuwenhuyzen, T.G. Youngs, Structure and solvation in ionic liquids, Accounts of chemical research 40(11) (2007) 1146-1155.

[82] M. Lee, A.K. Roy, S. Jo, Y. Choi, A. Chae, B. Kim, S.Y. Park, I. In, Exfoliation of black phosphorus in ionic liquids, Nanotechnology 28(12) (2017) 125603.

[83] C.X. Hu, Q. Xiao, Y.Y. Ren, M. Zhao, G.H. Dun, H.R. Wu, X.Y. Li, Q.Q. Yang, B. Sun, Y. Peng, Polymer Ionic Liquid Stabilized Black Phosphorus for Environmental Robust Flexible Optoelectronics, Advanced Functional Materials 28(51) (2018) 1805311.

[84] M. van Druenen, F.n. Davitt, T. Collins, C. Glynn, C. O'Dwyer, J.D. Holmes, G. Collins, Evaluating the surface chemistry of black phosphorus during ambient degradation, Langmuir 35(6) (2019) 2172-2178.

[85] M. Eredia, S. Bertolazzi, T. Leydecker, M. El Garah, I. Janica, G. Melinte, O. Ersen, A. Ciesielski, P. Samorì, Morphology and electronic properties of electrochemically exfoliated graphene, The Journal of Physical Chemistry Letters 8(14) (2017) 3347-3355.

[86] Z. Song, Y. Ma, J. Ye, Preparation of stable black phosphorus nanosheets and their electrochemical catalytic study, Journal of Electroanalytical Chemistry 856 (2020) 113595.

[87] S. Su, B. Xu, J. Ding, H. Yu, Large-yield exfoliation of few-layer black phosphorus nanosheets in liquid, New Journal of Chemistry 43(48) (2019) 19365-19371.

[88] J. Sun, H.-W. Lee, M. Pasta, H. Yuan, G. Zheng, Y. Sun, Y. Li, Y. Cui, A phosphorene–graphene hybrid material as a high-capacity anode for sodium-ion batteries, Nature nanotechnology 10(11) (2015) 980-985.

[89] Z.-C. Luo, M. Liu, Z.-N. Guo, X.-F. Jiang, A.-P. Luo, C.-J. Zhao, X.-F. Yu, W.-C. Xu, H. Zhang, Microfiber-based few-layer black phosphorus saturable absorber for ultra-fast fiber laser, Optics express 23(15) (2015) 20030-20039.

[90] J. Ma, S. Lu, Z. Guo, X. Xu, H. Zhang, D. Tang, D. Fan, Few-layer black phosphorus based saturable absorber mirror for pulsed solid-state lasers, Optics express 23(17) (2015) 22643-22648.

[91] X. Zheng, R. Chen, G. Shi, J. Zhang, Z. Xu, T. Jiang, Characterization of nonlinear properties of black phosphorus nanoplatelets with femtosecond pulsed Z-scan measurements, Optics letters 40(15) (2015) 3480-3483.

[92] L. Li, L. Chen, S. Mukherjee, J. Gao, H. Sun, Z. Liu, X. Ma, T. Gupta, C.V. Singh, W. Ren, Phosphorene as a polysulfide immobilizer and catalyst in high-performance lithium–sulfur batteries, Advanced Materials 29(2) (2017) 1602734.

[93] L. Kong, Z. Qin, G. Xie, Z. Guo, H. Zhang, P. Yuan, L. Qian, Black phosphorus as broadband saturable absorber for pulsed lasers from 1 μm to 2.7 μm wavelength, Laser Physics Letters 13(4) (2016) 045801.

[94] Y. Zhang, W. Sun, Z.-Z. Luo, Y. Zheng, Z. Yu, D. Zhang, J. Yang, H.T. Tan, J. Zhu, X. Wang, Functionalized few-layer black phosphorus with super-wettability towards enhanced reaction kinetics for rechargeable batteries, Nano Energy 40 (2017) 576-586.

[95] M. van Druenen, F. Davitt, T. Collins, C. Glynn, C. O'Dwyer, J.D. Holmes, G. Collins, Covalent functionalization of few-layer black phosphorus using iodonium salts and comparison to diazonium modified black phosphorus, Chemistry of Materials 30(14) (2018) 4667-4674.

[96] Y. Chang, A. Nie, S. Yuan, B. Wang, C. Mu, J. Xiang, B. Yang, L. Li, F. Wen, Z. Liu, Liquid-exfoliation of S-doped black phosphorus nanosheets for enhanced oxygen evolution catalysis, Nanotechnology 30(3) (2018) 035701.

[97] C. Jia, L. Zhao, M. Cui, F. Yang, G. Cheng, G. Yang, Z. Zeng, Surface coordination modification and electrical properties of few-layer black phosphorus exfoliated by the liquid-phase method, Journal of Alloys and Compounds 799 (2019) 99-107.

[98] Z. Li, L. Wu, H. Wang, W. Zhou, H. Liu, H. Cui, P. Li, P.K. Chu, X.-F. Yu, Synergistic antibacterial activity of black phosphorus nanosheets modified with titanium aminobenzenesulfanato complexes, ACS Applied Nano Materials 2(3) (2019) 1202-1209.

[99] Z. Qu, K. Wu, E. Jiao, W. Chen, Z. Hu, C. Xu, J. Shi, S. Wang, Z. Tan, Surface functionalization of few-layer black phosphorene and its flame retardancy in epoxy resin, Chemical Engineering Journal 382 (2020) 122991.

[100] Y.-L. Hsieh, W.-H. Su, C.-C. Huang, C.-Y. Su, Solution-processed black phosphorus nanoflakes for integrating nonvolatile resistive random access memory and the mechanism unveiled, Nanotechnology 30(44) (2019) 445702.

[101] G. Zhou, Z. Li, Y. Ge, H. Zhang, Z. Sun, A self-encapsulated broadband phototransistor based on a hybrid of graphene and black phosphorus nanosheets, Nanoscale Advances 2(3) (2020) 1059-1065.

[102] H. Zhao, H. Chen, Z. Guo, W. Zhang, H. Yu, Z. Zhuang, H. Zhong, Z. Liu, In situ Photothermal Activation of Necroptosis Potentiates Black Phosphorus-Mediated Cancer Photo-Immunotherapy, Chemical Engineering Journal (2020) 124314.

[103] R. Taheri, M. Farbod, Superb photocatalytic performance of single/few layer phosphorene prepared via sonication method, Physica E: Low-dimensional Systems and Nanostructures 119 (2020) 114009.

[104] T. Chen, Z. Cheng, Q. Tian, J. Wang, X. Yu, D. Ho, Nitrogen Dioxide Gas Sensor Based on Liquid-Phase Exfoliated Black Phosphorus Nanosheets, ACS Applied Nano Materials (2020).

[105] K. Ge, Y. Zhang, D. Wang, Z. Li, J. He, C. Fu, Y. Yang, M. Pan, L. Zhu, Highly Stable Reduced Graphene Oxide Wrapped Black Phosphorus Heterostructure with Superior Photocatalytic Performance under Visible Light, ACS Applied Materials & Interfaces 12(17) (2020) 20035-20043.

[106] Y. Zhou, F. Chu, S. Qiu, W. Guo, S. Zhang, Z. Xu, W. Hu, Y. Hu, Construction of Graphite Oxide Modified Black Phosphorus through Covalent Linkage: An efficient strategy for smoke toxicity and fire hazard suppression of epoxy resin, Journal of Hazardous Materials (2020) 123015.

[107] B. Zhang, F. Lou, R. Zhao, J. He, J. Li, X. Su, J. Ning, K. Yang, Exfoliated layers of black phosphorus as saturable absorber for ultrafast solid-state laser, Optics Letters 40(16) (2015) 3691-3694.

[108] C. Hao, F. Wen, J. Xiang, S. Yuan, B. Yang, L. Li, W. Wang, Z. Zeng, L. Wang, Z. Liu, Liquid-Exfoliated Black Phosphorous Nanosheet Thin Films for Flexible Resistive Random Access Memory Applications, Advanced Functional Materials 26(12) (2016) 2016-2024.

[109] S. Lin, Y. Li, W. Lu, Y. San Chui, L. Rogée, Q. Bao, S.P. Lau, In situ observation of the thermal stability of black phosphorus, 2D Materials 4(2) (2017) 025001.

[110] R. Wang, X. Yan, B. Ge, J. Zhou, M. Wang, L. Zhang, T. Jiao, Facile preparation of self-assembled black phosphorus-dye composite films for chemical gas sensors and surface-enhanced Raman scattering performances, ACS Sustainable Chemistry & Engineering 8(11) (2020) 4521-4536.

[111] Z. Qu, K. Wu, W. Meng, B. Nan, Z. Hu, C.-a. Xu, Z. Tan, Q. Zhang, H. Meng, J. Shi, Surface Coordination of Black Phosphorene for Excellent Stability, Flame Retardancy and Thermal Conductivity in Epoxy Resin, Chemical Engineering Journal (2020) 125416.

[112] M. Serrano-Ruiz, M. Caporali, A. Ienco, V. Piazza, S. Heun, M. Peruzzini, The Role of Water in the Preparation and Stabilization of High-Quality Phosphorene Flakes, Advanced materials interfaces 3(3) (2016) 1500441.

[113] H. Fu, Z. Li, H. Xie, Z. Sun, B. Wang, H. Huang, G. Han, H. Wang, P.K. Chu, X.-F. Yu, Different-sized black phosphorus nanosheets with good cytocompatibility and high photothermal performance, RSC advances 7(24) (2017) 14618-14624.

[114] C. Hao, B. Yang, F. Wen, J. Xiang, L. Li, W. Wang, Z. Zeng, B. Xu, Z. Zhao, Z. Liu, Flexible all-solid-state supercapacitors based on liquid-exfoliated black-phosphorus nanoflakes, Advanced Materials 28(16) (2016) 3194-3201.

[115] B. Yang, C. Hao, F. Wen, B. Wang, C. Mu, J. Xiang, L. Li, B. Xu, Z. Zhao, Z. Liu, Flexible black-phosphorus nanoflake/carbon nanotube composite paper for high-performance all-solid-state supercapacitors, ACS applied materials & interfaces 9(51) (2017) 44478-44484.

[116] A.E. Del Rio Castillo, V. Pellegrini, H. Sun, J. Buha, D.A. Dinh, E. Lago, A. Ansaldo, A. Capasso, L. Manna, F. Bonaccorso, Exfoliation of few-layer black phosphorus in low-boiling-point solvents and its application in Li-ion batteries, Chemistry of Materials 30(2) (2018) 506-516.

[117] D. Hanlon, C. Backes, E. Doherty, C.S. Cucinotta, N.C. Berner, C. Boland, K. Lee, A. Harvey, P. Lynch, Z. Gholamvand, Liquid exfoliation of solvent-stabilized few-layer black phosphorus for applications beyond electronics, Nature communications 6(1) (2015) 1-11.

[118] R. Rojaee, S. Cavallo, S. Mogurampelly, B.K. Wheatle, V. Yurkiv, R. Deivanayagam, T. Foroozan, M.G. Rasul, S. Sharifi-Asl, A.H. Phakatkar, Highly-Cyclable Room-Temperature Phosphorene Polymer Electrolyte Composites for Li Metal Batteries, Advanced Functional Materials (2020) 1910749.

[119] H. Mu, S. Lin, Z. Wang, S. Xiao, P. Li, Y. Chen, H. Zhang, H. Bao, S.P. Lau, C. Pan, Black phosphorus–polymer composites for pulsed lasers, Advanced Optical Materials 3(10) (2015) 1447-1453.

[120] Y. Zhang, N. Dong, H. Tao, C. Yan, J. Huang, T. Liu, A.W. Robertson, J. Texter, J. Wang, Z. Sun, Exfoliation of stable 2D black phosphorus for device fabrication, Chemistry of Materials 29(15) (2017) 6445-6456.

[121] Z. Yan, X. He, L. She, J. Sun, R. Jiang, H. Xu, F. Shi, Z. Lei, Z.-H. Liu, Solvothermal-assisted liquid-phase exfoliation of large size and high quality black phosphorus, Journal of Materiomics 4(2) (2018) 129-134.

[122] Z. Sun, Y. Zhang, H. Yu, C. Yan, Y. Liu, S. Hong, H. Tao, A.W. Robertson, Z. Wang, A.A. Pádua, New solvent-stabilized few-layer black phosphorus for antibacterial applications, Nanoscale 10(26) (2018) 12543-12553.

[123] Y. Wang, J. Xue, X. Zhang, J. Si, Y. Liu, L. Ma, M. Ikram, L. Li, K. Shi, Novel intercalated CuO/black phosphorus nanocomposites: Fabrication, characterization and NO2 gas sensing at room temperature, Materials Science in Semiconductor Processing 110 (2020) 104961.

[124] S. Luo, J. Zhao, J. Zou, Z. He, C. Xu, F. Liu, Y. Huang, L. Dong, L. Wang, H. Zhang, Self-standing polypyrrole/black phosphorus laminated film: promising electrode for flexible supercapacitor with enhanced capacitance and cycling stability, ACS applied materials & interfaces 10(4) (2018) 3538-3548.

[125] W. Liu, Y. Zhang, Y. Zhang, A. Dong, Black phosphorus nanosheets counteract bacteria without causing antibiotic resistance, Chemistry–A European Journal 26(11) (2020) 2478-2485.

[126] S. Wan, B. Zhang, S. Li, B. He, Y. Pu, Combination of PEG-decorated black phosphorus nanosheets and immunoadjuvant for photoimmunotherapy of melanoma, Journal of Materials Chemistry B 8(14) (2020) 2805-2813.

[127] J. Yi, X. Chen, Q. Weng, Y. Zhou, Z. Han, J. Chen, C. Li, A simple electrochemical pH sensor based on black phosphorus nanosheets, Electrochemistry Communications (2020) 106796.

[128] S. Lu, L. Miao, Z. Guo, X. Qi, C. Zhao, H. Zhang, S. Wen, D. Tang, D. Fan, Broadband nonlinear optical response in multi-layer black phosphorus: an emerging infrared and mid-infrared optical material, Optics express 23(9) (2015) 11183-11194.

[129] J. Gómez-Pérez, Z. Kónya, Á. Kukovecz, Acetone improves the topographical homogeneity of liquid phase exfoliated few-layer black phosphorus flakes, Nanotechnology 29(36) (2018) 365303.

[130] Y. Xu, X. Wang, M. Jin, K. Kempa, L. Shui, Water Splitting Performance Enhancement of the TiO2 Nanorod Array Electrode with Ultrathin Black Phosphorus Nanosheets, ChemElectroChem 7(1) (2020) 96-104.

[131] Z. Li, T. Guo, Y. Hu, Y. Qiu, Y. Liu, H. Wang, Y. Li, X. Chen, J. Song, H. Yang, A highly effective π–π stacking strategy to modify black phosphorus with aromatic molecules for cancer theranostics, ACS applied materials & interfaces 11(10) (2019) 9860-9871.

[132] W. Liu, Y. Zhu, Z. Chen, J. Lei, P. Feng, Multilayer black phosphorus exfoliated with the aid of sodium hydroxide: An improvement in electrochemical energy storage, Journal of Electronic Materials 47(8) (2018) 4793-4798.

[133] Z. Sofer, D. Bouša, J. Luxa, V. Mazanek, M. Pumera, Few-layer black phosphorus nanoparticles, Chemical Communications 52(8) (2016) 1563-1566.

[134] P. Qiu, C. Xu, N. Zhou, H. Chen, F. Jiang, Metal-free black phosphorus nanosheets-decorated graphitic carbon nitride nanosheets with CP bonds for excellent photocatalytic nitrogen fixation, Applied Catalysis B: Environmental 221 (2018) 27-35.

[135] H. Xiao, Z.-S. Wu, L. Chen, F. Zhou, S. Zheng, W. Ren, H.-M. Cheng, X. Bao, One-step device fabrication of phosphorene and graphene interdigital micro-supercapacitors with high energy density, ACS nano 11(7) (2017) 7284-7292.

[136] Y. Yang, X. Chen, P. Lian, R. Chen, Y. Liu, Y. Mei, Production of Phosphorene from Black Phosphorus via Sonication and Microwave Co-assisted Aqueous Phase Exfoliation, Chemistry Letters 47(12) (2018) 1478-1481.

[137] A.H. Phakatkar, E. Firlar, L. Alzate, B. Song, S. Narayanan, R. Rojaee, T. Foroozan, R. Deivanayagam, D.J. Banner, R. Shahbazian-Yassar, TEM Studies on Antibacterial Mechanisms of Black Phosphorous Nanosheets, International Journal of Nanomedicine 15 (2020) 3071.

[138] X. Zhang, Z. Zhang, S. Zhang, D. Li, W. Ma, C. Ma, F. Wu, Q. Zhao, Q. Yan, B. Xing, Size effect on the cytotoxicity of layered black phosphorus and underlying mechanisms, Small 13(32) (2017) 1701210.

[139] S. Seo, H.U. Lee, S.C. Lee, Y. Kim, H. Kim, J. Bang, J. Won, Y. Kim, B. Park, J. Lee, Triangular black phosphorus atomic layers by liquid exfoliation, Scientific reports 6 (2016) 23736.

[140] Y. Yang, H. Hou, G. Zou, W. Shi, H. Shuai, J. Li, X. Ji, Electrochemical exfoliation of graphene-like two-dimensional nanomaterials, Nanoscale 11(1) (2019) 16-33.

[141] Y. Fang, X. Li, J. Li, C. Yao, H.Y. Hoh, X. Hai, J. Lu, C. Su, Janus electrochemical exfoliation of two-dimensional materials, Journal of Materials Chemistry A 7(45) (2019) 25691-25711.

[142] Z. Zeng, Z. Yin, X. Huang, H. Li, Q. He, G. Lu, F. Boey, H. Zhang, Single-Layer Semiconducting Nanosheets: High-yield preparation and device fabrication, Angewandte Chemie 123(47) (2011) 11289-11293.

[143] S. Yang, P. Zhang, A.S. Nia, X. Feng, Emerging 2D Materials Produced via Electrochemistry, Advanced Materials 32(10) (2020) 1907857.

[144] Z. Huang, H. Hou, Y. Zhang, C. Wang, X. Qiu, X. Ji, Layer-tunable phosphorene modulated by the cation insertion rate as a sodium-storage anode, Advanced Materials 29(34) (2017) 1702372.

[145] B. Li, C. Lai, G. Zeng, D. Huang, L. Qin, M. Zhang, M. Cheng, X. Liu, H. Yi, C. Zhou, Black Phosphorus, a Rising Star 2D Nanomaterial in the Post-Graphene Era: Synthesis, Properties, Modifications, and Photocatalysis Applications, Small 15(8) (2019) 1804565.

[146] P. Yu, S.E. Lowe, G.P. Simon, Y.L. Zhong, Electrochemical exfoliation of graphite and production of functional graphene, Current opinion in colloid & interface science 20(5-6) (2015) 329-338.

[147] A. Ambrosi, M. Pumera, Exfoliation of layered materials using electrochemistry, Chemical Society Reviews 47(19) (2018) 7213-7224.

[148] M.B. Erande, S.R. Suryawanshi, M.A. More, D.J. Late, Electrochemically exfoliated black phosphorus nanosheets–prospective field emitters, European Journal of Inorganic Chemistry 2015(19) (2015) 3102-3107.

[149] M.B. Erande, M.S. Pawar, D.J. Late, Humidity sensing and photodetection behavior of electrochemically exfoliated atomically thin-layered black phosphorus nanosheets, ACS applied materials & interfaces 8(18) (2016) 11548-11556.

[150] A. Ambrosi, Z. Sofer, M. Pumera, Electrochemical exfoliation of layered black phosphorus into phosphorene, Angewandte Chemie 129(35) (2017) 10579-10581.

[151] J. Yang, Z. Pan, Q. Yu, Q. Zhang, X. Ding, X. Shi, Y. Qiu, K. Zhang, J. Wang, Y. Zhang, Free-Standing Black Phosphorus Thin Films for Flexible Quasi-Solid-State Micro-Supercapacitors with High Volumetric Power and Energy Density, ACS applied materials & interfaces 11(6) (2019) 5938-5946.

[152] S. Qiu, B. Zou, H. Sheng, W. Guo, J. Wang, Y. Zhao, W. Wang, R.K. Yuen, Y. Kan, Y. Hu, Electrochemically exfoliated functionalized black phosphorene and its polyurethane acrylate nanocomposites: synthesis and applications, ACS applied materials & interfaces 11(14) (2019) 13652-13664.

[153] J. Li, C. Chen, S. Liu, J. Lu, W.P. Goh, H. Fang, Z. Qiu, B. Tian, Z. Chen, C. Yao, Ultrafast electrochemical expansion of black phosphorus toward high-yield synthesis of few-layer phosphorene, Chemistry of Materials 30(8) (2018) 2742-2749.

[154] L. Shulenburger, A.D. Baczewski, Z. Zhu, J. Guan, D. Tomanek, The nature of the interlayer interaction in bulk and few-layer phosphorus, Nano letters 15(12) (2015) 8170-8175.

[155] S. Yang, K. Zhang, A.G. Ricciardulli, P. Zhang, Z. Liao, M.R. Lohe, E. Zschech, P.W. Blom, W. Pisula, K. Müllen, A delamination strategy for thinly layered defect-free high-mobility black phosphorus flakes, Angewandte Chemie 130(17) (2018) 4767-4771.

[156] H. Huang, M. Gao, Y. Kang, J. Li, J. Wang, L. Wu, P.K. Chu, Y. Huang, M.R. Ibarra, X.-F. Yu, Rapid and scalable production of high-quality phosphorene by plasma–liquid technology, Chemical Communications 56(2) (2020) 221-224.

[157] F. Luo, D. Wang, J. Zhang, X. Li, D. Liu, H. Li, M. Lu, X. Xie, L. Huang, W. Huang, Ultrafast Cathodic Exfoliation of Few-Layer Black Phosphorus in Aqueous Solution, ACS Applied Nano Materials 2(6) (2019) 3793-3801.

[158] H. Shuai, P. Ge, W. Hong, S. Li, J. Hu, H. Hou, G. Zou, X. Ji, Electrochemically Exfoliated Phosphorene–Graphene Hybrid for Sodium-Ion Batteries, Small Methods 3(2) (2019) 1800328.

[159] E. Kovalska, J. Luxa, T. Hartman, N. Antonatos, P. Shaban, E. Oparin, M. Zhukova, Z. Sofer, Non-aqueous solution-processed phosphorene by controlled low-potential electrochemical exfoliation and thin film preparation, Nanoscale 12(4) (2020) 2638-2647.

[160] Z. Huang, A. Chen, F. Mo, G. Liang, X. Li, Q. Yang, Y. Guo, Z. Chen, Q. Li, B. Dong, Phosphorene as Cathode Material for High-Voltage, Anti-Self-Discharge Zinc Ion Hybrid Capacitors, Advanced Energy Materials (2020) 2001024.

[161] E. Kovalska, J. Luxa, M. Melle-Franco, B. Wu, I. Marek, P.K. Roy, P. Marvan, Z. Sofer, Single-Step Synthesis of Platinoid-Decorated Phosphorene: Perspectives for Catalysis, Gas Sensing, and Energy Storage, ACS Applied Materials & Interfaces 12(45) (2020) 50516-50526.

[162] Z.-K. Shen, Y.-J. Yuan, P. Wang, W. Bai, L. Pei, S. Wu, Z.-T. Yu, Z. Zou, Few-Layer Black Phosphorus Nanosheets: A Metal-Free Cocatalyst for Photocatalytic Nitrogen Fixation, ACS Applied Materials & Interfaces 12(15) (2020) 17343-17352.

[163] T. Liang, Y. Liu, P. Zhang, C. Liu, F. Ma, Q. Yan, Z. Dai, Interface and valence modulation on scalable phosphorene/phosphide lamellae for efficient water electrolysis, Chemical Engineering Journal (2020) 124976.

[164] T. Liang, Y. Liu, Y. Cheng, F. Ma, Z. Dai, Scalable Synthesis of a MoS2/Black Phosphorus Heterostructure for pH-Universal Hydrogen Evolution Catalysis, ChemCatChem 12(10) (2020) 2840-2848.

[165] H. Xiao, M. Zhao, J. Zhang, X. Ma, J. Zhang, T. Hu, T. Tang, J. Jia, H. Wu, Electrochemical cathode exfoliation of bulky black phosphorus into few-layer phosphorene nanosheets, Electrochemistry Communications 89 (2018) 10-13.

[166] C. Xu, Y. Xu, M. Yang, Y. Chang, A. Nie, Z. Liu, J. Wang, Z. Luo, Black-Phosphorus-Incorporated Hydrogel as a Conductive and Biodegradable Platform for Enhancement of the Neural Differentiation of Mesenchymal Stem Cells, Advanced Functional Materials (2020) 2000177.

[167] M. Wen, D. Liu, Y. Kang, J. Wang, H. Huang, J. Li, P.K. Chu, X.-F. Yu, Synthesis of high-quality black phosphorus sponges for all-solid-state supercapacitors, Materials Horizons 6(1) (2019) 176-181.

[168] B. Wu, E. Kovalska, J. Luxa, P. Marvan, Š. Cintl, Z. Sofer, Free-standing black phosphorus foils for energy storage and catalysis, Chemistry–A European Journal (2020).

[169] S.E. Fosdick, K.N. Knust, K. Scida, R.M. Crooks, Bipolar electrochemistry, Angewandte Chemie International Edition 52(40) (2013) 10438-10456.

[170] J. Backhurst, J. Coulson, F. Goodridge, R. Plimley, M. Fleischmann, A preliminary investigation of fluidized bed electrodes, Journal of the Electrochemical Society 116(11) (1969) 1600.

[171] R.M. Crooks, Principles of bipolar electrochemistry, ChemElectroChem 3(3) (2016) 357-359.

[172] G. Loget, D. Zigah, L. Bouffier, N. Sojic, A. Kuhn, Bipolar electrochemistry: from materials science to motion and beyond, Accounts of Chemical Research 46(11) (2013) 2513-2523.

[173] L. Koefoed, S.U. Pedersen, K. Daasbjerg, Bipolar electrochemistry—A wireless approach for electrode reactions, Current Opinion in Electrochemistry 2(1) (2017) 13-17.

[174] N. Shida, Y. Zhou, S. Inagi, Bipolar Electrochemistry: A Powerful Tool for Electrifying Functional Material Synthesis, Accounts of Chemical Research 52(9) (2019) 2598-2608.

[175] A. Allagui, M.A. Abdelkareem, H. Alawadhi, A.S. Elwakil, Reduced graphene oxide thin film on conductive substrates by bipolar electrochemistry, Scientific reports 6 (2016) 21282.

[176] A. Allagui, J.M. Ashraf, M. Khalil, M.A. Abdelkareem, A.S. Elwakil, H. Alawadhi, All-Solid-State Double-Layer Capacitors Using Binderless Reduced Graphene

Oxide Thin Films Prepared by Bipolar Electrochemistry, ChemElectroChem 4(8) (2017) 2084-2090.

[177] I. Khakpour, A. Rabiei Baboukani, A. Allagui, C. Wang, Bipolar Exfoliation and in Situ Deposition of High-Quality Graphene for Supercapacitor Application, ACS Applied Energy Materials 2(7) (2019) 4813-4820.

[178] R.J. Toh, C.C. Mayorga-Martinez, Z.k. Sofer, M. Pumera, MoSe2 nanolabels for electrochemical immunoassays, Analytical chemistry 88(24) (2016) 12204-12209.

[179] C.C. Mayorga-Martinez, B. Khezri, A.Y.S. Eng, Z. Sofer, P. Ulbrich, M. Pumera, Bipolar Electrochemical Synthesis of WS2 Nanoparticles and Their Application in Magneto-Immunosandwich Assay, Advanced Functional Materials 26(23) (2016) 4094-4098.

[180] Y. Wang, C.C. Mayorga-Martinez, X. Chia, Z. Sofer, M. Pumera, Nonconductive layered hexagonal boron nitride exfoliation by bipolar electrochemistry, Nanoscale 10(15) (2018) 7298-7303.

[181] C.C. Mayorga-Martinez, N. Mohamad Latiff, A.Y.S. Eng, Z.k. Sofer, M. Pumera, Black phosphorus nanoparticle labels for immunoassays via hydrogen evolution reaction mediation, Analytical chemistry 88(20) (2016) 10074-10079.

[182] A.R. Baboukani, I. Khakpour, C. Wang, Bipolar exfoliation of black phosphorous into phosphorene, Google Patents, 2020.

[183] M. Bat-Erdene, M. Batmunkh, C.J. Shearer, S.A. Tawfik, M.J. Ford, L. Yu, A.J. Sibley, A.D. Slattery, J.S. Quinton, C.T. Gibson, Efficient and Fast Synthesis of Few-Layer Black Phosphorus via Microwave-Assisted Liquid-Phase Exfoliation, Small Methods 1(12) (2017) 1700260.

[184] M. Bat-Erdene, M. Batmunkh, S.A. Tawfik, M. Fronzi, M.J. Ford, C.J. Shearer, L. Yu, M. Dadkhah, J.R. Gascooke, C.T. Gibson, Efficiency Enhancement of Single-Walled Carbon Nanotube-Silicon Heterojunction Solar Cells Using Microwave-Exfoliated Few-Layer Black Phosphorus, Advanced Functional Materials 27(48) (2017) 1704488.

[185] C.-H. Choi, D.-H. Ko, H.Y. Jun, S.O. Ryu, D.-P. Kim, Rapid exfoliation for few-layer enriched black phosphorus dispersion via a superhydrophobic silicon-nanowire-embedded microfluidic process, Green Chemistry 22(3) (2020) 699-706.

[186] C.-H. Choi, Y.-J. Park, X. Wu, D.-P. Kim, Highly efficient and continuous production of few-layer black phosphorus nanosheets and quantum dots via acoustic-microfluidic process, Chemical Engineering Journal 333 (2018) 336-342.

[187] S.R. Suryawanshi, M.A. More, D.J. Late, Laser exfoliation of 2D black phosphorus nanosheets and their application as a field emitter, RSC advances 6(113) (2016) 112103-112108.

[188] M. Batmunkh, K. Vimalanathan, C. Wu, A.S. Bati, L. Yu, S.A. Tawfik, M.J. Ford, T.J. Macdonald, C.L. Raston, S. Priya, Efficient Production of Phosphorene Nanosheets via Shear Stress Mediated Exfoliation for Low-Temperature Perovskite Solar Cells, Small Methods 3(5) (2019) 1800521.

[189] J. Zhang, H. Shin, W. Lu, Highly ambient-stable few-layer black phosphorene by pulsed laser exfoliation and HEMM, Chemical Communications 55(18) (2019) 2601-2604.

[190] W. Zheng, J. Lee, Z.W. Gao, Y. Li, S. Lin, S.P. Lau, L.Y.S. Lee, Laser-Assisted Ultrafast Exfoliation of Black Phosphorus in Liquid with Tunable Thickness for Li-Ion Batteries, Advanced Energy Materials 10(31) (2020) 1903490.

[191] F. Xu, B. Ge, J. Chen, A. Nathan, L.L. Xin, H. Ma, H. Min, C. Zhu, W. Xia, Z. Li, Scalable shear-exfoliation of high-quality phosphorene nanoflakes with reliable electrochemical cycleability in nano batteries, 2D Materials 3(2) (2016) 025005.

[192] A. Sajedi-Moghaddam, C.C. Mayorga-Martinez, Z.k. Sofer, D. Bouša, E. Saievar-Iranizad, M. Pumera, Black phosphorus nanoflakes/polyaniline hybrid material for high-performance pseudocapacitors, The Journal of Physical Chemistry C 121(37) (2017) 20532-20538.

[193] R. Gusmão, Z.k. Sofer, M. Pumera, Functional protection of exfoliated black phosphorus by noncovalent modification with anthraquinone, ACS nano 12(6) (2018) 5666-5673.

[194] A.D.R. Castillo, V. Pellegrini, A. Ansaldo, F. Ricciardella, H. Sun, L. Marasco, J. Buha, Z. Dang, L. Gagliani, E. Lago, High-yield production of 2D crystals by wet-jet milling, Materials Horizons 5(5) (2018) 890-904.

[195] A.E.D.R. Castillo, C.D. Reyes-Vazquez, L.E. Rojas-Martinez, S.B. Thorat, M. Serri, A.L. Martinez-Hernandez, C. Velasco-Santos, V. Pellegrini, F. Bonaccorso, Single-step exfoliation and functionalization of few-layers black phosphorus and its application for polymer composites, FlatChem 18 (2019) 100131.

[196] A. Castellanos-Gomez, L. Vicarelli, E. Prada, J.O. Island, K. Narasimha-Acharya, S.I. Blanter, D.J. Groenendijk, M. Buscema, G.A. Steele, J. Alvarez, Isolation and characterization of few-layer black phosphorus, 2D Materials 1(2) (2014) 025001.

[197] D.K. Sang, H. Wang, Z. Guo, N. Xie, H. Zhang, Recent Developments in Stability and Passivation Techniques of Phosphorene toward Next-Generation Device Applications, Advanced Functional Materials 29(45) (2019) 1903419.

[198] W. Li, Y. Yang, G. Zhang, Y.-W. Zhang, Ultrafast and directional diffusion of lithium in phosphorene for high-performance lithium-ion battery, Nano letters 15(3) (2015) 1691-1697.

[199] S. Zhao, W. Kang, J. Xue, The potential application of phosphorene as an anode material in Li-ion batteries, Journal of Materials Chemistry A 2(44) (2014) 19046-19052.

[200] G.-C. Guo, D. Wang, X.-L. Wei, Q. Zhang, H. Liu, W.-M. Lau, L.-M. Liu, First-principles study of phosphorene and graphene heterostructure as anode materials for rechargeable Li batteries, The journal of physical chemistry letters 6(24) (2015) 5002-5008.

[201] C.M. Park, H.J. Sohn, Black phosphorus and its composite for lithium rechargeable batteries, Advanced materials 19(18) (2007) 2465-2468.

[202] J. Kim, B. Park, Fabricating and probing additive-free electrophoretic-deposited black phosphorus nanoflake anode for lithium-ion battery applications, Materials Letters 254 (2019) 367-370.

[203] J. Mei, Y. Zhang, T. Liao, X. Peng, G.A. Ayoko, Z. Sun, Black phosphorus nanosheets promoted 2D-TiO2-2D heterostructured anode for high-performance lithium storage, Energy Storage Materials 19 (2019) 424-431.

[204] R. Wang, X. Dai, Z. Qian, S. Zhong, S. Chen, S. Fan, H. Zhang, F. Wu, Boosting Lithium Storage in Free-Standing Black Phosphorus Anode via Multifunction of Nanocellulose, ACS Applied Materials & Interfaces 12(28) (2020) 31628-31636.

[205] Y. Zhang, L. Wang, H. Xu, J. Cao, D. Chen, W. Han, 3D Chemical Cross-Linking Structure of Black Phosphorus@ CNTs Hybrid as a Promising Anode Material for Lithium Ion Batteries, Advanced Functional Materials 30(12) (2020) 1909372.

[206] W. Xia, Q. Zhang, F. Xu, H. Ma, J. Chen, K. Qasim, B. Ge, C. Zhu, L. Sun, Visualizing the electrochemical lithiation/delithiation behaviors of black phosphorus by in situ transmission electron microscopy, The Journal of Physical Chemistry C 120(11) (2016) 5861-5868.

[207] K.P. Hembram, H. Jung, B.C. Yeo, S.J. Pai, H.J. Lee, K.-R. Lee, S.S. Han, A comparative first-principles study of the lithiation, sodiation, and magnesiation of black phosphorus for Li-, Na-, and Mg-ion batteries, Physical Chemistry Chemical Physics 18(31) (2016) 21391-21397.

[208] K. Hembram, H. Jung, B.C. Yeo, S.J. Pai, S. Kim, K.-R. Lee, S.S. Han, Unraveling the atomistic sodiation mechanism of black phosphorus for sodium ion batteries by first-principles calculations, The Journal of Physical Chemistry C 119(27) (2015) 15041-15046.

[209] V.V. Kulish, O.I. Malyi, C. Persson, P. Wu, Phosphorene as an anode material for Na-ion batteries: a first-principles study, Physical Chemistry Chemical Physics 17(21) (2015) 13921-13928.

[210] H. Liu, L. Tao, Y. Zhang, C. Xie, P. Zhou, H. Liu, R. Chen, S. Wang, Bridging covalently functionalized black phosphorus on graphene for high-performance sodium-ion battery, ACS applied materials & interfaces 9(42) (2017) 36849-36856.

[211] M. Li, N. Muralidharan, K. Moyer, C.L. Pint, Solvent mediated hybrid 2D materials: black phosphorus–graphene heterostructured building blocks assembled for sodium ion batteries, Nanoscale 10(22) (2018) 10443-10449.

[212] P. Simon, Y. Gogotsi, B. Dunn, Where do batteries end and supercapacitors begin?, Science 343(6176) (2014) 1210-1211.

[213] X. Wu, Y. Xu, Y. Hu, G. Wu, H. Cheng, Q. Yu, K. Zhang, W. Chen, S. Chen, Microfluidic-spinning construction of black-phosphorus-hybrid microfibres for non-woven fabrics toward a high energy density flexible supercapacitor, Nature communications 9(1) (2018) 1-11.

[214] J. Cao, P. He, J.R. Brent, H. Yilmaz, D.J. Lewis, I.A. Kinloch, B. Derby, Supercapacitor electrodes from the in situ reaction between two-dimensional sheets of black phosphorus and graphene oxide, ACS applied materials & interfaces 10(12) (2018) 10330-10338.

[215] H. Liu, Y. Zou, L. Tao, Z. Ma, D. Liu, P. Zhou, H. Liu, S. Wang, Sandwiched Thin-Film Anode of Chemically Bonded Black Phosphorus/Graphene Hybrid for Lithium-Ion Battery, Small 13(33) (2017) 1700758.

[216] X. Guo, W. Zhang, J. Zhang, D. Zhou, X. Tang, X. Xu, B. Li, H. Liu, G. Wang, Boosting Sodium Storage in Two-Dimensional Phosphorene/Ti3C2T x MXene Nanoarchitectures with Stable Fluorinated Interphase, ACS nano 14(3) (2020) 3651-3659.

3. Methodology

3.1 Introduction

In this section, the methodology adopted in this dissertation – for both material synthesis as well as material and electrochemical characterization is provided. For the material preparation in this thesis, three techniques were used to design the electrodes – i) *ball milling*, ii) *electrostatic spray deposition (ESD)*, and iii) *bipolar electrochemical exfoliation*. Moreover, all the developed materials were evaluated through different material and electrochemical characterization techniques.

3.2 Materials Synthesis

3.2.1 Ball Milling

High-energy ball milling or mechanical alloying is a common method widely used to grind materials into nanoparticles and blend them into composite structures for many years. This method is cost-effective, reliable, environmentally-friendly, and scalable which has found wide application in industry and academia. In general, this technique consists of a hollow cylindrical shell rotating around its axis and filled with balls made of stainless steel or ceramics. It depends on the energy released from impact and attrition between the balls and starting powders. During the process, the rapid collision applies a large compressive force on the surface of the original material [1, 2]. This technique is not only applied for electrode material production but also provides enough energy for a chemical reaction. In recent years, the high-energy ball milling method was used to fabricate novel electrode materials for high-performance energy storage devices [3].

3.2.2 Electrostatic Spray Deposition (ESD)

Electrostatic Spray Deposition (ESD) is an attractive thin film fabrication technique which developed in 1996 [4]. In this method, the applied high DC voltage between a metal nozzle and a substrate atomized the precursor solution into an aerosol spray and leading to solvent evaporation and deposition on the preheated substrate [5, 6]. The schematic of the ESD technique is shown in Figure 3.1. In this method, parameters such as applied voltage, substrate temperature, nozzle geometry, the distance between the substrate and nozzle, and flow rate are the attractive features of ESD to control the morphology of the resulting thin film. The feasibility of preparing a high-surface area and uniform thin film deposition makes ESD unique for energy storage devices. In recent years, ESD-based materials were used as an electrode for Li-ion batteries and supercapacitors [3, 7-10].

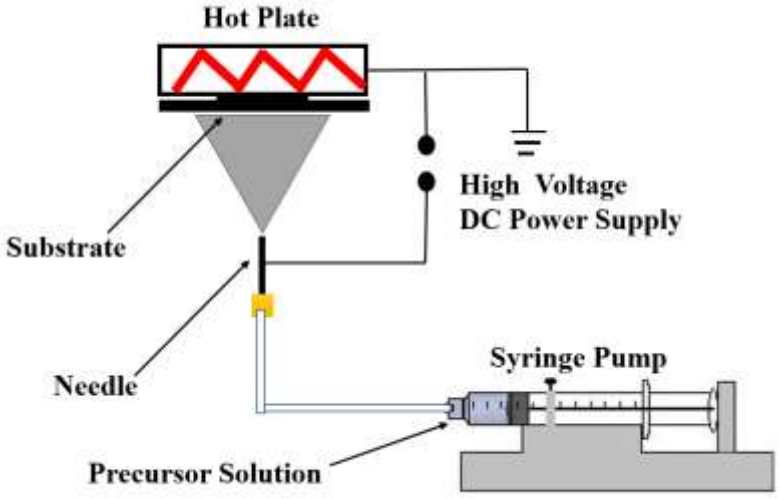

Figure 3.1: Schematic illustration of the ESD technique.

3.2.3 Bipolar Electrochemical Exfoliation (BPE)

Bipolar electrochemistry (BPE) is a technique based on the polarization of an isolated electrode (known as a bipolar electrode), under the presence of an external electric field. The concept of BPE was first introduced in the 1960s by Fleischmann et al, who evaluated fluidized bed electrodes comprising copper particles [11]. As shown in Figure 3.2, a bipolar electrode is immersed inside the solution in the presence of an external electric field applied between two feeding electrodes [12]. The electric field inside the solution and through the bipolar electrode is constant and depends on the applied potential (V) and distance (L) between two feeding electrodes. In the presence of the electric field, polarization potential (ΔV) arises due to the solution potential differences and conductive object and oxidation/reduction reactions happened on the two poles of bipolar electrode simultaneously in the presence of sufficient polarization potential [13, 14]. This technique has been used for different applications such as electro-sensing, optical detection, selective deposition, and electronic device fabrication due to its efficiency, low cost, and simplicity [15, 16].

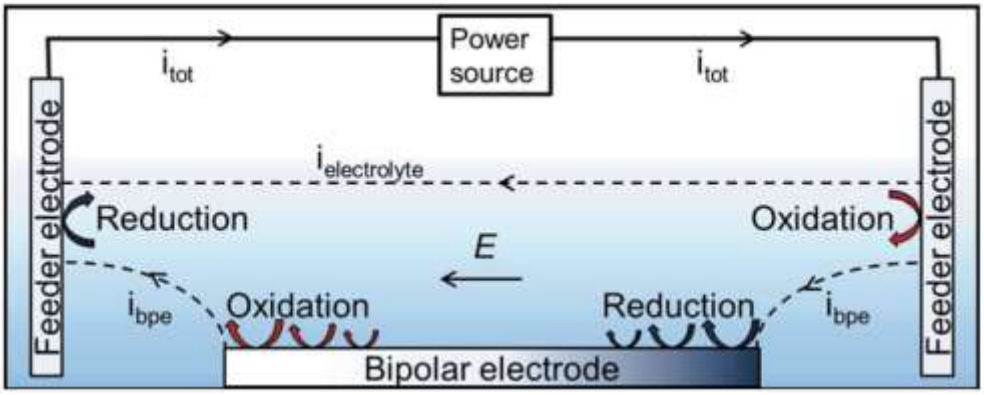

Figure 3.2: Schematic illustration of bipolar electrochemistry technique [12].

3.3 Material Characterization

The techniques used for characterization of the materials used in this thesis are described in this section:

3.3.1 Scanning Electron Microscopy (SEM)

In order to evaluate the morphology and microstructure of the synthesized materials, a field-emission scanning electron microscopy (JEOL 6330FE-SEM and JEOL FESEM 7000) was used with the accelerating voltages of 5-25 kV for a typical working distance between 5-40 mm.

3.3.2 Transmission Electron Microscopy (TEM)

To investigate the morphology, crystallinity, and properties of the synthesized materials, transmission electron microscopy (TEM-Philips CM-200 FEG and Tecnai TF 20 TEM) was used. Moreover, selected-area electron diffraction (SAED) patterns were conducted at an accelerating voltage of 200 kV using a field emission gun with a resolution of 2 °A.

3.3.3 X-Ray Diffraction (XRD)

X-Ray diffraction (XRD) analysis is a powerful technique to evaluate the crystallinity and crystallographic orientations of material. In this thesis, XRD analysis was used to study the phosphorus-based materials using Siemens D-5000 diffractometer (Cu Kα, λ=0.154056 nm, 40mA, and40 kV). After the XRD analysis, the results were identified using Joint Committee on Powder Diffraction Standards - International Center for Diffraction Data (JCPDS-ICDD) database.

3.3.4 Raman Spectroscopy

Raman spectroscopy is a powerful spectroscopic technique for the evaluation of vibrational modes and the fingerprint of chemical structures. This characterization method is based on the change of the vibrational quantum states of illuminated material which must be Raman active. After the interaction of laser with molecular vibrations, its energy being shift and this blue to red shift gives information about the vibrational mode of the chemical species. In this thesis, the Raman spectra of the samples were collected using a BaySpec Raman spectrometer with a 514 nm laser source.

3.3.5 Fourier Transform Infrared (FT-IR) Spectroscopy

Fourier transform infrared (FTIR) spectroscopy measures the range of wavelengths in the infrared region that are absorbed by a material. The sample's absorbance of the infrared light's energy at various wavelengths is measured to determine the material's molecular composition and structure. In this dissertation, FTIR analysis of the synthesized samples were carried out using a JASCO FTIR-4100 equipped with an attenuated total reflectance (ATR) accessory between 500-4000 cm^{-1}.

3.3.6 X-ray Photoelectron Spectroscopy (XPS)

X-ray photoelectron spectroscopy (XPS) is an advanced spectroscopic technique for analyzing the surface chemistry and overall electronic structure of the material. This method is based on irradiating a solid surface with an X-ray beam that can identify the elements and chemical bonding that exist within a material. A photoelectron spectrum is recorded by counting ejected electrons over a range of electron kinetic energies. Peaks

appear in the spectrum from atoms emitting electrons of a particular characteristic energy. In this thesis, the surface chemistry of the synthesized materials was evaluated by XPS-VAC-PHI 5000 and Physical Electronics 5400 ESCA instrument with Al Ka radiation (1486.6 eV).

3.4 Electrochemical Characterization

3.4.1 Electrochemical Impedance Spectroscopy (EIS)

Electrochemical impedance spectroscopy (EIS) is a frequency response technique where a sinusoidal potential is applied to the electrochemical system and the sinusoidal current signal is measured. Small amplitude perturbation signals are normally conducted in EIS analysis. In this dissertation, EIS analysis was performed for rechargeable batteries and supercapacitors using a Bio-logic versatile multichannel potentiostat (VMP3, BioLogic). Depends on the electrode materials, the EIS characterization was measured at different DC voltages and ac amplitudes from 1 mHz to1 MHz. To analyze the obtained EIS results, an equivalent electrical circuit model is developed to fit the Nyquist and Bode diagrams.

3.4.2 Cyclic Voltammetry (CV)

Cyclic voltammetry (CV) is a potentiodynamic electrochemical technique to understand the reversibility of electrochemical reactions. In this method, the potential is swept at a constant scan rate as a function of time. The current versus voltage (known as voltammogram) is generated at an applied scan rate and provides information about the electrochemical mechanisms of the system. In a typical CV test, the voltage first is swept in one direction and then in a reverse step to evaluate the reversibility of the device. Bio-

logic versatile multichannel potentiostat (VMP3, BioLogic) was used for CV analysis in this dissertation.

3.4.3 Galvanostatic Charge-discharge (GCD)

Galvanostatic charge-discharge (GCD) is an electrochemical analysis to study the cyclability, rate capability, and electrochemical reactions of the energy storage device. By this technique, the electrochemical performance of the device can be obtained in a plot of potential versus capacity (or time) during the charge/discharge process. To investigate the rate performance of the device, the charge/discharge process is carried out at different current densities. In this dissertation, GCD tests were performed at room temperature using BioLogic VMP3 potentiostat and NEWARE BTS-610 Battery Test System.

3.5 References

[1] C. Suryanarayana, Mechanical alloying and milling, Progress in materials science 46(1-2) (2001) 1-184.

[2] M.A. Taha, R.A. Youness, M.F. Zawrah, Review on nanocomposites fabricated by mechanical alloying, International Journal of Minerals, Metallurgy, and Materials 26(9) (2019) 1047-1058.

[3] A.R. Baboukani, I. Khakpour, E. Adelowo, V. Drozd, W. Shang, C. Wang, High-performance red phosphorus-sulfurized polyacrylonitrile composite by electrostatic spray deposition for lithium-ion batteries, Electrochimica Acta 345 (2020) 136227.

[4] C. Chen, E. Kelder, J. Schoonman, Unique porous LiCoO 2 thin layers prepared by electrostatic spray deposition, Journal of materials science 31(20) (1996) 5437-5442.

[5] X. Li, C. Wang, Engineering nanostructured anodes via electrostatic spray deposition for high performance lithium ion battery application, Journal of Materials Chemistry A 1(2) (2013) 165-182.

[6] A. Jaworek, A.T. Sobczyk, Electrospraying route to nanotechnology: An overview, Journal of electrostatics 66(3-4) (2008) 197-219.

[7] R. Agrawal, E. Adelowo, A.R. Baboukani, M.F. Villegas, A. Henriques, C. Wang, Electrostatic spray deposition-based manganese oxide films—From pseudocapacitive charge storage materials to three-dimensional microelectrode integrands, Nanomaterials 7(8) (2017) 198.

[8] R. Agrawal, A.R. Baboukani, C. Wang, Expanding the potential window of aqueous electrochemical capacitors with binder-free electrostatically sprayed manganese oxide composite cathode films, Materials Research Express 6(8) (2019) 085012.

[9] E. Adelowo, A.R. Baboukani, C. Chen, C. Wang, Electrostatically sprayed reduced graphene oxide-carbon nanotubes electrodes for lithium-ion capacitors, C—Journal of Carbon Research 4(2) (2018) 31.

[10] A.R. Baboukani, E. Adelowo, R. Agrawal, I. Khakpour, V. Drozd, W. Li, C. Wang, Electrostatic spray deposited Sn-SnO2-CNF composite anodes for Lithium ion storage, ECS Transactions 85(13) (2018) 331.

[11] J. Backhurst, J. Coulson, F. Goodridge, R. Plimley, M. Fleischmann, A preliminary investigation of fluidized bed electrodes, Journal of the Electrochemical Society 116(11) (1969) 1600.

[12] S. Munktell, Bipolar Electrochemistry for high throughput screening applications, Acta Universitatis Upsaliensis, 2016.

[13] G. Loget, D. Zigah, L. Bouffier, N. Sojic, A. Kuhn, Bipolar electrochemistry: from materials science to motion and beyond, Accounts of Chemical Research 46(11) (2013) 2513-2523.

[14] S.E. Fosdick, K.N. Knust, K. Scida, R.M. Crooks, Bipolar electrochemistry, Angewandte Chemie International Edition 52(40) (2013) 10438-10456.

[15] L. Koefoed, S.U. Pedersen, K. Daasbjerg, Bipolar electrochemistry—A wireless approach for electrode reactions, Current Opinion in Electrochemistry 2(1) (2017) 13-17.

[16] K.L. Rahn, R.K. Anand, Recent Advancements in Bipolar Electrochemical Methods of Analysis, Analytical Chemistry (2020).

4. High-Performance Red Phosphorus-Sulfurized Polyacrylonitrile Composite by Electrostatic Spray Deposition for Lithium-Ion Batteries

4.1 Introduction

In the past few years, due to rapidly increased global demand for energy storage devices such as advanced electronics, electric vehicles (EVs), and implantable medical devices, it is essential to develop novel materials for energy storage technologies [1]. Lithium-ion batteries (LIBs) have been the most popular and commercially available energy storage devices [2, 3]. However, anodes of LIBs still suffer poor theoretical capacity of graphite (372 mAh g^{-1}) [4]. Until now, several materials such as Sn-based electrode [5], Si-based electrode [6], Ge-based electrode [7], metal nitrides-based electrodes [8], and metal oxides-based electrode [9] utilizing either alloying or conversion mechanisms have been developed as an anode material for LIBs [10].

Recently, phosphorus as an anode material has attained much attention owing to its high theoretical capacity (2596 mAh/g) via Li_3P alloying formation [11]. White P (WP), black P (BP) and red P (RP) are the main three allotropes of solid phosphorus. WP is not stable in the air, flammable and very toxic, which impose safety concerns for LIBs. BP is the most thermodynamically stable form of phosphorus with an orthorhombic crystal structure. However, synthesis of BP via high-pressure and high-temperature process is expensive, which restricts its practical application [12, 13]. Compare to WP and BP, RP is non-toxic, low cost, eco-friendly, and easy to handle, making RP a promising anode for LIBs [14-17]. Nevertheless, the application of RP in LIBs is obstructed by two serious issues: low electrical conductivity of RP ($\sim 10^{-14}$ S cm^{-1}) [15], and huge volume change

(more than 300 %) during lithiation and delithiation causing the pulverization of the active materials which leads to significant capacity fading, and poor cycling performance [18, 19]. Different methods have been evaluated to resolve the issues and improve the electrochemical performance of P-based electrode materials. Compositing phosphorus with carbonaceous materials is one of the useful methods to increase the conductivity and control the volume expansion [11]. To date, different types of 1D and 2D carbon materials has been incorporated with RP, such as graphene-based materials [20], carbon nanotube (CNT) [14, 21], and carbon nanofibers (CNF) [4, 16]. Additionally, by decreasing the particle size of RP, using additives, encapsulation, and forming chemical bonding to enhance the stability of SEI, volume expansion can be effectively decreased, and cyclability can be improved [22]. For example, Sun et al. prepared TiO_2-modified RP and CNT composite by ball milling and ultrasonication technique which exhibited specific capacity of 750 mAh g^{-1} at 10 A g^{-1} [23]. Very recently, Li et al. demonstrated that encapsulated RP particles inside multi-walled carbon nanotubes showed high capacity of 1012 mAh g^{-1} at 0.1 A g^{-1} [24]. Song et al. found that strong P-O-C chemical bonding between RP and C matrix could enhance the cyclability of RP-C composite [25]. Yu et al. showed that the P-C chemical bonding could reduce the agglomeration of RP-based composite and improve cycling performance of electrode [26]. Since the first attempt to synthesize sulfurized polyacrylonitrile (SPAN) as functional polymer composite by Wang et al. in 2002 [27], SPAN-based electrodes have shown attractive electrochemical performance such as good cycling life and Coulombic efficiency due to its chemical compatibility for energy storage devices [28-31]. In addition, due to the low bonding energy of S-S (265 kJ mol^{-1}) [32] and its high reactivity to form additional

chemical bonds with RP, the conductive SPAN could be an ideal composite to increase the conductivity and control the volume expansion of RP in Li-ion batteries.

Electrostatic spray deposition (ESD) is a facile spraying technique, which involves applied DC voltage between a heated substrate and a spray nozzle with precursor solution [33-37]. By applying the voltage, the precursor atomizes into an aerosol and deposits uniformly on the substrate with various favorable morphologies particularly helpful for effectively buffer volume change for LIBs application [38, 39]. Herein, we developed a binder-free RP-SPAN hybrid composite through ball milling and ESD technique. The RP-SPAN hybrid electrode exhibited excellent specific capacity up to 1605 mAh g^{-1} at 0.1 A g^{-1} at 100 cycles. Moreover, a specific capacity of 320 mAh g^{-1} was maintained at 3 A g^{-1}. This study demonstrates that ESD-based RP-SPAN hybrid is a promising anode electrode with remarkable electrochemical performance for LIBs.

4.2 Materials and Methods

4.2.1 Materials Synthesis

Amorphous Red phosphorus powder (98.9%) was obtained from Alfa Aesar. Polyacrylonitrile (PAN), and sulfur (≥99%) as raw materials were purchased from Sigma Aldrich. SPAN was prepared from a mixture of PAN and sulfur (mass ratio of 2:1) which were uniformly mixed by using a mortar and pestle for 30 minutes. Then, the mixture was heated at 450 °C in Ar atmosphere using a tube furnace with a ramping rate of 5°C/min for 2 h [29]. To prepare the RP-SPAN hybrid, the synthesized SPAN and pure RP were mixed in a mass ratio of 1:5 and placed into a stainless steel vessel which was sealed inside a glovebox under Ar atmosphere. The ball milling was conducted in Ar

atmosphere under 100 bar pressure by Retsch PM 10 planetary ball mill for 36 h at 350 rpm. RP-SPAN composite anode on Ni foam electrode was fabricated via ESD technique. For preparing the ESD precursor, the RP-SPAN hybrid material (90 wt%) was mixed with super P Li (10 wt%) and dispersed in 1,2-propanediol (Sigma Aldrich) followed by stirring for 1 h and next, transferred to a syringe. Pure RP powders without SPAN were also prepared by a similar procedure for comparison. During the ESD, electrode films were deposited at 200 °C with a flow rate of 2 mL h^{-1} for 2 h. The distance between the substrate and needle was 3 cm and the applied voltage was about 6-7 kV.

4.2.2 Materials Characterization

The microstructure and elemental analysis were conducted using both scanning electron microscopy (SEM-JEOL 6330F) equipped with dispersive X-Ray spectroscopy (EDS-UltraDry) detector and transmission electron microscopy (TEM-Philips CM-200 FEG). X-ray diffraction (XRD) analysis was conducted using a Siemens 5000D diffractometer (λ=1.154056 Å, Cu Kα, 40 mA, and 40 kV). Raman spectroscopy was performed using a 514 nm laser excitation source. Surface chemistry of the materials was evaluated by Fourier transform infrared spectroscopy (JASCO FTIR-4100 equipped with an ATR-PRO 450S) and X-ray photoelectron spectroscopy (XPS-VAC-PHI 5000).

4.2.3 Electrochemical Characterization

Electrochemical properties were characterized using VMP3 Bio-Logic workstation. Swagelok electrochemical cell assembled in argon controlled glovebox was used for half-cell test, which contained RP-SPAN hybrid as a working electrode, and lithium as both counter and reference electrodes. A 100µl of 1M $LiPF_6$ in ethylene carbonate - diethyl

carbonate (1:1, volume ratio) was used as an electrolyte. Celgard 2400 polypropylene was used as a separator. Electrochemical Impedance Spectroscopy (EIS) was conducted between 100 kHz and 0.01 Hz. Cycling voltammetry (CV) test was performed in a voltage range from 0.01 to 3.0 V at a scan rate of 0.1 mV s^{-1}. Galvanostatic charge/discharge (GCD) and rate capability tests were conducted using a battery tester (NEWARE BTS-610).

4.3 Results and Discussion

The preparation process of RP-SPAN composite is shown in Figure 4.1. In brief, SPAN was synthesized through dehydrogenation of PAN and formation of bonding with S at 450 °C for 2 h taking advantage of low S-S bond energy (around 264 kJ mol^{-1}) [40]. Elemental analysis of the synthesized SPAN by EDS detected 38.2 wt% of sulfur. It was reported that sulfur content around 40 wt. % in SPAN revealed higher specific capacity and stable cycle life [28]. The morphologies of the RP and synthesized SPAN are shown in Figure 4S.1 (a, b). As shown in Figure 4S.1 (a), RP particles are irregular in shape with size ranging from less than 1 to 20 μm. In contrast, SPAN particles display uniform spherical shape with the particle size of around 300 nm. The featureless agglomerated morphology of the synthesized RP-SPAN hybrid is shown in Figure 4.2 (a). A typical TEM image with selected area electron diffraction pattern shown in Figure 4S.2 revealing the amorphous nature of the RP-SPAN hybrid.

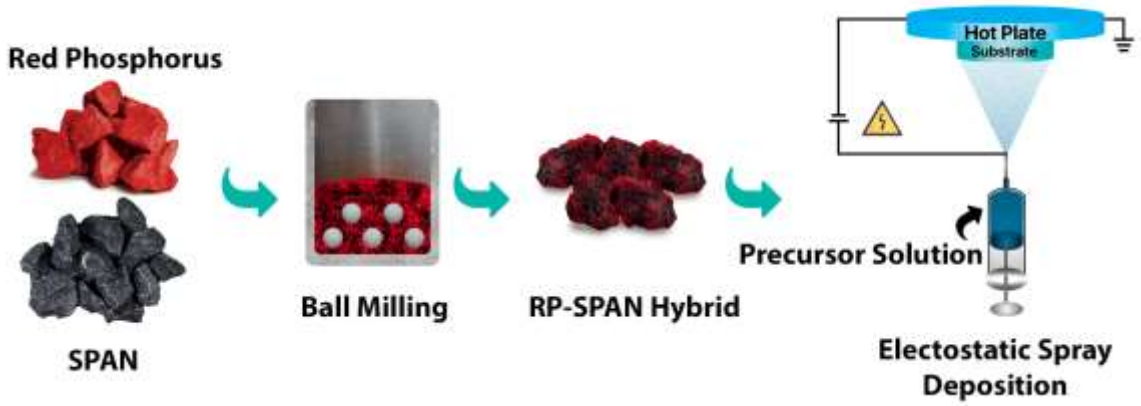

Figure 4.1: Schematic illustration of the RP-SPAN hybrid anode preparation.

The XRD patterns of the pure RP, SPAN, and RP-SPAN hybrid materials are shown in Figure 4.2 (b). One peak at around 15° and two broad peaks at around 32° and 55° are clear for the pure RP, indicating the medium-range ordered structure which is consistent with the previous studies [15, 41]. The XRD analysis of SPAN exhibited a broad peak at around 25°, which is related to the hexagonal graphitic (002) plane of amorphous carbon [29]. For the RP-SPAN hybrid, a small graphitic peak of SPAN and three broad peaks of RP appeared. The broader and weaker XRD peaks for the hybrid sample could be due to the further amorphization and strain/stress induced by the ball milling process. As shown in the Raman spectra in Figure 4.2 (c), for the pure RP, there are wide wavebands in the range of 300 to 500 cm^{-1} originated from the P9 cage of P and a broad luminescence peak centered around 1100 cm^{-1} [14]. Peaks at 498 and 956 cm^{-1} could be assigned to the S-S bonds in the SPAN [31]. For the hybrid sample, two peaks at around 1367 and 1578 cm^{-1} are related to the D (disordered carbon) and G (ordered graphitized carbon) bands, respectively [42]. No noticeable change was detected for the peak locations of SPAN and hybrid sample, confirming that the structure of SPAN was well-maintained in the RP-

SPAN hybrid. In addition, the Raman peaks of RP could not be detectable for the hybrid sample. The surface chemistry of samples was further studied by FTIR analysis (Figure 4.2 (d)). The bands of P=O (1034 cm^{-1}, and 1749 cm^{-1}) and P−OH (1263 cm^{-1}) vibrations are commonly observed in RP due to its surface oxidation [43, 44]. For the SPAN and hybrid sample, the modes in the region of 1150-1600 cm^{-1} can be assigned to C-S stretching at 1357 cm^{-1}, C=N symmetric stretching at 1260 cm^{-1}, C−C deformation at 1273 cm^{-1}, and C=C asymmetric stretching at 1590 cm^{-1}, respectively [40]. The peaks at 527, 675, and 947 cm^{-1} can be assigned to the S-S stretching, C-S stretching and the ring breath of the side-chain containing S-S bonds, respectively [45-47]. Specifically, peak at 929 cm^{-1} for RP-SPAN hybrid could be attributed to the P−O−S stretching, indicating the chemical bonding formation of phosphorus with sulfur [45, 48]. Due to the heteroaroamatic structure of SPAN, the C=N symmetric stretching is still present in the hybrid sample after ball milling. It has been reported that the chemical bond of P to the conductive matrix could contribute to the integrity of the electrode during cycling [49].

The XPS analysis of the samples are shown in Figure 3 (a-d). The P2p XPS spectrum of RP (Figure 4.3 (a)) reveals two major peaks of $P2p_{1/2}$ and $P2p_{3/2}$ components at around 130.7 and 129.7 eV, respectively. The broad peak at around 133.3 eV could be assigned to phosphates bond (POx), which indicates surface oxidation of RP after exposure to the air [15]. Figure 4.3 (b) shows two sets of double fitted peaks at about 161.8 and 163.0 eV, which belong to $S2p_{3/2}$, 162.9 and 164.1 eV, which belong to $S2p_{1/2}$, respectively. The main fitted $S2p_{3/2}$ peak at 163.0 eV is assigned to the 2p electrons of S atoms either bonded to sulfur or carbon [31, 40, 50]. The $S2p_{1/2}$ peak at 164.1 eV is attributed to the single S-S bond [51]. The $S2p_{3/2}$ and $S2p_{1/2}$ peaks at around 161.8 and 162.9 eV are

related to the C-S chemical bond [51-53]. For the P2p spectrum of RP-SPAN hybrid (Figure 4.3 (c)), a new peak centered at 134.1 eV can be attributed to S-P bond [54]. For the S2p spectrum of hybrid sample (Figure 4.3 (d)), two new $S2p_{3/2}$ and $S2p_{1/2}$ peaks at 162.0 eV and 163.1 eV are most likely attributed to the S-P bond, respectively [52, 54-56]. The $S2P_{3/2}$ and $S2p_{1/2}$ peaks at 162.7 and 163.8 eV are assigned to the S-S or S-C bond, respectively [50]. The spin orbit doublet at 160.3 and 161.3 eV, can be attributed to the $S2p_{3/2}$ and $S2p_{1/2}$ peaks of the C-S bond, respectively [50, 51].

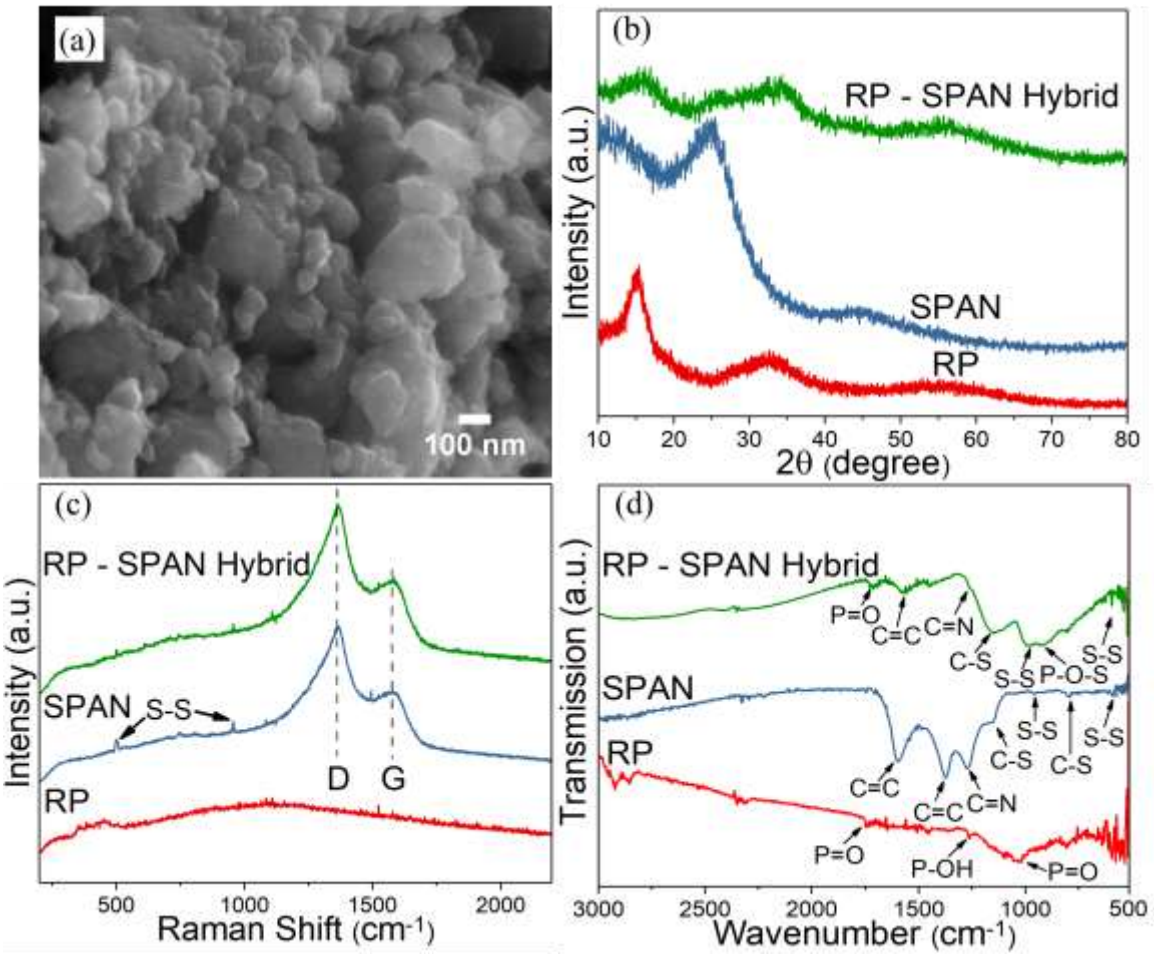

Figure 4.2: (a) Typical SEM image of RP-SPAN hybrid; (b) XRD patterns, (c) Raman and (d) FTIR spectra of RP, SPAN, and RP-SPAN hybrid.

The wide-scan survey spectrum and C1s spectrum of SPAN and RP-SPAN hybrid are shown in Figure 4S.3 (a-d). The C1s spectra of SPAN (Figure 4S.3 (c)) reveal C=N bonds (288.4 eV), C-S bonds (286.4 eV), and C-C bonds (284.7 eV). For the RP-hybrid, the peak at 285.4 eV is related to the C-P bond [57, 58]. The binding energies in RP-SPAN spectrum are shifted to the lower values most likely due to the amorphization and interaction of P with SPAN during ball milling [54].

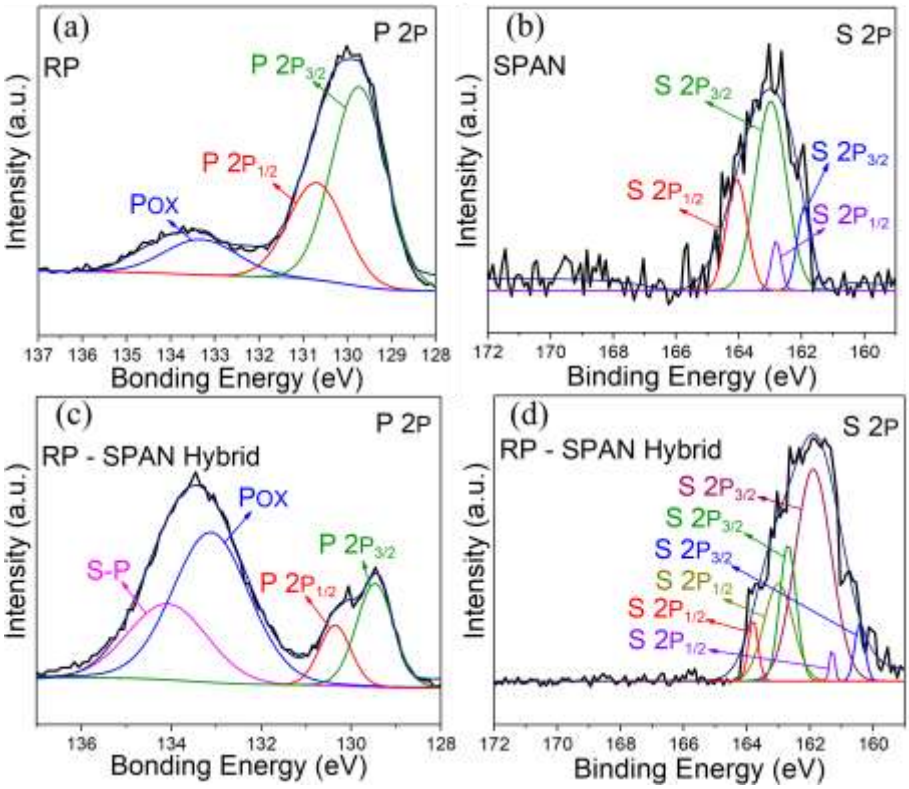

Figure 4.3: XPS spectra of (a) P2p of RP, (b) S2p of SPAN, and (c) S2p of RP-SPAN hybrid.

As shown in Figure 4.4 (a-f), the electrochemical characterization of the RP and RP-SPAN hybrid anodes was conducted. Figure 4.4 (a, b) shows the 1st, 5th, and 10th cycle of the CV test for the RP and RP-SPAN hybrid at 0.1 mV s^{-1}. Four cathodic peaks at 0.03, 1.09, 1.57 and 2.27 V were observed for pure RP in the first cycle and disappeared in the

subsequent cycles, which could be assigned to the decomposition of $LiPF_6$ and SEI formation. The cathodic peak at 0.63 V and anodic peak at 1.37 V are related to the lithiation/delithation mechanism of P-based anode material ($P + xLi^+ + xe^- \leftrightarrow Li_XP\ (1< x \leq 3)$) [57, 59]. For the RP-SPAN hybrid anode, in the initial cathodic scan, peaks at 0.41, 1.21 and 2.30 V are detected but disappear in the following cycles due to the SEI formation. The cathodic peak at 0.58 V can still be observed for the hybrid sample, but in the anodic scan, the main peak at 1.09 V shifted to the left compared to the pure RP. Besides, the reversible redox peaks at around 0.11, 0.18, and 0.24 V most likely correspond to the lithium intercalation with the carbon component in the composite [26]. Good reversibility was observed for the RP-SPAN hybrid in the subsequent CV curves. Compare to the hybrid sample, pure RP electrode shows low current density and low capacity.

Figure 4.4 (c, d) show the galvanostatic charge/discharge curves for the RP and RP-SPAN hybrid at 1^{st}, 2^{nd}, 5^{th}, 10^{th}, 25^{th}, 50^{th}, and 100^{th} cycles at the constant current density of 0.1 A g^{-1} from 0.01 to 3 V. Three major plateaus can be observed in Figure 4.4 (c) for pure RP sample at around 0.6, 1.5 and 2.2 V on the first discharge curve due to the SEI formation and disappeared in the next cycles which are slightly consistent with the peaks observed in CV test. The small shift in plateau positions in the cathadic peaks is probably due to the kinetics of reactions and complex alloying behavior of phosphorus [17, 49, 60]. Pure RP displays specific discharge/charge capacities of 3393/976, 1059/695, 787/598, 630/583, 575/557, 381/372, and 358/352 mAh g^{-1} at the 1^{st}, 2^{nd}, 5^{th}, 10^{th}, 25^{th}, 50^{th}, and 100^{th} cycle, respectively. The significant capacity fading for the RP sample is reported in the previous studies [4, 26].

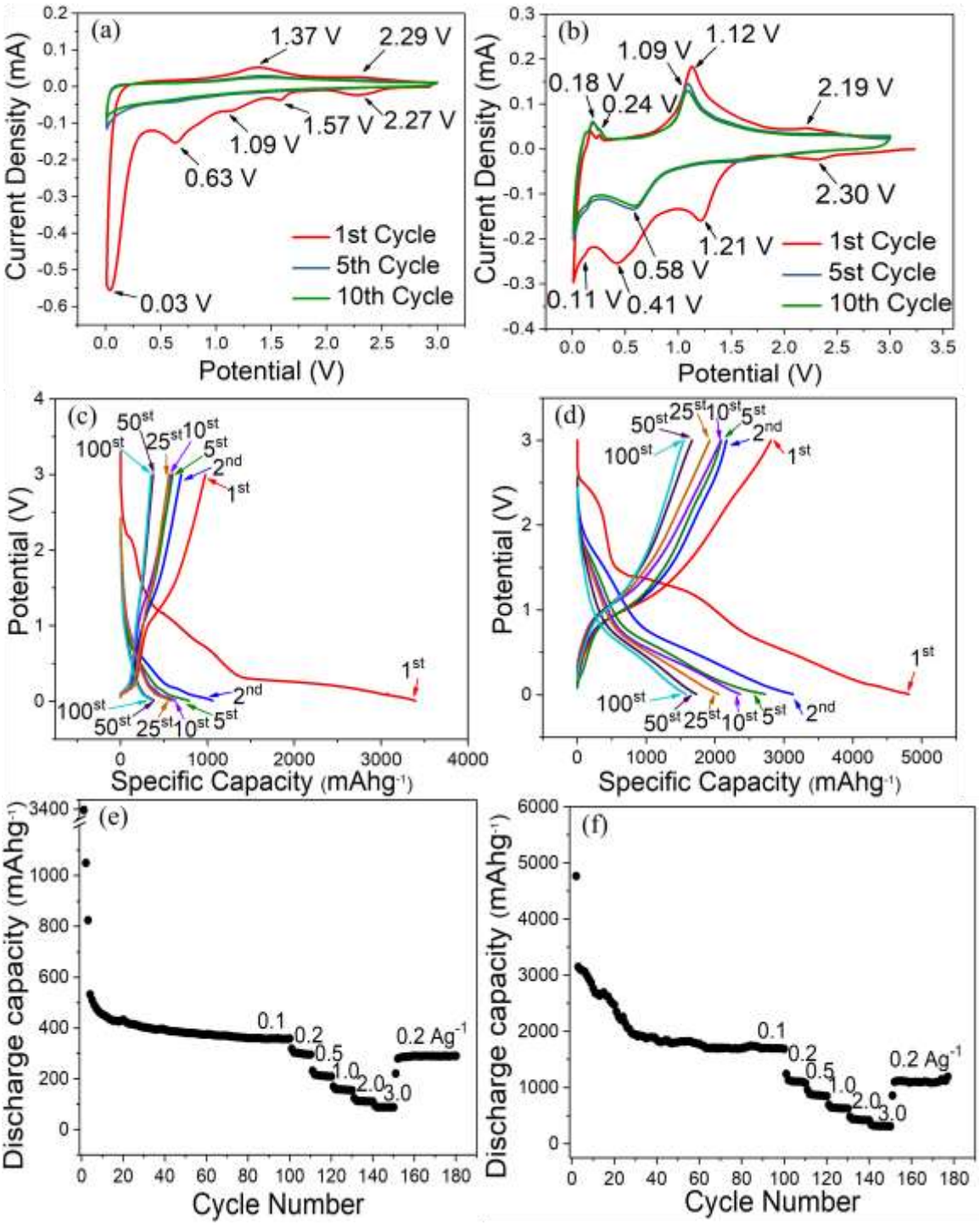

Figure 4.4: Electrochemical characterization of the pure RP and RP-SPAN hybrid anodes, Cyclic voltammetry at 0.1 mV s^{-1} for (a) pure RP, and (b) RP-SPAN hybrid. Typical charge/discharge profiles at 0.1 A g^{-1} for (c) pure RP, and (d) RP-SPAN hybrid. Cycling performance at 0.1 Ag^{-1} and rate capability at 0.2, 0.5, 1.0, 2.0, 3.0 Ag^{-1} for (e) pure RP and, (f) RP-SPAN hybrid.

Similar to the RP sample, for the hybrid sample (Figure 4.4 (d)), in the first discharge curve, the plateaus at around 2.3 and 1.5 V are observed and disappeared in the subsequent cycles. The plateaus at around 0.6 to 0.7 and 1.4 V on the first discharge and 1.0 V on the first charge curve are observed for RP-SPAN hybrid due to the stepwise lithiation and delithiation, which is consistent with the CV test. Plateaus stayed unchanged in subsequent cycles, confirming reversible lithiation/delithiation reactions for the hybrid electrode. The hybrid sample, delivered the specific discharge/charge capacity of 4810/2809, 3130/2162, 2724/2089, 2359/2084, 2052/1921, 1724/1664, and 1605/1579 mAh g^{-1} at the 1^{st}, 2^{nd}, 5^{th}, 10^{th}, 25^{th}, 50^{th}, and 100^{th} cycle, respectively. The high discharge capacity of 1605 mAh g^{-1} at 100 cycles for the hybrid sample is one of the best reported performances among the RP-based composite electrode in LIBs (Table 4S.1). The cycling performance and rate capability of the RP and hybrid samples are shown in Figure 4.4 (e, f). The curves remain stable after 50^{th} cycle, indicating high reversibility for both RP and hybrid sample. The rate performance of pure RP exhibited discharge capacities of 318, 231, 170, 124 and 88 mAh g^{-1} at 0.2, 0.5, 1.0, 2.0 and 3.0 A g^{-1}, respectively. The specific capacity of 287 mAh g^{-1} recovered when the current density returned back to 0.2 A g^{-1} after 150 cycles, which confirms good rate capability of ESD-based pure RP anode compare to previous studies [21, 61]. Furthermore, the hybrid sample delivered high discharge capacity of 1220, 956, 696, 480, and 320 mAh g^{-1}, at 0.2, 0.5, 1.0, 2.0, and 3.0 A g^{-1}, respectively. The capacity recovered to ~1210 mAh g^{-1} when the current density returned back to 0.2 A g^{-1} after 150 cycles, indicating higher discharge capacities of RP-SPAN hybrid electrode at different current densities compared to pure RP.

Figure 4.5 shows the EIS characterization of the RP and hybrid anodes before and after cycling. As shown, each Nyqiust curves consists of the semicircles and a straight line at high to low frequency, respectively. The Nuquist curves are simulated by the modified Randles equivalent circuit (inset of Figure 4.5) [62]. The elements in the circuit are solution resistance (R_1), charge transfer resistance (R_2), constant phase element (CPE), and Wurburg (W). The dashed lines are data fitted based on the equivalent circuit. The simulation parameters from the equivalent circuit are listed in Table 4S.2. The solution resistance for all the samples are similar before and after 180 cycles. The semicircle diameter of the Nuquist curve shows the charge transfer resistance. For the fresh cells, the charge transfer resistance of RP-SPAN hybrid anode (592 Ω) is much lower compared to the pure RP anode (1797 Ω), which indicates better electronic conductivity and kinetics of the hybrid sample. After 180 cycles, the hybrid electrode showed very low charge transfer resistance of 35 Ω compare to the fresh cell indicating improved charge transfer kinetics after cycling. The morphology of the prepared hybrid electrode before and after 180 cycles were evaluated by SEM (Figure 4S.4 (a, b)). The hybrid electrode still maintains its microstructural integrity without obvious degradation, indicating that the volume change didn't affect the structural stability.

Our results show that the ESD method is an effective approach to prepare RP-based composite with favorable morphology and composition in order to buffer mechanical stress and alleviate crack formation during cycling. The RP-SPAN hybrid delivered an excellent specific capacity of 1605 $mAhg^{-1}$ at 0.1 Ag^{-1}, which is among the best performance in P-based anodes for LIBs [11]. The RP-SPAN hybrid delivered high specific capacity most likely due to the synergetic effect of chemical bonding and

improved kinetics. For practical application, future study need to be done to evaluate the electrochemical performance of hybrid anode in a full cell setup.

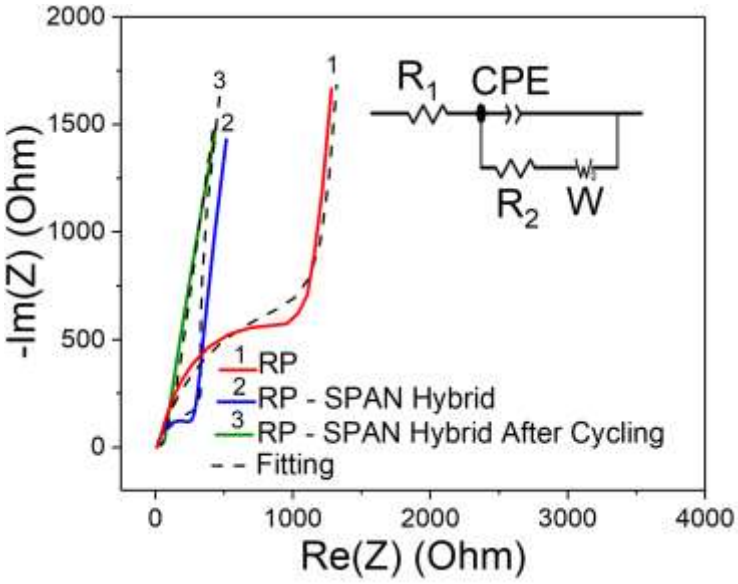

Figure 4.5: Electrochemical impedance characterization of RP and RP-SPAN hybrid before and after 180 cycles (the inset shows the equivalent circuit).

4.4 Conclusion

In summary, the RP-SPAN hybrid anode was fabricated for LIB application by the facile ball milling and ESD technique. The electrochemical characterization of the pure RP and hybrid electrodes revealed a specific discharge capacity of 358 and 1605 mAh g^{-1} at 0.1 A g^{-1} with good cyclability and rate capability. The highly reversible specific capacity of the hybrid electrode could be ascribed to the improved kinetics and chemical bonding formed during the ball milling and the electrode preparation through the binder-free ESD method. Considering the facile preparation and excellent electrochemical performance, our study demonstrates promising RP-SPAN hybrid anode for high-performance LIBs.

4.5 References

[1] Z. Yang, J. Zhang, M.C.W. Kintner-Meyer, X. Lu, D. Choi, J.P. Lemmon, J. Liu, Electrochemical Energy Storage for Green Grid, Chemical Reviews 111(5) (2011) 3577-3613.

[2] B. Scrosati, J. Hassoun, Y.-K. Sun, Lithium-ion batteries. A look into the future, Energy & Environmental Science 4(9) (2011) 3287-3295.

[3] C. Sun, J. Liu, Y. Gong, D.P. Wilkinson, J. Zhang, Recent advances in all-solid-state rechargeable lithium batteries, Nano Energy 33 (2017) 363-386.

[4] W. Li, Z. Yang, Y. Jiang, Z. Yu, L. Gu, Y. Yu, Crystalline red phosphorus incorporated with porous carbon nanofibers as flexible electrode for high performance lithium-ion batteries, Carbon 78 (2014) 455-462.

[5] M.-G. Park, D.-H. Lee, H. Jung, J.-H. Choi, C.-M. Park, Sn-Based Nanocomposite for Li-Ion Battery Anode with High Energy Density, Rate Capability, and Reversibility, ACS Nano 12(3) (2018) 2955-2967.

[6] D. Ma, Z. Cao, A. Hu, Si-Based Anode Materials for Li-Ion Batteries: A Mini Review, Nano-Micro Letters 6(4) (2014) 347-358.

[7] J. Liu, K. Song, C. Zhu, C.-C. Chen, P.A. van Aken, J. Maier, Y. Yu, Ge/C Nanowires as High-Capacity and Long-Life Anode Materials for Li-Ion Batteries, ACS Nano 8(7) (2014) 7051-7059.

[8] W. Ren, L. Xu, L. Zhu, X. Wang, X. Ma, D. Wang, Cobalt-Doped Vanadium Nitride Yolk–Shell Nanospheres @ Carbon with Physical and Chemical Synergistic Effects for Advanced Li–S Batteries, ACS Applied Materials & Interfaces 10(14) (2018) 11642-11651.

[9] Y. Yu, P. Karayaylali, Y. Katayama, L. Giordano, M. Gauthier, F. Maglia, R. Jung, I. Lund, Y. Shao-Horn, Coupled LiPF6 Decomposition and Carbonate Dehydrogenation Enhanced by Highly Covalent Metal Oxides in High-Energy Li-Ion Batteries, The Journal of Physical Chemistry C 122(48) (2018) 27368-27382.

[10] S. Xin, Z. Chang, X. Zhang, Y.-G. Guo, Progress of rechargeable lithium metal batteries based on conversion reactions, National Science Review 4(1) (2016) 54-70.

[11] W. Liu, H. Zhi, X. Yu, Recent progress in phosphorus based anode materials for lithium/sodium ion batteries, Energy Storage Materials 16 (2019) 290-322.

[12] Y. Zhang, X. Rui, Y. Tang, Y. Liu, J. Wei, S. Chen, W.R. Leow, W. Li, Y. Liu, J. Deng, Wet-Chemical Processing of Phosphorus Composite Nanosheets for High-Rate

and High-Capacity Lithium-Ion Batteries, Advanced Energy Materials 6(10) (2016) 1502409.

[13] A. Rabiei Baboukani, I. Khakpour, V. Drozd, A. Allagui, C. Wang, Single-step exfoliation of black phosphorus and deposition of phosphorene via bipolar electrochemistry for capacitive energy storage application, Journal of Materials Chemistry A 7(44) (2019) 25548-25556.

[14] D. Yuan, J. Cheng, G. Qu, X. Li, W. Ni, B. Wang, H. Liu, Amorphous red phosphorous embedded in carbon nanotubes scaffold as promising anode materials for lithium-ion batteries, Journal of Power Sources 301 (2016) 131-137.

[15] X. Jiao, Y. Liu, B. Li, W. Zhang, C. He, C. Zhang, Z. Yu, T. Gao, J. Song, Amorphous phosphorus-carbon nanotube hybrid anode with ultralong cycle life and high-rate capability for lithium-ion battery, Carbon 148 (2019) 518-524.

[16] L. Wang, J. Ju, N. Deng, B. Cheng, W. Kang, Embedding red phosphorus in hierarchical porous carbon nanofibers as anodes for lithium-ion battery, Materials Letters 240 (2019) 39-43.

[17] Z. Chen, Y. Zhu, Q. Wang, W. Liu, Y. Cui, X. Tao, D. Zhang, Fibrous phosphorus: A promising candidate as anode for lithium-ion batteries, Electrochimica Acta 295 (2019) 230-236.

[18] Z. Yu, J. Song, M.L. Gordin, R. Yi, D. Tang, D. Wang, Phosphorus-Graphene Nanosheet Hybrids as Lithium-Ion Anode with Exceptional High-Temperature Cycling Stability, Advanced Science 2(1-2) (2015) 1400020.

[19] H. Liu, S. Zhang, Q. Zhu, B. Cao, P. Zhang, N. Sun, B. Xu, F. Wu, R. Chen, Fluffy carbon-coated red phosphorus as a highly stable and high-rate anode for lithium-ion batteries, Journal of Materials Chemistry A 7(18) (2019) 11205-11213.

[20] A. Bai, L. Wang, J. Li, X. He, J. Wang, J. Wang, Composite of graphite/phosphorus as anode for lithium-ion batteries, Journal of Power Sources 289 (2015) 100-104.

[21] T. Yuan, J. Ruan, C. Peng, H. Sun, Y. Pang, J. Yang, Z.-F. Ma, S. Zheng, 3D red phosphorus/sheared CNT sponge for high performance lithium-ion battery anodes, Energy Storage Materials 13 (2018) 267-273.

[22] W. Li, Z. Yang, M. Li, Y. Jiang, X. Wei, X. Zhong, L. Gu, Y. Yu, Amorphous red phosphorus embedded in highly ordered mesoporous carbon with superior lithium and sodium storage capacity, Nano Letters 16(3) (2016) 1546-1553.

[23] L. Sun, Y. Zhang, H. Si, Y. Zhang, J. Liu, J. Liu, Y. Zhang, TiO2-modified red phosphorus nanosheets entangled in carbon nanotubes for high performance lithium ion batteries, Electrochimica Acta 297 (2019) 319-327.

[24] J. Li, H. Jin, Y. Yuan, H. Lu, C. Su, D. Fan, Y. Li, J. Wang, J. Lu, S. Wang, Encapsulating phosphorus inside carbon nanotubes via a solution approach for advanced lithium ion host, Nano Energy 58 (2019) 23-29.

[25] J. Song, Z. Yu, M.L. Gordin, S. Hu, R. Yi, D. Tang, T. Walter, M. Regula, D. Choi, X. Li, Chemically bonded phosphorus/graphene hybrid as a high performance anode for sodium-ion batteries, Nano letters 14(11) (2014) 6329-6335.

[26] Z. Yue, T. Gupta, F. Wang, C. Li, R. Kumar, Z. Yang, N. Koratkar, Utilizing a graphene matrix to overcome the intrinsic limitations of red phosphorus as an anode material in lithium-ion batteries, Carbon 127 (2018) 588-595.

[27] J. Wang, J. Yang, J. Xie, N. Xu, A novel conductive polymer–sulfur composite cathode material for rechargeable lithium batteries, Advanced Materials 14(13-14) (2002) 963-965.

[28] L. Wang, X. He, J. Li, M. Chen, J. Gao, C. Jiang, Charge/discharge characteristics of sulfurized polyacrylonitrile composite with different sulfur content in carbonate based electrolyte for lithium batteries, Electrochimica Acta 72 (2012) 114-119.

[29] S. Zhang, Understanding of sulfurized polyacrylonitrile for superior performance lithium/sulfur battery, Energies 7(7) (2014) 4588-4600.

[30] A. K. Haridas, J. Heo, Y. Liu, H. Ahn, X. Zhao, Z. Deng, M. Agostini, A. Matic, K.-K. Cho, J.-H. Ahn, Boosting high energy density lithium-ion storage via the rational design of FeS incorporated sulfurized polyacrylonitrile fiber hybrid cathode, ACS Applied Materials & Interfaces 11(33) (2019) 29924-29933.

[31] Y. Hu, B. Li, X. Jiao, C. Zhang, X. Dai, J. Song, Stable Cycling of Phosphorus Anode for Sodium-Ion Batteries through Chemical Bonding with Sulfurized Polyacrylonitrile, Advanced Energy Materials 28(23) (2018) 1801010.

[32] R. Steudel, Properties of sulfur-sulfur bonds, Angewandte Chemie International Edition in English 14(10) (1975) 655-664.

[33] C. Chen, E.M. Kelder, J. Schoonman, Functional ceramic films with reticular structures prepared by electrostatic spray deposition technique, Journal of the Electrochemical Society 144(11) (1997) L289-L291.

[34] M. Safa, E. Adelowo, A. Chamaani, N. Chawla, A.R. Baboukani, M. Herndon, C. Wang, B. El-Zahab, Poly(Ionic Liquid)-Based Composite Gel Electrolyte for Lithium Batteries, ChemElectroChem 6(13) (2019) 3319-3326.

[35] E. Adelowo, A.R. Baboukani, C. Chen, C. Wang, Electrostatically Sprayed Reduced Graphene Oxide-Carbon Nanotubes Electrodes for Lithium-Ion Capacitors, C - Journal of Carbon Research 4(2) (2018) 31.

[36] R. Agrawal, E. Adelowo, A. Baboukani, M. Villegas, A. Henriques, C. Wang, Electrostatic spray deposition-based manganese oxide films—From pseudocapacitive charge storage materials to three-dimensional microelectrode integrands, Nanomaterials 7(8) (2017) 198.

[37] R. Agrawal, A.R. Baboukani, C. Wang, Expanding the potential window of aqueous electrochemical capacitors with binder-free electrostatically sprayed manganese oxide composite cathode films, Materials Research Express 6(8) (2019) 085012.

[38] A.R. Baboukani, E. Adelowo, R. Agrawal, I. Khakpour, V. Drozd, W. Li, C. Wang, Electrostatic spray deposited Sn-SnO2-CNF composite anodes for Lithium ion storage, ECS Transactions 85(13) (2018) 331-336.

[39] X. Li, C. Wang, Engineering nanostructured anodes via electrostatic spray deposition for high performance lithium ion battery application, Journal of Materials Chemistry A 1(2) (2013) 165-182.

[40] A.K. Haridas, J. Heo, Y. Liu, H.-J. Ahn, X. Zhao, Z. Deng, M. Agostini, A. Matic, K.-K. Cho, J.-H. Ahn, Boosting High Energy Density Lithium-Ion Storage via the Rational Design of an FeS-Incorporated Sulfurized Polyacrylonitrile Fiber Hybrid Cathode, ACS Applied Materials & Interfaces 11(33) (2019) 29924-29933.

[41] Y. Sun, L. Wang, Y. Li, Y. Li, H.R. Lee, A. Pei, X. He, Y. Cui, Design of Red Phosphorus Nanostructured Electrode for Fast-Charging Lithium-Ion Batteries with High Energy Density, Joule 3(4) (2019) 1080-1093.

[42] C. Kim, K.S. Yang, M. Kojima, K. Yoshida, Y.J. Kim, Y.A. Kim, M. Endo, Fabrication of Electrospinning-Derived Carbon Nanofiber Webs for the Anode Material of Lithium-Ion Secondary Batteries, Advanced Energy Materials 16(18) (2006) 2393-2397.

[43] A.M. Puziy, O.I. Poddubnaya, A. Martínez-Alonso, F. Suárez-García, J.M.D. Tascón, Surface chemistry of phosphorus-containing carbons of lignocellulosic origin, Carbon 43(14) (2005) 2857-2868.

[44] L. Daasch, D. Smith, Infrared spectra of phosphorus compounds, Analytical Chemistry 23(6) (1951) 853-868.

[45] X.-g. Yu, J.-y. Xie, J. Yang, H.-j. Huang, K. Wang, Z.-s. Wen, Lithium storage in conductive sulfur-containing polymers, Journal of Electroanalytical Chemistry 573(1) (2004) 121-128.

[46] S. Wei, L. Ma, K.E. Hendrickson, Z. Tu, L.A. Archer, Metal–sulfur battery cathodes based on PAN–sulfur composites, Journal of the American Chemical Society 137(37) (2015) 12143-12152.

[47] H.M. Kim, J.-Y. Hwang, D. Aurbach, Y.-K. Sun, Electrochemical properties of sulfurized-polyacrylonitrile cathode for lithium–sulfur batteries: effect of polyacrylic acid binder and fluoroethylene carbonate additive, The journal of physical chemistry letters 8(21) (2017) 5331-5337.

[48] R. McIvor, C. Hubley, Infrared spectra of organo-phosphorus compounds: III. phosphoramidates, phosphoramidothionates, and related compounds Canadian Journal of Chemistry 37(5) (1959) 869-876.

[49] P. Xiong, P. Bai, S. Tu, M. Cheng, J. Zhang, J. Sun, Y. Xu, Red Phosphorus Nanoparticle@ 3D Interconnected Carbon Nanosheet Framework Composite for Potassium-Ion Battery Anodes, Small 14(33) (2018) 1802140.

[50] S. Brauman, Chemiluminescence studies of the low temperature thermooxidation of poly (phenylene sulfide), Journal of Polymer Science Part A: Polymer Chemistry 27(10) (1989) 3285-3302.

[51] Z.-Q. Jin, Y.-G. Liu, W.-K. Wang, A.-B. Wang, B.-W. Hu, M. Shen, T. Gao, P.-C. Zhao, Y.-S. Yang, A new insight into the lithium storage mechanism of sulfurized polyacrylonitrile with no soluble intermediates, Energy Storage Materials 14 (2018) 272-278.

[52] S. Li, Z. Han, W. Hu, L. Peng, J. Yang, L. Wang, Y. Zhang, B. Shan, J. Xie, Manipulating kinetics of sulfurized polyacrylonitrile with tellurium as eutectic accelerator to prevent polysulfide dissolution in lithium-sulfur battery under dissolution-deposition mechanism, Nano Energy 60 (2019) 153-161.

[53] H. Al Salem, G. Babu, C. V. Rao, L.M.R. Arava, Electrocatalytic polysulfide traps for controlling redox shuttle process of Li–S batteries, Journal of the American Chemical Society 137(36) (2015) 11542-11545.

[54] N. Tanibata, H. Tsukasaki, M. Deguchi, S. Mori, A. Hayashi, M. Tatsumisago, A novel discharge–charge mechanism of a S–P 2 S 5 composite electrode without electrolytes in all-solid-state Li/S batteries, Journal of Materials Chemistry A 5(22) (2017) 11224-11228.

[55] C.-C. Chuang, Y.-Y. Hsieh, W.-C. Chang, H.-Y. Tuan, Phosphorus-sulfur/graphene composites as flexible lithium-sulfur battery cathodes with super high volumetric capacity, Chemical Engineering Journal 387 (2020) 123904.

[56] J. Yan, W. Li, P. Feng, R. Wang, M. Jiang, J. Han, S. Cao, K. Wang, K. Jiang, Enhanced Na+ pseudocapacitance in a P, S co-doped carbon anode arising from the surface modification by sulfur and phosphorus with C–S–P coupling, Journal of Materials Chemistry A 8(1) (2020) 422-432.

[57] X. Jiao, Y. Liu, T. Li, C. Zhang, X. Xu, O. Kapitanova, C. He, B. Li, S. Xiong, J. Song, Crumpled Nitrogen-doped Graphene Wrapped Phosphorus Composite as a Promising Anode for Lithium-Ion Batteries, ACS Applied Materials & Interfaces 11(34) (2019) 30858-30864.

[58] X. Li, G. Chen, Z. Le, X. Li, P. Nie, X. Liu, P. Xu, H.B. Wu, Z. Liu, Y. Lu, Well-dispersed phosphorus nanocrystals within carbon via high-energy mechanical milling for high performance lithium storage, Nano Energy 59 (2019) 464-471.

[59] D. Zhao, J. Zhang, C. Fu, J. Huang, D. Xiao, M.M.F. Yuen, C. Niu, Enhanced cycling stability of ring-shaped phosphorus inside multi-walled carbon nanotubes as anodes for lithium-ion batteries, Journal of Materials Chemistry A 6(6) (2018) 2540-2548.

[60] Y. Wu, S. Hu, R. Xu, J. Wang, Z. Peng, Q. Zhang, Y. Yu, Boosting potassium-ion battery performance by encapsulating red phosphorus in free-standing nitrogen-doped porous hollow carbon nanofibers, Nano letters 19(2) (2019) 1351-1358.

[61] S. Liang, X. Pei, W. Jiang, Z. Xu, W. Wang, K. Teng, C. Wang, H. Fu, X. Zhang, Free-standing dual-network red phosphorus@ porous multichannel carbon nanofibers/carbon nanotubes as a stable anode for lithium-ion batteries, Electrochimica Acta 322 (2019) 134696.

[62] H. Yang, Y. Li, P. Long, J. Han, C. Cao, F. Yao, W. Feng, Amorphous red phosphorus incorporated with pyrolyzed bacterial cellulose as a free-standing anode for high-performance lithium ion batteries, RSC Advances 8(31) (2018) 17325-17333.

5. On the Electrochemical Stability Analysis of Red Phosphorus-Based Anode for Lithium-Ion Batteries

5.1 Introduction

The rechargeable lithium-ion battery (LIB) is probably the most actively investigated type of modern batteries. Its basic design consists of (i) a negative and a positive electrode with open crystalline structure capable of repeatedly allowing the intercalation and de-intercalation of lithium ions, in addition to (ii) an ionic conducting and chemically stable electrolyte compressed between the two electrodes. (iii) An electronic insulating, porous membrane (separator) is placed between the two electrodes to prevent electrical shorts and provide mechanical stability of the cell while allowing ionic movements [1]. This type of intercalation battery is truly a multi-physics, multi-scale system that involves nonequilibrium thermodynamics, interfacial chemistry and electrochemistry, material science, thermofluidics, charge and mass transfers, electrolytics, etc. [2-4]. At a system level it can be viewed as an energy conversion system converting its stored chemical energy to electrical energy when connected to an external load, and quasi-reversibly converting the electrical energy provided by a power supply back to chemical energy [4]. In fact, LIBs are able to store high energy densities per unit mass and volume, which makes them the solution of choice for a wide array of applications including consumer electronics, medical devices [5], industrial systems [6], automobile [7], military equipment [8] and aerospace [9, 10].

Research and development on LIBs has been focused on engineering new materials and new structures and designs for the constituting electrodes. The goal is always geared

towards potential advantages in terms of cost-effectiveness, safety and reliability, and electrochemical performance during discharge. However, the behavior of batteries in use, which includes alternating charge and discharge sequences of different forms and nature, is also of great importance for real-world applications [1, 2, 11]. This includes aging and lifetime analysis as well as stability considerations.

In a recent paper [12], some of us showed the high lithium storage capability of a binder-free red phosphorus sulfurized polyacrylonitrile (RP-SPAN) composite anode material in LIB. The main motivation of using this structured electrode is that RP possesses a considerably high theoretical specific capacity of 2596 mA hg^{-1} (in the reaction $3Li + P \rightarrow Li_3P$) while being earth-abundant and inexpensive [13]. However, amorphous RP is also known to have a very low conductivity (~ 10^{-14} S cm^{-1} [14]) and can show very large volume changes (~ 300% [15, 16]) during lithiation/delithiation sequences. As a result, this causes significant electrode material pulverization, and destabilization and thickening of solid electrolyte interface (SEI) film, and as such fast capacity fading [17]. One of the main effective techniques to overcome these issues is compositing RP with conductive agents such as carbonaceous materials (e.g. graphene, graphene oxide, carbon black, and carbon nanotubes [13]), which confirmed improved specific capacity, cyclability, and rate capability of RP/C composite when compared to pure RP [18]. Although, different RP/C composites have been evaluated as anode materials for LIBs, their application at high current densities is still limited, maybe due to the unstable P-C chemical bonds. In our previous study [12], we confirmed that SPAN did not act as a carbon source only, but the high-energy ball milling process used for the preparation of the material allowed the interaction of RP with sulfur to form strong P-S chemical bonds, which improved the

overall conductivity. In addition, the RP-SPAN composite anode helped accommodating the volume expansion during cycling with an outstanding specific capacity of over 1600 mA hg^{-1} at 100 mAg^{-1} with good long-term cyclability [12].

However, the question on the stability of the RP-SPAN-based anode is still unclear, and that is the main purpose of this work. Broadly speaking, stability of a dynamic system means that the system output is bounded in response to a bounded excitation (bounded-input/bounded-output stability) or the system output tends to an equilibrium state (asymptotic stability). In addition, for the case of batteries, studies are usually on the degradation of the electrodes materials because of mechanical, chemical or structural changes during the processes of charge and discharge. Here, we first inspect the stability of the frequency-domain transfer function estimate of the battery response to small amplitude sinusoidal voltage excitations from 1 MHz down to 1 mHz. This assumes a priori that the battery can be viewed as an impedance block which is a characteristic property of linear and time-invariant systems. The results show that all poles of the transfer function lie in the left-half of the complex s-plane which implies indeed stability of the system. Moreover, the Kramers-Kronig (KK) integral analysis shows clear departure of the experimental spectral data from the KK-transformable real and imaginary parts, and magnitude and phase functions at very low frequencies (below 100 mHz), which indicates that the system is more likely nonlinear time-invariant The system is also dissipative given its goodness-of-fit with non-integer, fractional-order impedance functions. These characteristics of the battery were in line with time-domain measurements of differential capacity (with respect to voltage) obtained from low-frequency constant current charging/discharging over 200 consecutive cycles.

5.2 Materials and Methods

5.2.1 Materials Synthesis

First, sulfurized polyacrylonitrile (SPAN) was prepared from a mixture of polyacrylonitrile (PAN, Sigma Aldrich) and sulfur (Sigma Aldrich) at the mass ratio of 2:1, which were uniformly mixed by using a mortar and pestle for30 minutes. The mixture was then heated at 450°C in Ar atmosphere using a tube furnace with a ramping rate of 5°C min^{-1} for 15 minutes. Second, SPAN and pure red phosphorus (RP, Alfa Aesar) were mixed at the mass ratio of1:5 and placed in a stainless steel vessel which was sealed inside a glovebox under Ar atmosphere. Subsequently, ball milling of the RP-SPAN composite was carried out using a Retsch PM 100 planetary ball mill at 350 rpm and under a pressure of 100 bar for a duration of 36 hours (Figure 5.1 (a)).

For preparing the RP-SPAN composite anode on Ni foam (current collector), we employed the well-known electrostatic spray deposition (ESD) technique (Figure 5.1 (a)), which is also referred to as electrostatic spray pyrolysis (ESP) [12, 19-22]. The ESD precursor solution consisted of mixing RP-SPAN material (90 wt.%) with super-P Li (10 wt.%) and dispersing in 1,2-propanediol (no binding agent is needed), followed by stirring for one hour and transferring to a syringe. For the ESD setup, we placed a Ni foam substrate at a distance of 3 cm from the needle, and we applied a terminal voltage of about 6-7 kV between the substrate and the precursor solution. The electrode films were deposited at 200°C (temperature of the hotplate in Figure 5.1 (a)) with a flow rate of 2 ml h^{-1} for a duration of two hours, resulting in a visually uniform and mechanically stable coating. The mass of active materials was 0.4 mg. CR2032 type lithium-ion coin cell

consisting of RP-SPAN composite as the working electrode, and battery grade lithium foils (Alfa Aesar, purity 99.9%, thickness: 0.75mm) as both counter and reference electrodes (half-cell) was assembled in Ar-filled glovebox (less than 0.1 ppm of oxygen and water). A volume of 100 μl from 1 mol l^{-1} of $LiPF_6$ in ethylene carbonate-diethyl carbonate (1:1 volume ratio) was used as an electrolyte. Microporous Celgard 2400 polypropylene membrane of 25 μm thickness was used as a separator. The geometrical area of the electrode was 0.5 in.

5.2.2 Materials Characterization

The morphological and microstructural properties of the synthesized and deposited RP-SPAN hybrid sample was evaluated by scanning electron microscopy (SEM-JEOL 6330F) in the secondary electron imaging (SEI) mode, with energy-dispersive X-Ray spectroscopy (EDS-Ultra-Dry). Powder X-ray diffraction (XRD) analysis was conducted on a Siemens 500D X-ray diffractometer with Cu Ka (λ= 0:154178 nm) radiation. Raman spectroscopy measurements were performed using a 514 nm laser excitation source BaySpec Raman spectrometer.

5.2.3 Electrochemical Characterization

All electrochemical measurements were conducted at room temperature on a Bio-Logic VMP3 workstation. All potentials are reported vs. Li/Li^+. First, we measured the spectral response of the battery with frequency sweep method (1 mHz to 1 MHz) under potentiostatic mode at open-circuit voltage, and with different ac amplitudes: 5, 10, 20, 30, 40, and 50mV. Then, measurements were conducted with a constant ac amplitude of 20mV but at different dc voltage biases from 2.5 V down to 10 mV. Constant current

charge/discharge tests were carried out between the voltage limits 0.01 V and 3.0 V. Cyclic voltammetry was performed at scan rates from 1 to 10 mVs^{-1}, also within the voltage range of 0.01–3.0 V.

5.3 Results and Discussion

In Figure 5.1 (b-e) we show results obtained from the materials characterization by means of SEM, XRD and Raman spectroscopy. The SEM micrograph in Figure 5.1 (b) presents the microscopic features of a sample of RP-SPAN composite material collected right after ball-milling process. One can observe that the high-energy mechanical grinding and blending by impact and friction forces on the constituting components led to the formation of polydisperse microaggregates. Figure 5.1 (c) presents a lower magnification SEM image of the RP-SPAN film after ESD coating on Ni foam. With this technique, under a high enough dc voltage, the solution precursor is atomized at the small orifice of the nozzle, and hence a conical spray of material is generated and dragged towards the substrate by electrostatic force. Upon contact with the heated substrate (set to 200°C in this study), fast pyrolysis of the precursors takes place leaving a relatively thin and uniform deposit. Visually, the Ni foam substrate is uniformly covered with porous, network-like morphology of inter-connected micro particles which is expected to be beneficial for solute wetting and ion diffusion and migration in LIB cell.

XRD patterns of pure RP and RP-SPAN composite material are given in Figure 5.1 (d). For the RP sample, the relatively broad diffraction peaks are within the range of 14-17°, 26-35° and 46-54° confirming the medium-range ordered structures of RP [23]. For the composite sample, the graphitic hkl Miller plane (002) of amorphous carbon is detected

at around 25° in addition to three broader and weaker peaks of RP. From the Raman spectroscopy results depicted in Figure 5.1 (e), the RP signature response corresponds to the low-intensity and wide wavebands in the range of 300-500 cm^{-1}. Whereas for the hybrid sample, two additional prominent peaks are observed at 1367 and 1571 cm^{-1} corresponding to the D-band (disordered structure in carbon matrix) and G-band (E2g graphitic mode) of SPAN carbon source [24], respectively. The characteristic peaks of the S-S bond at around 499 and 957 cm^{-1} were also detected for the composite sample [25].

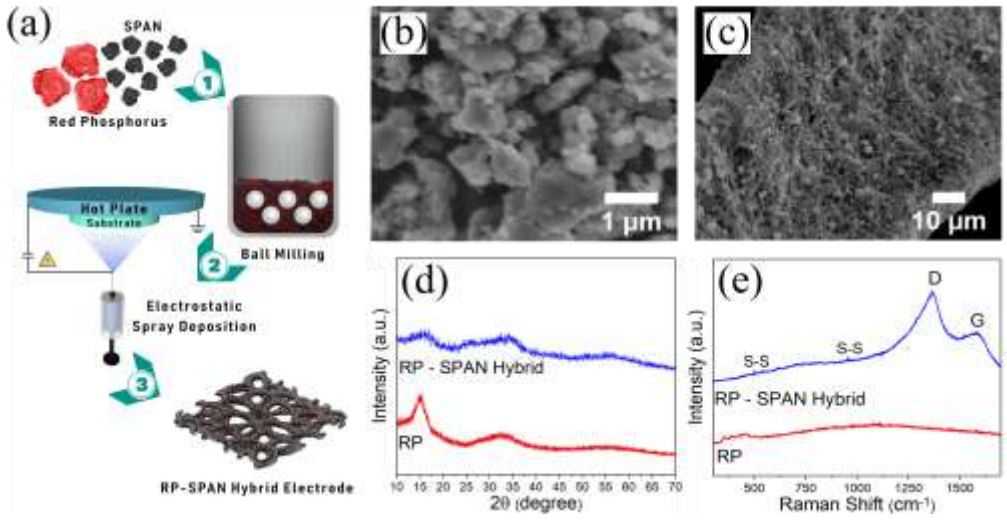

Figure 5.1: (a) Schematic of preparation procedure of RP-SPAN anode for LIB via ball-milling and electrostatic spray deposition; (b)-(c) SEM, (d) XRD, and (e) Raman spectroscopy characterization results of RF-SPAN composite material.

In Figure 5.2 we show results compiled from the spectral response of the battery half-cell measured at open-circuit voltage (zero net current flow) with steady-state sinusoidal voltage excitation (i.e. $v(t) = V_{dc} + V_{ac}\,\mathrm{Sin}(2\pi ft)$ with $V_{dc} = 0$). The spectral response of the system is described by the transfer function:

$$H(s) = \frac{F[v(t)]}{F[i(t)]} = \frac{V(s)}{I(s)} = H_r(s) + jH_i(s) \quad (5.1)$$

with F being the Fourier transform operator and s = j! is the Laplace complex number. These data cannot be considered as impedance data yet (see arguments below) which is characteristic of linear time-invariant (LTI) systems, and as such cannot be directly analyzed with equivalent (passive) circuit models. Figure 5.2 (a) presents the spectral data in the form of real vs. imaginary part (Nyquist plot) and Figure 5.2 (b) depicts the data in the form of magnitude and phase vs. frequency (Bode plot) using sinusoidal voltage excitations of different ac amplitudes from 10 to 50 mV (7.07 to 35.35 mV rms). The curves in both figures are relatively identical to each other whether a small 10 mV or a larger 50 mV perturbation is applied, which implies that the measurements are conducted within the linear regime of the battery cell at the operating open-circuit voltage (steady-state). Nonetheless, one can observe from the Nyquist plots increased variations between the measured real and imaginary parts of the data as the frequency is decreased. For example, for f = 1 mHz in Figure 5.2 (a) (outlined with red dashed rectangle), $(H_r;\ -H_i)$ = (14:783; 17:973) kΩ when using 10 mV ac perturbation and (16:006; 18:602) kΩ when using 50 mV, whereas for f = 521 mHz, we have much closer values, i.e. (0:2624; 0:3099) kΩ and (0:2766; 0:3189) kΩ, respectively.

We studied the stability of the transfer function estimate of the battery half-cell spectral response data acquired with 20 mV ac amplitude as an example, but similar results were found with the other ac magnitudes. This assumes a priori that the system is LTI. The estimation of the transfer function can be computed using either the function *tfest* or *fitfrd*

of MATLAB R2019b. We found that the data can be fitted with up to 98.3% normalized root mean squared error (NRMSE) with the following 4-poles, 4-zeros transfer function:

$$H_{est}(s) = \frac{42.62s^4 + 1389s^3 + 912.3s^2 + 47.92s + 0.3158}{s^4 + 1.454s^3 + 0.1771s^2 + 0.0031s + 3.941\times10^{-6}} \tag{5.2}$$

The system would be stable if and only if all of the poles in the partial fraction expansion occur in the left-half of the complex s-plane. Marginally stable parts correlate with a zero real part, and unstable parts to a positive real part. All 4 poles in Equation 5.2 are found to be negative (i.e. -1.3214, -0.1118, -0.0191, and -0.0014), that is they all lie in the left half of the complex s-plane, which confirms that the system stable around open-circuit voltage conditions.

Moreover, to properly assess the consistency of the measured data so that they qualify as impedance data (i.e. H(s) = Z(s)), it is necessary to apply the Kramers-Kronig (KK) transforms on the obtained results. Again, we take the spectral response acquired with 20 mV ac amplitude as an example (similar results were found using the other ac magnitude excitations). According to Kramers and Kronig, for causal, stable, linear time-invariant, and finite transfer functioned, one can calculate its imaginary part from its real part as [26, 27]:

$$\mathrm{Im}(Z_{KK}(\omega)) = -\frac{2\omega}{\pi}\int_0^\infty \frac{\mathrm{Re}(Z(x)) - \mathrm{Re}(Z(\omega))}{x^2 - \omega^2}dx \tag{5.3}$$

and its real part from its imaginary part as:

$$\mathrm{Re}(Z_{kk}(\omega)) = \mathrm{Re}(Z_{kk}(\infty)) + \frac{2}{\pi}\int_0^\infty \frac{x\,\mathrm{Im}(Z(x)) - \omega\,\mathrm{Im}(Z(\omega))}{x^2 - \omega^2}\,dx \tag{5.4}$$

if the high frequency asymptote for the real part is known, and as

$$\mathrm{Re}(Z_{kk}(\omega)) = \mathrm{Re}(Z_{kk}(0)) + \frac{2\omega}{\pi}\int_0^{\infty}\frac{(\omega/x)\,\mathrm{Im}(Z(x)) - \mathrm{Im}(Z(\omega))}{x^2-\omega^2}\,dx \tag{5.5}$$

if the zero-frequency asymptote for the real part is known. The results are shown in Figure 5.2 (c-f) in which the experimentally-measured real, imaginary, magnitude and phase of the transfer function are compared to those computed using the KK transforms ($Z_{KK}(s)$). It is clear that the data shows severe discrepancies with $Z_{KK}(s)$, and as such does not comply as a whole with the KK transforms and associated conditions. The impedance spectroscopy technique is recognized as a powerful tool for the characterization of electrical, thermal and aging behavior of batteries and other electrochemical systems. Unfortunately, the validation of the spectral data and their compliance with the KK transforms before proceeding with equivalent circuit modeling is often bypassed and overlooked in the literature. In particular, for our case, from Figure 5.2 (e, f) in which the relative deviations between the actual and KK-transformed measurable, i.e. $\Delta(\mathrm{Re}(Z))$, $\Delta(-\mathrm{Im}(Z))$, $\Delta(|Z|)$, and $\Delta(\phi(Z))$, are plotted vs. frequency, one can see that most of the discrepancies are localized at the low and high frequency tails, approximately below the 100 mHz and above 1 kHz limits. Thus, from the results of Figure 5.2, we can expect some forms of nonlinearities and/or instabilities at the extremities of the covered frequency range, and as such the transfer function may be identified as the impedance $Z(s)$ of the half-cell battery system only within the range of 100 mHz to 1 kHz [28]. Nonetheless, we recognize that errors in the estimation of the KK functions are

unavoidable at extreme (low and high) frequencies given that a low number of discrete data points are used for approximating the continuous KK functions, which require the integrations to be carried out from zero to infinity. Thus, in connection with the result found from the transfer function estimate and the KK transforms analyses, we may conclude at this point that at low frequencies (below the 100 mHz limit and at which batteries are expected to operate) the system is either nonlinear (but stable) or time variant or both. These two situations violate the validity conditions of the KK transforms. The time variance of the battery may appear at low frequencies because the measurement time is significantly long (e.g. 1000 seconds at 1 mHz). During this time, chemical and structural changes may still be active rendering the impedance time-varying as well. The high frequency region of the spectrum is usually assumed to be related to the electrolyte system, and we will not focus on it in this study. The main findings resulting from the spectral measurements carried out different dc biases from 2.5 V down to10 mV (not shown here) were relatively similar to those reported at open-circuit voltage.

Now that we have established that the measured frequency response H(s) may be identified as the impedance Z(s) of the battery half-cell configuration only within the intermediate frequency range 100 mHz to 1 kHz, it is safe to utilize the equivalent circuit model approach with the data [27]. We applied complex nonlinear least squares (CNLS) fitting of the data (from 109 mHz to 878 Hz) collected at open circuit voltage with 20 mV ac amplitude (taken as an example, but comparable results were found for the other ac amplitudes) to the double-dispersion, fractional-order impedance Cole-Cole function:

$$Z_{cc}(s) = R_s + \sum_{i=1}^{2} \frac{R_{Pi}}{1 + R_{Pi} s^{\alpha_i} C_{\alpha_i}} \tag{5.6}$$

This model, in which $1/s^{\alpha_i}C_{\alpha_i}$ corresponds to the impedance of a fractional-order capacitor or constant phase element(CPE), is known to be able to simulate with high fidelity the impedance of LIBs [29], and other energy materials and devices [30, 31]. The values of $\{R_s, C_{\alpha_1}, \alpha_1, R_{p_1}, C_{\alpha_2}, \alpha_2, R_{P_2}\}$ (Equation 6.2) where found to be 8.264 Ω, 0.043 $mFs^{-0.128}$, 0.769, 192 Ω, 1.111 $mFs^{-0.128}$, 0.873, and 11.246 kΩ, respectively with high degree of accuracy $(X^2/|Z| = 2.473\times10^{-3})$. We deduct from these values, and in particular from the values of $\alpha_i \neq 1$, that the system is dispersive (non-ideal) with built-in memory effects [32-34]. This can be attributed to the porous (open) structure and nature of the RP-SPAN electrode material. The polydisperse distribution of particles in the composite electrode (Figure 5.1 (a, b)) are self-arranged in a highly dimensional network along the thickness, and as such form interconnected spaces with irregular sizes. Such spatial features and their different length scales have direct implications on the electrical parameters of the cell and render them highly frequency-dependent [32, 35]. This deviation from regular RC semi-circles (Figure 5.2 (a)) is usually recognizable from relatively common features of LIBs: i.e. (i) the depressed mid-frequency arc which is due to the resistance/pseudocapacitance (fractional-order capacitance) associated with charge transfer processes and chemical/electrochemical reactions taking place during battery operation, and (ii) the inclined low-frequency branch which is attributed to solid-state diffusion and battery capacity [29]. Furthermore, one can compute an equivalent time constant for the high-frequency loop as $\tau_1 = (R_{P_1}C_{\alpha_1})^{1/\alpha_1} = 1.95\,\text{ms}$ (i.e. 511 Hz), and

similarly an equivalent time constant for the low-frequency arc as $\tau_2 = (R_{P_2} C_{\alpha_2})^{1/\alpha_2} = 18.0$ s (i.e. 55 mHz).

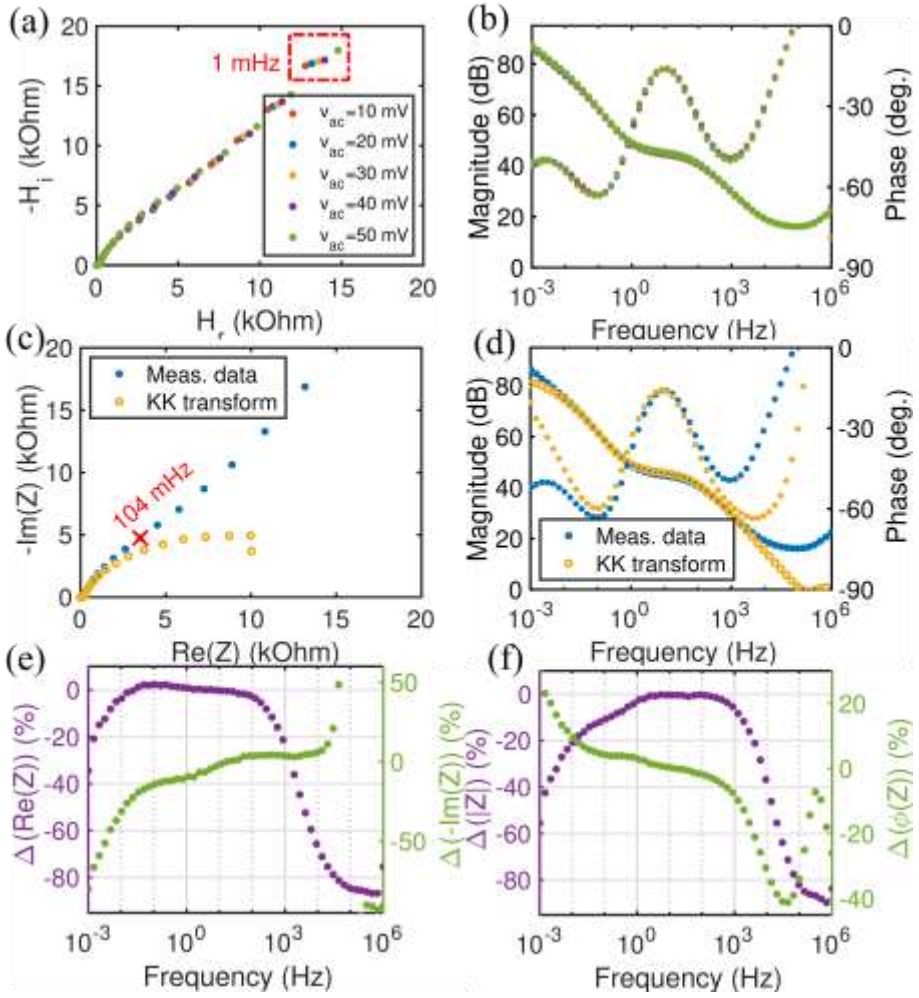

Figure 5.2: Spectral response results of RP-SPAN-based anode: (a) Nyquist plots and (b) Bode plots of data measured at V_{dc} = 0 with different values of ac sine perturbation, (c) Nyquist plots and (d) Bode plots of data measured at V_{dc} = 0 with V_{ac} = 20 mV compared to those computed with the Kramers and Kronig (KK) transforms. In (e) and (f) we illustrate the relative deviation of real and imaginary parts, and magnitude and phase of the measured data from those computed with the KK transforms.

Additional information on the dynamic behavior and stability of the RP-SPAN electrode for LIBs application can be deducted from time-domain measurements. In Figure 5.3 we show the battery response to an instantaneous step current from 45 mA down to zero. The device's voltage was increased and limited to 3 V during the charging period (t < 0 in the

figure), after which the cell was disconnected from the power amplifier of the electrochemical station, and the rest voltage was measured for up to 48 hours ($t > 0$ in the figure). It is clear that the relaxation voltage follows initially a power-law decay with time, and then rebounds to asymptotically tend to a stable, steady-state value of 2 V. However, the time needed for the quasi steady-state equilibration of the cell extends to more than 24 hours which leads to the conclusion that the system is still electrochemically evolving during this transition period with possible formation for instance of new crystalline structures. This further confirms that the prerequisite of stationarity is not strictly fulfilled when shorter measurements are conducted (1.88 hours to scan the frequency range 1 mHz to 1 MHz), and is in line with the fact that the low-frequency spectral data is not KK-compliant as shown in Figure 5.2.

In Figure 5.4, we present the results obtained from 200 consecutive cycles of charge/discharge using ±95 mA with the voltage limits set to 0.01 V and 3.0 V. Because of these two limiting values on the allowed potential window, it is understood that the excitation signal is not necessarily stationary because of capacity fading as we go with the measurements. This will render the duration of the charge/discharge periods shorter and shorter with time. Discrete Fourier transform of the signal is given in Figure 5.4 (a), and shows that most of the signal's power is nonetheless concentrated at the low frequencies end, below 0.2 mHz (the lower limit of spectral response of the battery half-cell system was set to 1 mHz). However, in order to fully capture how the square wave current excitation evolves with time, we carried out time-frequency analysis of the current signal as shown in the joint time-frequency spectrogram in Figure 5.4 (b). The spectrum is estimated over sliding windows; (stationarity is assumed in each window)

using short-time Fourier transform (STFT). The figure confirms that the signal's power is mostly in the very low frequencies but with some contributions from higher frequencies that tend to show up at higher cycle numbers (see the increase in concentration of green or magenta colors with time for a fixed frequency). The FFT and spectrogram results of time-domain voltage response are provided in Figure 5S.1 from which the same conclusions can be drawn.

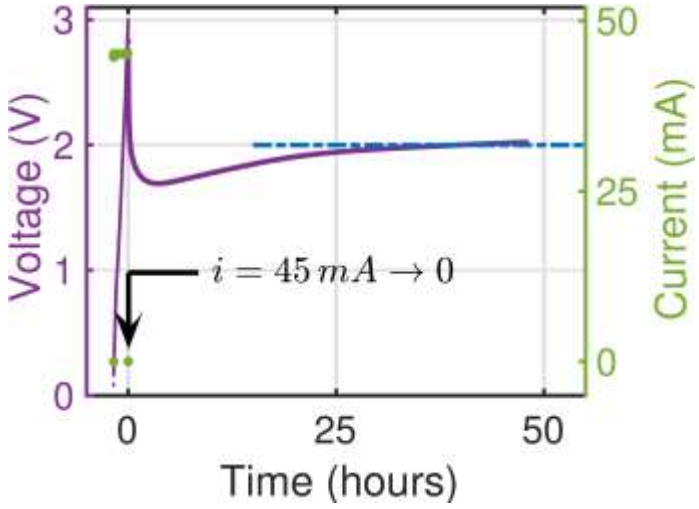

Figure 5.3: Rest voltage of RP-SPAN-based anode in response to step current from 45 to 0 mA.

We computed the differential capacity with respect to voltage, dQ/dV, from the alternating current steps ±95 mA test results. Differential capacity analysis (and its inverse, differential voltage dV/dQ, or delta differential capacity analysis [36]) is known to offer greater sensitivity than those based on traditional capacity vs. voltage measurements, and can probe much better the cell degradation with continuous cycling. Figure 5.4 (c) depicts the change in dQ/dV vs. voltage for different cycle numbers from 3 to 200. The fading of several peaks in the dQ/dV profiles with continued cycling from cycle #3 to cycle #100, whether during the charge or discharge of the battery, might be associated with active material loss and side reactions. This is somehow expected

because RP is known to undergo large volume expansion (more than 300% [15, 16]) during repeated lithium insertion and extraction causing the disintegration of the electrode's active materials. This leads to the structural destabilization or delamination of the solid-electrolyte interphase (SEI) film and the deterioration of proper electrical contact with the current collector [16]. In addition, the reduction in sulfur content, possibly by dissolution into the electrolyte (compare EDX elemental mapping results obtained from on a fresh and cycled RP-SPAN in Figure 5S.2 and 5S.3), could be another capacity fading reason during cycling [37-39]. However, we did not observe any detectable peak shifting to higher potentials for the first few cycles, which is usually an observable attributed to SEI growth and/or electrolyte oxidation [36]. We also remarked a relatively negligible change in the magnitude of dQ/dV between cycle #100 to cycle #200. This may indicate that the cell reached some sort of an endurance plateau that can be better visualized from the coulombic efficiency results presented in Figure 5.4 (d). It is clear that from cycle #75 onwards, the coulombic efficiency of the cell flattens and remains constant at approximately 103%. Nonetheless, there is a gradual capacity fading that seems to slow down after ~150 consecutive cycles (in average 0.21% loss of discharge capacity per cycle), which is due to the gradual competition between irreversible electrochemical processes and reversible lithium intercalation in the electrode [40].

We recall that the battery half-cell of this study consists of RP-SPAN lithium-ion insertion anode on the one hand, and concentrated solution of LiPF6 in ethylene carbonate-diethyl carbonate on the other hand. This means that the measurement of spectral response using stepped-frequency sinusoidal voltage from 1 mHz to 1 MHz (Fig.

2) will excite the cell's electrochemical adsorption and intercalation/deintercalation processes at all these frequencies. This takes up to 1.88 hours in measurement time. We can assume for instance the system of three reversible elementary steps [3]:

$$Li_E^+ + \Sigma_E \rightleftharpoons Li_{E.ads}^+ + \Omega_E \quad (5.7)$$

$$Li_{E,ads}^+ + e_{e,ads}^- + \Sigma_\alpha \rightleftharpoons Li_{a,ads} + \Sigma_E \quad (5.8)$$

$$Li_{a,ads} + \Omega_a \rightleftharpoons Li_a + \Sigma_a \quad (5.9)$$

where the subscripts "a", "E" and "ads" refer to the anode, electrolyte and surface adsorption, respectively, whereas Σ and Ω indicate surface vacancy and volume vacancy, respectively [3]. Reactions 5.7 and 5.8 describe the adsorption of lithium ions from the electrolyte onto the active electrode material coupled with electronic charge transfer, and reaction 9 describes the intercalation of the surface-adsorbed lithium atom into the bulk [41]. These reactions are interdependent, can take place at overlapping time scales and at different locations in the porous electrode/electrolyte interface, and can be accompanied with irreversible processes such as the formation of new crystalline structures and irreversible transformations [4]. In addition, the reactions rates depend on the state of charge, capacity, aging conditions of the battery as well as the type and structure of charging/discharging waveforms. The thermal decomposition of the $LiPF_6$ based electrolyte and the resulting adverse effects on its frequency-dependent conductivity and permittivity can also play significant roles in the overall electrical response of the cell [42-44]. Therefore, it is understood that since the spectral response is the result of cumulative signals originating from the different constituting elements of the battery, it is very difficult to identify their individual contributions from such

measurements. These effects are due not just to the responses of electrodes, supporting electrolyte and separator where multiple transport processes of charge, mass, and energy, as well as chemical and electrochemical reactions are taking place, but also to eventual impedance artifact due to battery peripherals such as current collectors and leads. Nonetheless, it is always instructive to characterize the system-level spectral response of the cell, especially when it can be qualify as an impedance and be simulated with equivalent circuit models as done using Eq. 6. The analysis provided also the information that the LIB cell's frequency response is not KK-compliant at low frequencies and as such maybe in breach of the conditions of stationarity and/or nonlinearity. It is not always correct to directly interpret the ratio of measured voltage to measured current at these frequencies as an impedance, which by definition is valid only for linear time-invariant systems. Figure 5.5 shows the current vs. voltage and capacity vs. voltage profiles of the battery half-cell in response to triangular charging/discharging waveforms at different scan rate from 1 to 10 mVs^{-1}. The cathodic and anodic peaks from the CV plots at around 0.6 V and 1.1 V are clear even at high scan rates which correspond to the intercalation/deintercalation of Li ion into the P-based electrodes. These results demonstrate clearly high degree of nonlinearities, asymmetry in charge-voltage profiles and general hysteresis effects [45].

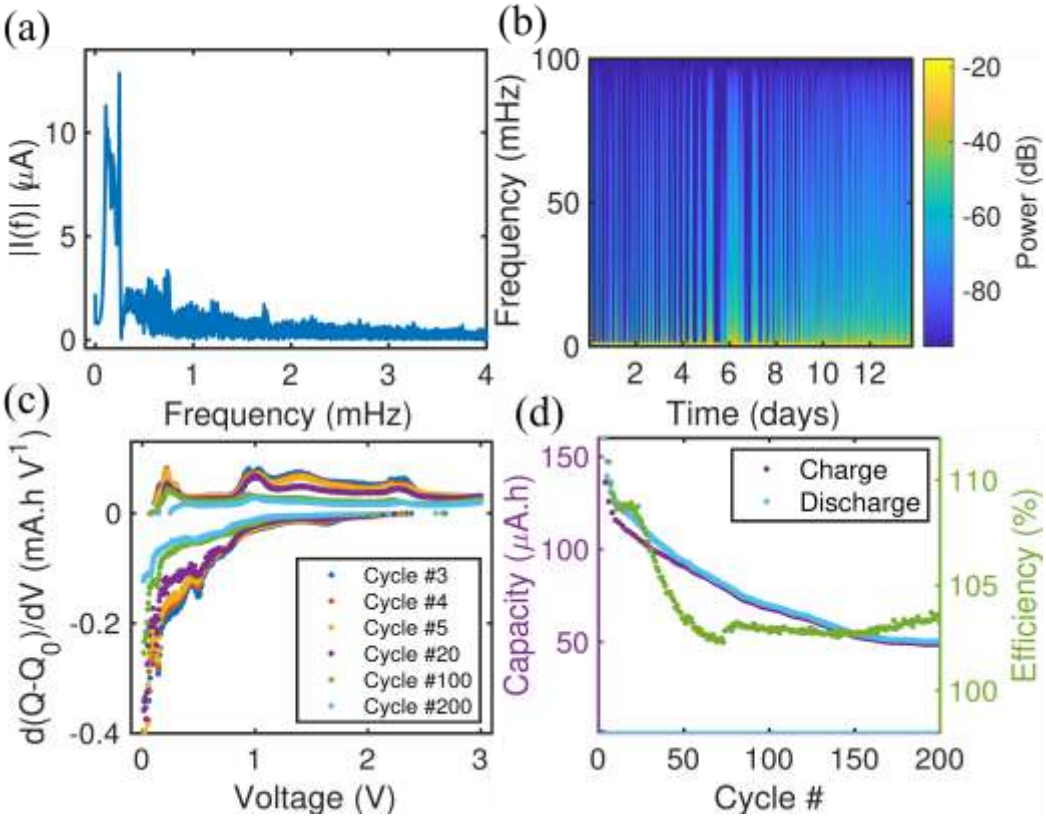

Figure 5.4: Results compiled from constant current -95 mA charging/discharging of RP-SPAN-based anode: (a) FFT of the time-domain input current signal; (b) spectrogram computed using short-time Fourier transform (STFT) which depicts the frequency content of the input current signal as it varies with time; (c) plots of differential capacity dQ/dV of the battery with respect to voltage for different cycles; (d) plots of the evolution of the battery capacity during charge and discharge, and the resulting coulombic efficiency vs. cycle number.

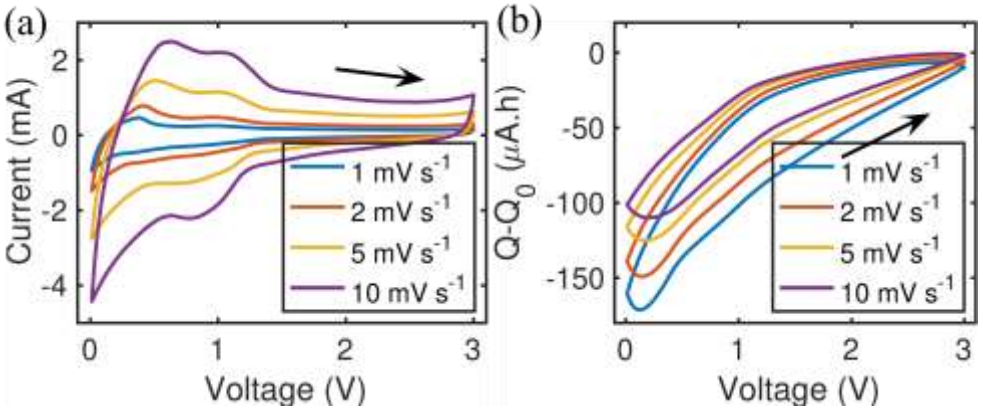

Figure 5.5: Cyclic voltammetry results of RP-SPAN-based anode at different low-frequency voltage scan rates: (a) current vs. voltage profiles; (b) capacity vs. voltage profiles.

At lower frequencies where batteries are usually operated at, other subsequent processes, such as the formation of new crystalline structures, can become the limiting kinetic steps [28]. The battery's behavior below the 100 mHz limit cannot be modeled with passive linear circuitry, and one may need other modeling tools such as active and nonlinear circuitry as recently shown for the low-frequency inductive loop in perovskite solar cells [30]. Referring to the measured phase angle (see Figure 5.2 (b)) which is always negative below 100 mHz, the possibility of inductive behavior is excluded [30]. Negative resistances or negative capacitances (or more generally negative impedances) are known to be obtainable from active, power-consuming circuits such as voltage-controlled voltage sources (VCVS) or current-controlled voltage sources (CCVS). A schematic of an equivalent circuit model of the battery is shown in Figure 5.6, wherein the voltage source and impedance block (Equation 5.6) are nonlinear and depend on the state-of-charge (SOC), C-rate, operating frequency, state-of-health (SOH) and age, temperature, etc. [46]. Further investigations are ongoing on this point.

However, a modified CPE function can be used to fit and interpret the low-frequency spectral data instead of developing nonlinear models. The modified CPE impedance is given as:

$$\mathrm{Z}_{\alpha,\beta} = \frac{1}{j^{\alpha}(\tau\omega)^{\beta}} \tag{5.10}$$

instead of the classical CPE impedance $\mathrm{Z}_{\alpha} = 1/(\tau j\omega)^{\alpha}$. In this three-parameter CPE function, the magnitude and phase are actually decoupled from each other (and as a consequence the real and imaginary parts), which renders the fitting of spectral response to do not be constrained by the KK transform rules. We verified the superiority of the

modified CPE compared to the classical one as shown in Fig. 6. The fitting parameters obtained by flower pollination algorithm are found to be $\alpha = 0.572, \beta = 0.637, \tau = 0.218 \times 10^{-6}$. This modified, linear CPE function can be viewed as roundabout way to model non-KK compliant data. Further investigations on the physical interpretation of the double-exponent CPE model are underway.

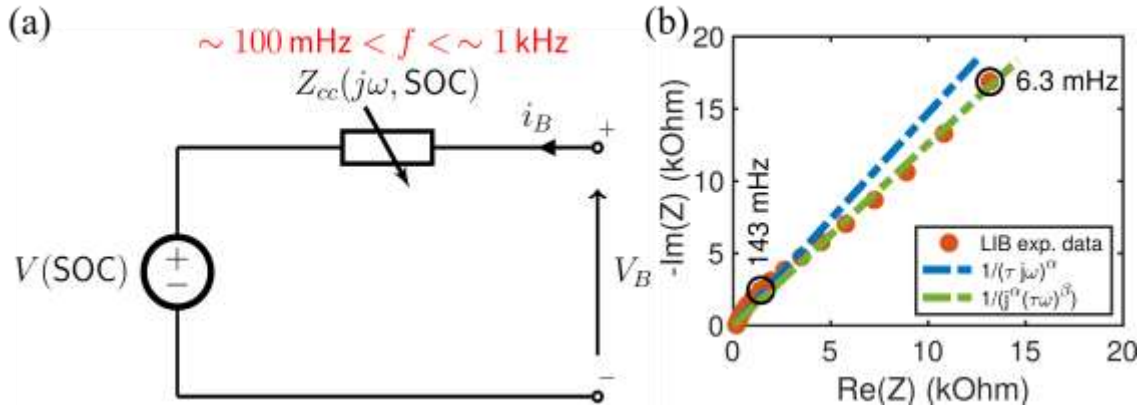

Figure 5.6: (a) Equivalent electric circuit model of RP-SPAN-based anode for LIB applications. (b) Fitting of spectral response data of using a standard CPE impedance compared to a modified CPE impedance given by equation 5.10.

5.4 Conclusion

In this chapter we investigated RP-SPAN-based anode spectral response to small-amplitude sinusoidal voltage excitations, and its time-domain constant-current charge/discharge dynamics in order to assess its stability, linearity/nonlinearity and time variance/invariancce. Low-frequency spectral data were found to be violating the KK transforms which indicates that the battery is either nonlinear or time-invariant or both. Nonlinearity arises from the existence of active processes within the cell (e.g. voltage-controlled voltage sources or current-controlled current sources) which are necessary to explain the appearance of inductive behavior [30] or the appearance of negative

impedances (this work) at low frequencies. On the other hand, time invariance can be easily violated at low frequencies due to the very long measurement time resulting from the frequency-sweep measurement technique employed in impedance analyzers. During this long measurement time (e.g. 1000 seconds at 10 Hz) irreversible chemical and electrochemical reactions may take place, hence changing the structural composition and properties of the material under test. Other impedance measurement methods such as those based on wide-band random excitations could be better measurement alternatives in order to reduce the measurement time while covering a wide frequency range [47]. It should be noted however that the KK transform itself requires caution when applying it at low frequencies due to the well-known tails problem. The error in calculating the imaginary part of an impedance from its real part (or vice versa) at a given frequency point depends on the amount of data points available to execute the computations. As a rule of thumb, data measured in the frequency range f_{min} to f_{max} implies that the KK transform can be accurately computed in the frequency range10 f_{min} to 0:1 f_{max} without showing tail frequency errors. This again suggests that the frequency-sweep measurements at very low frequencies are not optimal and should preferably be replaced by wide-band noise-like excitation signal measurement techniques that can guarantee a much larger number of data points to enable the accurate computation of the KK transform. Time-domain results, whether the differential capacity (with respect to voltage) as a function of both voltage and cycle number (from constant-current charging/discharging sequences) or cyclic voltammetry, are in line with the those found from spectral measurements. Nonlinearities and time-variance of the cell performance are clearly illustrated in Figure 5.4 and Figure 5.5. A modified CPE function given in

Equation 5.10 is proposed as an alternative model to fit such type of non-KK-compliant data.

5.5 References

[1] R. Korthauer, Lithium-ion batteries: basics and applications, Springer2018.

[2] K.S. Hariharan, P. Tagade, S. Ramachandran, Mathematical Modeling of Lithium Batteries: From Electrochemical Models to State Estimator Algorithms, Springer2017.

[3] M. Landstorfer, T. Jacob, Mathematical modeling of intercalation batteries at the cell level and beyond, Chemical Society Reviews 42(8) (2013) 3234-3252.

[4] M.Z. Bazant, Theory of chemical kinetics and charge transfer based on nonequilibrium thermodynamics, Accounts of chemical research 46(5) (2013) 1144-1160.

[5] D.C. Bock, A.C. Marschilok, K.J. Takeuchi, E.S. Takeuchi, Batteries used to power implantable biomedical devices, Electrochimica acta 84 (2012) 155-164.

[6] T.A. Stuart, W. Zhu, Modularized battery management for large lithium ion cells, Journal of Power Sources 196(1) (2011) 458-464.

[7] S. Sripad, V. Viswanathan, Evaluation of current, future, and beyond Li-ion batteries for the electrification of light commercial vehicles: challenges and opportunities, Journal of The Electrochemical Society 164(11) (2017) E3635.

[8] A.-A. Mamun, Z. Liu, D.M. Rizzo, S. Onori, An integrated design and control optimization framework for hybrid military vehicle using lithium-ion battery and supercapacitor as energy storage devices, IEEE Transactions on Transportation Electrification 5(1) (2018) 239-251.

[9] C.S. Rustomji, Y. Yang, T.K. Kim, J. Mac, Y.J. Kim, E. Caldwell, H. Chung, Y.S. Meng, Liquefied gas electrolytes for electrochemical energy storage devices, Science 356(6345) (2017).

[10] X. Dong, Z. Guo, Z. Guo, Y. Wang, Y. Xia, Organic batteries operated at− 70 C, Joule 2(5) (2018) 902-913.

[11] M. Wood, J. Li, R.E. Ruther, Z. Du, E.C. Self, H.M. Meyer III, C. Daniel, I. Belharouak, D.L. Wood III, Chemical stability and long-term cell performance of low-cobalt, Ni-Rich cathodes prepared by aqueous processing for high-energy Li-Ion batteries, Energy Storage Materials 24 (2020) 188-197.

[12] A.R. Baboukani, I. Khakpour, E. Adelowo, V. Drozd, W. Shang, C. Wang, High-performance red phosphorus-sulfurized polyacrylonitrile composite by electrostatic spray deposition for lithium-ion batteries, Electrochimica Acta (2020) 136227.

[13] W. Liu, H. Zhi, X. Yu, Recent progress in phosphorus based anode materials for lithium/sodium ion batteries, Energy Storage Materials 16 (2019) 290-322.

[14] P. Extance, S. Elliott, Pressure dependence of the electrical conductivity of amorphous red phosphorus, Philosophical Magazine B 43(3) (1981) 469-483.

[15] N. Yabuuchi, Y. Matsuura, T. Ishikawa, S. Kuze, J.Y. Son, Y.T. Cui, H. Oji, S. Komaba, Phosphorus Electrodes in Sodium Cells: Small Volume Expansion by Sodiation and the Surface-Stabilization Mechanism in Aprotic Solvent, ChemElectroChem 1(3) (2014) 580-589.

[16] J. Qian, X. Wu, Y. Cao, X. Ai, H. Yang, High capacity and rate capability of amorphous phosphorus for sodium ion batteries, Angewandte Chemie 125(17) (2013) 4731-4734.

[17] Y. Kim, Y. Park, A. Choi, N.S. Choi, J. Kim, J. Lee, J.H. Ryu, S.M. Oh, K.T. Lee, An amorphous red phosphorus/carbon composite as a promising anode material for sodium ion batteries, Advanced materials 25(22) (2013) 3045-3049.

[18] G. Wang, F. Li, D. Liu, D. Zheng, C.J. Abeggien, Y. Luo, X.-Q. Yang, T. Ding, D. Qu, High performance lithium-ion and lithium–sulfur batteries using prelithiated phosphorus/carbon composite anode, Energy Storage Materials 24 (2020) 147-152.

[19] X. Li, C. Wang, Engineering nanostructured anodes via electrostatic spray deposition for high performance lithium ion battery application, Journal of Materials Chemistry A 1(2) (2013) 165-182.

[20] A.R. Baboukani, E. Adelowo, R. Agrawal, I. Khakpour, V. Drozd, W. Li, C. Wang, Electrostatic spray deposited Sn-SnO2-CNF composite anodes for Lithium ion storage, ECS Transactions 85(13) (2018) 331.

[21] R. Agrawal, A.R. Baboukani, C. Wang, Expanding the potential window of aqueous electrochemical capacitors with binder-free electrostatically sprayed manganese oxide composite cathode films, Materials Research Express 6(8) (2019) 085012.

[22] E. Adelowo, A.R. Baboukani, C. Chen, C. Wang, Electrostatically sprayed reduced graphene oxide-carbon nanotubes electrodes for lithium-ion capacitors, C—Journal of Carbon Research 4(2) (2018) 31.

[23] W.-J. Li, S.-L. Chou, J.-Z. Wang, H.-K. Liu, S.-X. Dou, Simply mixed commercial red phosphorus and carbon nanotube composite with exceptionally reversible sodium-ion storage, Nano letters 13(11) (2013) 5480-5484.

[24] J. Song, Z. Yu, M.L. Gordin, S. Hu, R. Yi, D. Tang, T. Walter, M. Regula, D. Choi, X. Li, Chemically bonded phosphorus/graphene hybrid as a high performance anode for sodium-ion batteries, Nano letters 14(11) (2014) 6329-6335.

[25] L. Shi, Y. Liu, W. Wang, A. Wang, Z. Jin, F. Wu, Y. Yang, High-safety lithium-ion sulfur battery with sulfurized polyacrylonitrile cathode, prelithiated SiOx/C anode and carbonate-based electrolyte, Journal of Alloys and Compounds 723 (2017) 974-982.

[26] B.A. Boukamp, Practical application of the Kramers-Kronig transformation on impedance measurements in solid state electrochemistry, Solid State Ionics 62(1-2) (1993) 131-141.

[27] M. Urquidi-Macdonald, S. Real, D.D. Macdonald, Applications of Kramers—Kronig transforms in the analysis of electrochemical impedance data—III. Stability and linearity, Electrochimica Acta 35(10) (1990) 1559-1566.

[28] E. Barsoukov, J.R. Macdonald, Impedance Spectroscopy Theory, Experiment, and, Applications, 2nd ed.(Hoboken, NJ: John Wiley &Sons, Inc., 2005) (2005).

[29] Y. Xie, J. Li, C. Yuan, Mathematical modeling of the electrochemical impedance spectroscopy in lithium ion battery cycling, Electrochimica acta 127 (2014) 266-275.

[30] D. Zhang, A. Allagui, A.S. Elwakil, Z. Yan, H. Lu, Active circuit model of low-frequency behavior in perovskite solar cells, Organic Electronics 85 (2020) 105804.

[31] A. Allagui, A.S. Elwakil, B.J. Maundy, T.J. Freeborn, Spectral capacitance of series and parallel combinations of supercapacitors, ChemElectroChem 3(9) (2016) 1429-1436.

[32] A. Allagui, H. Alnaqbi, A.S. Elwakil, Z. Said, A.A. Hachicha, C. Wang, M.A. Abdelkareem, Fractional-order electric double-layer capacitors with tunable low-frequency impedance phase angle and energy storage capabilities, Applied Physics Letters 116(1) (2020) 013902.

[33] A. Allagui, D. Zhang, A.S. Elwakil, Short-term memory in electric double-layer capacitors, Applied Physics Letters 113(25) (2018) 253901.

[34] A. Allagui, D. Zhang, I. Khakpour, A.S. Elwakil, C. Wang, Quantification of memory in fractional-order capacitors, Journal of Physics D: Applied Physics 53(2) (2019) 02LT03.

[35] A. Mistry, K. Smith, P.P. Mukherjee, Stochasticity at Scales Leads to Lithium Intercalation Cascade, ACS Applied Materials & Interfaces 12(14) (2020) 16359-16366.

[36] A. Smith, J. Dahn, Delta differential capacity analysis, Journal of The Electrochemical Society 159(3) (2012) A290.

[37] R. Mukkabla, M.R. Buchmeiser, Cathode materials for lithium–sulfur batteries based on sulfur covalently bound to a polymeric backbone, Journal of Materials Chemistry A 8(11) (2020) 5379-5394.

[38] X. Wang, Y. Qian, L. Wang, H. Yang, H. Li, Y. Zhao, T. Liu, Sulfurized polyacrylonitrile cathodes with high compatibility in both ether and carbonate electrolytes for ultrastable lithium–sulfur batteries, Advanced Functional Materials 29(39) (2019) 1902929.

[39] M. Safa, Y. Hao, A. Chamaani, E. Adelowo, N. Chawla, C. Wang, B. El-Zahab, Capacity fading mechanism in lithium-sulfur battery using poly (ionic liquid) gel electrolyte, Electrochimica Acta 258 (2017) 1284-1292.

[40] M.B. Pinson, M.Z. Bazant, Theory of SEI formation in rechargeable batteries: capacity fade, accelerated aging and lifetime prediction, Journal of the Electrochemical Society 160(2) (2012) A243.

[41] F. Hall, S. Wußler, H. Buqa, W.G. Bessler, Asymmetry of discharge/charge curves of lithium-ion battery intercalation electrodes, The Journal of Physical Chemistry C 120(41) (2016) 23407-23414.

[42] T.-F. Yi, Y. Xie, Y.-R. Zhu, R.-S. Zhu, H. Shen, Structural and thermodynamic stability of Li4Ti5O12 anode material for lithium-ion battery, Journal of Power Sources 222 (2013) 448-454.

[43] B. Ravdel, K. Abraham, R. Gitzendanner, J. DiCarlo, B. Lucht, C. Campion, Thermal stability of lithium-ion battery electrolytes, Journal of Power Sources 119 (2003) 805-810.

[44] C.L. Campion, W. Li, B.L. Lucht, Thermal decomposition of LiPF6-based electrolytes for lithium-ion batteries, Journal of the Electrochemical Society 152(12) (2005) A2327.

[45] M.E. Fouda, A. Allagui, A.S. Elwakil, S. Das, C. Psychalinos, A.G. Radwan, Nonlinear charge-voltage relationship in constant phase element, AEU-International Journal of Electronics and Communications 117 (2020) 153104.

[46] M. Bahramipanah, D. Torregrossa, R. Cherkaoui, M. Paolone, Enhanced equivalent electrical circuit model of lithium-based batteries accounting for charge redistribution,

state-of-health, and temperature effects, IEEE Transactions on Transportation Electrification 3(3) (2017) 589-599.

[47] S. Majzoub, A. Allagui, A.S. Elwakil, Fast Spectral Impedance Measurement Method Using a Structured Random Excitation, IEEE Sensors Journal (2020).

6. Single-Step Exfoliation of Black Phosphorus and Deposition of Phosphorene via Bipolar Electrochemistry for Capacitive Energy Storage Application

6.1 Introduction

Alongside with graphene and its fascinating properties [1], other two-dimensional (2D) materials, such as transition metal oxides [2], layered transition metal dichalcogenides (TMDs) [3], and boron nitride [4] have stimulated significant research interest for next-generation electronic and optoelectronic devices because of their outstanding structural and physical properties [5-7]. Among all 2D materials, graphene has the highest charge carrier mobility (up to 100,000 $cm^2 V^{-1} s^{-1}$), but its zero bandgap prohibits its operation as a semiconducting material in electronic applications [8, 9]. Molybdenum disulphide presents a remarkable bandgap but suffers from limited carrier mobility [10]. Recently, black phosphorus (BP), which was discovered by Bridgman back in 1914 [11], has recaptured attention due to its promising physical and chemical properties [12-14]. In terms of structure, which is similar to graphite, strong P-P covalent bonds in each layer of BP form a puckered honeycomb structure, and neighbouring layered BP nanosheet (known as a phosphorene) adhered together with a weak van der Waals interlayer interactions (see Figure 6S.1) [15]. BP is a p-type semiconductor which shows a tuneable direct bandgap in a desirable range from 0.3 eV for bulk to 2.0 eV for a few-layer BP [16, 17], high carrier mobility (up to 1000 $cm^2 V^{-1} s^{-1}$) [18], and acceptable mechanical flexibility compared to the other 2D materials [19]. Furthermore, BP is the most stable allotrope of phosphorus compared to the white

phosphorus and red phosphorus (RP) [20]. These exclusive properties suggest the possible usage of phosphorene in nanoelectronics and optical devices. Additionally, due to its high surface area and high theoretical capacity, phosphorene is viewed as a great candidate for electrochemical energy storage devices, such as batteries and supercapacitors [21, 22].

According to theoretical studies and experimental characterizations [23], the real application of BP depends on the method of preparation and exfoliation of few-layer phosphorene from the bulk material [24]. To date, different top-down and bottom-up approaches have been used to prepare phosphorene nanosheets. The top-down processes are more common and rely on chemically or mechanically weakening and breaking the interlayer interactions, while the bottom-up techniques are based on chemical synthesis from phosphorus precursors [25]. Smith et al. synthesized a few-layer phosphorene films of 3.4 to 600 nm thickness on a silicon substrate through the bottom-up chemical vapor deposition (CVD) method using RP as a starting material [26]. Besides CVD, there are limited bottom-up synthesis methods due to the lack of suitable precursors and the associated high costs of preparation [27]. Top-down methods are mostly used for the formation of phosphorene based on mechanical and liquid exfoliation of BP. The well-known Scotch tape method of micromechanical cleavage was applied by Li et al. to exfoliate and fabricate phosphorene on SiO_2/Si substrate [28]. However, this method suffers from low yield and poor scalability. As an alternative, liquid-phase exfoliation revealed promising results for BP exfoliation. It consists of the dispersion of BP in a solvent (deionized (DI) water or organic/inorganic solutions), sonication, and centrifugation of the exfoliated materials [29, 30].

Brent et al. obtained two layers of phosphorene using a one-step ultrasonication of BP in N-methylpyrrolidone (NMP) solution [31]. By controlling the sonication power and centrifuge speed of rotation, large quantities and to a certain extent controllable size of phosphorene nanosheets (a few nanometres to several tens of micrometres) have been produced, which makes this method more favourable compared to the mechanical exfoliation [32, 33]. Yasaei et al. used dimethylformamide (DMF) and dimethyl sulfoxide (DMSO) as a stripping solvent to synthesize large scale and highly crystalline phosphorene nanosheets with the thickness of 11 nm [34]. Isopropyl alcohol (IPA) [35], ionic liquids [36] and N-cyclohexyl-2-pyrrolidone (CHP) [37] were also reported as solvents for liquid exfoliation of BP. Very recently, Yan et al. developed a simple solvothermal-assisted exfoliation method with acetonitrile as a solvent to synthesize a few-layer phosphorene within a size range up to 10 μm. Acetonitrile was shown to weaken the van der Waals bonds and decrease the sonication time [38]. However, the use of hazardous solvents and the high concentration of structural defects in the final products remain the major disadvantages of liquid exfoliation methods, which may limit their widespread adoption. Electrochemical exfoliation is another liquid-based exfoliation technique to prepare a few-layer phosphorene that is faster, inexpensive and more tractable [39]. In this method, the exfoliation occurs in organic or aqueous solutions by applying a fixed voltage between the bulk BP and an inert platinum electrode [40, 41]. Li et al. successfully synthesized highly crystalline phosphorene nanosheets using BP as a cathode in a nonaqueous electrolyte (0.01 M tetraalkylammonium salt in DMSO) and by applying a

cathodic voltage of -5 V [42]. Ambrosi et al. used 0.5 mol l^{-1} H_2SO_4 solution and a BP anode. First, they applied 1 V to the bulk BP to initiate the intercalation of the electrolyte anions and then 3 V for the exfoliation process [43]. Although the electrochemical exfoliation methods can successfully exfoliate bulk BP into phosphorene, they are nonetheless multi-step and time-consuming procedures, and thus less attractive for practical applications. It is therefore necessary to develop alternative techniques that can fabricate a few-layer BP-modified substrate in a facile, single-step, scalable, and eco-friendly manner.

In this study, we propose a novel and straightforward two-in-one process to exfoliate BP into phosphorene nanosheets in DI water, which are then dragged electrophoretically to be deposited on a conductive substrate. The procedure is based on the mechanism of bipolar electrochemistry (BPE). BPE is a well-known technique since 1960s which is based on applying a sufficiently high voltage to generate electrochemical reactions between two feeding electrodes and a conductive bipolar electrode placed wirelessly between them [44]. The difference in the electric potential between the solution and the bipolar electrode drive redox reactions on the cathodic and anodic poles of the bipolar electrode [45]. This method has been used for different applications such as electronic devices manufacturing, electrochemical sensing, and optical detection due to its low cost, user-friendly, and high-efficient operation [46, 47]. It has been recently used for the simultaneous exfoliation of graphene from graphite and its deposition on stainless steel feeding electrode [48-50]. As mentioned earlier, liquid-based exfoliation of BP is mainly conducted in organic solvents that are adsorbed by the

surface of exfoliated BP and are very difficult to be removed later. Here, we use DI water as a solvent for the exfoliation of BP, which makes this technique cost-effective and environmental-friendly. The exfoliated-and-deposited BP nanosheets were characterized morphologically, optically and chemically using scanning electron microscopy (SEM), transmission electron microscopy (TEM), Raman spectroscopy and X-ray photoelectron spectroscopy (XPS). The electrochemical characterization of the phosphorene-modified positive feeding electrode showed a fractional-order capacitive behaviour with discharge energy of 22.8 nW.h cm^{-2} recoverable with very high efficiency after 10000s of charge/discharge cycles. Fractional-order capacitors or constant phase elements (CPE) have an impedance of the form $Z(s) = 1/s^{\alpha}C_{\alpha}$, $(0<\alpha<1)$ and constant impedance phase angle $\varphi(Z) = -\alpha\pi/2$ independently of the frequency, which is suitable for instance for oscillator circuits for timing applications, filters for frequency selectivity purposes, and in fractional-order proportional–integral–derivative controllers.

6.2 Materials and Methods

6.2.1 Materials Synthesis

Two 316 stainless steel electrodes (1×4 cm^2) serving as positive and negative feeding electrodes were placed vertically in DI water (18 MΩ·cm resistivity) at a distance of 3 cm from each other (see BPE cell in Figure 6.1). A 1 cm long and 2.5 mm in diameter bulk poly-crystalline BP bar (99.998% purity, supplied by Smart-Elements, Germany) was placed wirelessly between the two feeding electrodes. A multi-channel DC Power Analyzer (Agilent Technologies N6705A) was used to

drive the BPE process, which was conducted with 30 Vdc (i.e. electric field of 10 V cm^{-1}) for continuous 24 hours at ambient conditions.

6.2.2 Materials Characterization

The microstructural and morphological properties of the exfoliated BP were characterized by field-emission scanning electron microscopy (JEOL FESEM 7000) and field-emission transmission electron microscopy (Tecnai TF 20 TEM). High-resolution TEM (HRTEM) with selected-area electron diffraction (SAED) were conducted at an accelerating voltage of 200 kV, and the field emission gun with a resolution of 2 Å. Focused Ion Beam (Quanta 3D; Dual Beam) was used for the TEM sample preparation. The Raman spectra were collected on a BaySpec Raman spectrometer using a 514-nm laser excitation. The chemical composition of the exfoliated-and-deposited phosphorene on the stainless steel substrates was evaluated using X-ray photoelectron spectroscopy (XPS) on a Physical Electronics 5400 ESCA instrument with Al Kα radiation (1486.6 eV).

6.2.3 Electrochemical Characterization

The electrochemical measurements were performed on a VMP3 Bio-Logic potentiostat. Two symmetric positive feeding electrodes (after BP exfoliation) of 0.5×0.5 cm^2 were assembled in a Swagelok electrochemical cell using 1 mol l^{-1} Na_2SO_4 solution and Celgards 2400 microporous polypropylene separator. The spectral impedance of the device was measured at 0 Vdc with 10 mV ac perturbations from 1 MHz down to 10 mHz. The cyclic voltammetry (CV) tests at the scan rates of 2 to 1000 mV s^{-1} and galvanostatic charge/discharge (GCD) at

different current densities from 25 to 500 μA cm^{-2} were carried out over the voltage range of 0 to 0.7 V.

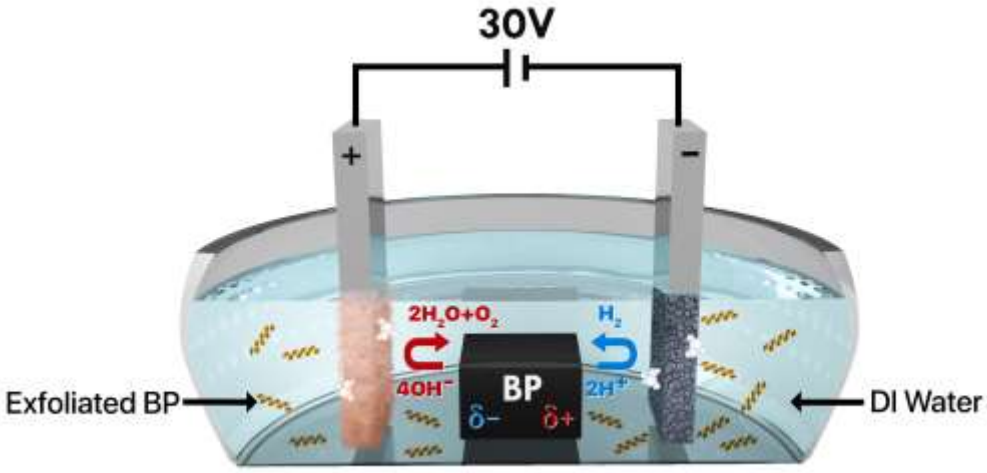

Figure 6.1: Schematic illustration of the two-in-one bipolar electrochemical cell used for (i) BP exfoliation into phosphorene, and (ii) subsequent electrophoretical deposition of the suspended phosphorene on the feeding electrodes.

6.3 Results and Discussion

The BPE setup used to exfoliate-and-deposit phosphorene nanosheets starting from bulk BP is shown in Figure 6.1. In brief, a BP bar was placed wirelessly in the centre of the cell pre-filled with DI water, and two stainless steel feeding electrodes were placed at a distance of 3 cm apart. Figure 6S.2 which shows typical SEM images of the bulk BP before exfoliation consisting of an angular, closely-stacked and layered structure. Due to the concept of bipolar electrochemistry, in general the induced voltage on the two pole of bulk BP depends on the applied voltage, length of BP electrode, and distance between two feeding electrodes. By applying higher voltage, using longer bulk BP and decreasing distance between two feeding electrodes, the induced voltage will

increase. The typical electric field was reported as around 5 to 15 Vcm^{-1} for successful BPE exfoliation of graphite [48-51]. In this study, cell voltage of 30 V was selected based on the electric field of 10 Vcm^{-1}. The extremities of the BP substrate across the direction of the electric field get polarized in the opposite polarity to the feeding electrodes resulting in the wireless compartmentalization of the BP into anodic and cathodic poles [46]. The bulk BP remains almost isopotential during BPE. When the bipolar potential is large enough hydrogen and oxygen bubbles were generated at the surface of the negative and positive poles of bulk BP, respectively, as a result of water electrolysis reaction, and can be easily visualized (Supplementary Video 1). Given the "crumbly" and layered nature of the bulk BP bar, H^+ and OH^- ions generated during the water decomposition can be intercalated to the bulk BP and overcome the weak van der Waals forces of BP layers. Therefore, 2D phosphorene particles can be detached and exfoliated from the bulk BP. Due to the Vdc electrophoresis phenomena, 2D phosphorene nanosheets will be transported and deposited on to the feeding electrode. Figure 6S.3 shows the change of the cell current versus time during the exfoliation process. It is clear that the current progressively increased with the time as a result of increased conductivity of the solution, which can be attributed to the collective effect of water electrolysis and by-products from BP exfoliation.

After 24 hours of BPE, the bulk BP did not show any noticeable change, however, obvious deposition of a thin film on the positive electrode of the bipolar cell can be observed. It should be noted that in our recent study of graphene exfoliation via BPE [50], deposition occurs on both positive and negative feeding electrodes.

More detailed study needs to be done to investigate the possible deposition of phosphorene on the negative feeding electrode. Typical SEM micrographs of the positive feeding electrode after 24 hours of operation are shown in Figure 6.2 (a-c) at different magnifications. One can observe a homogeneous distribution of thin phosphorene nanosheets on the substrate with a structured and fractal structure. The Raman spectroscopy results of the same feeding electrode are shown in Figure 6.2 (d) along with the Raman spectrum of the bulk BP for comparison. From the six theoretical Raman vibration modes of black phosphorus, three prominent peaks appear in the range from 300 cm^{-1} to 500 cm^{-1} [52, 53] which confirms that the BP exfoliation/deposition was successful. These peaks are A_g^1 (out of plane), B_{2g}, and A_g^2 (in-plane) vibration modes at 361 cm^{-1}, 439 cm^{-1}, and 467 cm^{-1}, respectively, indicating good agreement with previous results [54-56]. For the exfoliated BP, compared to the bulk BP, blue-shifts by about 3.1 cm^{-1}, 7.0 cm^{-1}, and 5.7 cm^{-1} can be observed for the Raman modes A_g^1, B_{2g}, and A_g^2, respectively. These shifts may be associated with the less hindered vibration of the phosphorus atoms due to the weakened interlayer van der Waals forces [30, 37]. The observed blue shifts for the exfoliated BP confirm the reduction in the number of BP layers. It is also clear that due to the reduction of BP thickness, the intensity of the three bands decreased significantly for the phosphorene nanosheets [57-59]. The number of phosphorene layers after exfoliation could be estimated as 3 to 5 layers based on the intensity ratio of 2.75 for the A_g^2/A_g^1 vibration modes [60].

XPS spectra of the bulk BP and exfoliated BP nanosheets (Figure 6.2 (e)) revealed two well-defined $P2P_{1/2}$ and $P2P_{3/2}$ components at a binding energy of about 130.8 eV and 129.8 eV, respectively, which are related to the crystalline black phosphorus peaks. A broad peak can be observed at around 133.0 eV and 132.8 eV for bulk BP and exfoliated BP nanosheets, respectively, which could be assigned to phosphorus-oxygen bond (POx) [61]. The POx bond can be attributed to the high reactivity of BP and spontaneous formation of surface oxide layer in air [43]. The XPS spectrum of the exfoliated phosphorene on the stainless steel show less intense POx peak compared to the bulk BP indicating that the bipolar exfoliated phosphorene has higher degree of oxidation because high surface area phosphorene nanosheets are more reactive and sensitive to oxygen. The peak shifts for the POx, $P2P_{1/2}$and $P2P_{3/2}$ are around 0.3, 0.2, and 0.09 eV to the lower values, respectively. The peaks shift to the lower binding energies could be attributed to the reduced number of layers of BP nanosheets after bipolar exfoliation [62, 63].

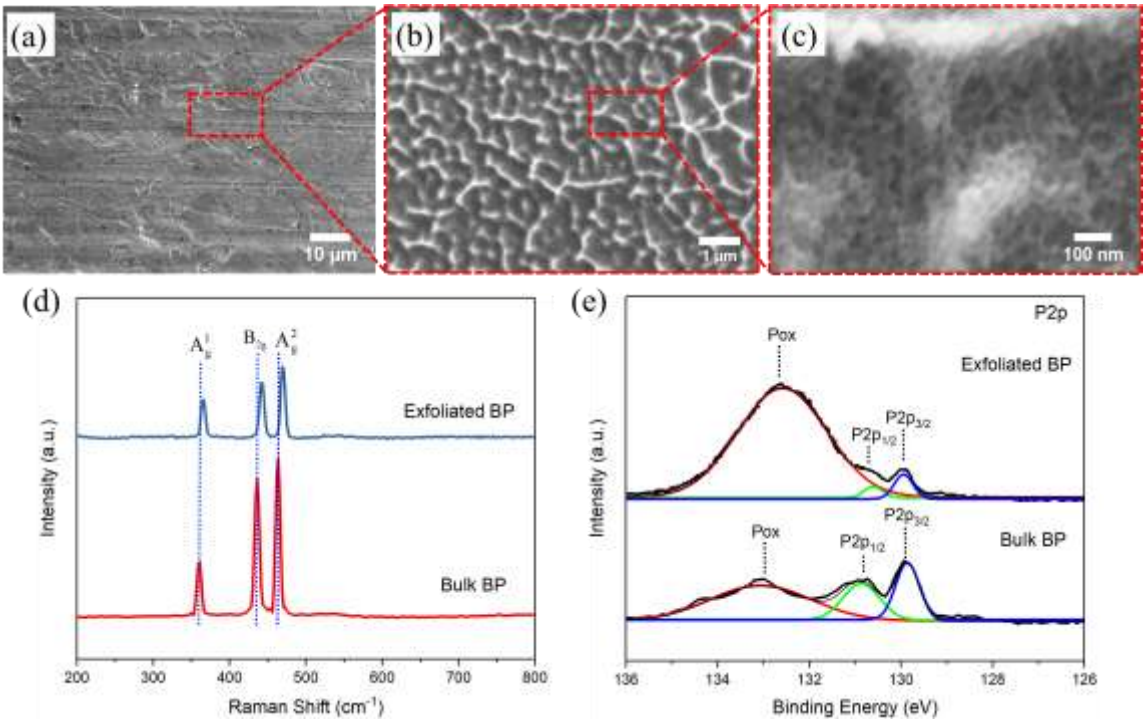

Figure 6.2: (a-c) Typical SEM images of exfoliated and deposited black phosphorus nanosheets on the positive electrode in different magnification. (d) Raman spectra, and (e) XPS spectra of the BP crystal and bipolar exfoliated-and-deposited BP nanosheets.

In order to investigate the morphology of the exfoliated BP nanosheets as well as the crystalline quality, TEM characterization was carried out. The TEM images of the exfoliated BP nanosheets collected from the DI water after the 24-hour BPE operation are shown in Figure 6.3 (a-f). Figure 6.3 (a), shows a low-resolution TEM image of electron-transparent, thin phosphorene nanosheets with lateral size in the range of a few hundreds of nanometres which demonstrate the successful exfoliation of BP by bipolar electrochemistry method [43, 64]. HRTEM images confirming the crystallinity of the phosphorene are shown in Figure 6.3 (b-f). The interplanar distances and corresponding Miller indices of the BP nanosheets are labelled on the HRTEM images. It is clear from Figure 6.3 (b-f) that the orthorhombic crystal structure of BP appears to be not affected by the bipolar

exfoliation, which confirms a low defect concentration in produced phosphorene nanosheets. The exfoliated BP nanosheets revealed different lattice fringes with interplanar distances of 0.34, 0.21, 0.23, and 0.25 nm, which could be assigned to the (021), (002), (041), and (111) atomic planes of orthorhombic black phosphorus, respectively. From SAED pattern presented in the insets of Figure 6.3 (e, f), the orthorhombic single crystals of the exfoliated BP is confirmed which is in good agreement with previous reports [36, 65]. The possible reason for various size of crystalline domains of phosphorene nanosheets after bipolar exfoliation could be due to the poly-crystalline nature of the bulk BP. The interplanar distances are matched with the d-spacing of orthorhombic black phosphorus (JCPDS No 96-101-0326).

Finally, owing to the structured surface of the exfoliated-and-deposited phosphorene nanosheets, the electrochemical performance of the positive feeding electrode was evaluated for capacitive energy storage application in a two-electrode symmetric configuration. We first analysed the open-circuit spectral impedance of the device which was measured with 10 mV ac amplitude excitations from 1 MHz down to 10 mHz. The Nyquist plot and Bode plot (inset) are depicted in Figure 6.4 (a). The spectral phase is relatively constant at an average of -66.5 deg. in the low-to-medium frequencies (less than 1000 Hz) and heads towards the resistive, and then inductive behaviour as the frequency is increased. The non-ideal behaviour can be attributed to the crystalline inhomogeneity and surface roughness of the electrode. Such non-ideality can be modelled using the fractional-order Randles model (see inset in Figure 6.4 (a)) of impedance:

$$Z(j\omega) = R_s + \frac{R_p}{R_p C_\alpha (j\omega)^\alpha + 1} \quad (6.1)$$

The model includes a series resistance R_s, a parallel resistance R_p, and a constant phase element (CPE) of impedance proportional to $1/(j\omega)^\alpha$ ($Z_{CPE} = 1/C_\alpha(j\omega)^\alpha$ where C_α is the CPE parameter and α is a dispersion coefficient that can take values between 0 and 1) [66]. Using nonlinear least square fitting (Figure 4(a) in dashed line), the value of R_s was found to be 3.135 Ω, R_p = 251 kΩ, C_α = 0.103 mF $s^{-0.261}$, and α = 0.739. In the time domain, this non-ideal behaviour can be viewed as a fractional differentiation of order α performed by the capacitive part of the device, i.e. $i(t) = C_\alpha d^\alpha v(t)/dt^\alpha$ [67-69]. This is different from the first-order differentiation $i(t) = Cdv(t)/dt$ known for ideal capacitors, and can find application in fractional-order PID controllers [70], impedance matching circuits [71], filters [72], etc.

A particular output of the fractional differentiation operation of the device is its response to a step function. For a step current input (i.e. $i(t) = 0$ for $t < 0$, and $i(t) = I_{cc}$ for $t \geq 0$), and given that $R_p \gg R_s$, the voltage-time response is actually proportional to a power law function and not a linear function, such that [69]:

$$v(t) = V_0 + I_{cc}\left[R_s + \frac{t^\alpha}{C_\alpha \Gamma(1+\alpha)}\right] \quad (6.2)$$

Here V_0 is the initial voltage on the device and $\Gamma(\cdot)$ is the Gamma function. The same can be adapted to a step decrease using $-$Icc which results in a power law decrease [73]. In Figure 6.4 (b) we show the resulting voltage-time profiles in response to GCD tests with different values of I_{cc} from 25 to 500 μA cm^{-2}. Using discrete Fourier decomposition, these responses correspond to fundamental frequencies from about 50 mHz to 1 Hz. At low current rates, it is clear that the

device voltage discharge is relatively linear with negligible low Ohmic drop. However, a clear transition from linear to nonlinear, power law voltage-time relationship can be observed as the current charging/discharging is increased. Nonlinear least-squares fitting of the experimental discharge data using equation 6.2 (Figure 6.4 (b) in dashed lines) resulted in the values of the dispersion coefficient α being 0.927, 0.978, 0.844, 0.800 and 0.759 and those of C_α being 0.188, 0.210, 0.224, 0.259 and 0.297 mF $s^{\alpha-1}$ for the discharge currents 25, 50, 100, 250 and 500 μA cm^{-2}, respectively. The values of α for the five corresponding charging waveforms were found to be practically constant with an average of 0.674 and a small standard deviation of 0.008, with C_α being 0.268, 0.282, 0.237, 0.236 and 0.253 mF $s^{\alpha-1}$. The variation in the values of α in these cases is actually a characteristic feature of fractional-order capacitive devices. Contrary to ideal capacitors, these devices possess an inherent memory effect that makes their response sensitive to the type and form of the applied excitation [74], as well as to the pathway they followed to reach a given state [67]. The same applies to the different parameters values extracted from the EIS modelling at which the device is perturbed with small signals around its equilibrium state (open-circuit voltage), whereas with the square wave currents, the device is operating in dynamic mode.

For the sake of comparison, it is convenient to define, with caution, an effective capacitance $C_{eff} = C_\alpha\Gamma(1+\alpha)t^{1-\alpha}$ in units of Farads that combines both parameters α and C_α and this by equating the term $t^\alpha/C_\alpha\Gamma(1+\alpha)$ in equation 6.2 with t/C_{eff} as if the device is an ideal capacitor (i.e. $\alpha=1$) [69]. The values of C_{eff} computed for the charging/discharging sequences at the increasing currents ±25, ±50, ±100, ±250

and ±500 μA cm^{-2} were found to be decreasing as expected, i.e. 0.369, 0.300, 0.244, 0.194 and 0.165 mF, and 0.305, 0.288, 0.243, 0.196 and 0.164 mF, respectively. The difference between the two sets of values, especially at low rates, can be attributed to (i) possible electrochemical irreversibility, (ii) increased resistive behavior of the device (see the Bode plot in the inset of Fig. 6.4 (a) in the low frequency window), and (iii) the fact that the parameters of fractional-order devices are dependent on the past history of the device (e.g. charge or discharge).

The dynamic performance of the device was then characterized using CV test. Figure 6.4 (c) shows the current-voltage response of the phosphorene-based device recorded at the scan rate of 1000 mV s^{-1} compared to that of a bare stainless steel-based device. Clearly, the phosphorene coating exhibits a capacitive electrical energy storage capability. In Figure 6.4 (d), the performance of the device was measured at different voltage scan rates (2 to 1000 mV s^{-1}). The voltammograms get wider with the increase of scan rate. The curves are nearly rectangular without any noticeable peaks belongs to reversible redox reactions, implying the storage mechanism of the device based on double-layer charge storage. (this do not exclude completely the existence of some parasitic redox reaction that may take place).

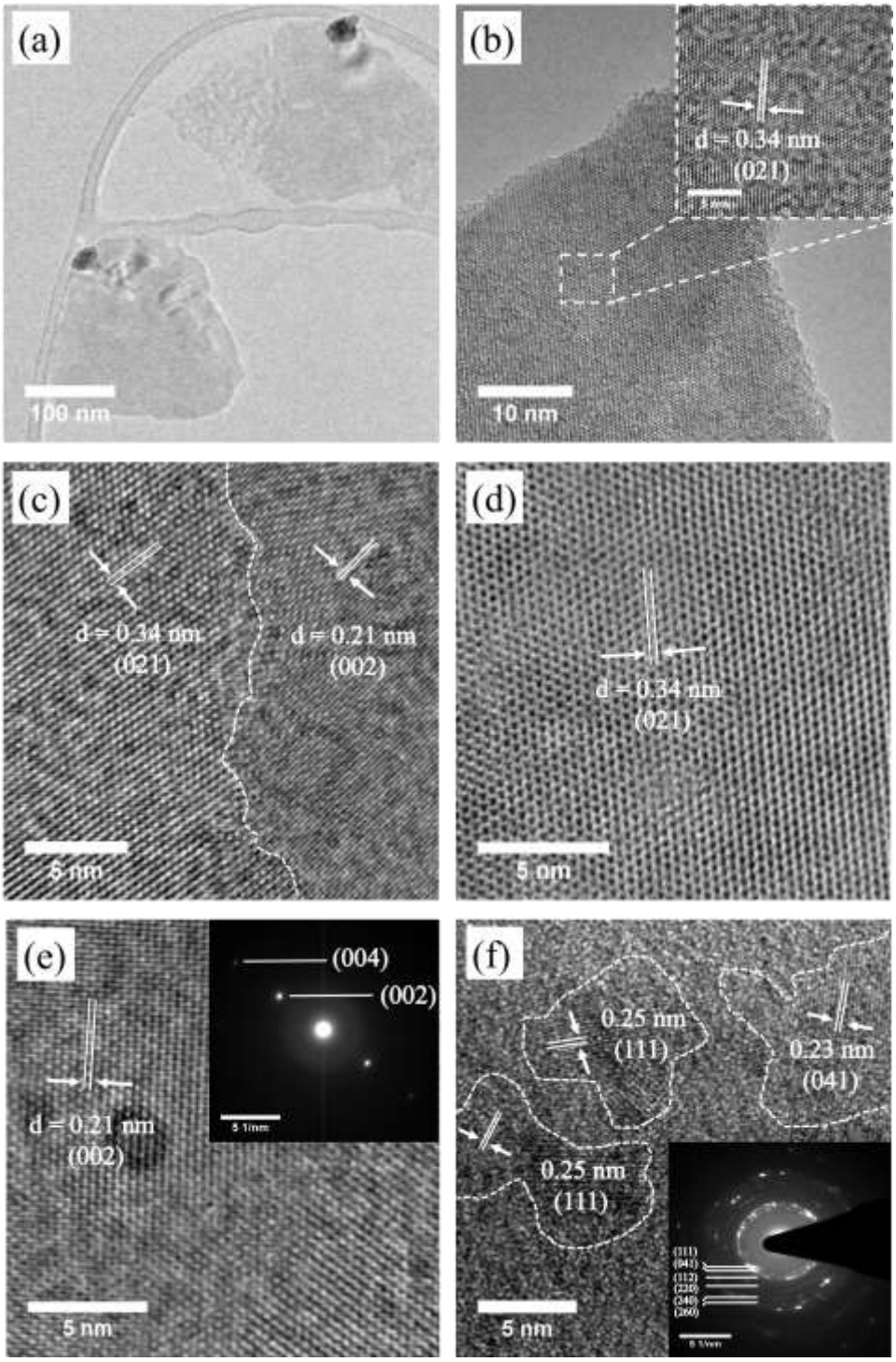

Figure 6.3: (a) Typical low-magnification TEM image of the BP nanosheets. (b-f) HRTEM images of exfoliated BP nanosheets. The insets of (e, f) are the SAED patterns of exfoliated BP nanosheets.

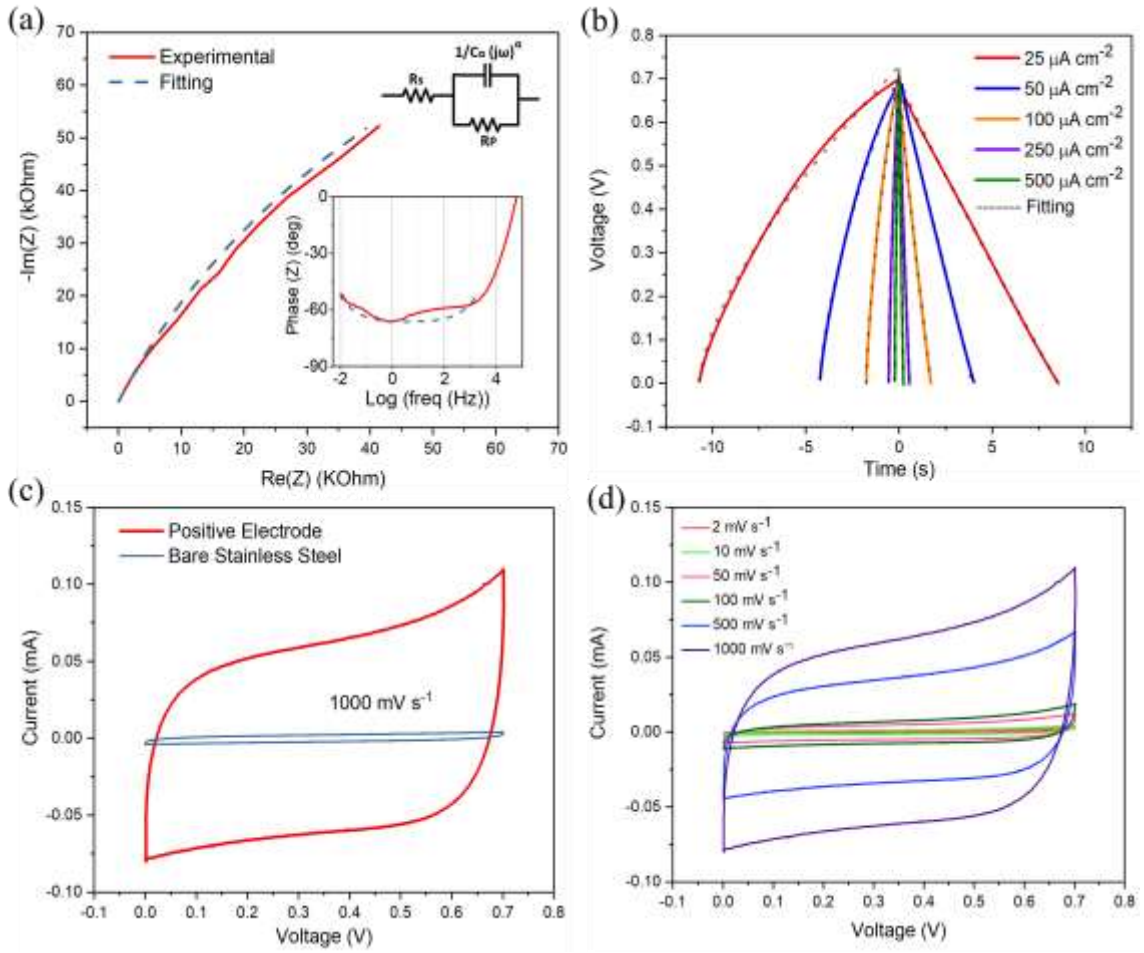

Figure 6.4: Electrochemical characterization results of positive feeding electrode-based device: (a) Complex-plane representation of real versus imaginary parts of impedance; the inset shows the impedance phase angle plot versus frequency and circuit of the fractional-order Randles model. (b) Voltage-time profiles resulting from constant-current charging/discharging measurements. (c) Cyclic voltammetry profile compared to that of a bare stainless steel-based device at the same voltage scan rate of 1000 mVs^{-1}. (d) Cyclic voltammetry profiles at different scan rates.

We also evaluated the electrochemical stability of the device. Figure 6.5 shows the results of its rate capability performance computed from tests conducted at different constant charging/discharging currents for 40000 successive cycles. The plot shows the discharged energy vs. cycle number which is directly computed from the time-integral of the instantaneous power, i.e. $e(t) = \int p(t)dt$ with $p(t)= i(t).v(t)$, and not from the computation of the capacitance which, again, can be

ambiguous to define for this case given the fractional-order nature of the device. The discharge energy of the electrode with area of 0.5 cm^2 prepared by BPE method provides 22.8 nW.h cm^{-2} for a constant current density of 25 μA cm^{-2}. The flatness of the curves for the different applied currents demonstrates the superior stability and reliability of the phosphorene electrodes used for the fabrication of the device. Furthermore, the recovery of the same discharge energy for I_{cc} = 25 μA cm^{-2} after 30000 charge/discharge cycles is clear an evidence of its excellent reversibility and long-term stability.

The delivered energy density vs. power density computed from the response of the device at different discharge currents from 25 to 500 μA cm^{-2} are plotted in Figure 6.6. Again, the energy and power are computed directly from the current and voltage time recordings and not from any particular electric model, which are believe to represent better the true performance of the device. The delivered energy density at current density of 500 μAcm^{-2} reaches 0.01 μWh cm^{-2} which is comparable to MXene/CNT (0.05 μWh cm^{-2} at 2 μAcm^{-2} [REF 8 from SI of chapter 6]) and MXene/CNF (0.08 μWh cm^{-2} at 570 μAcm^{-2} [REF 10 from SI of chapter 6]), but lower than the energy performance reported for other 2D materials-based devices (see Table 6S.1). This energy storage capability could be enhanced for instance by further increasing the deposition time and/or chemically or physically post-process the active material to increase its electrical conductivity. However, the power performance is outstanding with 351 μW cm^{-2} at a constant current rate of 0.5 mA cm^{-2}, which is comparable with other 2D materials-based devices (see Table 6S.1), such as MXene (2.4 μW cm^{-2} at 2 μA cm^{-2} for

MXene/CNT [REF 8 in SI of chapter 6] or 145 μW cm^{-2} at 570 μA cm^{-2} for MXene/CNF [REF 10 in SI of chapter 6]), 2D MnO_2 (639 μW cm^{-2} at 500 μA cm^{-2} [REF 7 in SI of chapter 6]), and comparable to graphene (750 μW cm^{-2} at 20 mA cm^{-2} [REF 3 in SI]) and graphene oxide (1051 μW cm^{-2} at 1100 μA cm^{-2} [REF 11 in SI of chapter 6]). This high-rate energy delivery capability is in line with the CPE behaviour in the low-to-medium frequencies as reported in Figure 6.4 (a). The results indicate that BP is a promising candidate for capacitive energy storage application.

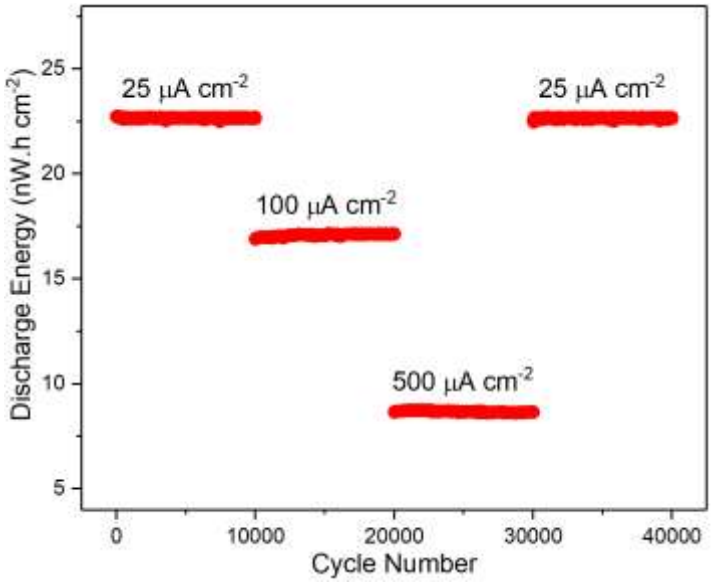

Figure 6.5: Discharge energy vs. cycle number measured at different currents of the exfoliated-and-deposited phosphorene on the positive electrode.

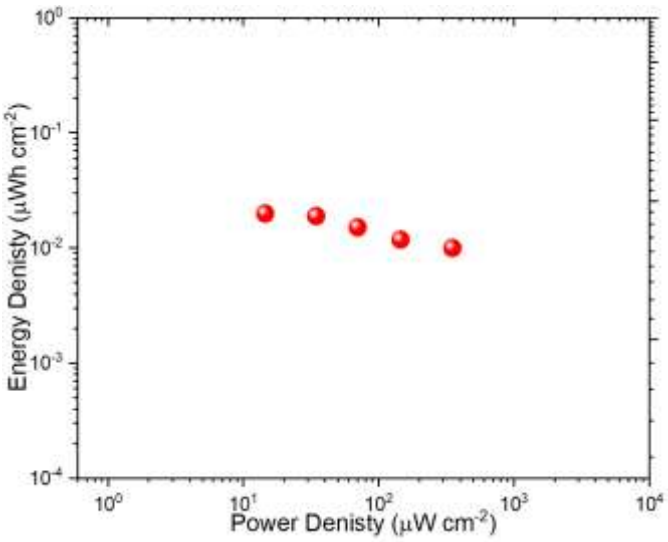

Figure 6.6: Ragone plot of energy density vs. power density at different currents from 25 to 500 μA cm^{-2} of the exfoliated-and-deposited phosphorene on the positive electrode.

In order to study the exfoliation and deposition of phosphorene nanosheets on the negative feeding electrode, the modified bipolar setup was employed as shown in Figure 6.7. As shown in Figure 6.7, one stainless steel electrode serving as negative feeding electrode and platinum wire acted as a positive side and were placed vertically in DI water similar to the regular bipolar setup. After 25 hours of BPE, partially 2D reduced phosphorene nanosheets were deposited on the surface of negative feeding electrode. The SEM images of the negative feeding electrode after 24 hours of operation are shown in Figure 6.8 (a-c). As it is clear, 2D vertically aligned reduced phosphorene nanosheets were deposited on negative feeding electrode. The Raman spectroscopy and XPS results of the same feeding electrodes are shown in Figure 6.8 (d, e). Similar to the positive feeding electrode, blue-shift by about 6.1 cm^{-1}, 9.2 cm^{-1}, and 7.2 cm^{-1}, confirms the exfoliation of BP into reduced phosphorene nanosheets on the surface of negative feeding electrode. The higher amounts of shift for the peaks in negative feeding electrode compared to the positive feeding electrode may related to the 2D

morphology of reduced phosphorene nanosheets. The XPS spectrum of the exfoliated reduced phosphorene nanosheets on the negative feeding electrode show similar intense of POx peak indicating the reduction of phosphorene nanosheets on the negative feeding electrode compared to the positive feeding electrode.

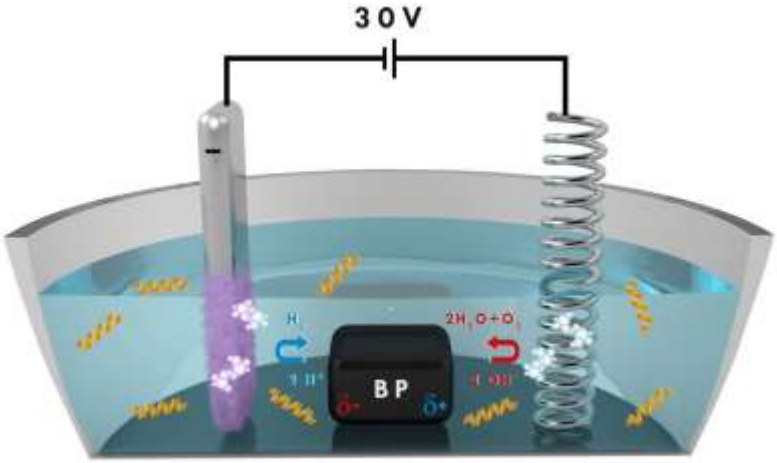

Figure 6.7: Schematic illustration of the modified bipolar electrochemistry setup.

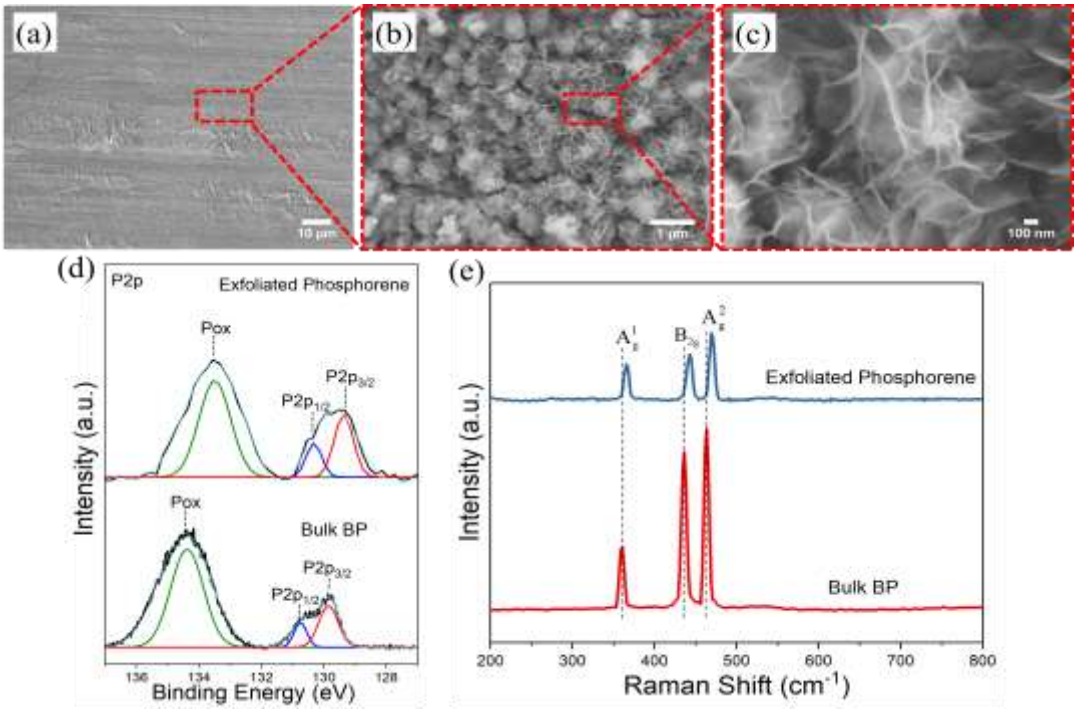

Figure 6.8: (a-c) SEM images of exfoliated and deposited reduced phosphorene nanosheets on the negative electrode in different magnification. (d) Raman spectra, and (e) XPS spectra of the BP and reduced phosphorene nanosheets.

Due to the 2D morphology reduced phosphorene nanosheets, the electrochemical performance of the negative feeding electrode was analyzed for supercapacitor application. The Nyguist plot and Bode plot (inset) of the device is shown in Figure 6.9 (a). The spectral phase is relatively constant at an average of -78.7 deg. in the low-to-medium frequencies and compared to the positive feeding electrode, presented a more capacitor behavior. This is because of the 2D morphology of reduced phosphorene nanosheets on the negative feeding electrode. The performance of these devices was also studied by galvanostatic charge/discharge (GCD) and cyclic voltammetry (CV) test (Figure 6.9 (b-c)). The electrical behavior of the device based on negative electrode is closer to that of a capacitor based on positive feeding electrode because its GCD curves are highly symmetric and linear with negligible ohmic losses. In terms of CV results, the curves are almost rectangular in shape at different scan rates which demonstrates an electric double-layer capacitor (EDLC) behavior similar to the positive feeding electrode. The symmetry of the curves with respect to the zero y-axis shows the excellent reversibility of device. The deposited reduced phosphorene nanosheets delivered a high specific capacitance of 11 mF cm^{-2} at the scan rate of 2 mV s^{-1}. Moreover, the deposited reduced phosphorene nanosheets delivered specific capacitance of 8.57, 7.62, 6.66, 5.0, 4.65, 4.01, 3.32, and 2.86 mF cm^{-2} at the scan rate of 5, 10, 20, 50, 100, 200, 500, and 1000 mV s^{-1}, respectively.

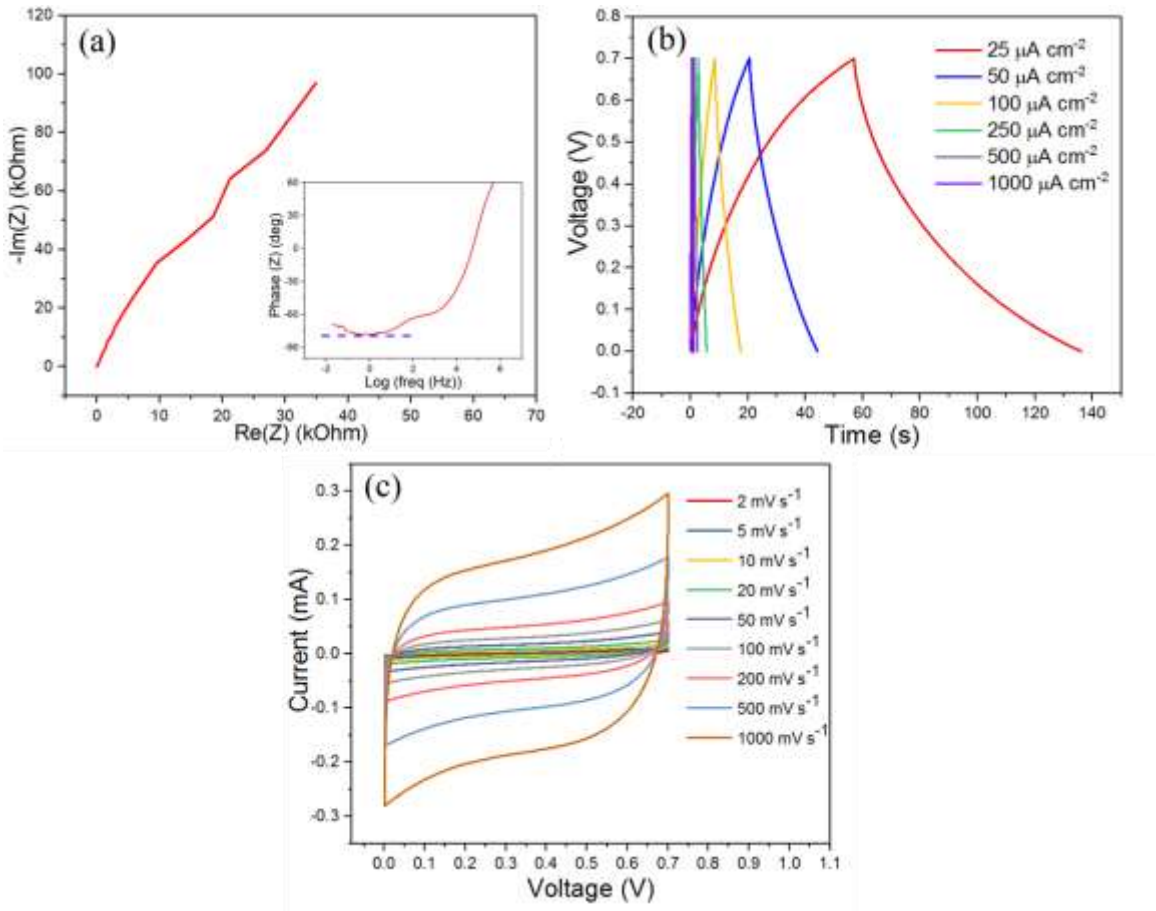

Figure 6.9: (a) Complex-plane representation of real versus imaginary parts of impedance; the inset shows the impedance phase angle plot versus frequency. (b) Constant-current charging/discharging results, and (c) Cyclic voltammetry results of the negative feeding electrode.

6.4 Conclusion

In summary, a novel two-in-one exfoliation and deposition from bulk BP to phosphorene nanosheets were carried out for the first time via BPE method. In addition to the main advantage of this technique, which is the two-in-one exfoliation-and-deposition process, this method is proven to be simple, reliable, and eco-friendly. It is operated at ambient temperature in DI water without any chemical additives which makes it more attractive compared to previously reported electrochemical exfoliation approaches. In principle, a large number of conductive

substrates can be coated at once with this method using a single dc power supply without any Ohmic connection to the bipolar electrode, which could be positive attribute for scaling up purposes for different applications. The high-quality exfoliated BP nanosheets were then analyzed with different microscopic and spectroscopic techniques, revealing thin layers of phosphorene with orthorhombic crystal structure and lateral dimensions up to a few hundreds of nanometers. Furthermore, the electrochemical evaluation of the positive feeding electrode assembled in a symmetric configuration revealed a relatively acceptable discharge energy of 0.01 μWh cm^{-2} at a constant current load discharge of 500 μA cm^{-2} but with a very high rate of 351 μW cm^{-2}. The device exhibited a fractional order capacitive behavior in the low-to-medium frequency, and a high stability and reversibility for at least to 40000 cycles. In the modified bipolar setup, vertically aligned reduced phosphorene nanosheets were deposited on the negative feeding electrode. In terms of electrochemical performance, the fabricated device based on the negative feeding electrode revealed a specific capacitance of 11 mF cm^{-2} at the scan rate of 2 mV s^{-1} which is around 10 times higher than the positive feeding electrode. We believe that this study could open up new horizons for the exfoliation and deposition of not only BP, but also other 2D materials for electronic and electrochemical energy storage device applications.

6.5 References

[1] K.S. Novoselov, D. Jiang, F. Schedin, T. Booth, V. Khotkevich, S. Morozov, A.K. Geim, Two-dimensional atomic crystals, Proceedings of the National Academy of Sciences of the United States of America 102(30) (2005) 10451-10453.

[2] S. Surnev, M. Ramsey, F.J.P.i.s.s. Netzer, Vanadium oxide surface studies, Progress in Surface Science 73(4-8) (2003) 117-165.

[3] Q.H. Wang, K. Kalantar-Zadeh, A. Kis, J.N. Coleman, M.S.J.N.n. Strano, Electronics and optoelectronics of two-dimensional transition metal dichalcogenides, Nature Nanotechnology 7(11) (2012) 699.

[4] D. Golberg, Y. Bando, Y. Huang, T. Terao, M. Mitome, C. Tang, C.J.A.n. Zhi, Boron nitride nanotubes and nanosheets, ACS Nano 4(6) (2010) 2979-2993.

[5] K.S. Novoselov, V. Fal, L. Colombo, P. Gellert, M. Schwab, K.J.n. Kim, A roadmap for graphene, Nature 490(7419) (2012) 192.

[6] D. Akinwande, C.J. Brennan, J.S. Bunch, P. Egberts, J.R. Felts, H. Gao, R. Huang, J.-S. Kim, T. Li, Y.J.E.M.L. Li, A review on mechanics and mechanical properties of 2D materials—Graphene and beyond, Extreme Mechanics Letters 13 (2017) 42-77.

[7] C. Zhu, D. Du, Y.J.D.M. Lin, Graphene and graphene-like 2D materials for optical biosensing and bioimaging: A review, 2D Materials 2(3) (2015) 032004.

[8] J.-H. Chen, C. Jang, S. Xiao, M. Ishigami, M.S.J.N.n. Fuhrer, Intrinsic and extrinsic performance limits of graphene devices on SiO 2, Nature Nanotechnology 3(4) (2008) 206.

[9] T. Wang, Y. Zhu, Q.J.T.J.o.P.C.C. Jiang, Bandgap opening of bilayer graphene by dual doping from organic molecule and substrate, The Journal of Physical Chemistry C 117(24) (2013) 12873-12881.

[10] H. Zhang, S. Lu, J. Zheng, J. Du, S. Wen, D. Tang, K.J.O.e. Loh, Molybdenum disulfide (MoS 2) as a broadband saturable absorber for ultra-fast photonics, Optics Express 22(6) (2014) 7249-7260.

[11] P.J.J.o.t.A.C.S. Bridgman, FURTHER NOTE ON BLACK PHOSPHORUS, Journal of the American Chemical Society 38(3) (1916) 609-612.

[12] X. Ling, H. Wang, S. Huang, F. Xia, M.S.J.P.o.t.N.A.o.S. Dresselhaus, The renaissance of black phosphorus, Proceedings of the National Academy of Sciences of the United States of America 112(15) (2015) 4523-4530.

[13] H. Liu, A.T. Neal, Z. Zhu, Z. Luo, X. Xu, D. Tománek, P.D.J.A.n. Ye, Phosphorene: an unexplored 2D semiconductor with a high hole mobility, ACS Nano 8(4) (2014) 4033-4041.

[14] H. Huang, B. Jiang, X. Zou, X. Zhao, L.J.S.B. Liao, Black phosphorus electronics, Science Bulletin 64 (2019) 1067-1079.

[15] X. Wang, A.M. Jones, K.L. Seyler, V. Tran, Y. Jia, H. Zhao, H. Wang, L. Yang, X. Xu, F.J.N.n. Xia, Highly anisotropic and robust excitons in monolayer black phosphorus, Nature Nanotechnology 10(6) (2015) 517.

[16] X. Zhang, H. Xie, Z. Liu, C. Tan, Z. Luo, H. Li, J. Lin, L. Sun, W. Chen, Z.J.A.c.i.e. Xu, Black phosphorus quantum dots, Angewandte Chemie 54(12) (2015) 3653-3657.

[17] S. Das, W. Zhang, M. Demarteau, A. Hoffmann, M. Dubey, A.J.N.l. Roelofs, Tunable transport gap in phosphorene, Nano Letters 14(10) (2014) 5733-5739.

[18] F. Xia, H. Wang, Y.J.N.c. Jia, Rediscovering black phosphorus as an anisotropic layered material for optoelectronics and electronics, Nature Communications 5 (2014) 4458.

[19] Q. Wei, X.J.A.P.L. Peng, Superior mechanical flexibility of phosphorene and few-layer black phosphorus, Applied Physics Letters 104(25) (2014) 251915.

[20] V. Eswaraiah, Q. Zeng, Y. Long, Z.J.S. Liu, Black phosphorus nanosheets: synthesis, characterization and applications, Small 12(26) (2016) 3480-3502.

[21] C. Hao, B. Yang, F. Wen, J. Xiang, L. Li, W. Wang, Z. Zeng, B. Xu, Z. Zhao, Z. Liu, Y. Tian, Flexible All-Solid-State Supercapacitors based on Liquid-Exfoliated Black-Phosphorus Nanoflakes, Advanced Materials 28(16) (2016) 3194-3201.

[22] Z. Guo, W. Ding, X. Liu, Z. Sun, L.J.A.M.T. Wei, Two-dimensional black phosphorus: A new star in energy applications and the barrier to stability, Applied Materials Today 14 (2019) 51-58.

[23] F. Xia, H. Wang, J.C. Hwang, A.C. Neto, L. Yang, Black phosphorus and its isoelectronic materials, Nature Reviews Physics 1 (2019) 306-317.

[24] R. Gusmao, Z. Sofer, M.J.A.C.I.E. Pumera, Black phosphorus rediscovered: from bulk material to monolayers, Angewandte Chemie 56(28) (2017) 8052-8072.

[25] Y. Zhang, Y. Zheng, K. Rui, H.H. Hng, K. Hippalgaonkar, J. Xu, W. Sun, J. Zhu, Q. Yan, W. Huang, 2D Black Phosphorus for Energy Storage and Thermoelectric Applications, Small 13(28) (2017) 1700661.

[26] J.B. Smith, D. Hagaman, H.-F. Ji, Growth of 2D black phosphorus film from chemical vapor deposition, Nanotechnology 27(21) (2016) 215602.

[27] Z. Yang, J. Hao, S. Yuan, S. Lin, H.M. Yau, J. Dai, S.P. Lau, Field-Effect Transistors Based on Amorphous Black Phosphorus Ultrathin Films by Pulsed Laser Deposition, Advanced Materials 27(25) (2015) 3748-3754.

[28] L. Li, Y. Yu, G.J. Ye, Q. Ge, X. Ou, H. Wu, D. Feng, X.H. Chen, Y.J.N.n. Zhang, Black phosphorus field-effect transistors, Nature Nanotechnology 9(5) (2014) 372.

[29] S. Lin, Y. Chui, Y. Li, S.P.J.F. Lau, Liquid-phase exfoliation of black phosphorus and its applications, FlatChem 2 (2017) 15-37.

[30] H. Wang, X. Yang, W. Shao, S. Chen, J. Xie, X. Zhang, J. Wang, Y.J.J.o.t.A.C.S. Xie, Ultrathin black phosphorus nanosheets for efficient singlet oxygen generation, Journal of the American Chemical Society 137(35) (2015) 11376-11382.

[31] J.R. Brent, N. Savjani, E.A. Lewis, S.J. Haigh, D.J. Lewis, P.J.C.c. O'Brien, Production of few-layer phosphorene by liquid exfoliation of black phosphorus, Chemical Communications 50(87) (2014) 13338-13341.

[32] C. Xing, J. Zhang, J. Jing, J. Li, F. Shi, Preparations, properties and applications of low-dimensional black phosphorus, Chemical Engineering Journal 370 (2019) 120-135.

[33] Y. Zhang, H. Wang, Z. Luo, H.T. Tan, B. Li, S. Sun, Z. Li, Y. Zong, Z.J. Xu, Y.J.A.E.M. Yang, An air-stable densely packed phosphorene–graphene composite toward advanced lithium storage properties, Advanced Energy Materials 6(12) (2016) 1600453.

[34] P. Yasaei, B. Kumar, T. Foroozan, C. Wang, M. Asadi, D. Tuschel, J.E. Indacochea, R.F. Klie, A.J.A.M. Salehi-Khojin, High-quality black phosphorus atomic layers by liquid-phase exfoliation, Advanced Materials 27(11) (2015) 1887-1892.

[35] S. Lin, Y. Li, W. Lu, Y. San Chui, L. Rogée, Q. Bao, S.P.J.D.M. Lau, In situ observation of the thermal stability of black phosphorus, 2D Materials 4(2) (2017) 025001.

[36] W. Zhao, Z. Xue, J. Wang, J. Jiang, X. Zhao, T.J.A.a.m. Mu, interfaces, Large-scale, highly efficient, and green liquid-exfoliation of black phosphorus in ionic liquids, ACS Applied Materials & Interfaces 7(50) (2015) 27608-27612.

[37] D. Hanlon, C. Backes, E. Doherty, C.S. Cucinotta, N.C. Berner, C. Boland, K. Lee, A. Harvey, P. Lynch, Z.J.N.c. Gholamvand, Liquid exfoliation of solvent-stabilized few-layer black phosphorus for applications beyond electronics, Nature Communications 6 (2015) 8563.

[38] Z. Yan, X. He, L. She, J. Sun, R. Jiang, H. Xu, F. Shi, Z. Lei, Z.-H.J.J.o.M. Liu, Solvothermal-assisted liquid-phase exfoliation of large size and high quality black phosphorus, Journal of Materiomics 4(2) (2018) 129-134.

[39] A. Abdelkader, A. Cooper, R. Dryfe, I.J.N. Kinloch, How to get between the sheets: a review of recent works on the electrochemical exfoliation of graphene materials from bulk graphite, Nanoscale 7(16) (2015) 6944-6956.

[40] M.B. Erande, M.S. Pawar, D.J.J.A.a.m. Late, interfaces, Humidity sensing and photodetection behavior of electrochemically exfoliated atomically thin-layered black phosphorus nanosheets, ACS Applied Materials & Interfaces 8(18) (2016) 11548-11556.

[41] S. Qiu, B. Zou, H. Sheng, W. Guo, J. Wang, Y. Zhao, W. Wang, R.K. Yuen, Y. Kan, Y.J.A.a.m. Hu, interfaces, Electrochemically Exfoliated Functionalized Black Phosphorene and Its Polyurethane Acrylate Nanocomposites: Synthesis and Applications, ACS Applied Materials & Interfaces 11 (2019) 13652-13664.

[42] J. Li, C. Chen, S. Liu, J. Lu, W.P. Goh, H. Fang, Z. Qiu, B. Tian, Z. Chen, C.J.C.o.M. Yao, Ultrafast Electrochemical Expansion of Black Phosphorus toward High-Yield Synthesis of Few-Layer Phosphorene, Chemistry of Materials 30(8) (2018) 2742-2749.

[43] A. Ambrosi, Z. Sofer, M.J.A.C.I.E. Pumera, Electrochemical Exfoliation of Layered Black Phosphorus into Phosphorene, Angewandte Chemie 56(35) (2017) 10443-10445.

[44] J. Backhurst, J. Coulson, F. Goodridge, R. Plimley, M.J.J.o.t.E.S. Fleischmann, A preliminary investigation of fluidized bed electrodes, Journal of the Electrochemical Society 116(11) (1969) 1600-1607.

[45] L. Koefoed, S.U. Pedersen, K.J.C.O.i.E. Daasbjerg, Bipolar electrochemistry—A wireless approach for electrode reactions, Current Opinion in Electrochemistry 2(1) (2017) 13-17.

[46] S.E. Fosdick, K.N. Knust, K. Scida, R.M.J.A.C.I.E. Crooks, Bipolar electrochemistry, Angewandte Chemie 52(40) (2013) 10438-10456.

[47] G. Loget, D. Zigah, L. Bouffier, N. Sojic, A.J.A.o.c.r. Kuhn, Bipolar electrochemistry: from materials science to motion and beyond, Accounts of Chemical Research 46(11) (2013) 2513-2523.

[48] A. Allagui, M.A. Abdelkareem, H. Alawadhi, A.S.J.S.r. Elwakil, Reduced graphene oxide thin film on conductive substrates by bipolar electrochemistry, Scientific Reports 6 (2016) 21282.

[49] A. Allagui, J.M. Ashraf, M. Khalil, M.A. Abdelkareem, A.S. Elwakil, H.J.C. Alawadhi, All-Solid-State Double-Layer Capacitors Using Binderless Reduced Graphene Oxide Thin Films Prepared by Bipolar Electrochemistry, ChemElectroChem 4(8) (2017) 2084-2090.

[50] I. Khakpour, A. Rabiei Baboukani, A. Allagui, C. Wang, Bipolar Exfoliation and in Situ Deposition of High-Quality Graphene for Supercapacitor Application, ACS Applied Energy Materials 2(7) (2019) 4813-4820.

[51] H. Hashimoto, Y. Muramatsu, Y. Nishina, H. Asoh, Bipolar anodic electrochemical exfoliation of graphite powders, Electrochemistry Communications 104 (2019) 106475.

[52] N. Mao, S. Zhang, J. Wu, J. Zhang, L.J.S.M. Tong, Lattice vibration and Raman scattering in anisotropic black phosphorus crystals, Small Methods 2(6) (2018) 1700409.

[53] Z. Guo, H. Zhang, S. Lu, Z. Wang, S. Tang, J. Shao, Z. Sun, H. Xie, H. Wang, X.F.J.A.F.M. Yu, From black phosphorus to phosphorene: basic solvent exfoliation, evolution of Raman scattering, and applications to ultrafast photonics, Advanced Functional Materials 25(45) (2015) 6996-7002.

[54] A. Favron, E. Gaufrès, F. Fossard, A.-L. Phaneuf-L'Heureux, N.Y. Tang, P.L. Lévesque, A. Loiseau, R. Leonelli, S. Francoeur, R.J.N.m. Martel, Photooxidation and quantum confinement effects in exfoliated black phosphorus, Nature Materials 14(8) (2015) 826.

[55] X. Ren, J. Zhou, X. Qi, Y. Liu, Z. Huang, Z. Li, Y. Ge, S.C. Dhanabalan, J.S. Ponraj, S.J.A.E.M. Wang, Few-layer black phosphorus nanosheets as electrocatalysts for highly efficient oxygen evolution reaction, Advanced Energy Materials 7(19) (2017) 1700396.

[56] F. Luo, D. Wang, J. Zhang, X. Li, D. Liu, H. Li, M. Lu, X. Xie, L. Huang, W.J.A.A.N.M. Huang, Ultrafast Cathodic Exfoliation of Few-Layer Black Phosphorus in Aqueous Solution, ACS Appl. Nano Mater. 2 (2019) 3793-3801.

[57] A. Castellanos-Gomez, L. Vicarelli, E. Prada, J.O. Island, K. Narasimha-Acharya, S.I. Blanter, D.J. Groenendijk, M. Buscema, G.A. Steele, J.J.D.M. Alvarez, Isolation and characterization of few-layer black phosphorus, 2D Materials 1(2) (2014) 025001.

[58] Y. Feng, J. Zhou, Y. Du, F. Miao, C.-G. Duan, B. Wang, X.J.J.o.P.C.M. Wan, Raman spectra of few-layer phosphorene studied from first-principles calculations, Journal of Physics: Condensed Matter 27(18) (2015) 185302.

[59] J.-Y. Xu, L.-F. Gao, C.-X. Hu, Z.-Y. Zhu, M. Zhao, Q. Wang, H.-L.J.C.C. Zhang, Preparation of large size, few-layer black phosphorus nanosheets via phytic acid-assisted liquid exfoliation, Chemical Communications 52(52) (2016) 8107-8110.

[60] W. Lu, H. Nan, J. Hong, Y. Chen, C. Zhu, Z. Liang, X. Ma, Z. Ni, C. Jin, Z. Zhang, Plasma-assisted fabrication of monolayer phosphorene and its Raman characterization, Nano Research 7(6) (2014) 853-859.

[61] K.L. Kuntz, R.A. Wells, J. Hu, T. Yang, B. Dong, H. Guo, A.H. Woomer, D.L. Druffel, A. Alabanza, D.J.A.a.m. Tománek, interfaces, Control of surface and edge oxidation on phosphorene, ACS Applied Materials & Interfaces 9(10) (2017) 9126-9135.

[62] H. Xiao, M. Zhao, J. Zhang, X. Ma, J. Zhang, T. Hu, T. Tang, J. Jia, H. Wu, Electrochemical cathode exfoliation of bulky black phosphorus into few-layer phosphorene nanosheets, Electrochemistry Communications 89 (2018) 10-13.

[63] Z. Sun, Y. Zhang, H. Yu, C. Yan, Y. Liu, S. Hong, H. Tao, A.W. Robertson, Z. Wang, A.A. Pádua, New solvent-stabilized few-layer black phosphorus for antibacterial applications, Nanoscale 10(26) (2018) 12543-12553.

[64] D.J.J.M. Late, M. Materials, Liquid exfoliation of black phosphorus nanosheets and its application as humidity sensor, Microporous and Mesoporous Materials 225 (2016) 494-503.

[65] J. Kang, J.D. Wood, S.A. Wells, J.-H. Lee, X. Liu, K.-S. Chen, M.C.J.A.n. Hersam, Solvent exfoliation of electronic-grade, two-dimensional black phosphorus, ACS Nano 9(4) (2015) 3596-3604.

[66] M. Fouda, A. Elwakil, A. Radwan, A. Allagui, Power and energy analysis of fractional-order electrical energy storage devices, Energy 111 (2016) 785-792.

[67] A. Allagui, D. Zhang, A.S. Elwakil, Short-term memory in electric double-layer capacitors, Applied Physics Letters 113(25) (2018) 253901.

[68] A. Allagui, T.J. Freeborn, A.S. Elwakil, M.E. Fouda, B.J. Maundy, A.G. Radwan, Z. Said, M.A.J.J.o.P.S. Abdelkareem, Review of fractional-order electrical characterization of supercapacitors, Journal of Power Sources 400 (2018) 457-467.

[69] A. Allagui, T.J. Freeborn, A.S. Elwakil, B.J.J.S.r. Maundy, Reevaluation of performance of electric double-layer capacitors from constant-current charge/discharge and cyclic voltammetry, Scientific Reports 6 (2016) 38568.

[70] I.J.I.T.o.a.c. Podlubny, Fractional-order systems and PI/sup/spl lambda//D/sup/spl mu//-controllers, IEEE Transactions on Automatic Control 44(1) (1999) 208-214.

[71] A.G. Radwan, A. Shamim, K.N.J.I.M. Salama, W.C. Letters, Theory of fractional order elements based impedance matching networks, IEEE Microwave and Wireless Components Letters 21(3) (2011) 120-122.

[72] A.S.J.I.C. Elwakil, S. Magazine, Fractional-order circuits and systems: An emerging interdisciplinary research area, IEEE Circuits and Systems Magazine 10(4) (2010) 40-50.

[73] M.E. Fouda, A. Allagui, A.S. Elwakil, A. Eltawil, F. Kurdahi, Supercapacitor discharge under constant resistance, constant current and constant power loads, Journal of Power Sources 435 (2019) 226829.

[74] M.E. Fouda, A. Allagui, A.S. Elwakil, A. Eltawil, F.J.J.o.P.S. Kurdahi, Supercapacitor discharge under constant resistance, constant current and constant power loads, Journal of Power Sources 435 (2019) 226829.

7. Defects Investigation of Bipolar Electrochemically Exfoliated Phosphorene Nanosheets Using Transmission Electron Microscopy

7.1 Introduction

Motivated by the discovery of graphene [1], other diversified atomically thin two-dimensional (2D) materials such as transition metal dichalcogenides (TMDs) [2], hexagonal boron nitride (hBN) [3], and layered transition metal oxides [4] have been evaluated for different applications due to their distinctive properties. Black phosphorus (BP) nanosheets (so-called phosphorene) as a unique member of 2D materials, has recently attracted considerable attention due to its physical and chemical properties [5-7]. In the structure of BP, each P atom is connected to three neighboring P atoms covalently and form a honeycomb puckered layered structures with an interlayer distance of around 5.3 Å [8]. BP can be exfoliated into a few or monolayer of 2D BP nanosheets through bottom-up and top-down techniques [9, 10]. Compared to the expensive and low-yield bottom-up methods, mechanical and liquid-based exfoliations of BP into phosphorene nanosheets have been successfully demonstrated in numerous studies [5, 11]. Very recently, we developed a novel bipolar electrochemical (BPE) approach for simultaneous exfoliation and deposition of phosphorene nanosheets on conductive substrates [12, 13].

In general, 2D materials inevitably incorporate different structural defects such as point defects, grain boundaries (GBs), impurities, and dislocations [14-16]. Due to the non-negligible effect of structural defects on the physical, chemical, and optical properties of 2D materials, investigating the defect structure is essential for further practical applications [17]. Besides, through the defect engineering of 2D materials, their

properties can also be tailored for specific applications [18]. With the rapid progress in high-resolution transmission electron microscopy (HR-TEM) as the most commonly used techniques, 2D materials have extensively been characterized in terms of atomic structure, the motion of atoms, chemical composition, and structure transformations in real-time [19, 20]. Moreover, large area diffraction can be performed to evaluate the crystallinity of exfoliated materials with atomic resolution [21]. Direct evidence by high-resolution transmission electron microscopy (HR-TEM) analysis has revealed the various types of defects, the modulation of the electronic structure and dopants within the lattice of their monolayer of graphene, TMDs, and hBN [22, 23]. Although invariable degradation of phosphorene nanosheets have been reported [24-27], its in-details defect characterization using TEM is still missing.

Recently, Density Functional Theory (DFT) calculations have been employed to evaluate the defects formation and their stability on the phosphorene nanosheets. DFT calculation predict different types of defects in phosphorene nanosheets with intriguing electronic properties [28]. For example, Wang and co-workers predicted the various stable defects such as single vacancies (SW), double vacancies (DV), and self-interstitials [29]. Theoretical calculations confirmed that the formation energies of these point defects are much lower compared to those in graphene, hBN, and TMDs [30]. On the other hand, Li et al. demonstrated that the migration and aggregation of point defects such as anisotropic SVs and DVs provided GBs between domains of different orientations in phosphorene nanosheets [31]. The formation energy of less than 1.5 eV nm^{-1}, revealing the thermodynamically stable phosphorene GBs [32].

In this study, we conducted the TEM investigation for the BPE exfoliated phosphorene nanosheets and obtained direct evidence of point defects, GBs, and amorphous regions on the phosphorene. Moreover, DFT calculations reveal that the amorphization occurs as a result of surface oxidation of phosphorene. Combining TEM analysis and DFT calculation provides new insight to understand the effect of the BPE method on defect formation and surface properties of phosphorene nanosheets.

7.2 Materials and Methods

7.2.1 Materials Synthesis

The schematic and in-details setup for the bipolar exfoliation of BP into phosphorene has been reported in our previous study [12]. In brief, a 1 cm long and 3 mm in diameter bulk BP bar (99.998% purity from Smart-Elements) was placed between the two 316 stainless steel feeding electrodes (1×2 cm^2) in deionized water. The 30 Vdc (i.e. an electric field of 10 V cm^{-1}) was applied between the two feeding electrodes for 24 hours under an ambient environment using a multichannel DC power analyzer (Agilent Technologies N6705A).

7.2.2 Material Characterization

After the bipolar exfoliation process, the dispersed phosphorene nanosheets were collected with DI water for HRTEM analysis (model Tecnai TF 20 TEM). The HRTEM analysis was conducted at an accelerating voltage of 200 kV, using a field emission gun with a 2 Å resolution. For the sample preparation, after the separation and dispersion of phosphorene nanosheets through sonication, one droplet of the solution was transferred

on the TEM grid covered by formvar carbon transparent film, and then, the TEM grids were stored in a dry atmosphere to remove the remaining liquids.

7.2.3 Computational Details

The first-principles density functional theory (DFT) calculations were performed by Atomistix ToolKit (ATK) package [33-35] using Generalized Gradient Approximation of Perdew–Burke–Ernzerhof (GGA-PBE) functionals with a double-ζ polarized basis set. To include the long-range van der Waals interactions, the Grimme vdW correction (PBE-D2) [36, 37] was considered. A supercell of monolayer phosphorene that contains 64 phosphorus atoms was assumed (Figure S1a). A vacuum space of 20 Å was added on both sides of the phosphorene plane in the direction that the sheet is not periodic (*z*) in order to avoid the image-image interactions. The oxygen atom was placed on various adsorption sites (top of phosphorus atoms, above hollow site, and top of a bridge between two phosphorus atoms) on phosphorene. All the possible structures were fully relaxed using the limited-memory Broyden-Fletcher-Goldfarb-Shanno (LBFGS) quasi-Newton method, with 0.01 eV/Å force tolerance and 0.001 eV/Å^3 stress tolerance. The electronic temperature was 300 K and the density mesh cut-off was set to be 125 Rydberg. Moreover, Monkhorst-Pack k-points mesh of 5 × 5 × 1 and 11×11×1 were used to sample the Brillouin zones during geometry optimization and to calculate the total energy and the electronic band structures. The adsorption energy per oxygen atom on the phosphorene sheet was calculated using equation 7.1 to find the most stable adsorption configuration (with the most negative adsorption energy).

$$E_{ad} = \frac{1}{n}[E_{Phosphorene+nO} - (E_{Phosphorene} + nE_O)] \quad (7.1)$$

where n, $E_{Phosphorene+nO}$, $E_{Phosphorene}$, and E_0 are the number of O atoms, total energies of the phosphorene-n oxygen atoms complex, pristine phosphorene sheet, and the isolated oxygen atom, respectively.

7.3 Results and Discussion

Similar to other 2D materials, phosphorene nanosheets could be damaged by electron irradiation during the TEM investigation. In order to obtain atomic-resolution images from the phosphorene nanosheets, the exposure of the material to the electron beam has to be minimized. The TEM images of the phosphorene nanosheets collected from DI water after 24-hour BPE exfoliation are shown in Figure 7.1 (a-d) and Figure 7.2 (a-d). The interplanar distances and the corresponding Miller indices are labeled on the TEM images. The exfoliated phosphorene nanosheets revealed different lattice fringes with interplanar distances of 0.21, 0.34, 0.25, and 0.23 nm, which could be assigned to the (002), (021), (111), and (041) atomic planes of orthorhombic BP crystal structure (JCPDS no 96-101-0326) [12]. These various plane orientations and domains of phosphorene nanosheets indicate the polycrystalline nature of the bulk BP. It is clear from the TEM images that the crystal structure of phosphorene nanosheets appears to be not affected much during the BPE exfoliation. However, as shown in Figure 7.1 (a), point defects as mono- and di-vacancies are present in phosphorene nanosheets (black patches indicated by red dashed circles). As shown in Figure 7.1 (a), the smallest defect located at the center of the image and labeled in red as (1) is related to the mono-vacancy. According to the DFT calculations, the simplest type of defect in phosphorene nanosheets

is the missing of one or two lattice atoms [28]. In general removal of a single phosphorus atom in phosphorene nanosheet and creating three dangling atoms distributed in two neighbors can form mono-vacancies on the nanosheet. The di-vacancies labeled in red as (2) in Figure 7.1 (a) could be created either by removing two neighboring phosphorus atoms or by coalescence of two mono-vacancies during the exposure of exfoliated phosphorene nanosheets to ambient environment or inside the TEM chamber [30]. Kistanov et al. theoretically demonstrated that the mono- and di-vacancies, which consist of pentagon-nonagon (59) and pentagon-heptagon-pentagon-heptagon (5757) rings, are the most common point defects in phosphorene nanosheets from the viewpoint of energetic stability [38].

Figure 7.1 (b) shows a few heavier bright atoms sprinkled over the whole surface of the phosphorene nanosheets, which are impurities as an ad-atom defect. The zoomed-in TEM image confirmed the presence of ad-atom. However, its origin is not entirely clear. It might present due to the contact with sample preparation equipment, impurity atoms in the TEM chamber or it could be introduced during the BPE exfoliation process where the stainless steel as a feeding electrode in DI-water were used. Clarification of this issue requires the employment of additional analytical methods, i.e., electron energy loss spectroscopy (EELS) which has been successfully employed to characterize impurities on the atomic scale in other 2D materials [39]. The zoomed-in TEM image on Figure 7.1 (b) revealed the honeycomb crystal structure of phosphorene nanosheets where each phosphorus atom is distinguished, and the pattern is repeated throughout the image.

Figure 7.1 (c, d) show the GBs defect composed of linear dislocation arrays of the (021) and (002) atomic planes of exfoliated phosphorene nanosheets. The main reason for the

GB formation in 2D materials is typically related to the polycrystalline nature of bulk material. As shown in Figure 7.1 (c), the GB region presents larger brightness than the rest of the nanosheet because of the high partial charge density around the GBs. Liu and co-workers theoretically confirmed that the GB energies in phosphorene nanosheets are lower than those in graphene, TMDs, and hBN [32]. This suggests higher stability of phosphorene nanosheets against lattice distortions compared to other 2D materials. Moreover, in a theoretical study by Zhu et al. high reactivity of GB regions with O atom as an impurity in phosphorene nanosheets has been confirmed. The GB defects in phosphorene do not have a significant effect on its electronic properties [16, 40]. The TEM images of the exfoliated phosphorene nanosheets via BPE method confirmed that the atomic network remains coherent with minor perturbations in the bond lengths.

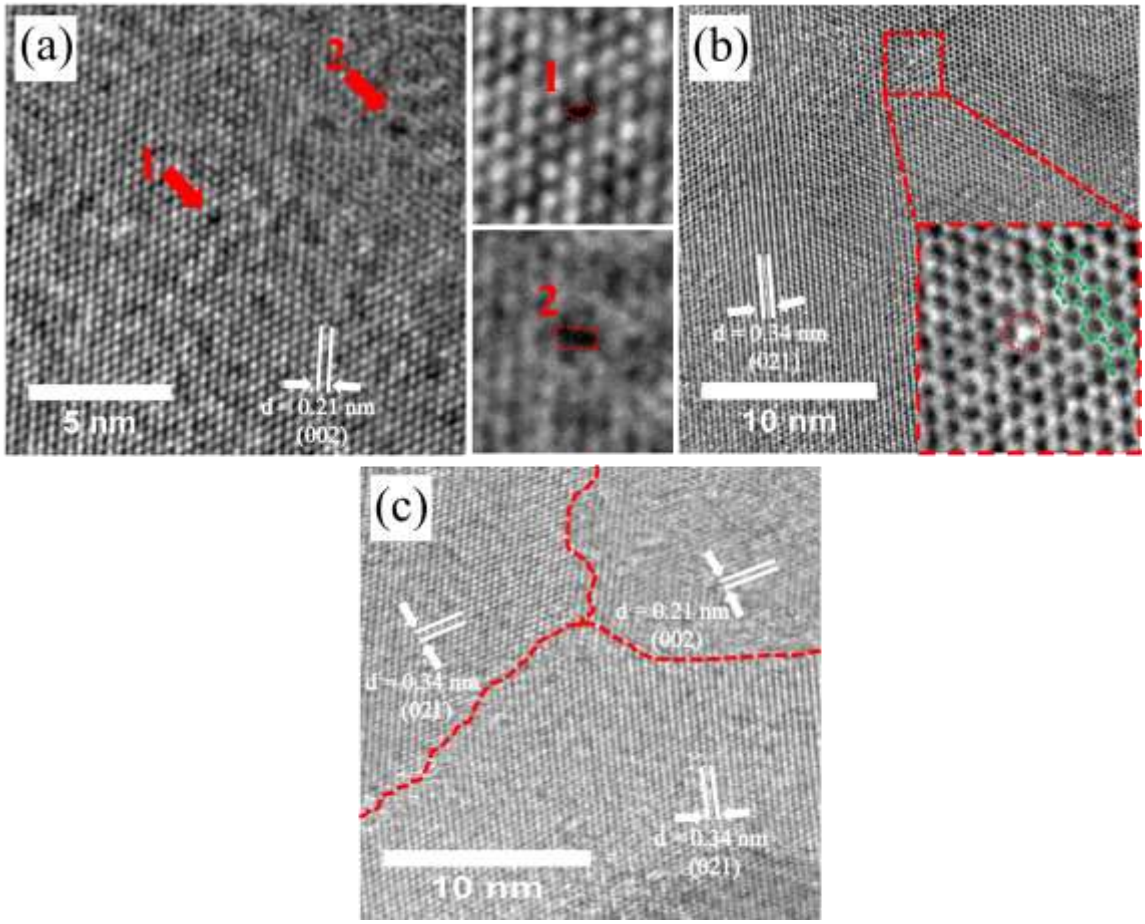

Figure 7.1: HRTEM images of (a) intrinsic mono- and di-vacancies, (b) ad-atom, and (c) grain boundary defects in phosphorene nanosheets obtained via bipolar electrochemistry method.

Figure 7.2 (a-c) shows the TEM images of phosphorene nanosheets with amorphous regions, which are most likely produced during the exfoliation of BP in DI water or exposure of nanosheets during sample preparation for TEM. The uniform amorphous layer can be easily visualized on the edge of (021) phosphorene nanosheets with less than 10nm thickness, as shown in Figure 7.2 (a, c). In Figure 7.2 (b), an amorphous domain with a size of about 10nm could be found in another (021) nanosheet. The instability of the phosphorene nanosheets upon exposure to the ambient environment was initially evaluated by theoretical calculations [41]. Several studies have shown that oxygen and

water degrade the phosphorene nanosheets [42-44]. Previous studies also confirmed that the phosphorene nanosheet rapidly degraded in vacuum at 300 kV accelerating voltage of e-beam [24]. The TEM images of phosphorene nanosheets obtained via BPE method revealed relatively good stability under the accelerated voltage of 200 kV. Figure 7.2 (a, c) shows the oxidation and amorphization on the edges of the phosphorene nanosheet which is likely related to the presence of phosphorus oxide along the edge of the nanosheets. The amorphous domains on the phosphorene nanosheet in Figure 7.2 (b) may be related to the polycrystalline nature of bulk BP. However, e-beam could also create oxygen radicals and degraded the phosphorene nanosheets. Especially, the phosphorus atoms on the surface do not have to be squeezed into an interstitial site; as a result, they are free to leave the nanosheets and then enter the chamber of the microscope. The theoretical calculations confirmed that due to the low displacement threshold in phosphorene nanosheets even a 80 kV beam should rapidly provide considerable damage [45]. Degradation of the sample exposed to ambient atmosphere confirms the high sensitivity of phosphorene nanosheets to oxygen and/or water molecules.

The stability of the pristine phosphorene sheet in the presence of an atomic oxygen was investigated by DFT calculations to further comprehend the degradation of the nanosheets during the bipolar exfoliation process, there storage and handling. The lattice constants for a monolayer of phosphorene were found to be a = 3.32 Å, b = 4.41 Å and the bandgap was calculated to be ~ 0.923 eV at the Γ point of the Brillouin zone, as shown in Figure 7S.1 that is in agreement with the previous reports [46].

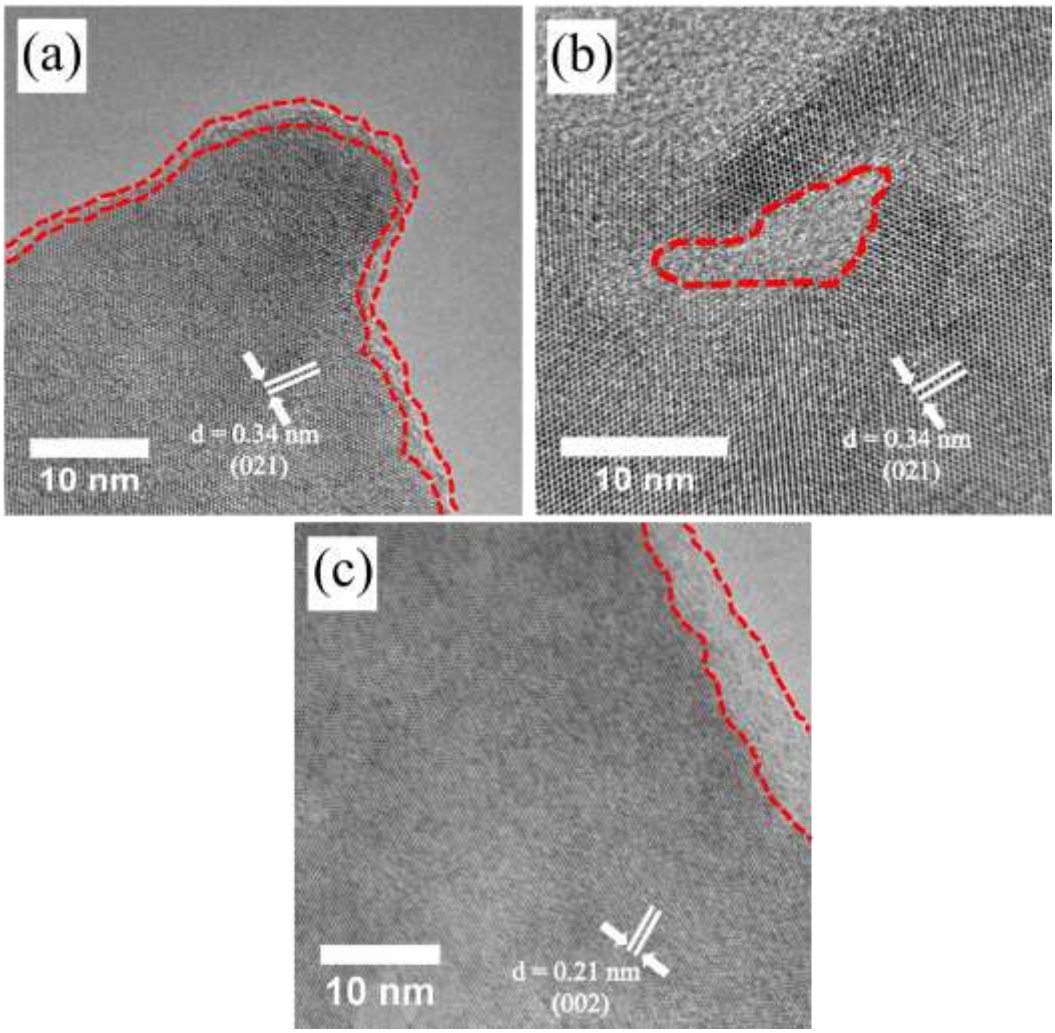

Figure 7.2: HRTEM images of (a-c) amorphization on the edges and surfaces of phosphorene nanosheets.

Due to the electron lone pair on the P atoms on the surface of phosphorene, P atoms are preferential sites to form bonds with O atoms. For the adsorption of a single oxygen atom, the most energetically favorable position was found to be on top of a phosphorus atom in the phosphorene's top sublattice (with P-O bond length of 1.52 Å and O-P-P angle of 113.06°, as shown in Figure 7.3 (a)). The large adsorption energy of −2.936 eV suggests that phosphorene can be easily oxidized through an oxygen atom's chemisorption. Figure 7.3 (b) shows the change in adsorption energy per oxygen atom on

the monolayer phosphorene as a function of the of oxygen concentration. With increasing the number of oxygen atoms in the supercell, the adsorption energies first increase (the structure becomes less stable) to −2.861 eV (for 4 oxygen atoms), then decrease (the structure becomes more stable) to −2.877 eV (for 8 oxygen atoms), are almost constant (1 meV fluctuations) for 8, 12, and 16 oxygen atoms, where the half of phosphorus atoms in the top sublattice of the phosphorene are oxidized. By increasing the number of oxygen atoms from 16 to 32 (where all the phosphorus atoms on the top side were oxidized), the adsorption energy was dramatically decreased with the rate of 0.028 eV/oxygen atom and reached −2.419 eV for 32 oxygen atoms. The most stable adsorption configurations for phosphorene oxide sheets with various oxygen concentrations (1-32) were provided in Figure 7S.2, and their adsorption energies were listed in Table 7.1. While the phosphorene sheet retains its initial puckered structure for 1-28 adsorbed oxygen atoms, its structure was distorted upon adsorption of 32 oxygen atoms, as shown in Figure 7.3 (a). From Figure 7S.3, one can see that fraction of oxygen atoms is adsorbed at the top site with P-O bond length of 1.49 Å and O-P-P bond angle of 133.56°, while others are embedded in the bridge between two phosphorus atoms with P-O bond lengths of 1.63 Å and 1.70 Å and P-O-P bond angle of 111.49°, resulting in cleavage of P-P bonds. The P-P bond length changed from 2.24 Å in bare phosphorene to 2.87 Å in phosphorene with 32 O atoms. Figure 7S.4 shows the energy band structures of phosphorene oxide sheets with various oxygen concentrations. Although the energy bandgap values for phosphorene with 1, 2, 4, 8, 20, and 24 oxygen atoms are larger than that of bare phosphorene, the presence of 12, 16, 28, and 32 oxygen atoms reduces the energy bandgap of the

phosphorene. Interestingly, the bandgap reduction caused by half top side oxygenated (16 atoms) and all top side oxygenated (32 atoms) are more highlighted.

In summary, the high adsorption energy obtained for an O atom on phosphorene suggests a chemisorption process and high sensitivity of phosphorene nanosheets to oxygen that is in agreement with TEM observations. Furthermore, our DFT data indicated that the breakage of P-P bonds in phosphorene upon oxidation results in amorphization, which correlates well with the TEM data observed in Figure 7.2 (c-d).

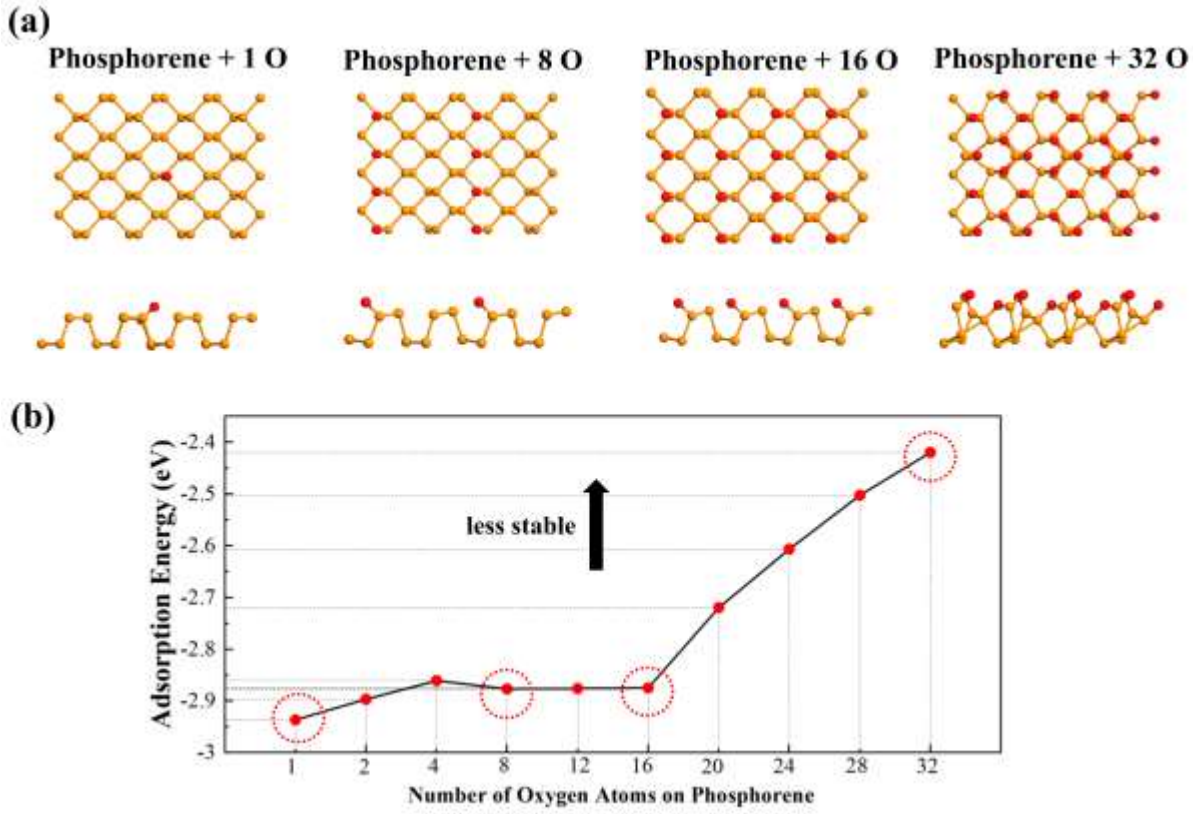

Figure 7.3: (a) The representative structures of phosphorene oxides with 1, 8, 16, 32 oxygen atoms. (b) Adsorption energy per oxygen atom as a function of oxygen concentration (P: Orange and O: red).

Table 7.1: The calculated adsorption energy per oxygen atom (Ead) and energy bandgap (Eg) for bare phosphorene and phosphorene oxide sheets with various oxygen concentrations.

System	$E_{ad\ per\ O\ atom}$ (eV)	E_g (eV)
Bare Phosphorene	-	0.923
Phosphorene + 1 O	−2.936	0.985
Phosphorene + 2 O	−2.896	1.039
Phosphorene + 4 O	−2.861	1.060
Phosphorene + 8 O	−2.877	1.099
Phosphorene + 12 O	−2.876	0.901
Phosphorene + 16 O	−2.875	0.852
Phosphorene + 20 O	−2.719	0.980
Phosphorene + 24 O	−2.606	1.129
Phosphorene + 28 O	−2.502	0.912
Phosphorene + 32 O	−2.419	0.377

7.4 Conclusion

Since the novel 2D materials will function significantly in the future development of materials, evaluating the relationship between their atomic structure and properties is vital. In this study, for the first time, we present a study on defects in bipolar exfoliated phosphorene nanosheets. We have shown in this chapter that different types of atomic defects can directly be determined via high-resolution TEM imaging. TEM characterization suggests that the point defects, GBs and amorphous regions are formed in phosphorene nanosheet. It observed that the exposure of phosphorene for several days to ambient conditions leads to very fast degradation of phosphorene nanosheets. Finally, DFT results disclosed that surface oxidation of the phosphorene caused the breakage of P-P bonds and the amorphization. The atomistic insight into the phosphorene nanosheets from our study will likely benefit future experimental and theoretical studies on BP for novel futuristic applications.

7.5 References

[1] K.S. Novoselov, A.K. Geim, S.V. Morozov, D. Jiang, Y. Zhang, S.V. Dubonos, I.V. Grigorieva, A.A. Firsov, Electric field effect in atomically thin carbon films, science 306(5696) (2004) 666-669.

[2] Z. Zeng, Z. Yin, X. Huang, H. Li, Q. He, G. Lu, F. Boey, H. Zhang, Single-Layer Semiconducting Nanosheets: High-yield preparation and device fabrication, Angewandte Chemie 123(47) (2011) 11289-11293.

[3] W.-Q. Han, L. Wu, Y. Zhu, K. Watanabe, T. Taniguchi, Structure of chemically derived mono-and few-atomic-layer boron nitride sheets, Applied Physics Letters 93(22) (2008) 223103.

[4] K. Kalantar-zadeh, J.Z. Ou, T. Daeneke, A. Mitchell, T. Sasaki, M.S. Fuhrer, Two dimensional and layered transition metal oxides, Applied Materials Today 5 (2016) 73-89.

[5] A. Rabiei Baboukani, I. Khakpour, V. Drozd, C. Wang, Liquid-Based Exfoliation of Black Phosphorus into Phosphorene and Its Application for Energy Storage Devices, Small Structures (2021) 2000148.

[6] D.K. Sang, H. Wang, Z. Guo, N. Xie, H. Zhang, Recent Developments in Stability and Passivation Techniques of Phosphorene toward Next-Generation Device Applications, Advanced Functional Materials 29(45) (2019) 1903419.

[7] Y. Tao, T. Huang, C. Ding, F. Yu, D. Tan, F. Wang, Q. Xie, S. Yao, Few-layer phosphorene: An emerging electrode material for electrochemical energy storage, Applied Materials Today 15 (2019) 18-33.

[8] T. Low, A. Rodin, A. Carvalho, Y. Jiang, H. Wang, F. Xia, A.C. Neto, Tunable optical properties of multilayer black phosphorus thin films, Physical Review B 90(7) (2014) 075434.

[9] S. Witomska, T. Leydecker, A. Ciesielski, P. Samorì, Production and patterning of liquid phase–exfoliated 2D sheets for applications in optoelectronics, Advanced Functional Materials 29(22) (2019) 1901126.

[10] S. Yang, P. Zhang, A.S. Nia, X. Feng, Emerging 2D Materials Produced via Electrochemistry, Advanced Materials 32(10) (2020) 1907857.

[11] C. Xing, J. Zhang, J. Jing, J. Li, F. Shi, Preparations, properties and applications of low-dimensional black phosphorus, Chemical Engineering Journal 370 (2019) 120-135.

[12] A.R. Baboukani, I. Khakpour, V. Drozd, A. Allagui, C. Wang, Single-step exfoliation of black phosphorus and deposition of phosphorene via bipolar electrochemistry for capacitive energy storage application, Journal of Materials Chemistry A 7(44) (2019) 25548-25556.

[13] A.R. Baboukani, I. Khakpour, C. Wang, Bipolar exfoliation of black phosphorous into phosphorene, Google Patents, 2020.

[14] Z. Lin, A. McCreary, N. Briggs, S. Subramanian, K. Zhang, Y. Sun, X. Li, N.J. Borys, H. Yuan, S.K. Fullerton-Shirey, 2D materials advances: from large scale synthesis and controlled heterostructures to improved characterization techniques, defects and applications, 2D Materials 3(4) (2016) 042001.

[15] Z. Wu, Z. Ni, Spectroscopic investigation of defects in two-dimensional materials, Nanophotonics 6(6) (2017) 1219-1237.

[16] Y. Guo, S. Zhou, J. Zhang, Y. Bai, J. Zhao, Atomic structures and electronic properties of phosphorene grain boundaries, 2D Materials 3(2) (2016) 025008.

[17] D. Rhodes, S.H. Chae, R. Ribeiro-Palau, J. Hone, Disorder in van der Waals heterostructures of 2D materials, Nature materials 18(6) (2019) 541.

[18] J. Pei, X. Gai, J. Yang, X. Wang, Z. Yu, D.-Y. Choi, B. Luther-Davies, Y. Lu, Producing air-stable monolayers of phosphorene and their defect engineering, Nature communications 7(1) (2016) 1-8.

[19] H.I. Rasool, C. Ophus, A. Zettl, Atomic defects in two dimensional materials, Advanced materials 27(38) (2015) 5771-5777.

[20] D. Muller, L.F. Kourkoutis, M. Murfitt, J. Song, H. Hwang, J. Silcox, N. Dellby, O. Krivanek, Atomic-scale chemical imaging of composition and bonding by aberration-corrected microscopy, Science 319(5866) (2008) 1073-1076.

[21] P.Y. Huang, C.S. Ruiz-Vargas, A.M. Van Der Zande, W.S. Whitney, M.P. Levendorf, J.W. Kevek, S. Garg, J.S. Alden, C.J. Hustedt, Y. Zhu, Grains and grain boundaries in single-layer graphene atomic patchwork quilts, Nature 469(7330) (2011) 389-392.

[22] J. Hong, C. Jin, J. Yuan, Z. Zhang, Atomic Defects in Two-Dimensional Materials: From Single-Atom Spectroscopy to Functionalities in Opto-/Electronics, Nanomagnetism, and Catalysis, Advanced Materials 29(14) (2017) 1606434.

[23] T. Susi, D. Kepaptsoglou, Y.-C. Lin, Q.M. Ramasse, J.C. Meyer, K. Suenaga, J. Kotakoski, Towards atomically precise manipulation of 2D nanostructures in the electron microscope, 2D Materials 4(4) (2017) 042004.

[24] A.E. Naclerio, D.N. Zakharov, J. Kumar, B. Rogers, C.L. Pint, M. Shrivastava, P.R. Kidambi, Visualizing Oxidation Mechanisms in Few-Layered Black Phosphorus via In Situ Transmission Electron Microscopy, ACS Applied Materials & Interfaces 12(13) (2020) 15844-15854.

[25] C. Hyun, J.H. Kim, J.-Y. Lee, G.-H. Lee, K.S. Kim, Atomic scale study of black phosphorus degradation, RSC Advances 10(1) (2020) 350-355.

[26] M. van Druenen, F.n. Davitt, T. Collins, C. Glynn, C. O'Dwyer, J.D. Holmes, G. Collins, Evaluating the surface chemistry of black phosphorus during ambient degradation, Langmuir 35(6) (2019) 2172-2178.

[27] K.L. Kuntz, R.A. Wells, J. Hu, T. Yang, B. Dong, H. Guo, A.H. Woomer, D.L. Druffel, A. Alabanza, D. Tománek, Control of surface and edge oxidation on phosphorene, ACS applied materials & interfaces 9(10) (2017) 9126-9135.

[28] Y. Cai, Q. Ke, G. Zhang, B.I. Yakobson, Y.-W. Zhang, Highly itinerant atomic vacancies in phosphorene, Journal of the American Chemical Society 138(32) (2016) 10199-10206.

[29] V. Wang, Y. Kawazoe, W. Geng, Native point defects in few-layer phosphorene, Physical Review B 91(4) (2015) 045433.

[30] W. Hu, J. Yang, Defects in phosphorene, The Journal of Physical Chemistry C 119(35) (2015) 20474-20480.

[31] X. Li, L. Ma, D. Wang, X.C. Zeng, X. Wu, J. Yang, Point defects in lines in single crystalline phosphorene: directional migration and tunable band gaps, Nanoscale 8(41) (2016) 17801-17808.

[32] Y. Liu, F. Xu, Z. Zhang, E.S. Penev, B.I. Yakobson, Two-dimensional mono-elemental semiconductor with electronically inactive defects: the case of phosphorus, Nano letters 14(12) (2014) 6782-6786.

[33] J. Taylor, H. Guo, J. Wang, Ab initio modeling of quantum transport properties of molecular electronic devices, Physical Review B 63(24) (2001) 245407.

[34] M. Brandbyge, J.-L. Mozos, P. Ordejón, J. Taylor, K. Stokbro, Density-functional method for nonequilibrium electron transport, Physical Review B 65(16) (2002) 165401.
[35] Q. Simulator, Atomistix ToolKit (ATK), 2012.

[36] S. Grimme, Semiempirical GGA-type density functional constructed with a long-range dispersion correction, Journal of computational chemistry 27(15) (2006) 1787-1799.

[37] S. Grimme, C. Mück-Lichtenfeld, J. Antony, Noncovalent interactions between graphene sheets and in multishell (hyper) fullerenes, The Journal of Physical Chemistry C 111(30) (2007) 11199-11207.

[38] A.A. Kistanov, Y. Cai, K. Zhou, S.V. Dmitriev, Y.-W. Zhang, The role of H2O and O2 molecules and phosphorus vacancies in the structure instability of phosphorene, 2D Materials 4(1) (2016) 015010.

[39] U. Bangert, A. Stewart, E. O'Connell, E. Courtney, Q. Ramasse, D. Kepaptsoglou, H. Hofsäss, J. Amani, J.-S. Tu, B. Kardynal, Ion-beam modification of 2-D materials-single implant atom analysis via annular dark-field electron microscopy, Ultramicroscopy 176 (2017) 31-36.

[40] Z.-L. Zhu, W.-Y. Yu, X.-Y. Ren, Q. Sun, Y. Jia, Grain boundary in phosphorene and its unique roles on C and O doping, EPL (Europhysics Letters) 109(4) (2015) 47003.

[41] A. Castellanos-Gomez, L. Vicarelli, E. Prada, J.O. Island, K. Narasimha-Acharya, S.I. Blanter, D.J. Groenendijk, M. Buscema, G.A. Steele, J. Alvarez, Isolation and characterization of few-layer black phosphorus, 2D Materials 1(2) (2014) 025001.

[42] D. Grasseschi, D. Bahamon, F. Maia, A.C. Neto, R. Freitas, C. De Matos, Oxygen impact on the electronic and vibrational properties of black phosphorus probed by synchrotron infrared nanospectroscopy, 2D Materials 4(3) (2017) 035028.

[43] Y. Huang, J. Qiao, K. He, S. Bliznakov, E. Sutter, X. Chen, D. Luo, F. Meng, D. Su, J. Decker, W. Ji, R.S. Ruoff, P. Sutter, Interaction of Black Phosphorus with Oxygen and Water, Chemistry of Materials 28(22) (2016) 8330-8339.

[44] W. Luo, D.Y. Zemlyanov, C.A. Milligan, Y. Du, L. Yang, Y. Wu, D.Y. Peide, Surface chemistry of black phosphorus under a controlled oxidative environment, Nanotechnology 27(43) (2016) 434002.

[45] V. Vierimaa, A.V. Krasheninnikov, H.-P. Komsa, Phosphorene under electron beam: from monolayer to one-dimensional chains, Nanoscale 8(15) (2016) 7949-7957.

[46] H. Liu, A.T. Neal, Z. Zhu, Z. Luo, X. Xu, D. Tománek, P.D. Ye, Phosphorene: an unexplored 2D semiconductor with a high hole mobility, ACS nano 8(4) (2014) 4033-4041.

8. Conclusions and Outlook

8.1 Summary

This dissertation presents design, construction, and materials/electrochemical characterizations of phosphorus-based electrodes for high-performance Li-ion batteries and supercapacitors. Increasing the conductivity and controlling the volume expansion are the main solutions to enhance the electrochemical performances of P-based electrodes. In terms of 2D phosphorene nanosheet synthesis, several top-down and bottom-up exfoliation techniques are proposed which are multi-step and toxic. To overcome these issues, bipolar electrochemical exfoliation technique has been adopted in order to maximize the materials and electrochemical performance of the BP-based electrodes. The major findings of this dissertation are summarized as follows:

In this first phase of this project, red phosphorus/sulfurized polyacrylonitrile (RP-SPAN) hybrid anode was synthesized and analyzed for high-performance Li-ion batteries (LIBs) through high-energy ball milling and electrostatic spray deposition (ESD) technique. The fabricated electrodes were evaluated as an anode material against a lithium as counter and reference electrode and delivered a highly reversible specific capacity of 1605 mAh g^{-1} at 100 mAh g^{-1} and high-rate capability of 696 mAh g^{-1} at 1 A g^{-1}. The superior cell characteristics of RP-SPAN composite were attributed to the improved kinetics and chemical bonding formed of SPAN with RP during the ball milling and binder-free ESD technique which improved the conductivity and control the volume change of P-based electrodes.

In the second phase of this project, RP-SPAN hybrid anode were synthesized using ball milling and ESD techniques and investigated its stability in both frequency and time domains using the transfer function stability analysis, the Kramers-Kronig (KK) integral relations, and the differential capacity analysis for LIB application. The electrochemical behavior of RP-SPAN electrodes was evaluated in terms of stationarity, stability and linearity, as well as dissipation and degradation with extended charge/discharge cycling. we inspected the stability of the frequency-domain transfer function estimate of the battery response to small amplitude sinusoidal voltage excitations from 1 MHz down to 1 mHz. The results show that the system is highly nonlinear and time-variant at the low-frequencies spectrum which is in line with the 0.21% average capacity loss per cycle that we computed from consecutive charge/discharge measurements. We proposed a modified constant phase element in which magnitude and phase, and thus real and imaginary parts, of spectral response are decoupled to fit the low-frequency non-KK-compliant data. These characteristics of the battery were in line with time-domain measurements of differential capacity obtained from constant current cycling.

In the third phase of this project, a novel two-in-one exfoliation and deposition from bulk BP to phosphorene nanosheets was carried out via bipolar electrochemical exfoliation (BPE) method for supercapacitor applications. In the initial step of this phase, in the presence of Vdc electrophoresis phenomenon, exfoliated phosphorene nanosheets were transferred and deposited on the positive feeding electrode. Materials characterization techniques confirmed the orthorhombic crystal structure of the deposited materials on stainless steel. Furthermore, the fabricated device based on the symmetric in a two-electrode symmetric configuration delivered a discharge energy of 0.01 mW h

cm^{-2} at a constant current load discharge of 500 mA cm^{-2} but with a high power density of 351 mW cm^{-2}, which is comparable with other 2D-based devices. The nearly rectangular cyclic voltammetry curves of the fabricated device confirmed the double-layer charge storage mechanism. The device also exhibited a fractional order capacitive behavior in the low-to-medium frequency range, and a high stability and reversibility for at least 40000 cycles. To further examine the utility of BPE in the exfoliation of BP and in the modified BPE setup, positive feeding electrode was replaced with platinum wire to evaluate the possible deposition of exfoliated phosphorene nanosheets on the negative feeding electrode. After 24 hours of the process, obvious 2D reduced phosphorene nanosheets were deposited uniformly on the stainless steel substrate. Using X-ray photoelectron spectroscopy (XPS) and Raman analysis confirmed the successful exfoliation and deposition of phosphorene nanosheets on the negative feeding electrode.

In the last phase of this project, a combination of high-resolution transmission electron microscopy (HRTEM) imaging and density functional theory (DFT) calculations were provided to study the defects formation of phosphorene nanosheets obtained via BPE process. The TEM results demonstrated that the mono- and di-vacancies, ad-atoms, and grain boundary defects are formed in phosphorene nanosheets. However, the atomic orthorhombic crystal structure of phosphorene shows a minor perturbation. Moreover, the DFT calculations confirmed the breakage of P-P bonds of phosphorene nanosheets upon surface oxidation, which results in amorphization. The defect analysis of phosphorene nanosheets obtained from this phase could benefit both fundamental research and technological applications. In summary, in this dissertation, a systematic study of P-based

electrodes from materials and electrochemical point of view were evaluated for energy storage applications. Also, from stability point of view, the in-details P-based electrodes were analysis using TEM analysis and DFT calculation.

8.2 Future Works

The present dissertation has introduced novel techniques to fabricate phosphorus-based electrodes for high-performance energy storage devices. Based on the current work, the author suggests the following future work to be undertaken:

1. ***Optimization of P-based electrodes for energy storage devices:*** Continuous efforts should be made to optimize the morphology and microstructure of the conductive polymer matrix in the developed P-based electrode. A comprehensive theoretical calculation for predicting the optimum composition of phosphorus with the conductive matrix is essential for high-performance energy storage devices. Exfoliated phosphorene provided continuous pathways for ion transport in energy storage applications. However, the mass loading of phosphorene nanosheets and the specific capacitance is still low compared to the graphene-based devices.
2. ***In-depth understanding of the reaction mechanism of P-based electrodes:*** Although the performance of the P-based electrodes is exceptional in different energy storage devices, the detailed systematic evaluation on the reaction dynamics and electrochemical mechanisms are still missing. For instance, using operando spectroscopy analysis (in situ XRD, TEM, SEM) to study the intercalation and degradation mechanism of P-based electrodes will be helpful.

3. ***Layer-by-layer exfoliation and deposition of phosphorene nanosheets with other 2D materials:*** One of the major goals in dissertation was based on the exfoliation of BP into phosphorene nanosheets for energy storage devices. Design the experimental setup to exfoliate and synthesized a nanostructured phosphorene/graphene hybrid or other 2D materials with a layer-by-layer sandwiched structure and its material and electrochemical properties will reveal useful information. The author believes that the 2D layer-by-layer structure of phosphorene/graphene would increase the conductivity and control the volume change and as a result better energy storage properties.
4. ***Full-cell characterization of P-based electrodes:*** To the best of our knowledge, most of the recent research have focused on the design and characterization of P-based electrodes as a half-cell or symmetric device. Evaluation of P-based electrodes in a full-cell setup for practical applications is a necessary future research direction.
5. ***Control the degradation of exfoliated phosphorene nanosheets:*** Single-step exfoliation and deposition of BP into phosphorene nanosheets via eco-friendly BPE is an attractive technique. However, the surface stability of phosphorene nanosheets in this method is still difficult to control and it needs a synergy approach to overcome this issue. Introducing an additive into the DI water during the exfoliation may control the degradation of nanosheets for device applications.

APPENDIX

Supplementary Information for Chapter 4

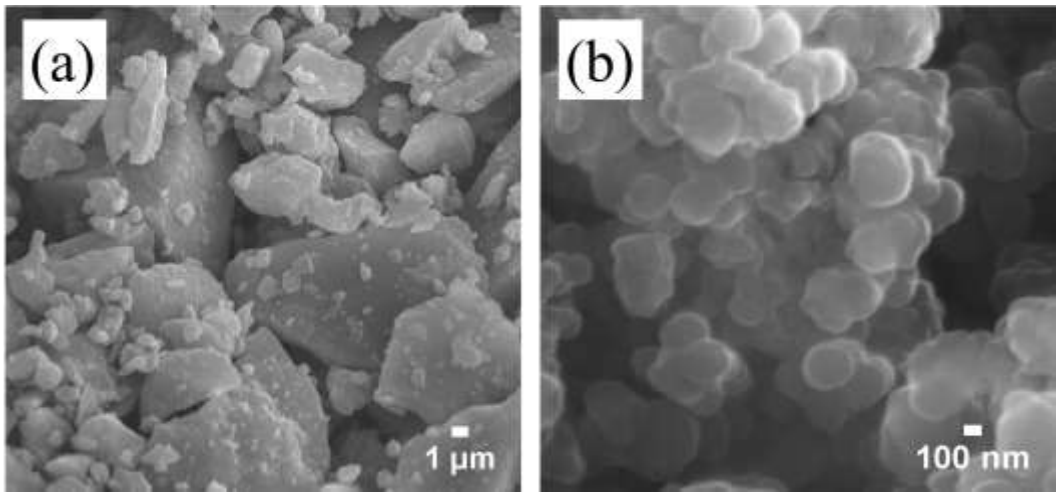

Figure 4S.1: Typical SEM images of (a) pure RP, (b) SPAN.

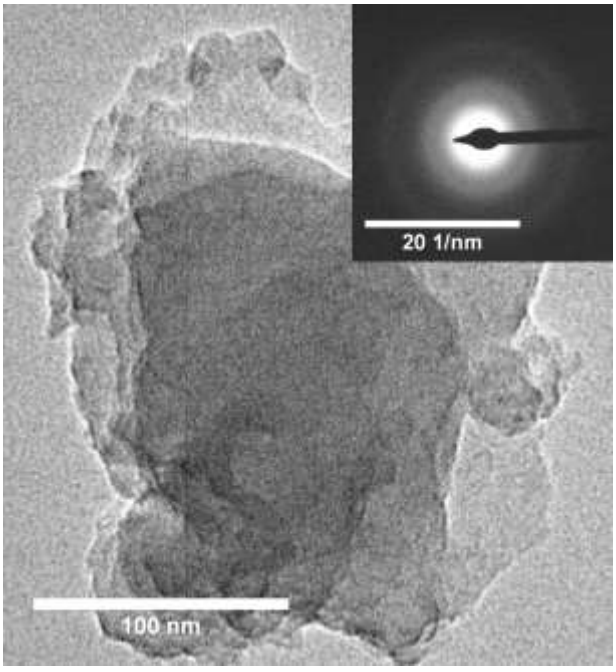

Figure 4S.2: TEM image of RP-SPAN hybrid (the insert showing the SAED pattern).

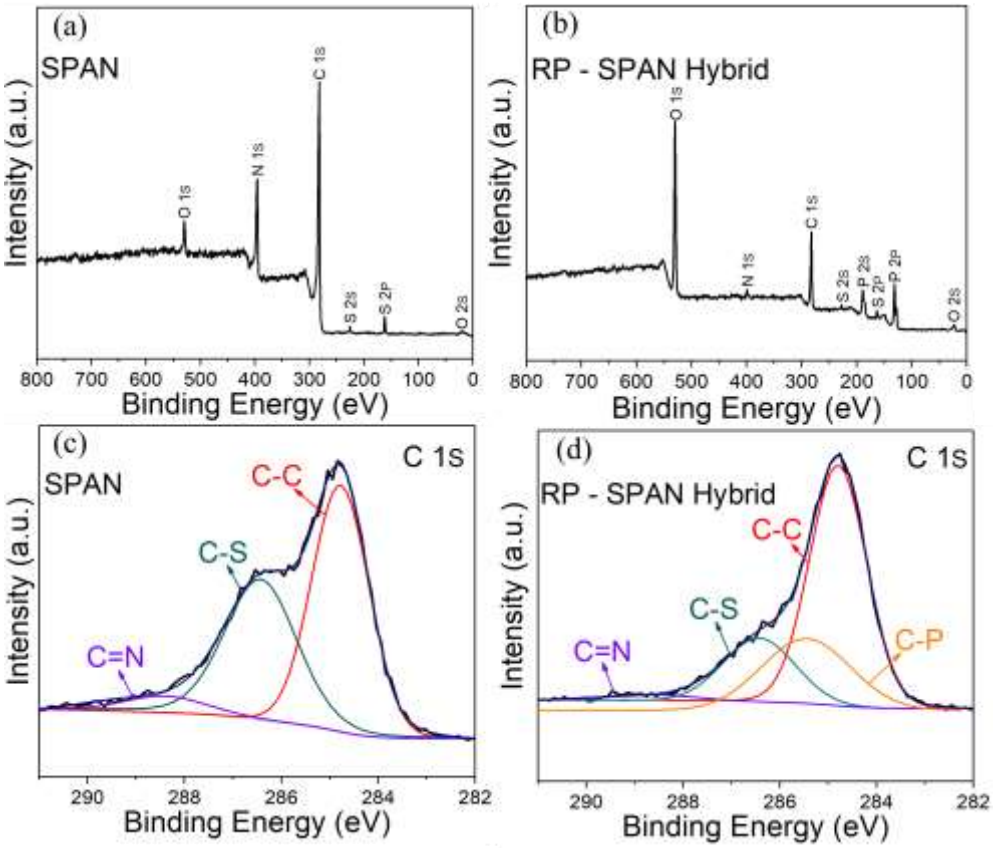

Figure 4S.3: XPS survey and C1S spectra of (a, c) SPAN, and (b, d) RP-SPAN hybrid.

Table 4S.1: Electrochemical performance of P-based composite as an anode material for LIBs.

Sample	Preparation Method	Potential Window (V)	Retained Discharge Capacity ($mAhg^{-1}$)	Current Density (mAg^{-1})	Cycle Number	Ref.
RP/Bacterial cellulose	Vaporization-condensation	0.01-2.5	1039	260	100	[1]
RP/Porous CNF	Electrospinning	0.01-3.0	900	100	35	[2]
RP/CNT hybrid	Ball milling	0.01-2.0	1850	780	50	[3]
RP/TiO_2/CNT	Ultrahigh Sonication	0.01-3.0	1250	200	300	[4]
RP/CNT	Solution approach	0.01-2.0	1012	100	100	[5]
RP/Graphene	Electrospraying	0.01-3.0	1450	50	100	[6]
RP/rGO	Hydrothermal	0.01-2.5	1000	100	80	[7]
RP/Fluffy carbon	Ball milling	0.01-3.0	1480	130	100	[8]
RP/Graphene	Ball milling	0.01-2.0	1283	130	100	[9]
RP/CNT	Ball milling	0.01-2.5	1640	50	50	[10]
RP/CNT	Solution approach	0.01-3.0	960	200	120	[11]
RP/CNT sponge	Hydrothermal	0.01-3.0	1600	100	50	[12]
RP/SPAN	Ball milling/ESD	0.01-3.0	1605	100	100	This work

Table 4S.2: Electrochemical parameters of the equivalent circuit for the prepared electrodes.

Sample	R_1 (Ω)	R_2 (Ω)	CPE (F)	W (Ω $S^{-0.5}$)
RP	9.95	1797	1.50×10^{-4}	163.50
RP – SPAN hybrid before cycling	8.33	592	1.80×10^{-4}	71.71
RP – SPAN hybrid after cycling	7.53	35	2.07×10^{-4}	35.11

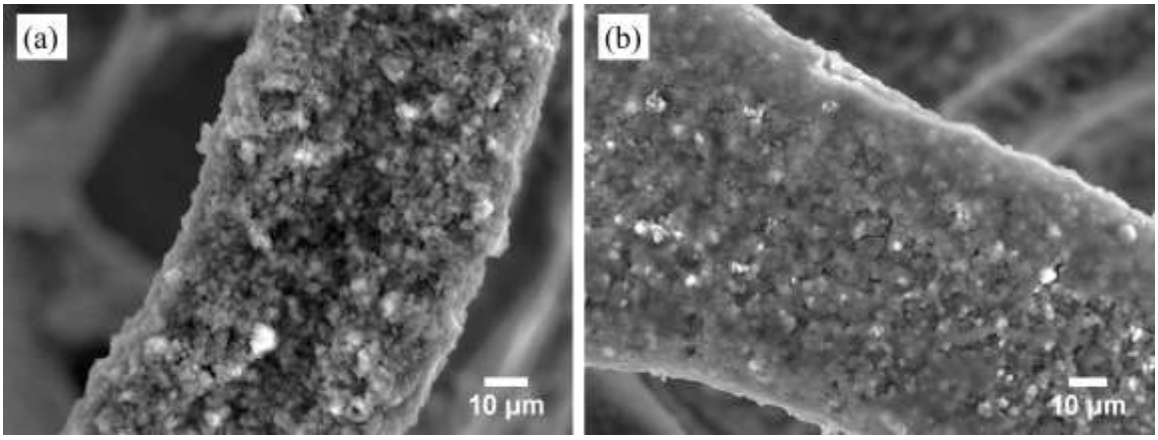

Figure 4S.4: SEM images of the ESD-based RP-SPAN hybrid electrode, (a) before, and (b) after 180 cycles charge/discharge cycles.

References

[1] H. Yang, Y. Li, P. Long, J. Han, C. Cao, F. Yao, W. Feng, Amorphous red phosphorus incorporated with pyrolyzed bacterial cellulose as a free-standing anode for high-performance lithium ion batteries, RSC Advances 8(31) (2018) 17325-17333.

[2] L. Wang, J. Ju, N. Deng, B. Cheng, W. Kang, Embedding red phosphorus in hierarchical porous carbon nanofibers as anodes for lithium-ion battery, Materials Letters 240 (2019) 39-43.

[3] X. Jiao, Y. Liu, B. Li, W. Zhang, C. He, C. Zhang, Z. Yu, T. Gao, J. Song, Amorphous phosphorus-carbon nanotube hybrid anode with ultralong cycle life and high-rate capability for lithium-ion battery, Carbon 148 (2019) 518-524.

[4] L. Sun, Y. Zhang, H. Si, Y. Zhang, J. Liu, J. Liu, Y. Zhang, TiO2-modified red phosphorus nanosheets entangled in carbon nanotubes for high performance lithium ion batteries, Electrochimica Acta 297 (2019) 319-327.

[5] J. Li, H. Jin, Y. Yuan, H. Lu, C. Su, D. Fan, Y. Li, J. Wang, J. Lu, S. Wang, Encapsulating phosphorus inside carbon nanotubes via a solution approach for advanced lithium ion host, Nano Energy 58 (2019) 23-29.

[6] Z. Yue, T. Gupta, F. Wang, C. Li, R. Kumar, Z. Yang, N. Koratkar, Utilizing a graphene matrix to overcome the intrinsic limitations of red phosphorus as an anode material in lithium-ion batteries, Carbon 127 (2018) 588-595.

[7] X. Zhu, Z. Yuan, X. Wang, G. Jiang, J. Xiong, S. Yuan, Hydrothermal synthesis of red phosphorus@ reduced graphene oxide nanohybrid with enhanced electrochemical performance as anode material of lithium-ion battery, Applied Surface Science 433 (2018) 125-132.

[8] H. Liu, S. Zhang, Q. Zhu, B. Cao, P. Zhang, N. Sun, B. Xu, F. Wu, R. Chen, Fluffy carbon-coated red phosphorus as a highly stable and high-rate anode for lithium-ion batteries, Journal of Materials Chemistry A 7(18) (2019) 11205-11213.

[9] Z. Yu, J. Song, M.L. Gordin, R. Yi, D. Tang, D. Wang, Phosphorus-Graphene Nanosheet Hybrids as Lithium-Ion Anode with Exceptional High-Temperature Cycling Stability, Advanced Science 2(1-2) (2015) 1400020.

[10] Z. Xu, Y. Zeng, L. Wang, N. Li, C. Chen, C. Li, J. Li, H. Lv, L. Kuang, X. Tian, Nanoconfined phosphorus film coating on interconnected carbon nanotubes as ultrastable anodes for lithium ion batteries, Journal of Power Sources 356 (2017) 18-26.

[11] L. Sun, Y. Zhang, D. Zhang, J. Liu, Y. Zhang, Amorphous red phosphorus anchored on carbon nanotubes as high performance electrodes for lithium ion batteries, Nano Research 11(5) (2018) 2733-2745.

[12] T. Yuan, J. Ruan, C. Peng, H. Sun, Y. Pang, J. Yang, Z.-F. Ma, S. Zheng, 3D red phosphorus/sheared CNT sponge for high performance lithium-ion battery anodes, Energy Storage Materials 13 (2018) 267-273.

Supplementary Information for Chapter 5

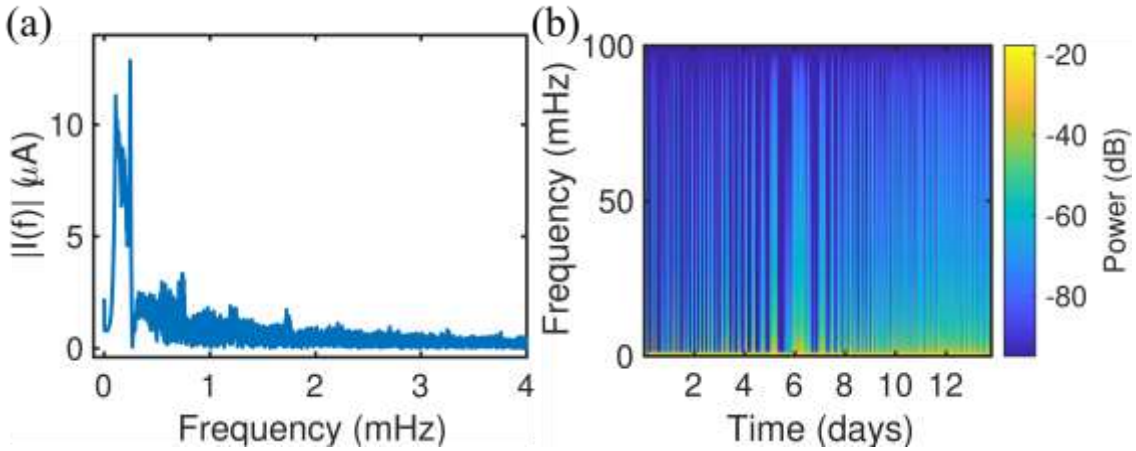

Figure 5S.1: Results of constant current ±95 mA charging/discharging of the battery cell: (a) FFT of the time-domain outup voltage signal; (b) spectrogram computed using short-time Fourier transform (STFT) which depicts the frequency content of the output voltage signal as it varies with time.

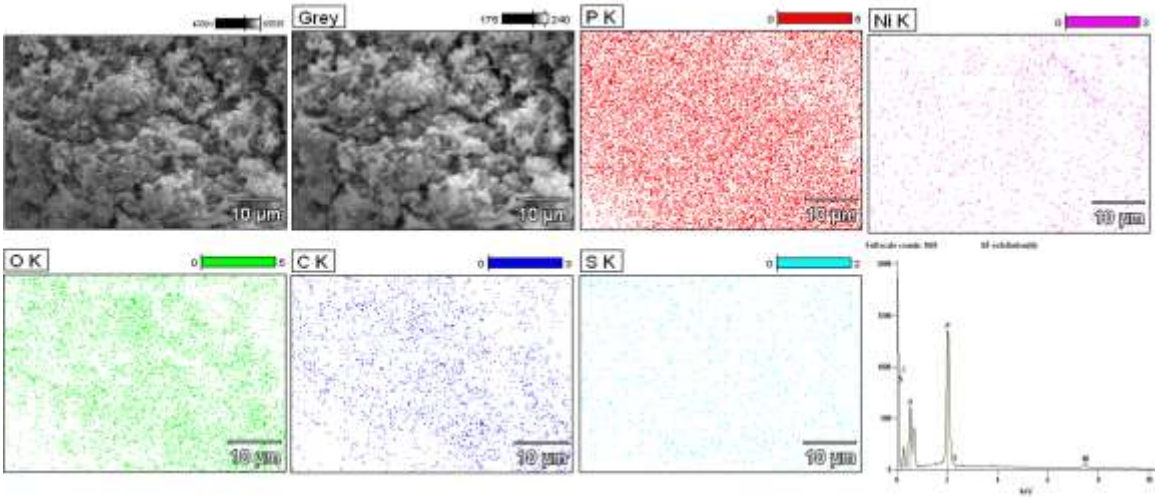

Figure 5S.2: EDS elemental mapping images for P, Ni, O, C, and S in RP-SPAN hybrid composite.

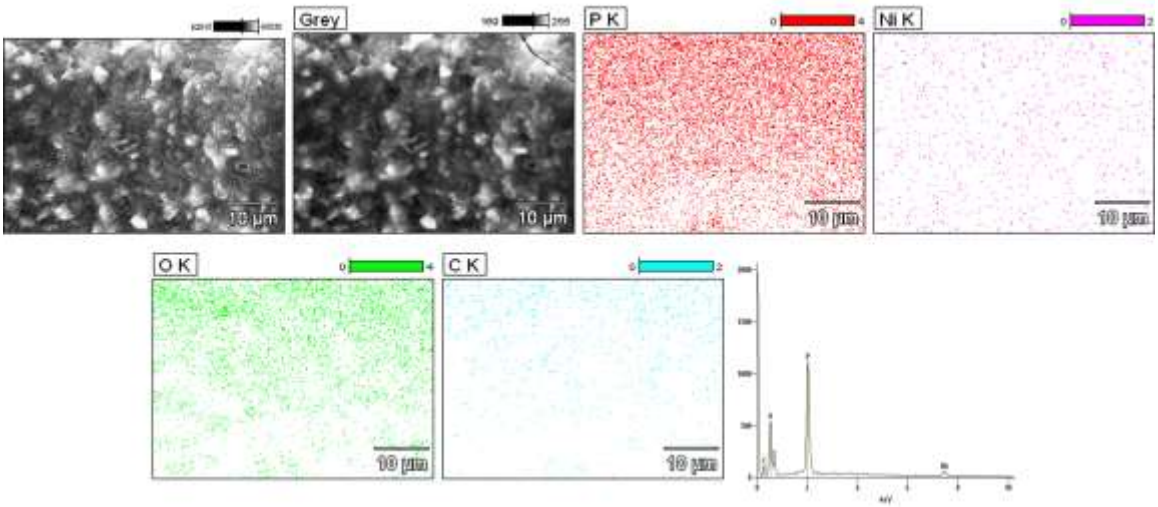

Figure 5S.3: EDS elemental mapping images for P, Ni, O, and C in RP-SPAN hybrid composite after cycling.

Supplementary Information for Chapter 6

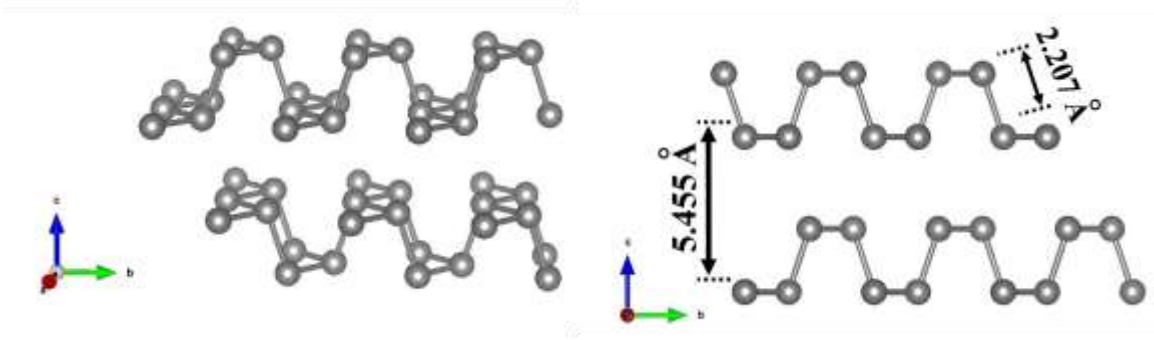

Figure 6S.1: Atomic structure of black phosphorus.

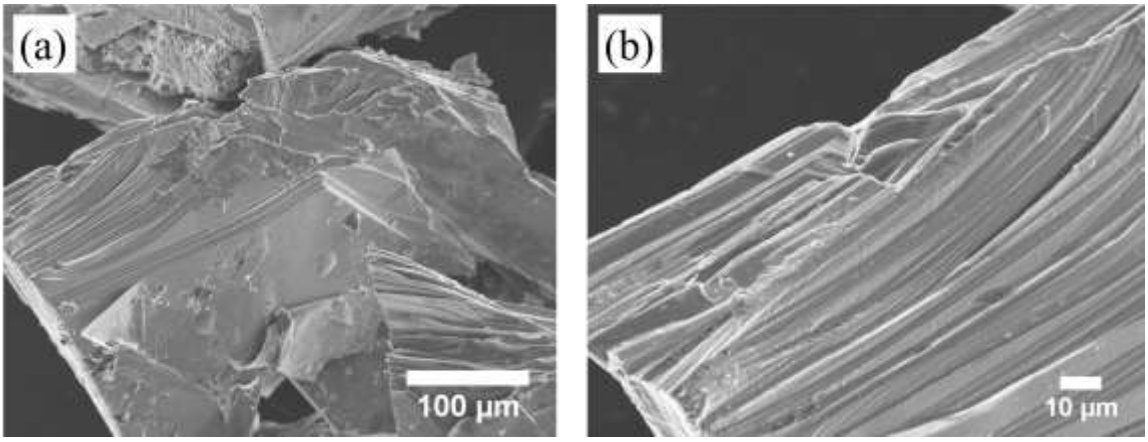

Figure 6S.2: FESEM images of bulk crystal of black phosphorus.

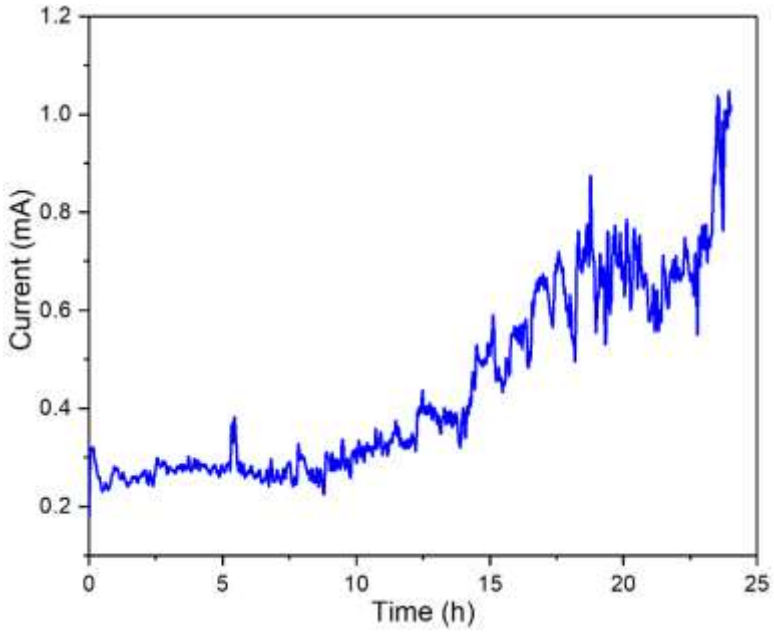

Figure 6S.3: Change of current vs. time during the bipolar exfoliation.

Table 6S.1: Summary of electrochemical performance of 2D materials for micro-supercapacitor application.

Material	Experiment Parameter	Power Density ($\mu W\ cm^{-2}$)	Energy Density ($\mu Wh\ cm^{-2}$)	Ref.
Polyelectrolyte-wrapped Graphene/CNT	100 μAcm^{-2}	20	3.84	[1]
CNT/MnO_2/Polymer Fiber	420 μAcm^{-2}	66.9	2.6	[2]
Modified Graphene sheets	20 $mAcm^{-2}$	749.8	109.6	[3]
Vertically aligned CNT	10	1000	0.1	[4]
Graphene-Ag-3D graphene foam	0.67 $mAcm^{-2}$	270	3.4	[5]
3D Graphene/graphite	500 μAcm^{-2}	24.5	1.24	[6]
2D MnO_2	0.5 Acm^{-2}	639	9.0	[7]
MXene/CNT	2 μAcm^{-2}	2.4	0.05	[8]
PANI/GO	3 $mAcm^{-2}$	200	2.52	[9]
MXene/CNF	0.57 $mAcm^{-2}$	145	0.08	[10]
Laser-assisted GO	1100 μAcm^{-2}	1051	32.1	[11]
Bipolar Exfoliated Phosphorene	500 μAcm^{-2}	351	0.01	This Work

References

[1] L. Kou, T. Huang, B. Zheng, Y. Han, X. Zhao, K. Gopalsamy, H. Sun, C. Gao, Coaxial wet-spun yarn supercapacitors for high-energy density and safe wearable electronics, Nature Communications 5 (2014) 3754.

[2] C. Choi, S.H. Kim, H.J. Sim, J.A. Lee, A.Y. Choi, Y.T. Kim, X. Lepró, G.M. Spinks, R.H. Baughman, S.J. Kim, Stretchable, Weavable Coiled Carbon Nanotube/MnO2/Polymer Fiber Solid-State Supercapacitors, Scientific Reports 5 (2015) 9387.

[3] L. Gao, J. Song, J.U. Surjadi, K. Cao, Y. Han, D. Sun, X. Tao, Y. Lu, Graphene-Bridged Multifunctional Flexible Fiber Supercapacitor with High Energy Density, ACS Applied Materials & Interfaces 10(34) (2018) 28597-28607.

[4] B. Hsia, J. Marschewski, S. Wang, J.B. In, C. Carraro, D. Poulikakos, C.P. Grigoropoulos, R. Maboudian, Highly flexible, all solid-state micro-supercapacitors from vertically aligned carbon nanotubes, Nanotechnology 25(5) (2014) 055401.

[5] L. Manjakkal, C.G. Núñez, W. Dang, R. Dahiya, Flexible self-charging supercapacitor based on graphene-Ag-3D graphene foam electrodes, Nano Energy 51 (2018) 604-612.

[6] A. Ramadoss, K.-Y. Yoon, M.-J. Kwak, S.-I. Kim, S.-T. Ryu, J.-H. Jang, Fully flexible, lightweight, high performance all-solid-state supercapacitor based on 3-Dimensional-graphene/graphite-paper, Journal of Power Sources 337 (2017) 159-165.

[7] J. Qin, S. Wang, F. Zhou, P. Das, S. Zheng, C. Sun, X. Bao, Z.-S. Wu, 2D mesoporous MnO2 nanosheets for high-energy asymmetric micro-supercapacitors in water-in-salt gel electrolyte, Energy Storage Materials 18 (2019) 397-404.

[8] C. Zhang, B. Anasori, A. Seral-Ascaso, S.-H. Park, N. McEvoy, A. Shmeliov, G.S. Duesberg, J.N. Coleman, Y. Gogotsi, V. Nicolosi, Transparent, Flexible, and Conductive 2D Titanium Carbide (MXene) Films with High Volumetric Capacitance, Advanced Materials 29(36) (2017) 1702678.

[9] H. Wei, J. Zhu, S. Wu, S. Wei, Z. Guo, Electrochromic polyaniline/graphite oxide nanocomposites with endured electrochemical energy storage, Polymer 54(7) (2013) 1820-1831.

[10] W. Tian, A. VahidMohammadi, M.S. Reid, Z. Wang, L. Ouyang, J. Erlandsson, T. Pettersson, L. Wågberg, M. Beidaghi, M.M. Hamedi, Multifunctional Nanocomposites with High Strength and Capacitance Using 2D MXene and 1D Nanocellulose, Advanced Materials 0(0) 1902977.

[11] J. Gao, C. Shao, S. Shao, C. Bai, U.R. Khalil, Y. Zhao, L. Jiang, L. Qu, Laser-Assisted Multiscale Fabrication of Configuration-Editable Supercapacitors with High Energy Density, ACS Nano 13(7) (2019) 7463-7470.

Supplementary Information for Chapter 7

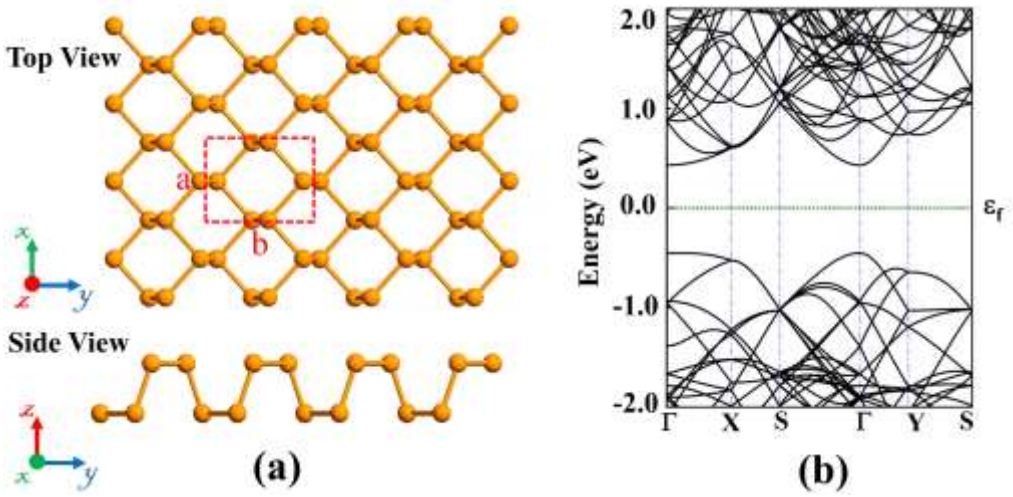

Figure 7S.1: (a) The optimized structure of a bare phosphorene sheet (Top and side view (b) and its corresponding electronic band structure. The dotted green line indicates the Fermi level, which is set to zero (P: Orange and O: red). The unit cell is outlined with red dashed lines.

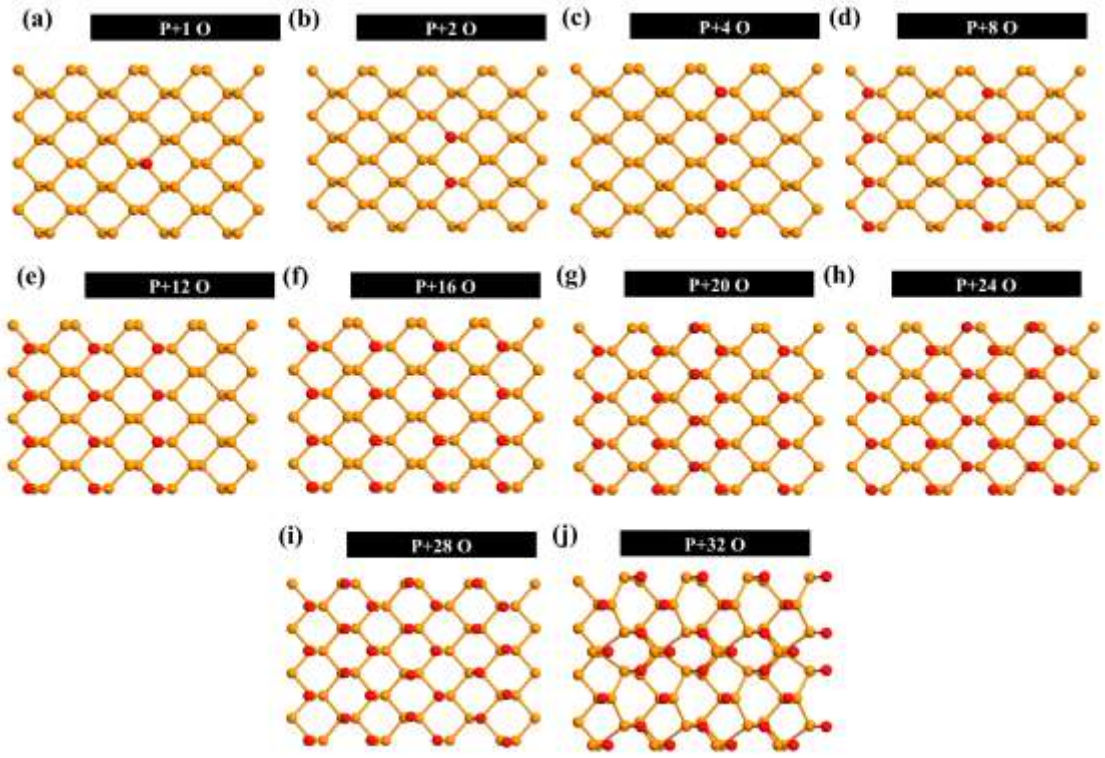

Figure 7S.2: The most stable adsorption configurations for phosphorene oxide sheets with various oxygen concentrations (1-32) (P: Orange and O: red).

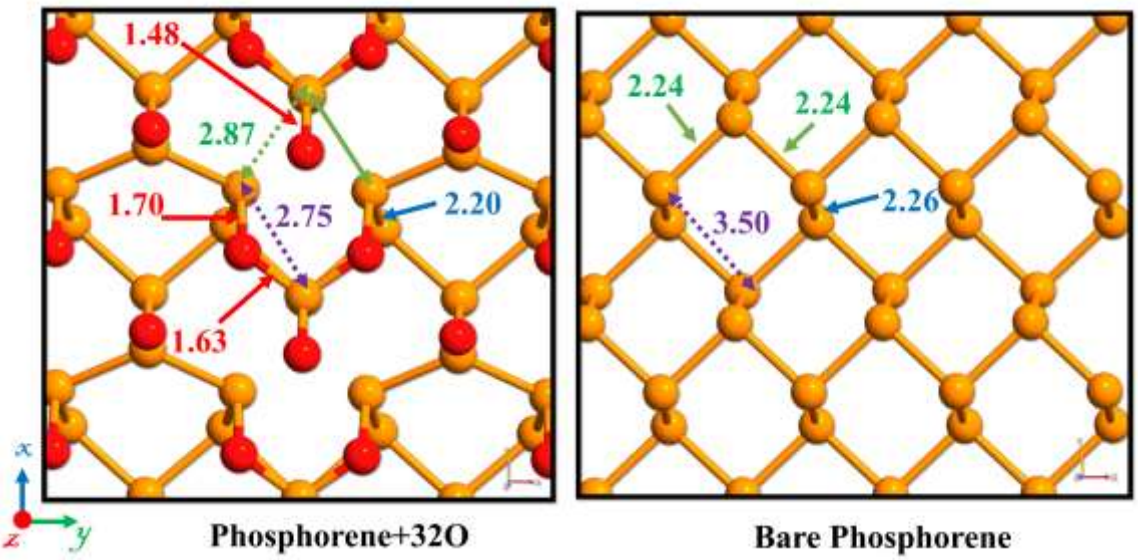

Figure 7S.3: Optimized structures of bare phosphorene and phosphorene with 32 O atoms (P: Orange and O: red). All bond lengths are in Å.

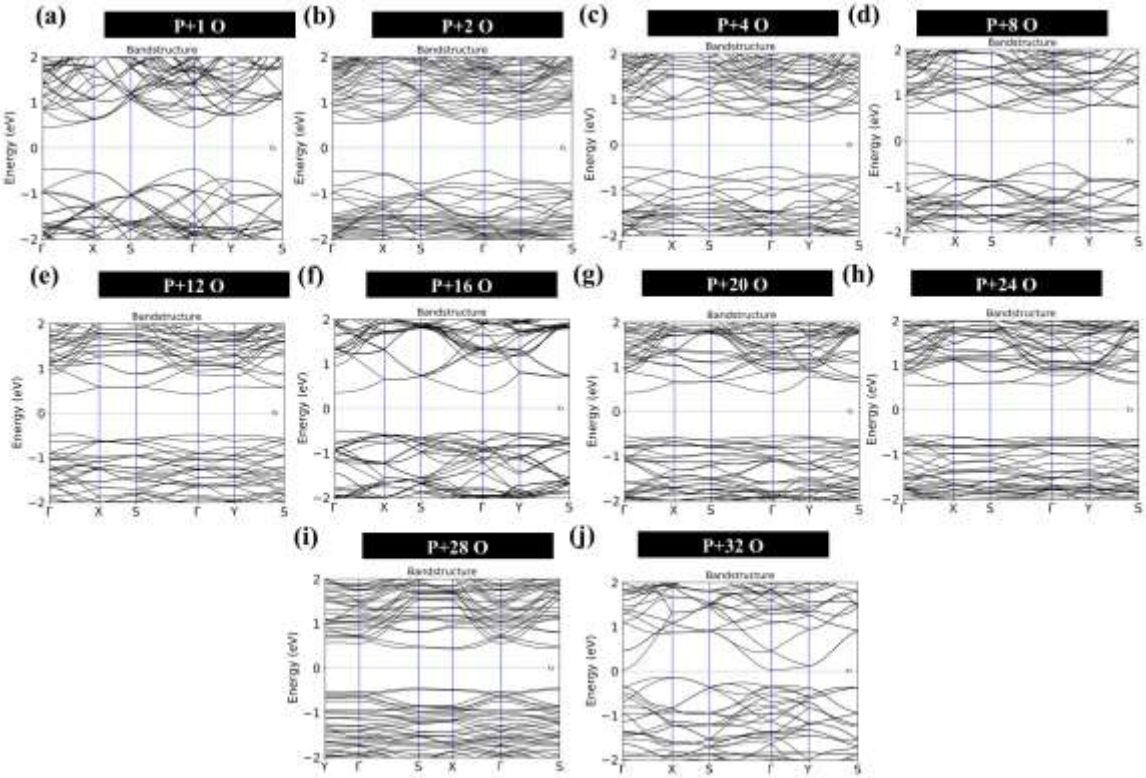

Figure 7S.4: Energy band structures of phosphorene oxide sheets with various oxygen concentrations (1-32). The dotted green line indicates the Fermi level, which is set to zero.

VITA

AMIN RABIEI BABOUKANI

2006-2010	B.Sc., Materials Science and Engineering Azad University of Najafabad Najafabad, Isfahan, Iran
2010-2013	M.Sc., Materials Science and Engineering Azad University of Najafabad Najafabad, Isfahan, Iran
2017-2021	Doctoral Candidate (Ph.D.), Materials Science and Engineering Florida International University Miami, FL, USA

- Dissertation Year Fellowship, Florida International University (2020)
- Doctoral Evidence Acquisition (DEA) Fellowship, Florida International University (2020)

SELECTED PUBLICATIONS:

1. Amin Rabiei Baboukani, Iman Khakpour, Vadym Drozd, Chunlei Wang, "*Liquid-Based Exfoliation of Black Phosphorus into Phosphorene and its Application for Energy Storage Devices*", Small Structures, 306, 2000148, 2021.
2. Amin Rabiei Baboukani, Iman Khakpour, Ebenezer Adelowo, Vadym Drozd, Wei Shang, and Chunlei Wang, "*High-Performance Red Phosphorus-sulfurized polyacrylonitrile Composite by Electrostatic Spray Deposition for Lithium-Ion Batteries*", Electrochimica Acta, 345, 136227, 2020.
3. Amin Rabiei Baboukani, Iman Khakpour, Vadym Drozd, Anis Allagui, Chunlei Wang, "*Single-Step Exfoliation of Black Phosphorus and Deposition of Phosphorene via Bipolar Electrochemistry for Capacitive Energy Storage Application*", Journal of Materials Chemistry A, 7(44), 25548-25556, 2019.
4. Amin Rabiei Baboukani, Ebenezer Adelowo, Richa Agrawal, Iman Khakpour, Vadym Drozd, Wenzhi Li, Chunlei Wang, "*Electrostatic Spray Deposited Sn-SnO2-CNF Composite Anodes for Lithium Ion Storage*", ECS Transactions 85(13): 331-336, 2018.
5. Amin Rabiei Baboukani, Sadegh Mehdi Aghaei, Iman Khakpour, Vadym Drozd, Chunlei Wang, "*Defects Investigation of Bipolar Electrochemically Exfoliated Phosphorene Nanosheets*", Nanotechnology, Under Review.
6. Amin Rabiei Baboukani, Iman Khakpour, Vadym Drozd, Chunlei Wang, *Deposition of Exfoliated Reduced Phosphorene Nanosheets Through Modified Bipolar Electrochemistry for High-Performance Energy Storage Applications*, To be submitted.

7. Amin Rabiei Baboukani, Iman Khakpour, Vadym Drozd, Anis Allagui, Chunlei Wang, "*Deposition of Exfoliated 2D Reduced Phosphorene Nanosheets on the Negative Feeding Electrode*", US Patent 17,015,237, 2021.
8. Amin Rabiei Baboukani, Iman Khakpour, Chunlei Wang, "*Bipolar Exfoliation of Black Phosphorus into Phosphorene*", US Patent 10,676,357, 2020.
9. Anis Allagui*, Amin Rabiei Baboukani*, Ahmed S. Elwakil, Chunlei Wang, "*On the electrochemical stability analysis of red phosphorus-based anode for lithium-ion batteries*", Electrochimica Acta, Under review, *Co-first Author.
10. Ebenezer Adelowo, Amin Rabiei Baboukani, Omena Okpowe, Iman Khakpour, Meer Safa, Chunhui Chen, Chunlei Wang, "*A High-Energy Aqueous On-Chip Lithium-Ion Capacitor Based on Interdigital 3D Carbon Microelectrode Arrays*", Journal of Power Sources, 455, 227987, 2020.
11. Iman Khakpour, Amin Rabiei Baboukani, Anis Allagui, Chunlei Wang, "*Bipolar Exfoliation and In-situ Deposition of High-Quality Graphene for Supercapacitor Application*", ACS Applied Energy Materials, 2(7), 4813-4820, 2019.
12. Meer Safa, Ebenezer Adelowo, Amir Chamaani, Neha Chawla, Amin Rabiei Baboukani, Marcus Herndon, Chunlei Wang, Bilal El-Zahab, "*Poly(Ionic Liquid) based Composite Gel Electrolyte for Lithium Batteries*", ChemElectroChem, 6 (13), 3319-3326, 2019.
13. Richa Agrawal, Amin Rabiei Baboukani, Chunlei Wang, "*Expanding the potential window of aqueous electrochemical capacitors with binder-free electrostatically sprayed manganese oxide composite cathode films*", Materials Research Express, 6 (8), 085012, 2019.
14. Richa Agrawal, Ebenezer Adelowo, Amin Rabiei Baboukani, Michael Franc Villegas, Alexandra Henriques, Chunlei Wang, "*Electrostatic Spray Deposition-Based Manganese Oxide Films-From Pseudocapacitive Charge Storage Materials to Three-Dimensional Microelectrode Integrands*", Nanomaterials, 7(8), 198, 2017.
15. Amin Rabiei Baboukani, Iman Khakpour, Vadym Drozd, Chunlei Wang, "*Exfoliation and Deposition of 2D Phosphorene Nanosheets via Bipolar Electrochemistry for High-Performance Capacitive Energy Storage Applications*", MRS Fall Meeting (virtual), 2020.
16. Amin Rabiei Baboukani, Iman Khakpour, Ebenezar Adelowo, Vadym Drozd, Chunlei Wang, "*Red Phosphorus-Span Composite Anode through Electrostatic Spray Deposition for High Performance Lithium-Ion Batteries*", 235th Electrochemical Society Meeting (ECS), Dallas, 2019.
17. Amin Rabiei Baboukani, Iman Khakpour, Chunlei Wang, "*Exfoliation of black phosphorus into phosphorene by bipolar electrochemistry*", Energy Harvesting and Storage: Materials, Devices, and Applications IX, SPIE Defense + Commercial Sensing 2019, Maryland, (2019).